

Low Temperature Collisions and Reactions in a 22-Pole Ion Trap

Inaugural-Dissertation
zur
Erlangung des Doktorgrades
der Mathematisch-Naturwissenschaftlichen Fakultät
der Universität zu Köln
vorgelegt von
Sven Fanghänel
aus Gera

Köln, 2018

Berichterstatter: Prof. Dr. Stephan Schlemmer
Prof. Dr. Gereon Niedner-Schatteburg

Tag der mündlichen Prüfung: 11.01.2018

When the Going Gets Tough, the Tough Get Going.

- Billy Ocean
- Oskar Asvany (15/11/17)

Zusammenfassung

Die vorliegende Arbeit ist unterteilt in einen experimentellen und einen theoretischen Teil. Der experimentelle Teil befasst sich mit der Untersuchung von Ionen-Molekül Reaktionen in einem temperaturregelbaren 22 Pol Ionenspeicher. Im theoretischen Teil werden verschiedene Aspekte von Radio Frequenz Ionenspeichern und die Dynamik von geladenen Teilchen in diesen analysiert.

Hierfür werden zunächst in Kapitel 3 grundlegende Konzepte für die Beschreibung von geladenen Teilchen in oszillierenden elektrischen Feldern erläutert. Anschließend wird auf die Berechnung dieser Felder mittels verschiedener numerischer Verfahren eingegangen (Kapitel 4). Als besonders effiziente Methode zur Berechnung elektrostatischer Potenziale erwies sich die Randelemente Methode, die daher detailliert erläutert wird. Mittels analytisch lösbarer elektrostatischer Fragestellungen werden die zuvor numerisch berechneten Felder auf ihre Genauigkeit hin untersucht. Für die dafür notwendigen Berechnungen wurden sowohl eigene numerische Routinen entwickelt als auch bestehende Routinen verwendet. Es wird aufgezeigt, wie mit Hilfe einer geeigneten Multipolentwicklung die numerisch berechneten Felder in eine analytische Beschreibung überführt werden können. Dies ermöglicht eine effiziente Simulation und Untersuchung der Dynamik von geladenen Teilchen in Ionenspeichern.

Mittels Simulationen verschiedener existierender Multipol Ionenspeicher (Kapitel 5) wird so das Verhalten von Ionen in elektrischen Wechselfeldern u.a. in Hinblick auf die Erhöhung der Translationsenergie, die Energieverteilung und Verschiebungen der sekulären Oszillationsfrequenz durch höhere Anharmonizitäten analysiert. Darüber hinaus werden Raumladungseffekte und Störungen der Felder durch mechanische Fehljustierungen von Elektroden in die Analyse mit einbezogen. Damit leistet diese Arbeit einen Beitrag zur Optimierung bestehender sowie zur Entwicklung von neuen und besseren Ionenspeichern.

Im Fokus des experimentellen Teils steht die Reaktion von Stickstoffionen N^+ mit Wasserstoffmolekülen H_2 unter Berücksichtigung der Feinstrukturzustände der Stickstoffionen und der Kernspinzuständen des Wasserstoffmoleküls. Diese Reaktion stellt den ersten Prozess bzw. die Vorstufe zur Bildung von interstellarem Ammoniak dar. Trotz jahrzehntelanger Forschung ist diese fundamentale Reaktion bis zum heutigen Tage nicht im Detail verstanden. So ist zum Beispiel offen, ob diese Reaktion endotherm ist oder nur durch eine Barriere gehemmt wird. Weiter ist ungeklärt inwieweit die Energie der Feinstrukturzustände der Stickstoffionen diese Reaktion begünstigt. All diese Fragen sind von großer Relevanz für die Astrochemie bei tiefen Temperaturen. Zur Klärung dieser Fragen möchte diese Arbeit beitragen.

Unter Anwendung eines nicht adiabatischen Reaktionsmodells und einer globalen Anpassung an die gemessenen Daten werden feinstrukturspezifische Ratenkoeffizienten für die oben genannte Reaktion bestimmt (Kapitel 7).

Zunächst wurden hierfür eine Vielzahl verschiedener Testmessungen durchgeführt, um den Einfluss unterschiedlicher Messparameter wie z.B. der Temperatur oder der Teilchenzahldichte auf die gemessenen Ratenkoeffizienten hin zu untersuchen (Kapitel 6). Anhand dieser Testmessungen konnten mögliche Ursachen in Bezug auf die anfänglich teils schlechte Reproduzierbarkeit von Messergebnissen identifiziert werden. Daraufhin wurden verschiedene Messabläufe optimiert, um den Fehler in den zu messenden Ratenkoeffizienten zu minimieren. Als Folge dieser Testmessungen wurden ebenfalls Ratenkoeffizienten für die Reaktion von N_2^+ mit Wasserstoff in einem Temperaturbereich von 10 bis 120 K sowie ternäre Ratenkoeffizienten zur Bildung von Stickstoff-Helium Clustern $(\text{NHe}_n)^+$ ($n = 1, 2$) bei Temperaturen zwischen 10 und 13 K bestimmt (Kapitel 9). Weiterhin wurden Messungen in Hinblick auf eine mögliche Umbesetzung der Feinstrukturzustände der Stickstoffionen durch Stöße mit Helium durchführt.

Darüberhinaus beinhaltet diese Arbeit die Charakterisierung eines piezo-elektrischen Ventils (Kapitel 10). Diese wurde mittels der Reaktion von Argonionen mit Wasserstoffmolekülen durchgeführt. Die Absicht dieser Charakterisierung ist es, die für Ionen-Molekül Reaktionen verwendete Messmethode weiter zu entwickeln. So soll ermöglicht werden, die translatorische Thermalisierung der Ionen sowie deren Relaxation intern angeregter Zustände, von der Reaktion zu trennen. Schlussendlich konnte ein Modell entwickelt werden, welches den Reaktionsgasfluss von Wasserstoff als Funktion der Zeit, der Temperatur und des Reaktionsgasdrucks beschreibt.

Abstract

This work consists of two major parts, a theoretical and an experimental one. The latter part investigates ion molecule reactions performed in a temperature variable 22-pole ion trap. The former one analyses different aspects of radio frequency ion traps and the dynamics of charged particles located inside.

Therefore, fundamental concepts for the description of charged particles in oscillating electrical fields are discussed on as a first step (Chapter 3). The calculation of these fields via different numerical methods is elaborated on subsequently (Chapter 4). The boundary element method (BEM) has proven highly adequate for the calculation of electrostatic potentials. Hence it is depicted in detail. Using analytically solvable electrostatic problems, the previously calculated fields will be tested with respect to their accuracy. To perform the necessary calculations both own numeric routines have been developed and available routines have been employed. This work shows how the numerically, calculated fields can be converted into an analytical description *via* appropriate multipole expansion. This permits an efficient simulation and investigation of the dynamics of charged particles in ion traps. Simulations of different existing multipole ion trap geometries help to analyze the behavior of ions in oscillating fields with respect to, *inter alia*, the increase of their translational energy, their energy distribution and shifts of the secular frequency caused by higher anharmonicities (Chapter 5). Furthermore, space charge effects and perturbations of the fields due to mechanical misalignments of electrodes are included here. Consequently, this work is meant to contribute to the optimization of existing ion traps and to the development of new and better ones.

The experimental part focuses on the reaction of nitrogen ions with hydrogen molecules taking into account the fine structure state of N^+ and the nuclear-spin state of H_2 . This reaction can be considered as the first process or step in the formation of interstellar ammonia. Up to date this very fundamental reaction – although having been studied in several laboratories for decades – is not fully understood. For example, it remains unclear whether or not the reaction really endothermic or it is just inhibited by a barrier. Also, it is not known to what extent the fine structure state energy N^+ favours/promotes this reaction. All these questions are of great relevance for low temperature astrochemistry.

Applying a non-adiabatic reaction model and a global fit, fine structure state specific rate coefficients for the reaction mentioned above could be derived (Chapter 7). Initially, a large number of test measurements were conducted in order to clarify the impact of different measurement parameters like e.g. temperature or number density on measured rate coefficients (Chapter 6).

On the basis of these test measurements probable conclusions of initial difficulties with reproducing test results could be drawn. Thereupon, experimental processes were optimized to minimize errors in determination the rate coefficients. As a result, rate coefficients for the reaction of N_2^+ und CO^+ with hydrogen in a temperature range between 10 to 120 K were determined as well as ternary rate coefficients for the formation of nitrogen-helium-clusters $(\text{NHe}_n)^+$ ($n = 1, 2$) in a temperature range between 10 – 13 K (Chapter 9). Also, measurements were performed with respect to fine structure state changing collisions of the nitrogen ion due to helium. Moreover, this work contains the characterization of a piezoelectric valve which was performed using the reaction of Ar^+ ions with H_2 (Chapter 10). The purpose of the characterization is to develop a new experimental method for the study of ion molecule reactions. This aims at separating translational thermalization of ions as well as their relaxation of the internal excited states from the reaction process. A quantitative model could be developed in order to describe the reaction gas flow as a function of time, temperature and reaction gas pressure.

Contents

1	Introduction	1
2	Charged Particle Traps	3
2.1	Principle of Storing Charged Particles	3
2.2	The Poisson Equation	5
3	Motion of Ions in Oscillating Electric Fields	7
3.1	The Motion of Ions in an Ideal Quadrupole Field	7
3.2	The Motion of Ions in Inhomogeneous Fields	9
3.2.1	The Effective Potential Approximation	9
3.2.2	The Numerical Calculation of the Motion of Ions in Oscillating Fields	14
3.3	The Stability Parameter η	16
4	Methods for Calculations of Electrical Potentials of Ion Traps	18
4.1	Ideal Multipole Traps	18
4.1.1	Two Dimensional Hyperbolic Shaped Multipole Traps	19
4.1.2	Three Dimensional Hyperbolic Shaped Multipole Traps	19
4.2	The Calculation of Electric Fields for Arbitrary Geometries	20
4.2.1	Numerical Methods for the Calculation of Electrical Fields	21
4.3	Multipole Expansions for Different Types of Ion Traps	29
5	Simulations of Different Types of Ion Traps	31
5.1	Approximation of Hyperbolic Shaped Electrodes	31
5.1.1	The Ideal Ratio R/r_0 of a Linear Multipole Trap	32
5.1.2	Influence of Higher Order Multipole Components on a Quadrupole	35
5.2	Influence of the Finite Size of Hyperbolic Electrodes	41
5.3	The Split Ring Electrode Trap	42
5.4	The 22 Pole Ion Trap	49
5.4.1	The Kinetic Energy Distribution	53
5.4.2	Mechanical Misalignments of the RF Electrodes	61
5.5	A Linear 24 Pole Quadrupole Trap	64
5.6	Space Charge Effects	70

6	Experimental Work	84
6.1	Experimental Setup and Techniques	84
6.1.1	Determination of the Reaction Gas Density	86
6.2	Time Evolution of Chemical Reactions	87
6.3	Testing the LIRtrap Setup	88
6.3.1	Tests to Improve the LIRtrap Setup	90
7	$\text{N}^+ + \text{H}_2 \longrightarrow \text{NH}^+ + \text{H}$	98
7.1	The $\text{N}^+(\text{}^3\text{P}_{\text{ja}}) + \text{H}_2(\text{j})$ Reaction	99
7.1.1	The Adiabatic Model	100
7.1.2	The Non-Adiabatic Model	103
7.1.3	Results	114
8	The $\text{N}^+ + \text{H}_2$ Reaction Chain	119
9	Ternary Reaction Processes	124
9.1	$(\text{N}-\text{He}_n)^+$ Cluster	124
9.2	The Ternary Reaction of $\text{N}^+ + \text{H}_2 + \text{He} \rightarrow \text{NH}_2^+ + \text{He}$	126
10	Characterization of a Piezoelectric Valve	132
11	Conclusion and Outlook	153
11.1	Experimental Part	153
11.2	Theoretical Part	154
A	Appendix	164
A.1	Approximation of Hyperbolic Shaped Electrodes	164
A.2	Space Charge Effects	166
A.3	Tests to Improve the LIRtrap Setup	166
A.3.1	The Stability of Guiding and Trapping the Ions	166
A.3.2	Saturation Effects of the Ion Detection System	168
A.3.3	Temperature Behavior of the Reaction Gas Calibration and the $\text{N}_2^+ + \text{H}_2$ Reaction	172
A.3.4	The Number Density of the Reaction Gas at Low Temperatures	177
A.3.5	Measuring Rate Coefficients during the Cool Down Phase of the Apparatus	179
A.3.6	Steady State of the Apparatus	180
A.3.7	Improving the Measurement Procedure	181
A.4	The $\text{N}^+(\text{}^3\text{P}_{\text{ja}}) + \text{H}_2(\text{j})$ Reaction	185
A.4.1	A Simple Approach for the Analysis of Reaction $\text{N}^+ + \text{H}_2(\text{j})$	185
A.5	The Ternary Reaction of $\text{N}^+ + \text{H}_2 + \text{He} \rightarrow \text{NH}_2^+ + \text{He}$	188

CONTENTS

A.6 Characterization of a Piezoelectric Valve	190
Danksagung	192
Lebenslauf	194

Chapter 1

Introduction

Star-formation processes, starting with the collapse of a dense cloud ending with the dying of a star, are the major topics in astrophysics and is ultimately related to the question of the formation of our own solar system and the origin of life on earth. To gain insight into star formation, electromagnetic radiation is the main source of information on the structure and properties of cosmological objects. Here, the interstellar medium (ISM) plays an important role. The temporal evolution of the ISM is determined and accompanied to a large degree by the chemistry and the formation of small molecules in the gas phase. In order to understand gas phase processes, the knowledge of chemical reaction rate coefficients is of fundamental importance. These rate coefficients are used in astronomical network models to calculate molecular abundances, the age of an object or to predict or model the dynamics of interstellar clouds. Ion-molecule reactions are very efficient at very low temperatures in the ISM as many of such reactions have no or low activation energies. Initially, ionization is driven by cosmic rays (high-energy α -particles or protons) $\text{H}_2 + \text{cosmic rays} \rightarrow \text{H}_2^+ + e^-$ or photo-ionization $\text{H} + h\nu \rightarrow \text{H}^+ + e^-$ followed by fundamental reactions such as:



that are the key to the synthesis of more complex molecules in the following. In this respect, rate coefficients of ion-molecule reactions are of fundamental importance for the quantitative understanding of the chemistry in the ISM.

Ion-molecule reactions and their rate coefficients are not only relevant for the insight into astronomical processes but they also play an important role for the chemistry in the ionosphere of the earth (altitude $\gtrsim 100$ km). The main source of ionization is the photo-ionization by solar ultraviolet light or by cosmic rays^[1]. For example, since electrons are able to reflect electromagnetic waves, the electron density in the ionosphere is of practical relevance for the transmission of radio waves. This electron density is determined by the balance between the ionization of atoms and dissocia-

tive recombination of ions with free electrons. This equilibrium is mainly governed by the ion-molecule rate coefficients^[2].

This thesis is divided in two parts, a theoretical and an experimental one. The experimental part is focused on the investigations of astrophysical relevant ion-molecule reactions in a temperature variable 22-pole ion trap apparatus. Here special attention is paid to the reaction of the N^+ with molecular hydrogen under the consideration of the fine structure population of the nitrogen ion in dependence of the nuclear spin configuration of H_2 . This fundamental reaction, which is the first step in the reaction chain to form interstellar ammonia has been investigated by several groups over the last three decades remains is not well understood until today. Here, the role of the energy provided by the fine structure of the nitrogen ion in promoting this reaction is rather unclear whereas the role of the energy dependence on the nuclear spin configuration of the hydrogen molecule is largely understood. To allow precise predictions of the chemical evolution of ammonia a detailed understanding of this reaction mechanism is required. Therefore fine structure specific rate coefficients for this reaction are of great astrophysical interest. A further aspect which makes the reaction so interesting is, that this system is very sensitive to the nuclear spin configuration (ortho/para) of the hydrogen molecule and can therefore be used to investigate the purity of a para hydrogen sample.

The theoretical part covers different aspects of trapping charged particles. Among others, different methods to describe the dynamics of charged particles in inhomogeneous oscillating electric fields will be given. In this context also different methods for the calculation of such electric fields will be presented. Here, especially the boundary element method and their accuracy is described in detail. Based on simulations of various existing radio frequency trapping devices, it will be demonstrated to what extent such calculations can help to understand the behavior of ions in oscillating electric fields and to develop new or to optimize existing trapping devices.

Chapter 2

Charged Particle Traps

Charged particle traps are a powerful tool to investigate the dynamics of charged particles and which are used nowadays in various scientific and commercial applications. Different types of such traps are used e.g. for spectroscopic investigations of ions, for the determination of rate coefficients of chemical reactions or for the measuring and manipulation of quantum systems which may be used for the development of quantum computers.

The development of trapping charged particles in such devices was expedited by W.Paul^[3] and H.G.Dehmelt^[4] who got the Nobel prize in Physics 1989 'for the development of the ion trap technique'. A comprehensive historical overview about storing charged particles can be found in Refs.[5, 6].

The idea of a charged particle trap is to confine or control the trajectories of positive or negative charged particles, using electromagnetic fields. In general, such instruments consist of electrodes to which voltages are applied surround a certain volume (see Fig. 2.1). A detailed description of storing charged particles will be given in the following sections.

2.1 Principle of Storing Charged Particles

In general electromagnetic fields are used to store, guide or mass select positive or negative charged particles. The Lorentz force \mathbf{F}_l influences the trajectories $\mathbf{r}(t)$ of charged particles in an external electric or magnetic field.

$$m\ddot{\mathbf{r}} = \mathbf{F}_l = q\mathbf{E} + e\mathbf{v} \times \mathbf{B} \quad (2.1)$$

Here is \mathbf{E} the electric field, \mathbf{B} the magnetic field, $\mathbf{v} = \dot{\mathbf{r}}$ is the velocity and e respectively m are the charge and the mass of the particle. In the following sections only electrical radio frequency (rf) trapping devices will be discussed ($\mathbf{B} = 0$, $\mathbf{E} \neq 0$). A good overview about many kinds of charged particle traps is given in the book of Major, Gheorghe and Werth^[6].

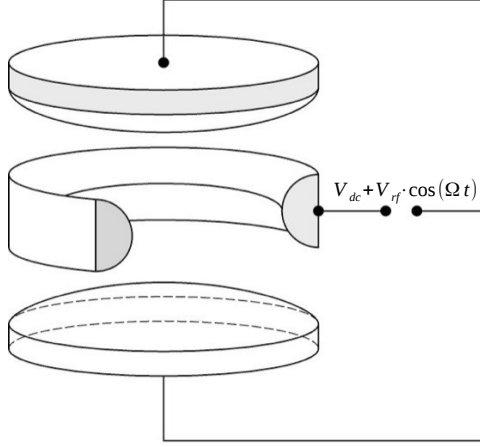


Figure 2.1: The sketch shows a possible electrode configuration of a charged particle trap (<http://www.spektrum.de/lexikon/physik/atom-und-ionenfallen/885>).

A consequence of the 'Earnshaw theorem' is, that it is not possible to store charged particles in static electric fields. One option to avoid this problem is the periodic change of the polarity of an electric field with an angular frequency Ω (see Fig. 2.1) which will result in an oscillating motion of the particle.

In order to describe the behavior or the motion of charged particles in electric trapping devices (ion traps), the knowledge on the driving electric field $\mathbf{E}(t, \mathbf{r})$ is necessary. Here the electric field \mathbf{E} can be calculated from the Maxwell equations. A simplification of the problem is, that one may calculate the electric field in the quasielectrostatic limit^[7] of

$$\frac{\Omega \cdot L}{c} \ll 1. \quad (2.2)$$

Here Ω is the angular frequency of the time varying field, L the length of the device in which the field changes and c the speed of light. Typical values for an ion trap are $L = 0.01 \text{ m}$ and $\Omega = 100 \text{ MHz}$ which leads to:

$$\frac{\Omega \cdot L}{c} = \frac{100 \text{ MHz} \cdot 0.01 \text{ m}}{3 \cdot 10^8 \text{ m/s}} = 0.0033 \ll 1.$$

As a consequence time dependent propagation of electromagnetic waves can be neglected resulting on a separation of the electric field in an oscillating part with an angular frequency Ω and a static part.

$$\mathbf{E}(\mathbf{r}, t) = \cos(\Omega t) \cdot \mathbf{E}(\mathbf{r}) \quad (2.3)$$

Since $\mathbf{E} = -\nabla\Phi$, with the electrostatic potential Φ and $\nabla \cdot \mathbf{E} = \frac{\rho(\mathbf{r})}{\epsilon_0}$ with ρ the space charge, the whole problem reduces to the Poisson equation.

2.2 The Poisson Equation

In general a static electric field $\mathbf{E}(\mathbf{r})$ or the electrostatic potential $\Phi(\mathbf{r})$ of an ion trap are determined by the size, the alignment, the geometry and the applied voltage of its electrodes. Assuming no space charge effects induced by charge particles, the problem of finding the electrostatic potential Φ reduces to the 'Laplace-equation' with Dirichlet boundary conditions

$$\Delta\Phi = 0 \quad \text{with } \Phi_0 \text{ on boundary} \quad (2.4)$$

with being Φ_0 the applied voltage on the electrodes. If one have a relevant amount of charged particles between the electrodes then space charge has taken into account and the electrostatic potential Φ is governed by the 'Poisson-equation'

$$\Delta\Phi = \frac{\rho(\mathbf{r})}{\epsilon_0} \quad \text{with } \Phi_0 \text{ on boundary,,} \quad (2.5)$$

where denotes $\rho(\mathbf{r})$ the space charge distribution induced by the charged particles. The effect of space charge will be discussed in section 5.6. Hence

$$\mathbf{E} = -\nabla\Phi \Rightarrow \nabla\mathbf{E} = -\Delta\Phi = 0 \quad (2.6)$$

a possible solution for ϕ or \mathbf{E} can be found by integrating Eq. 2.6.

$$\mathbf{E}(x, y, z) = ax\mathbf{e}_x + by\mathbf{e}_y + cz\mathbf{e}_z \quad (2.7)$$

If the constants a, b, c are set to $a = b = -2$ and $c = 4$ the electrostatic potential Φ fulfill the Laplace equation (Eq. 2.4).

$$\Phi(x, y, z) = x^2 + y^2 - 2z^2 \quad (2.8)$$

To find the shape of the boundary (the geometry of the electrodes) which fulfills Eq. 2.4 one has to set $\Phi = \Phi_0$. For simplicity one may also set $y = 0$ leading to $\phi_0 = x^2 - 2z^2$. The latter describes equipotential lines with a hyperbolic shape. This implies only infinitively long hyperbolic shaped electrodes have the correct boundary conditions to fulfill the Laplace Equation. If one chooses $r_0 = \sqrt{x_0^2 + y_0^2}$, which is the shortest distance to the electrodes in radial direction, and divide Eq. 2.8 by the constant factor of $2r_0^2$ than Eq. 2.8 results in:

$$\Phi(x, y, z) = \frac{-x^2 - y^2 + 2z^2}{2r_0^2} \quad (2.9)$$

This theoretical example is known as the so called spherical or 3 dimensional 'Paul Trap', which is named after its inventor Wolfgang Paul^[8]. This kind of ion trap consists of two hyperbolic shaped 'endcap' electrodes with a distance to the center of $z_0 = \frac{r_0}{\sqrt{2}}$ and a hyperbolic shaped ring electrode with a distance to the center of r_0 (see Fig. 4.2a). Setting the constants $a = b = -2$ and $c = 0$ in Eq. 2.7 will also

result in a possible solution for the 2 dimensional Laplace equation which is known as the electric potential of the rf part of a linear quadrupol mass filter (QMF) (see Fig. 2.2).

$$\Phi(x, y) = \frac{x^2 - y^2}{r_0^2}. \quad (2.10)$$

These two analytic solutions for the electrostatic potentials are only valid if one assumes infinitively long hyperbolic shaped electrodes. Multiplying Φ by a time varying factor $V_{rf} \cos(\Omega t)$, with V_{rf} being its amplitude, Eq. 2.11 will represent the time varying electric potential.

$$\Phi(\mathbf{r}, t) = V_{rf} \cos(\Omega t) \cdot \Phi(\mathbf{r}) \quad (2.11)$$

The time varying electric field can be calculated as follows:

$$\mathbf{E}(\mathbf{r}, t) = -V_{rf} \cos(\Omega t) \nabla \Phi(\mathbf{r}). \quad (2.12)$$

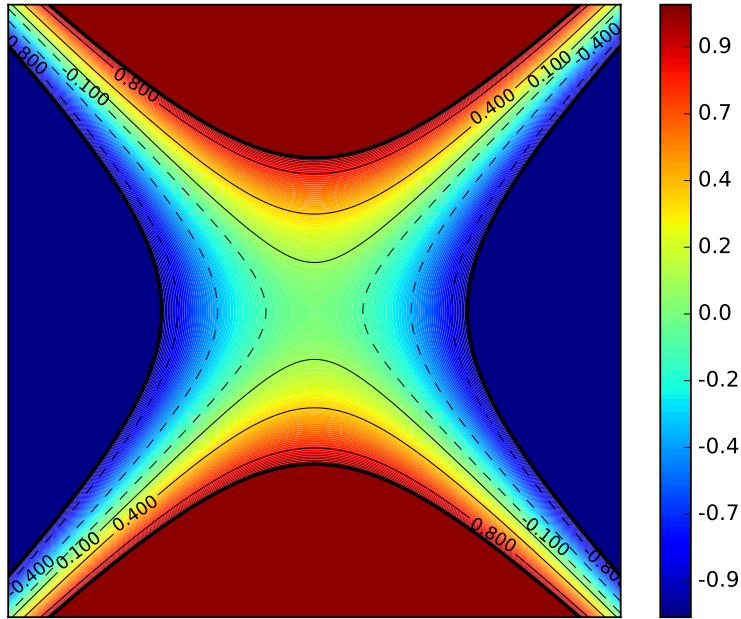


Figure 2.2: The plot shows the electrostatic potential of a QMF (eq. 2.10) produced by hyperbolic electrodes. The thick black lines indicate the boundary of the hyperbolic electrodes.

Some other analytic solutions for special trap geometries can be found in Ref.[5].

Chapter 3

Motion of Ions in Oscillating Electric Fields

In order to describe the motion of ions, one can make use of Newtons Equations of Motion (EoM). Using Newtons law $\mathbf{F} = m\mathbf{a} = e\mathbf{E}(\mathbf{r}, t) = -e\nabla\Phi(\mathbf{r}, t)$, where e is the elementary charge and m is the mass, the motion of ions in time varying electric fields can be described with the classical equation of motion.

$$\ddot{\mathbf{r}}(t) = \frac{e}{m} \cdot \mathbf{E}(\mathbf{r}(t), t) = -\frac{e}{m} \cdot \nabla\Phi(\mathbf{r}(t), t) \quad (3.1)$$

In general it is not possible to find an analytically solution of this equation because it is a highly coupled second order differential equation. Only for some special field geometries Φ it is possible to calculate the motion of the ions analytically.

3.1 The Motion of Ions in an Ideal Quadrupole Field

An ideal oscillating quadrupole field can be described by Eq. 2.11. Additionally, this field can be superimposed by a static potential V_{dc} , which will be defined as follows:

$$\Phi(\mathbf{r}, t) = (V_{dc} - V_{rf} \cos(\Omega t)) \cdot \phi(\mathbf{r}). \quad (3.2)$$

Here, Eq. 2.11 describes only a guiding field for the ions. The static field V_{dc} lead to an additional drift which can be used to select ions by their charge to mass ratio. This means, for certain values of V_{dc} only ions with a specific charge to mass ratio will have stable trajectories in an ideal quadrupole field. For such ideal quadrupole fields an analytic description of stable ion trajectories is possible. With equations. 3.2 and 2.12 the Equations of Motions for a QMF (Eq. 2.10) are:

$$\begin{aligned} \ddot{x}(t) &= -\frac{2e}{mr_0^2} (V_{dc} - V_{rf} \cos(\Omega t)) \cdot x(t) \\ \ddot{y}(t) &= \frac{2e}{mr_0^2} (V_{dc} - V_{rf} \cos(\Omega t)) \cdot y(t) \end{aligned} \quad (3.3)$$

This is a system of second order decoupled time dependent differential equations. Given the following substitution $a_x = -\frac{8eV_{dc}}{m\Omega^2 r_0^2}$, $q_x = \frac{4eV_{rf}}{m\Omega^2 r_0^2}$, $a_y = \frac{8eV_{dc}}{m\Omega^2 r_0^2}$, $q_y = -\frac{4eV_{rf}}{m\Omega^2 r_0^2}$ and $\xi = \frac{\Omega t}{2}$ one can rewrite Eq. 3.3 such as:

$$\frac{d^2 u(\xi)}{d\xi^2} = \pm (a_i - 2q_i \cos(2\xi)) u(\xi) \quad (3.4)$$

with $u = (x, y)$. These differential equations are known as the 'Mathieu Differential Equation'. Using 'Floquets-Theorem', the solution of Eq. 3.3 have the following form [6]:

$$u(t) = Ae^{i\omega_u t} \sum_n C_{2n} e^{in\Omega t} + Be^{-i\omega_u t} \sum_n C_{2n} e^{-in\Omega t} \quad (3.5)$$

Here $\omega_u = \frac{\beta_u \Omega}{2}$. β_u depends on the substituted parameters in the Mathieu equation a_u and q_u . The solutions are stable for $0 \leq \beta_u \leq 1$. A more detailed description of these procedure can be found in Refs. [6, 9]. For each direction (x, y) one will find regions of stability in the a, q plane. The overlap of both regions defines the stability region or so-called stability diagram. Figure 3.1 shows the stability diagram of the first stable region of a QMF.

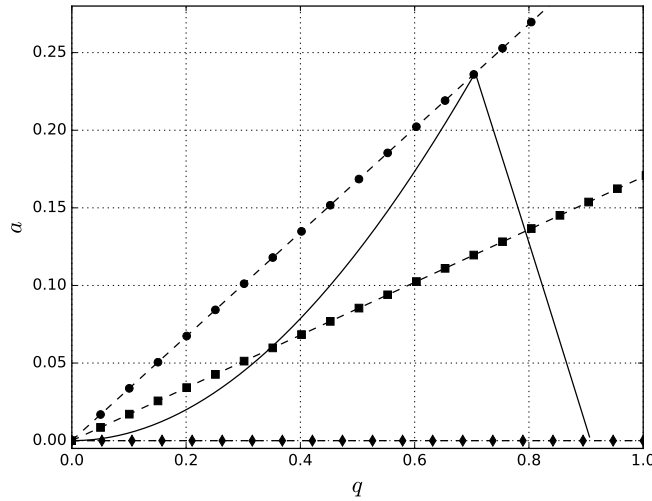


Figure 3.1: The plot shows the stability diagram of the first stability region of a QMF. The solid lines indicate the boundaries of the stable region. The dashed lines illustrate the different operation modes of a QMF. The circles, squares and diamonds represent different masses, where high masses are more left (from $q = 0$) and low masses come from the right side of the plot. In practice a fixed angular frequency Ω is chosen. To receive a mass-spectrum the QMF will operated with a so-called load line or working line which is defined as the ratio of a/q (with a and q defined above). If $V_{dc} = 0$ (diamonds) the QMF will work as a high-pass which means all masses about a critical mass can pass the QMF. If the slope is exactly $V_{dc}/V_{rf} = \frac{1}{2} \cdot \frac{a}{q} = \frac{1}{2} \cdot \frac{0.23699}{0.706}$ (the point which define the top of the stability triangle) the QMF will select to pass through only one mass (circle on the top of the stability triangle). For amplitudes $0 < V_{dc}/V_{rf} < \frac{1}{2} \cdot \frac{0.23699}{0.706}$ all masses (squares) in between the stability triangle will pass the QMF.

Generally there are more than one stability regions. For practical reasons ion traps are operated in the first stable region to avoid exceedingly high values of the angular frequency Ω and the amplitudes of V_{rf} and V_{dc} .

3.2 The Motion of Ions in Inhomogeneous Fields

As mentioned before, it is not possible to find in general analytical solutions to the EoM's because they are nonlinear coupled second order differential equations. One approach is to calculate the trajectories with numerical integration routines or to describe the motion within the so called effective potential approximation¹. In the following a mathematical description of the motion of an ion using the effective potential approximation will be given.

3.2.1 The Effective Potential Approximation

Due to the superposition principle of electric fields, the motion of a charged particle can be described by the following differential equation:

$$\frac{m}{e}\ddot{\mathbf{r}} = \mathbf{E}(\mathbf{r}, t) = \mathbf{E}_{rf}(\mathbf{r}) \cos(\Omega t) + \mathbf{E}_{st}(\mathbf{r}) \quad (3.6)$$

with $\mathbf{E}_{rf}(\mathbf{r})$ being the time varying part and $\mathbf{E}_{st}(\mathbf{r})$ the electrostatic component of the electric field. If one assume that one can superimpose the solution \mathbf{r} as smooth drift motion \mathbf{R}_0 and a fast oscillating motion \mathbf{R}_1 (see Fig. 3.7), one can write \mathbf{r} as:

$$\mathbf{r}(t) = \mathbf{R}_0(t) + \mathbf{R}_1(t) = \mathbf{R}_0(t) - \mathbf{a}(t) \cos(\Omega t) \quad (3.7)$$

where $\mathbf{a}(t)$ is the amplitude of the fast oscillating motion depending on the strength of the electric field at the position $\mathbf{R}_0(t)$. Furthermore one may assume a small spatial variation of $\mathbf{E}(\mathbf{r}, t)$ in time, and expand $\mathbf{E}(\mathbf{r}, t)$ to the first order in $\mathbf{R}_0(t)$

$$\begin{aligned} \mathbf{E}(\mathbf{R}_0(t) - \mathbf{a}(t) \cos \Omega t) &= \mathbf{E}_{rf}(\mathbf{R}_0) \cos(\Omega t) - \mathbf{J}_{\mathbf{E}_{rf}}(\mathbf{R}_0) \cdot \mathbf{a}(t) \cos^2(\Omega t) \\ &+ \mathbf{E}_{st}(\mathbf{R}_0) - \mathbf{J}_{\mathbf{E}_{st}}(\mathbf{R}_0) \cdot \mathbf{a}(t) \cos(\Omega t), \end{aligned} \quad (3.8)$$

where $\mathbf{J}_{\mathbf{E}_i}$ is the Jacobian matrix of the static and the radio frequency electric field. Utilizing the notation $\frac{\partial}{\partial x_i} = \partial_{x_i}$ the Jacobian matrix of an electric field $\mathbf{E} = (E_1, E_2, E_3)$ is defined as follows:

$$\mathbf{J}_{\mathbf{E}} = [\partial_{x_i} E_j] \quad (3.9)$$

Substituting Eq. 3.8 in Eq. 3.6 leads to the following equation.

$$\begin{aligned} m \cdot \left(\ddot{\mathbf{R}}_0(t) - \frac{d^2}{dt^2}(\mathbf{a}(t) \cos(\Omega t)) \right) &= e \mathbf{E}_{rf}(\mathbf{R}_0) \cos(\Omega t) - e \mathbf{J}_{\mathbf{E}_{rf}}(\mathbf{R}_0) \cdot \mathbf{a}(t) \cos^2(\Omega t) \\ &+ e \mathbf{E}_{st}(\mathbf{R}_0) - e \mathbf{J}_{\mathbf{E}_{st}}(\mathbf{R}_0) \cdot \mathbf{a}(t) \cos(\Omega t) \end{aligned} \quad (3.10)$$

¹Also known as the adiabatic approximation.

with

$$\frac{d^2}{dt^2}(\mathbf{a}(t) \cos(\Omega t)) = -\cos(\Omega t) \cdot \Omega^2 \mathbf{a}(t) + \cos(\Omega t) \cdot \ddot{\mathbf{a}}(t) - 2\dot{\mathbf{a}}(t) \Omega \sin(\Omega t) \quad (3.11)$$

If the angular frequency Ω is large and one have slow variation of the amplitude of the fast oscillating motion $\mathbf{a}(t)$ in time then $\dot{\mathbf{a}} \ll \Omega \mathbf{a}$, $\dot{\mathbf{a}} \Omega \ll \Omega^2 \mathbf{a}$ and also $\ddot{\mathbf{a}} \ll \Omega^2 \mathbf{a}$, one can neglect the last two terms in Eq. 3.11.

$$\frac{d^2}{dt^2}(\mathbf{a}(t) \cos(\Omega t)) \approx -\Omega^2 \mathbf{a}(t) \cos(\Omega t) \quad (3.12)$$

Furthermore assuming that $\mathbf{a}(t)$ only changes in time along the smooth drift motion \mathbf{R}_0 one can write $\mathbf{a}(t)$ as (see Ref. [5]).

$$\mathbf{a}(\mathbf{R}_0) = \frac{e\mathbf{E}_{rf}(\mathbf{R}_0)}{m\Omega^2} \quad (3.13)$$

The time dependent fast oscillating term can now be written as:

$$\mathbf{R}_1(t) = -\frac{e\mathbf{E}_{rf}(\mathbf{R}_0)}{m\Omega^2} \cdot \cos(\Omega t) \quad (3.14)$$

Substituting the latter in Eq. 3.10 will lead to:

$$\begin{aligned} m \cdot \ddot{\mathbf{R}}_0(t) + e\mathbf{E}_{rf}(\mathbf{R}_0) \cos(\Omega t) &= e\mathbf{E}_{rf}(\mathbf{R}_0) \cos(\Omega t) \\ &\quad - \frac{e^2}{m\Omega^2} \mathbf{J}_{\mathbf{E}_{rf}}(\mathbf{R}_0) \cdot \mathbf{E}_{rf}(\mathbf{R}_0) \cos^2(\Omega t) \\ &\quad + e\mathbf{E}_{st}(\mathbf{R}_0) - \frac{e^2}{m\Omega^2} \mathbf{J}_{\mathbf{E}_{st}}(\mathbf{R}_0) \cdot \mathbf{E}_{rf}(\mathbf{R}_0) \cos(\Omega t) \end{aligned} \quad (3.15)$$

If one write \mathbf{E} as the negative gradient of the electric potential $\mathbf{E} = -\nabla\Phi$ and using Schwarz's theorem^[10], one may simplify $\mathbf{J}_{\mathbf{E}} \cdot \mathbf{E}$ to

$$\mathbf{J}_{\mathbf{E}} \cdot \mathbf{E} = \frac{1}{2} \nabla \cdot \mathbf{E}^2 \quad (3.16)$$

Canceling out the two equal terms on the left and right side of Eq. 3.15 leads to:

$$\begin{aligned} m \cdot \ddot{\mathbf{R}}_0(t) &= -\frac{e^2}{2m\Omega^2} \nabla \mathbf{E}_{rf}^2(\mathbf{R}_0) \cos^2(\Omega t) \\ &\quad + e\mathbf{E}_{st}(\mathbf{R}_0) - \frac{e^2}{m\Omega^2} \mathbf{J}_{\mathbf{E}_{st}}(\mathbf{R}_0) \cdot \mathbf{E}_{rf}(\mathbf{R}_0) \cos(\Omega t) \end{aligned} \quad (3.17)$$

Averaging Eq. 3.17 with respect to time, $\langle \cos^2(\Omega t) \rangle_t$ becomes $\frac{1}{2}$ and $\langle \cos(\Omega t) \rangle_t$ becomes 0. This leads to a differential equation for the smooth drift motion \mathbf{R}_0 without an oscillating part. Replacing $\mathbf{E}_{st}(\mathbf{R}_0)$ by $-\nabla\Phi_{st}(\mathbf{R}_0)$, the time average of Eq. 3.17 is:

$$m \cdot \ddot{\mathbf{R}}_0 = -\frac{e^2}{4m\Omega^2} \nabla \cdot \mathbf{E}_{rf}^2(\mathbf{R}_0) - e\nabla\Phi_{st}(\mathbf{R}_0) \quad (3.18)$$

If one set

$$V^*(\mathbf{R}_0) = \frac{e^2 \mathbf{E}_{rf}^2(\mathbf{R}_0)}{4m\Omega^2} + e\Phi_{st}(\mathbf{R}_0), \quad (3.19)$$

the ion motion can be described by a time independent potential V^* . The equation of motion for the secular motion or macro motion \mathbf{R}_0 can be written as:

$$m \cdot \ddot{\mathbf{R}}_0 = -\nabla V^*(\mathbf{R}_0) \quad (3.20)$$

The potential V^* has different names like the effective potential, pseudo potential, ponderomotive potential or high frequency potential. If one integrate Eq. 3.20 with respect to time one obtain the following expression

$$\frac{1}{2}m\dot{\mathbf{R}}_0^2 + \frac{e^2 \mathbf{E}_{rf}^2(\mathbf{R}_0)}{4m\Omega^2} + e\Phi_{st}(\mathbf{R}_0) = E_0. \quad (3.21)$$

Hence, in the limit of the adiabatic approximation the energy is a constant which can be converted from the kinetic energy of the macro motion into the effective potential energy. It is straight forward to see that the second term in Eq. 3.21 is the same as the time average of the kinetic energy of the fast oscillating motion $\mathbf{R}_1(t)$ and also similar to the radio frequency part of the effective potential V^* .

$$\left\langle \frac{1}{2}m\dot{\mathbf{R}}_1^2 \right\rangle = \left\langle \frac{e^2 \mathbf{E}_{rf}^2(\mathbf{R}_0)}{2m\Omega^2} \sin^2(\Omega t) \right\rangle = \frac{e^2 \mathbf{E}_{rf}^2(\mathbf{R}_0)}{4m\Omega^2} \quad (3.22)$$

This proves: "The motion through an inhomogeneous field leads to a permanent exchange between three different forms of energy, the kinetic energies, $\frac{1}{2}m\dot{\mathbf{R}}_0^2$ and $\frac{1}{2}m\dot{\mathbf{R}}_1^2$ and the electrostatic potential energy $e\Phi_{st}$ " (Gerlich^[5], p. 14). Figures 3.4 and 3.5 show the different forms of energies of an ion moving in a real 22-pole trap. The validity of this approximation can be proven by integrating Eq. 3.20 and superimposing this motion with the fast oscillating motion, Eq. 3.14. Figures 3.2 and 3.3 show a comparison of the full numerical calculated trajectories of an ion moving in 22-pole trap with a superimposed static electric field \mathbf{E}_{st} ($V_{dc} = 1.5V$) and the trajectories calculated within the adiabatic approximation. For demonstration purposes the stability parameter $\eta(\mathbf{R}_0)$ ^[5] was chosen to be 0.28 at the edge of the stability region. The meaning of the stability parameter $\eta(\mathbf{r})$ will be explained in the next section 3.3.

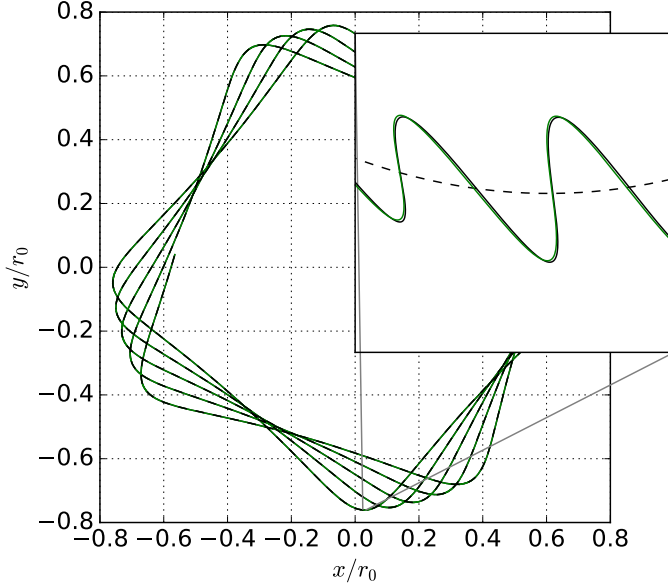


Figure 3.2: The plot shows a comparison of the numerically calculated trajectories (black) of an ion moving in a 22-pole trap with a superimposed static electric field \mathbf{E}_{st} ($V_{dc} = 1.5V$, $\eta(\mathbf{R}_0) = 0.28$) and the trajectories calculated within the effective potential approximation (green). The dashed line in the zoom marks the trajectories of the macro motion.

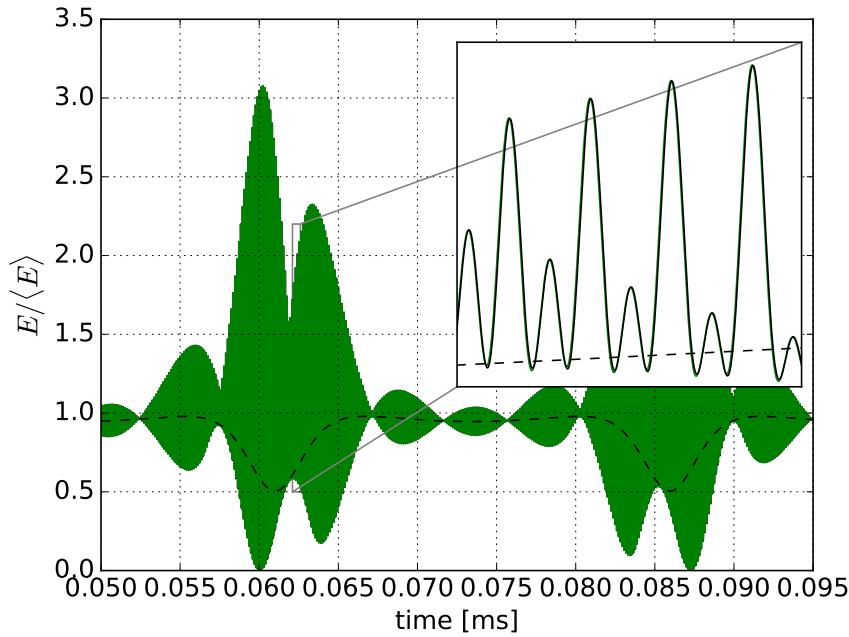


Figure 3.3: The plot shows a comparison of the numerically calculated kinetic energy (black) of an ion moving in a 22-pole trap with a superimposed static electric field \mathbf{E}_{st} ($V_{dc} = 1.5V$, $\eta(\mathbf{R}_0) = 0.28$) and the kinetic energy calculated within the adiabatic approximation (green). The dashed line marks the kinetic energy of the macro motion.

For reasons of completeness the phase dependent initial energy can be expressed in the following form.

$$E_0 = \frac{1}{2}m[\dot{\mathbf{R}}_0(t=0) + \dot{\mathbf{R}}_1(t=0)]^2 + \frac{e^2\mathbf{E}_{rf}^2(\mathbf{R}_0(t=0))}{4m\Omega^2} + e\Phi_{st}(\mathbf{R}_0(t=0)) \quad (3.23)$$

The dependence of the initial phase δ can be taken into account if one sets

$$\dot{\mathbf{R}}_1(t) = \frac{e\mathbf{E}_{rf}(\mathbf{R}_0)}{m\Omega} \cdot \sin(\Omega t + \delta). \quad (3.24)$$

For $\delta = 0$ Eq. 3.23 will lead to Eq. 3.21.

Figures 3.4 and 3.5 illustrate that the total time averaged energy (Eq. 3.25) of the ion motion is a constant.

$$\langle E_{total}(t) \rangle = \langle \frac{1}{2}m[\dot{\mathbf{R}}_0(t) + \dot{\mathbf{R}}_1(t)]^2 + e\Phi_{st}(\mathbf{R}_0(t)) \rangle = const. \quad (3.25)$$

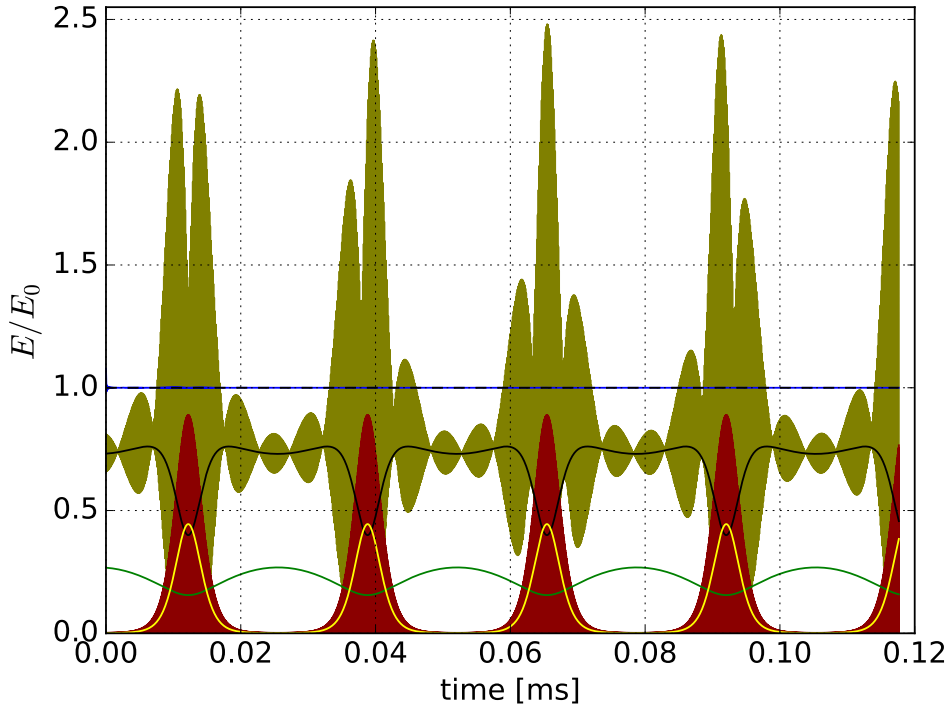


Figure 3.4: The plot shows the different forms of energies for an ion moving in a real 22-pole trap ($V_{dc} = 1.5V$, $\eta(\mathbf{R}_0) = 0.28$) as a function of the time. The green line shows the potential energy of the static electric field $\mathbf{E}_{st}(\mathbf{R}_0(t))$. The yellow line illustrates the energy from the rf-part of the effective potential $V_{rf}^*(\mathbf{R}_0(t))$. The solid black line shows the energy of the macro motion $\dot{\mathbf{R}}_0(t)$ and the red line from the micro motion $\dot{\mathbf{R}}_1(t)$. The dashed black line shows the sum of the potential energy from the static electric field, the energy from the rf-part of the effective potential and the energy from the macro motion. This sum confirms Eq.3.21. The olive colored line shows the sum of the energy from the macro and micro motion. The blue line (behind the black dashed line) shows the cumulative time average $\langle \frac{1}{2}m[\dot{\mathbf{R}}_0(t) + \dot{\mathbf{R}}_1(t)]^2 + e\Phi_{st}(\mathbf{R}_0(t)) \rangle$.

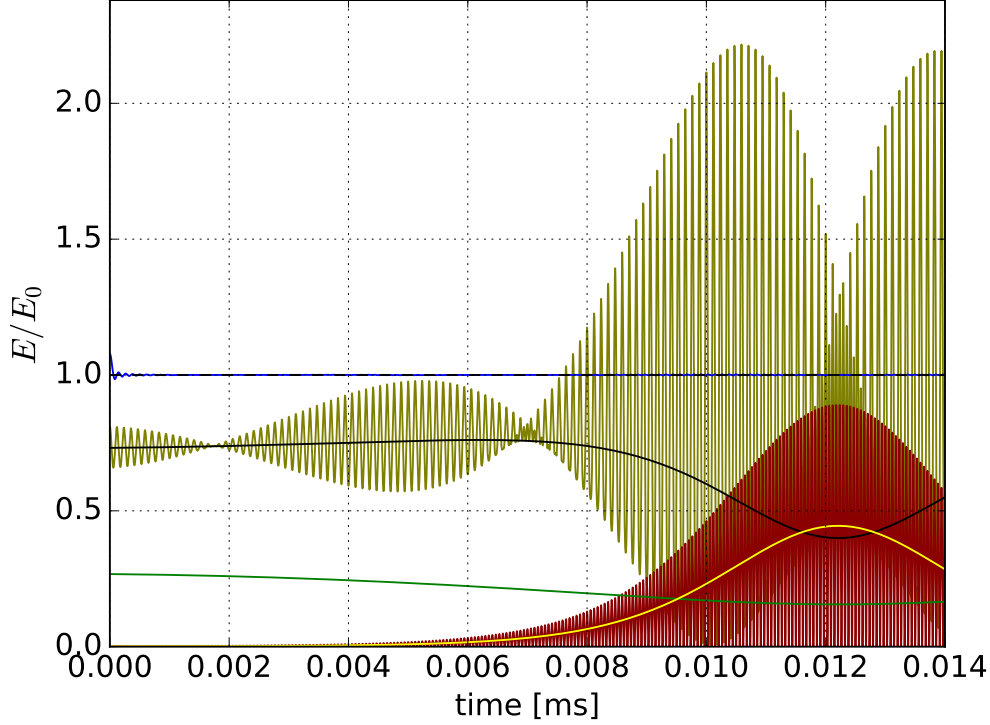


Figure 3.5: The plot shows a zoom for the first time interval of Figure 3.4. The blue line, the cumulative time average $\langle \frac{1}{2}m[\dot{\mathbf{R}}_0(t) + \dot{\mathbf{R}}_1(t)]^2 + e\Phi_{st}(\mathbf{R}_0(t)) \rangle$ reach a stable value after a few rf-periods. This nicely illustrates, that the mean total energy is conserved.

3.2.2 The Numerical Calculation of the Motion of Ions in Oscillating Fields

To investigate the consequences of non ideal fields to the ion motion inside an ion trap one has to observe and evaluate the trajectories of the ions. This can also be done by calculating the trajectories of ions moving in inhomogeneous fields with numerical methods. From such calculations one gets an explicit impression of the behavior (micro and macro-motion) of ions in an oscillating electrical field. Additionally collisions with a background gas inside a trap or space charge effects, which arise from the coulomb repulsion of an ion cloud can be included and evaluated statistically in such simulations. For this purpose the Equations of Motions (Eq. 3.1) have to be solved numerically. In order to do so one has to integrate these equations twice in time. This can be done with different numerical integration algorithms like the Euler method or Runge Kutta methods (for example, Ref. [11]). To solve second order differential equations there are special numeric algorithms like the Nystrom-Kutta method. For all the numerical calculations of trajectories in this thesis the Runge-Kutta-Nystroem-method^[12] of fourth order, with a fixed step size h of $h = \pi/60$ was used. The used algorithm was tested and compared to the analyt-

ical solution of an ideal quadrupole (see Sec. 3.1) to ensure that the step size is small enough to be sensitive to small perturbations of $\Phi(\mathbf{r}(t), t)$. Figures 3.6 and 3.7 show the comparison for trajectories calculated with the Runge-Kutta-Nystroem-method and the analytical solution, derived by mathematica, for $a = 0.23651$ and $q = 0.706$ and initial values of $(x_0, y_0) = (0.1 \cdot \cos(\frac{1}{8}\pi), 0.1 \cdot \sin(\frac{1}{8}\pi))$ with an initial velocity of $(u_0, v_0) = (0, 0)$. The comparison shows, that a step size of $h = \pi/60$ is appropriate for numerical calculations of ion trajectories.

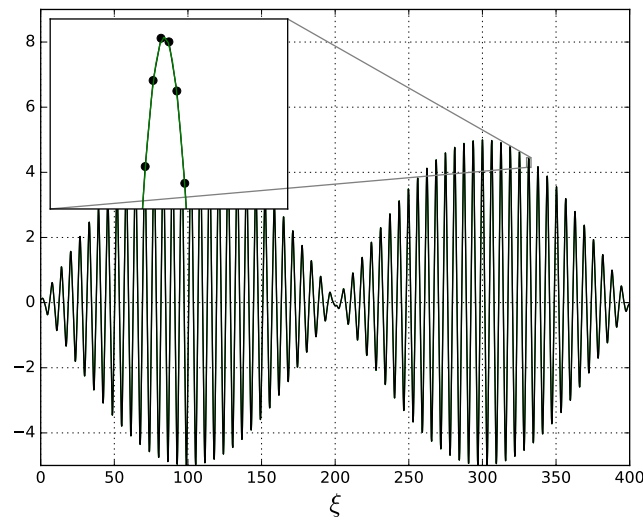


Figure 3.6: The plot shows the comparison of the analytic (black dots) and numeric (green line) solution for the trajectory for $x(\xi)$.

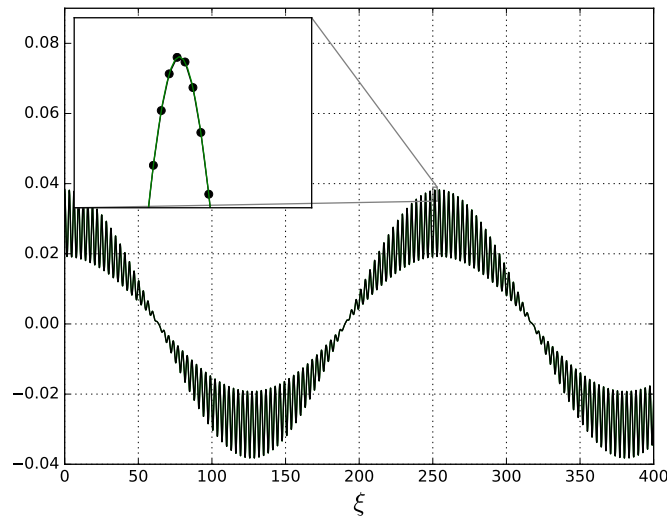


Figure 3.7: The plot shows the comparison of the analytic (black dots) and numeric (green line) solution for the trajectory for $y(\xi)$.

3.3 The Stability Parameter η

As mentioned above, regions of stability as a function of the parameters a, q can only be given for the special case of a quadrupole field. This is based on the fact, to best of my knowledge, that no analytical solutions of the equation of motions for oscillating inhomogeneous fields (eq. 3.1) are available. One possibility to find regions of stability for higher order multipole traps is to simulate numerical trajectories as a function of their initial conditions. This was done by Hägg and Szabo^[13] for the transmission of a hexapole and octopole. Due to the enormous amount of initial parameters such an approach lead to a huge numerical effort. To evaluate the influence of inhomogeneities of the field to the stable ion motion, such an effort has to be done for each individual trap design.

A different approach is to evaluate the stability in the adiabatic approach of the effective potential approximation. Gerlich^[5] introduced a dimensionless stability parameter $\eta(\mathbf{r})$ which is defined as follows:

$$\eta(\mathbf{r}) = \left| \frac{2e}{m\Omega^2} \nabla |\mathbf{E}(\mathbf{r})| \right| \quad (3.26)$$

Gerlich^[5] gives a heuristic criterion $\eta(\mathbf{r}) \leq 0.3$ for save or stable operations in an ion trap. In general η is a scalar function of the spatial coordinate \mathbf{r} (see Fig. 3.8). Another approach is to compare the force of the trapping field

$$|\mathbf{F}_{trap}(\mathbf{r})| = e|\mathbf{E}(\mathbf{r})| \quad (3.27)$$

to the force of the effective potential.

$$|\mathbf{F}_{effective}(\mathbf{r})| = |\nabla V^*(\mathbf{r})| \propto 2|\mathbf{E}(\mathbf{r})| |\nabla |\mathbf{E}(\mathbf{r})|| \quad (3.28)$$

The ratio of Eq.3.28 and 3.27 lead to a parameter which is proportional to η .

$$\frac{|\mathbf{F}_{effective}(\mathbf{r})|}{|\mathbf{F}_{trap}(\mathbf{r})|} = \frac{1}{4}\eta(\mathbf{r}) \quad (3.29)$$

In case of a 2 dimensional quadrupole field Eq.2.10 the parameter η is identical with the rf-parameter q in the Mathieu equation 3.4.

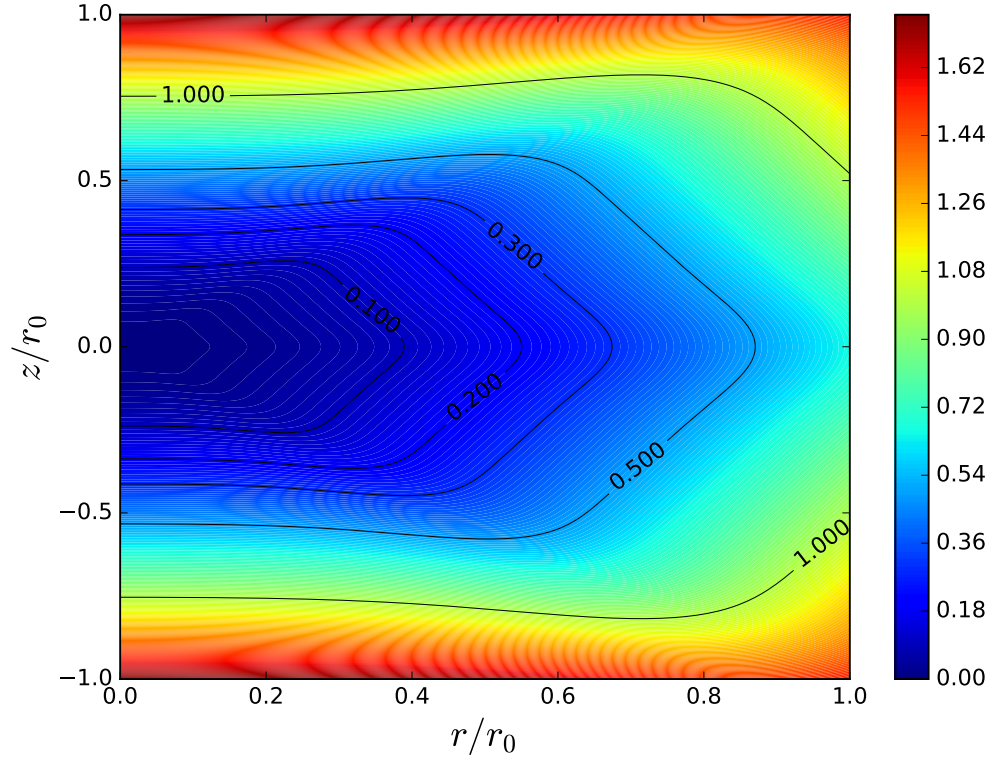


Figure 3.8: The plot shows the η -map for a spherical octopole with the rf voltage $V = 400$ V, the mass $m = 100$ [amu] and the frequency $f = 2$ Mhz. The solid lines indicate different values of η for a given set of trapping parameters V , m , and f . It can be seen that $\eta \leq 0.3$ is valid for radii $\lesssim 40\%$ of r_0 .

Chapter 4

Methods for Calculations of Electrical Potentials of Ion Traps

In this chapter an overview will be given about methods for the calculations of electric potentials. First, the electric potentials of a linear quadrupole mass filter (QMF) and spherical quadrupole (Paul-Trap) will be discussed. Furthermore, it will be demonstrated how to calculate numerically electric potentials for arbitrary trap geometries. Also a short overview about the different numerical methods for such calculations will be given. Especially the Boundary Element Method and its accuracy based on examples will be discussed in detail. Following this, it will be shown how these numerical solutions can be transferred in an analytical expression based on an appropriate multi-pole expansions.

As mentioned in chapter 2.1, the electrical potential Φ has to fulfill the Laplace equation. A general solution of the Laplace equation 2.4 in spherical coordinates is represented by the following expansion:

$$\Phi(r, \theta, \phi) = \sum_{l=0}^{\infty} \sum_{m=0}^l c_{m,l} \left(\frac{r}{r_0} \right)^l (Y_{m,l}(\theta, \phi)). \quad (4.1)$$

Here $c_{m,l}$ are the multipole coefficients of order m, l . r the distance from the origin, r_0 the normalized length, and

$$Y_{m,l} = P_{m,l}(\cos(\theta))e^{im\phi} \quad (4.2)$$

the spherical harmonics and $P_{m,l}$ the associated Legendre polynomials. With this expansion it is possible to give simple formulas for ideal multipole traps. (More practicable formulas can be found in many textbooks Ref.[5–7, 14]).

4.1 Ideal Multipole Traps

A theoretical, ideal multipole trap consists of perfectly shaped and infinitively long conductors. The shape of these conductors has to fulfill the boundary conditions

of the Laplace equation 2.4. Following Eq. 4.1 the shape can be derived for a fixed order m, l lines at a fixed potential Φ_0 .

$$\Phi_0 = c_{m,l} \left(\frac{r}{r_0} \right)^n P_n^l(\cos(\theta)) e^{im\phi} \quad (4.3)$$

Φ_0 describes the shape of conductors (electrodes) of the multipole trap. For certain symmetries and dimensions Eq. 4.1 can be simplified.

4.1.1 Two Dimensional Hyperbolic Shaped Multipole Traps

Assuming infinitely long conductors as electrodes, the z dependence of the electric potential can be neglected and Eq. 4.1 reduces in polar coordinates to

$$\Phi(r, \phi) = \sum_{n=0}^{\infty} \left(\frac{r}{r_0} \right)^n (a_n \cos(n\phi) + b_n \sin(n\phi)) \quad (4.4)$$

where a_n, b_n are the symmetric and antisymmetric expansion coefficients and r_0 is the closest distance from the center of the trap to the electrode surface (normalized length). The electric field $\mathbf{E} = -\nabla\Phi$ of two dimensional multipole traps in polar coordinates can be written as:

$$\begin{aligned} \mathbf{E} &= - \left(\frac{\partial}{\partial r} \Phi(\mathbf{r}), \frac{1}{r} \frac{\partial}{\partial \phi} \Phi(\mathbf{r}) \right) \\ &= \sum_{n=1}^{\infty} \frac{n}{r_0} \left(\frac{r}{r_0} \right)^{n-1} [-(a_n \cos(n\phi) + b_n \sin(n\phi)), (a_n \sin(n\phi) - b_n \cos(n\phi))] \end{aligned} \quad (4.5)$$

or in Cartesian coordinates:

$$(E_x, E_y) = \sum_{n=1}^{\infty} \frac{n}{r_0} \left(\frac{r}{r_0} \right)^{n-1} [-(a_n \cos(\tilde{n}\phi) + b_n \sin(\tilde{n}\phi)), (a_n \sin(\tilde{n}\phi) - b_n \cos(\tilde{n}\phi))]$$

with $\tilde{n} = n - 1$. For $n = 2$ and a symmetric alignment of the electrodes Eq. 4.4 reduces to

$$\Phi(r, \phi) = a_2 \left(\frac{r}{r_0} \right)^2 \cos(2\phi) = a_2 \frac{x^2 - y^2}{r_0^2}. \quad (4.6)$$

This equation represents the quadrupole potential with hyperbolic shaped surfaces as electrodes (see Fig. 2.2).

4.1.2 Three Dimensional Hyperbolic Shaped Multipole Traps

If one assumes some symmetry with respect to the z -axis, this induces an independence on the angle ϕ , Eq. 4.1 reduces to

$$\Phi(r, \theta) = \sum_{n=0}^{\infty} c_n \left(\frac{r}{r_0} \right)^n P_n(\cos(\theta)) \quad (4.7)$$

where $P_n(\cos(\theta))$ are the Legendre polynomials of order n with respect to the angle θ and r_0 is the distance from the center of the trap to the electrode surface. For $n = 2$ and $c_2 = 1$ Φ reduces to

$$\Phi(r, \theta) = \left(\frac{r}{r_0}\right)^2 P_2(\cos(\theta)) = \frac{-r^2 + 2z^2}{2r_0^2} \quad (4.8)$$

the electric potential of time varying part (Φ_{rf}) of a spherical Paul-Trap (see Eq. 2.9). It is clearly visible, that the description for the two and three dimensional case is only valid under the assumption of hyperbolic shaped and infinitely long electrodes. For real trap geometries other methods have to be applied in order to solve for the electric potential.

4.2 The Calculation of Electric Fields for Arbitrary Geometries

In this section, different numerical methods to calculate electrical potentials will be highlighted. Advantages and disadvantages of different numerical methods will be shown. A short mathematical introduction to the Boundary Element Method (BEM) will be given. In addition, the accuracy of the calculated solutions with BEM will be discussed in detail based on three examples. Also the benefit of the description of the solutions via an appropriate multipole expansion will be explained based on real existing examples.

Due to the superposition principle, the electrical field of an ion trap can be represented by a time dependent oscillating part $\mathbf{E}_{rf}(\mathbf{r}, t)$ and static part $\mathbf{E}_{st}(\mathbf{r})$ which leads into

$$\mathbf{E}(\mathbf{r}, t) = \mathbf{E}_{rf}(\mathbf{r}, t) + \mathbf{E}_{st}(\mathbf{r}) = \cos(\omega t + \theta) \cdot \mathbf{E}_{rf}(\mathbf{r}) + \mathbf{E}_{st}(\mathbf{r}) \quad (4.9)$$

With Eq. 2.6 the electric potential Φ can be expressed by:

$$\Phi(\mathbf{r}, t) = \Phi_{rf}(\mathbf{r}, t) + \Phi_{st}(\mathbf{r}) = \cos(\omega t + \theta) \cdot \Phi_{rf}(\mathbf{r}) + \Phi_{st}(\mathbf{r}) \quad (4.10)$$

where θ is an arbitrary phase. To separate the oscillating rf part from the static part of the field two cases must be calculated:

1. $\cos(\omega t_0 + \theta) = 1 \Rightarrow \Phi_0(\mathbf{r}, t_0)$
2. $\cos(\omega t_1 + \theta) = -1 \Rightarrow \Phi_1(\mathbf{r}, t_1)$

The addition and subtraction of these cases results into the static and oscillating part of the field.

$$\implies \Phi_{st}(\mathbf{r}) = \frac{1}{2} \cdot (\Phi_0 + \Phi_1) \text{ and } \Phi_{rf}(\mathbf{r}) = \frac{1}{2} \cdot (\Phi_0 - \Phi_1) \quad (4.11)$$

4.2.1 Numerical Methods for the Calculation of Electrical Fields

For two dimensional problems like the electric potential Φ of a QMF with circular electrodes instead of hyperbolic shaped ones, it is possible to calculate the electric potential with semi analytical methods. Under the assumption of an infinite length and use of complex analysis it is possible to calculate the electric potential with a so called conformal mapping^[15].

To the best of my knowledge, for real traps with a finite geometry, there are no analytic solutions available. Therefore one has to calculate the potential numerically. There are several methods to do this. The main idea is the discretization of the continuous problem and the conversion into a system of linear equations. The most popular methods are:

1. the finite difference method (FDM)
2. the finite element method (FEM)
3. the boundary element method (BEM)

There is a lot of commercial software (Simion¹, Comsol², CPO³, Integrated⁴ ...) available which using the different methods.

The FDM method makes use of the Taylor theorem to approximate the solution applying the central difference method on a grid^[12,16]. This gives a $n \times n$ system of linear equations for a one dimensional problem with n grid points.

The FEM also discretizes the space where the solution is required. The problem is disassembled on a grid in so called ansatzfunctions. With a linear combination of these ansatzfunctions one gets an approximated solution of the problem^[17].

The BEM method makes use of Greens second identity to reformulate the problem in an integral equation. This will be explained in more detail in the following section. The first two methods (FDM, FEM) have major disadvantages compared to the BEM method. For the formulation of the numeric problem one has to discretize the complete space, i.e. the electrodes and the space between the electrodes. For calculations with high accuracy (especially for three dimensional problems) this will lead to a tremendous pc-memory effort. Another disadvantage is that one can calculate the solution only on given grid points. For points inbetween one has to interpolate which leads to numerical errors. A further problem of these two methods are that discretized space is finite, leading to the question: What are the right boundary conditions? However, the advantage of these two methods is that it allows for solving a huge amount of linear and nonlinear problems in physics and engineering. Furthermore, these methods are mathematically simpler (less computationally demanding) to implement in numeric algorithms.

¹<http://simion.com/>

²<https://www.comsol.de/>

³<http://simion.com/cpo/>

⁴<https://www.integratedsoft.com/>

The Boundary Element Method

In difference to the FDM and FEM, the BEM needs only a discretization of the boundary. Actually this is the reason for the name of the method. In the case of electrostatic problems, only the surface of the electrodes needs to be discretized. Therefore the problem is reduced by one dimension (the surface of a three dimensional manifold is two dimensional).

As mentioned before, the BEM method make use of Green's second identity^[18]. This allows to write the solution $\Phi(\mathbf{x})$ for a $\mathbf{x} \in \Omega \subset \mathbb{R}^n$ as an integral equation^[19],

$$\Phi(\mathbf{x})\eta(\mathbf{x}) = \oint_{\Gamma} g(\mathbf{x}, \mathbf{y}) \frac{\partial}{\partial n} \Phi(\mathbf{y}) d\Gamma(\mathbf{y}) - \oint_{\Gamma} \frac{\partial}{\partial n} g(\mathbf{x}, \mathbf{y}) \Phi(\mathbf{y}) d\Gamma(\mathbf{y}) \quad (4.12)$$

$\mathbf{x} \in \Omega$, $\mathbf{y} \in \Gamma$ with Γ a smooth boundary (surface of the electrodes), $\Phi(\mathbf{y})$ (the applied voltage at the electrodes) and $\eta(\mathbf{x})$ defined as:

$$\eta(\mathbf{x}) = \begin{cases} 0 & \text{if } \mathbf{x} \text{ inside the electrodes} \\ 1 & \text{if } \mathbf{x} \text{ outside the electrodes} \\ \frac{1}{2} & \text{if } \mathbf{x} \text{ on the electrodes.} \end{cases} \quad (4.13)$$

$\frac{\partial}{\partial n} = n_x \frac{\partial}{\partial x} + n_y \frac{\partial}{\partial y} + n_z \frac{\partial}{\partial z}$ denotes the normal derivative and $g(\mathbf{x}, \mathbf{y})$ is the fundamental solution for the Laplace problem for $n = 2, 3$.

$$g(\mathbf{x}, \mathbf{y}) = \begin{cases} -\frac{1}{2\pi} \ln |\mathbf{x} - \mathbf{y}|, & n = 2 \\ \frac{1}{4\pi |\mathbf{x} - \mathbf{y}|}, & n = 3. \end{cases} \quad (4.14)$$

For electrostatic problems Eq. 4.12 can be simplified. In electrostatic problems electrodes are held on a fixed potential. Therefore $\Phi(\mathbf{y}) = \Phi_0$ is a constant for each electrode. This corresponds to the so called exterior Dirichlet problem. The only unknown in Eq. 4.12 is $\frac{\partial}{\partial n} \Phi(\mathbf{y})$ which is proportional to the surface charge density^[7]. The first and second integral on the right side of Eq. 4.12 are often denoted as single and double layer potential operators.

$$S(\mathbf{x}) = \oint_{\Gamma} g(\mathbf{x}, \mathbf{y}) \frac{\partial}{\partial n} \Phi(\mathbf{y}) d\Gamma(\mathbf{y}) \quad (4.15)$$

$$D(\mathbf{x}) = \oint_{\Gamma} \frac{\partial}{\partial n} g(\mathbf{x}, \mathbf{y}) \Phi(\mathbf{y}) d\Gamma(\mathbf{y}) \quad (4.16)$$

One can show, that in the case of a fixed potential ($\Phi_0 = \text{const.}$ at each electrode) the double layer potential $D(\mathbf{x})$ reduces to^[20]:

$$D(\mathbf{x}) = \begin{cases} 0 & \text{if } \mathbf{x} \text{ outside the electrodes} \\ \Phi_0 & \text{if } \mathbf{x} \text{ inside the electrodes} \\ \frac{\Phi_0}{2} & \text{if } \mathbf{x} \text{ on the electrodes} \end{cases} \quad (4.17)$$

With this and for $\mathbf{x} \in \Gamma$ Eq. 4.12 simplifies to:

$$\Phi(\mathbf{x}) = \oint_{\Gamma} g(\mathbf{x}, \mathbf{y}) \frac{\partial}{\partial n} \Phi(\mathbf{y}) d\Gamma(\mathbf{y}) \quad (4.18)$$

To illustrate how to work with Eq. 4.18 an example for the 2 dimensional case will be given.

First one has to discretize the boundary (surface of the electrodes) in N elements Γ_e , which in this case are linear elements. Dividing the surface in more and more elements a better approximation for the electrodes is obtained (see Fig 4.1).

Assuming that $\frac{\partial}{\partial n} \phi$ is unknown but constant over each linear element, and ϕ is the applied voltage on each electrode, then one can rewrite Eq. 4.18 in a set of $N \times N$ linear equations by choosing \mathbf{x} to be on one of the n 'th element of Γ .

$$-\phi(\xi_l) = \sum_{e=1}^N \frac{\partial \phi_e}{\partial n} \int_{\Gamma_e} -\frac{1}{2\pi} \ln |\mathbf{x}_e - \xi_l| d\Gamma_e \quad (4.19)$$

Here, ξ_l , $l = 1, \dots, N$ is the midpoint of the l th boundary element and \mathbf{n}_e is the outward pointing unit normal vector at Γ_e (see Fig.4.1). This results in a system of N linear equations.

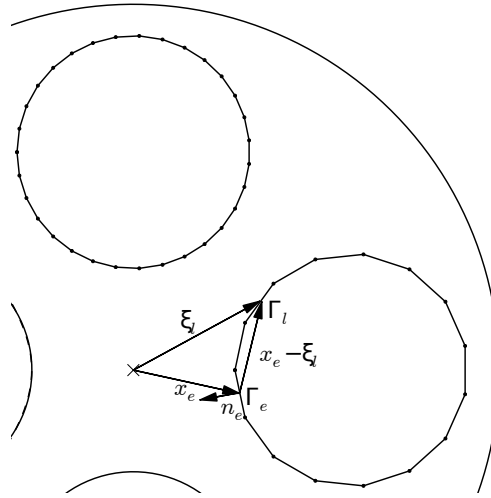


Figure 4.1: The sketch illustrates the calculation for one boundary element (Eq. 4.19) for the 2 dimensional case. The example shows a part of a quadrupole with cylindrical electrodes with two different numbers of linear elements which represent the surface of the electrodes. The rod on the right side is divided in 16 boundary elements which leads in a rather poor approximation of the electrode. The upper rod is divided in 32 boundary elements which is a better approximation for the electrode for the BEM calculations

$$\mathbf{b} = \mathbf{A} \cdot \frac{\partial \phi}{\partial \mathbf{n}} \quad (4.20)$$

with the unknown $\frac{\partial \phi}{\partial n}$. The integrals in Eq. 4.19 and the solution of Eq. 4.20 can be calculated with numerical routines. The solution $\frac{\partial \phi_l}{\partial n}$ on each element is, as

mentioned before, proportional to the surface charge density of the electrodes^[7]. With the solution of Eq. 4.20 and Eq. 4.19, it is possible to calculate the resulting potential for an arbitrary point \mathbf{x} around the electrodes. One advantage from this method over the FDM and FEM method is, that one has to calculate the unknown $\frac{\partial \phi_i}{\partial n}$ for each electrode configuration only once. Based upon this the field can be calculated at an arbitrary point whenever it is necessary. For the FDM and FEM methods one has to repeat the whole calculation if one wants to know the potential at another point or interpolate between points.

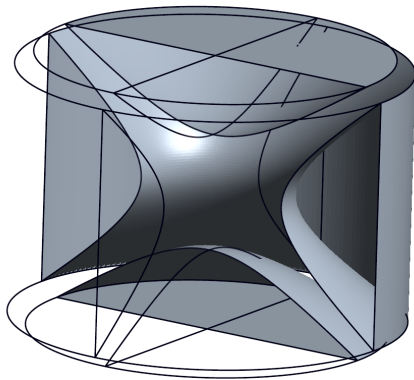
Also the electric field $\mathbf{E} = -\nabla\Phi$ can be calculated directly with Eq. 4.18 using the partial derivatives in each direction.

$$\mathbf{E}(\mathbf{x}) = \oint_{\Gamma} \frac{\partial}{\partial \mathbf{x}_i} g(\mathbf{x}, \mathbf{y}) \frac{\partial}{\partial n} \Phi(\mathbf{y}) d\Gamma(\mathbf{y}) \quad (4.21)$$

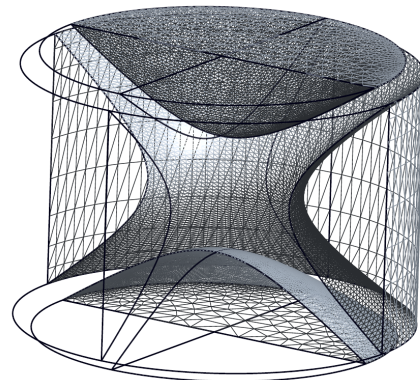
A more mathematically detailed description of the BEM method can be found in [18, 19].

Discretization of the Electrodes

The initial step for running the BEM calculation is to build a model of the trap which contains geometry, alignment and size of the electrodes. This can be done with a normal CAD program. The next step is the discretization of the model. In order to do this a so-called mesh from the CAD model which represents the surface of the electrodes has to be build. This mesh consists for two dimensional geometries of line elements and for the three dimensional geometries of triangles or rectangles. Figure 4.2a and 4.2b illustrate these steps based on a model for a Paul trap. For



(a) CAD model of a Paul trap



(b) mesh over CAD model

Figure 4.2: Figure (a) shows a CAD model of a spherical Paul-Trap. Figure (b) shows the same model with a triangular mesh over the surface. These figures illustrates the process of generating a mesh for the BEM calculations.

simple geometries like cylindrical conductors without holes, the CAD-model can be build directly by a so called mesh generator. For the calculations in this thesis,

the Gmsh^[21], a three-dimensional finite element mesh generator, which is freely available, was used. For more complicated electrode structures (e.g. conductors with holes), first a model has to be build using a CAD program like pro engineer⁵. Following this a mesh can be generated from this model. Before one generates the mesh, it is important to declare the physical boundaries (lines and surfaces of the electrodes). This means, each electrode gets a specific number so that the BEM algorithm can distinguish between different electrodes.

The BEM Code

For running the calculations a numerical BEM routine is required. For this some commercial software like CPO⁶ (charged particle optics) or Integrated⁷ can be used. For a better understanding of the problem and to have the full control about the complete solving procedure, a own BEM routines were developed for two dimensional and three dimensional problems with symmetry w.r.t. the z -axis. Another reason for developing an own code is that these complete software solutions are expensive and not freely available. For full three dimensional problems without any symmetry an existing open-source Galerkin boundary element library BEM++^[22] that handles Laplace, Helmholtz and Maxwell problems on bounded and unbounded domains to run the calculations was used.

The implementation of the BEM-code is written in python 2.7. To reduce the calculation time, all time consuming parts of the calculation (evaluation of singular and hypersingular integrals) are translated into C-code. To save computation time the calculations are computed in parallel. All codes can be found in the supplementary material.

The Accuracy of the Calculated Fields

The accuracy of the numerical calculation of all mentioned methods are strongly dependent on the fineness of the discretization. In case of the BEM method this is the size of the boundary elements. In order to get an estimate on the accuracy of the BEM calculations the numerical solutions were compared to the exact analytic solution for three examples w.r.t. the chosen boundary element size (meshsize). To find an adequate balance between the accuracy of the calculations and their required CPU time, all examples have been calculated for different sizes (meshsize) of the boundary elements. Figure 4.1 shows a two dimensional model for the BEM calculation (Eq. 4.19) for different meshsizes. The following examples were used:

1. Calculation of the potential around a sphere with fixed potential
2. Calculation of the potential between two spherical conductors

⁵<http://www.ptc-de.com/cad/pro-engineer>

⁶<http://simion.com/cpo/>

⁷<https://www.integratedsoft.com/>

3. Calculation of the potential and electric field of a spherical deflection analyzer

These three examples are tested with the rotational symmetric and full three dimensional routine. For the two-dimensional BEM routine, the accuracy was compared to the results from the semi-analytical calculations of A.Reuben [15] for multi-pole traps with circular rods.

The accuracy of the first two examples is measured as the relative L_2 -error (Eq.4.22). The $L_{2,\text{error}}$ calculates the deviation of a numerical u_{num} result to the exact solution u_e .

$$L_{2,\text{error}} = \sqrt{\frac{\sum_{k=1}^n (u_e(k) - u_{\text{num}}(k))^2}{\sum_{k=1}^n u_e^2(k)}} \quad (4.22)$$

The size of the boundary elements (triangles or line elements) which is given in the following results, is measured as the perimeter or area of the electrode divided by the number of elements (for all examples the size of all elements was chosen to be equal). For the third example I have used the same error indicator as used by D.Cubric [23].

The Electrical Potential of a Spherical Conductor

As model a sphere at a fixed potential of $V_0 = 1$ Volt and a radius of $R = 1$ cm was used. The analytic solution is given by the following expression^[14]:

$$\Phi(\mathbf{r}) = V_0 \cdot \frac{R}{r} \quad (4.23)$$

Since the potential has to be a constant around a circle, the potential was calculated around a circle of a radius $r = 1.25$ cm which leads to in a potential of $\Phi(1.25) = 0.8[V]$.

number of elements		relativ error [%]
full 3d routine	area of triangles	
48	0.2618	24.96190
776	0.0161	0.48810
4716	0.0026	0.08339
11918	0.0011	0.03317
32162	0.0004	0.01245
3d axis symmetric routine	length of elements	
18	0.17453	0.26849
38	0.08267	0.05864
78	0.04028	0.01431
158	0.01988	0.00356

Table 4.1: The table shows the $L_{2,\text{error}}$ of the numerical results in dependence of the meshsize for the electrical potential of a spherical conductor. The error of the calculations becomes smaller for more (\Rightarrow smaller) boundary elements.

The Electrical Potential between two Spherical Conductors

As a model two spheres at potential $+V$ and $-V$ with a radius R and a distance of $2l$ aligned the z -axis (see Fig. 4.3) was used. For this case an analytic solution in bi-polar coordinates is available^[24]. Table 4.2) compared the numeric solution with the analytic solution w.r.t. the relative $L_{2,\text{error}}$ for 200 points between the two spheres.

number of elements		relative error [%]
full 3d routine	area of triangles	
128	0.19635	15.01781
744	0.03378	1.17306
4512	0.00557	0.20474
24612	0.00102	0.03699
62820	0.00040	0.01439
3d axis symmetric routine	length of elements	
36	0.17453	0.29639
76	0.08267	0.06532
156	0.04027	0.01537
316	0.01988	0.00373

Table 4.2: The table shows the $L_{2,\text{error}}$ of the numerical results in dependence of the meshsize for the electrical potential between two spherical conductors. The error of the calculations becomes smaller for more (\Rightarrow smaller) boundary elements.

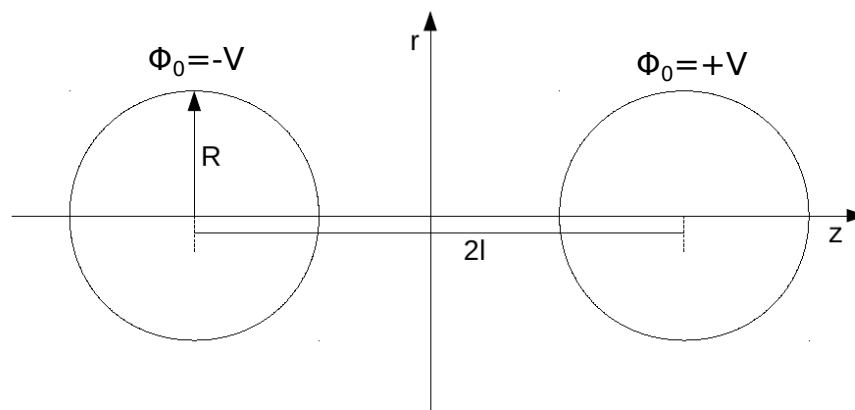


Figure 4.3: Two conducting spheres held on constant voltages $\pm V$

The Electric Field of a Spherical Deflection Analyzer

Next, the results of the BEM-routines will be compared to an example which is used by D. Cubric^[23] to benchmark the accuracy. (In his calculations the CPO software

was used to calculate the electric field.) The model for this purpose is an ideal spherical deflection analyzer, consisting of two concentric spheres of radius 0.75 cm and 1.25 cm and potential Φ of $\frac{5}{3}$ V and $\frac{3}{5}$ V, respectively. For a radius of 1 cm the electric potential and the electric field $E(\theta)$ are 1 V and 2 V/cm. To compare the accuracy with Cubric, the same error indicator $\bar{\varepsilon}$ was used which is defined as follows:

$$\bar{\varepsilon} = \frac{1}{2} \cdot \bar{E} - 1 \quad \text{with} \quad \bar{E} = \frac{1}{n} \sum_i E(\theta_i) \quad (4.24)$$

Table 4.3 shows the results for the axis-symmetric and full 3-D routine.

method	$\bar{\varepsilon}$ in [%] this work	$\bar{\varepsilon}$ in [%] Cubric[23]
3d axis symmetric	$5.6 \cdot 10^{-6}$	$6.4 \cdot 10^{-4}$
full 3d	$1.1 \cdot 10^{-4}$	$2.4 \cdot 10^{-2}$

Table 4.3: Comparison of the relative mean field $\bar{\varepsilon}$ in [%] for a spherical deflection analyzer.

Conclusions

To obtain a rather high accuracy the full 3-dimensional calculations need a lot of RAM (up to $\approx 30 - 40$ GB) and a huge calculation time compared to the axis symmetric calculations. Therefore, for three dimensional trap geometries with symmetry w.r.t. the z -axis it is preferred to use rotational symmetric routines because the calculations become more accurate compared to the full three dimensional routine. This is because the boundary elements are lines instead of triangles and therefore the components of the trap model can be divided in smaller elements (a better approximation of the electrodes) with less computational effort. In this way, the axis symmetric approach is more efficient. For non symmetrically aligned electrode structures, the full 3-dimensional routine has to be used. As expected, the achieved accuracy of electric fields and electric potentials with the BEM method depends strongly on the discretization of the electrode surface. In example 1 (spherical conductor) an accuracy of about 0.013% is achieved for the full 3D calculations. For the 3D symmetrical calculations an accuracy of about 0.004% can be achieved. For the second example (two spherical conductors) one got an accuracy of about 0.015% for the full 3D calculations and 0.004% for the 3D symmetrical calculations compared to the analytical solution. The third example demonstrated, that the accuracy of the used routines is a factor of ≈ 100 better than what is reported by D. Cubric. The accuracy of the two dimensional BEM routine shows exactly the same results in terms of multi-pole expansion coefficients (see in section 4.3) as reported by A. Reuben [15]. To investigate trapping potentials (usually in the range of tens of Volts) as a function of the trap parameters, one has to analyze a change in the range of meV . This implies an accuracy of less than 0.1%. The examples above show that the implemented BEM method is an appropriate technique to determine electric potentials for arbitrary electrode structures/arrangements.

4.3 Multipole Expansions for Different Types of Ion Traps

As already mentioned it is not possible to describe the electrical potentials of real ion traps by an analytic expression. Therefore it is the goal to find an appropriate multipole expansion to characterize the electrical potentials of real trap geometries by a small set of parameters. The advantage of this method is that complicated potentials can be described with a set of only a few "numbers", called the multipole coefficients. With these numbers it is possible to investigate properties of the calculated numerical potential and to find a practical and optimized arrangement for the electrodes.

In 2 dimensions the multipole expansion for the quasi-static part of the electric potential Φ is presented by Eq. 4.4. The multipole expansion for the 3 dimensional case with symmetry to the z-axis can be expressed by Eq. 4.7. The multipole expansion for the 3 dimensional case without symmetry is given by Eq. 4.1.

To calculate the multipole coefficients $a_n, b_n, c_n, c_{m,l}$ (see equations 4.4, 4.7 and 4.1, respectively) one can make use of the so called 'Fourier's Trick'^[7]. With the orthogonality of the trigonometric functions and Legendre polynomials one integrates the calculated numerical potential along a path around a circle (2D) or a half circle (3D) around the center of the trap. For the 2 dimensional case the coefficients can be then calculated by:

$$\tilde{a}_k = \frac{1}{\pi} \int_0^{2\pi} \Phi(\phi, r) \cos(k\phi) d\phi \quad \text{and} \quad a_k = \tilde{a}_k \cdot \left(\frac{r_0}{r}\right)^k \quad (4.25)$$

$$\tilde{b}_k = \frac{1}{\pi} \int_0^{2\pi} \Phi(\phi, r) \sin(k\phi) d\phi \quad \text{and} \quad b_k = \tilde{b}_k \cdot \left(\frac{r_0}{r}\right)^k \quad (4.26)$$

For the 3 dimensional symmetric case, the coefficients are:

$$c_k = j_k \cdot \int_0^\pi P_k(\cos(\theta)) \cdot \sin(\theta) \cdot \Phi(r, \theta) d\theta$$

$$j_k = \left(\frac{r_0}{r}\right)^k \cdot \frac{2k+1}{2} \quad (4.27)$$

For the 3 dimensional without any symmetry, the coefficients are:

$$c_{m,l} = j_{m,l} \cdot \int_0^\pi \int_0^{2\pi} (Y_{m,l}(\theta, \phi)) \cdot \sin(\theta) \cdot \Phi(r, \theta, \phi) d\theta d\phi$$

$$j_{m,l} = \left(\frac{r_0}{r}\right)^l \frac{2l+1}{2} \quad \text{for } m = 0 \quad (4.28)$$

$$j_{m,l} = \left(\frac{r_0}{r}\right)^l 2l+1 \quad \text{for } m \neq 0$$

Remark: Fitting the coefficients to an expansion is not appropriate to calculate the

expansion coefficients, because one has to fit a finite set of functions to the solution. These fitted coefficients will not represent exactly the right contribution for each multipole component of the field.

The accuracy of the calculated multipole coefficient depends on the number of nodes and the integration. To reach a high precision, the integration was performed by the 'Gauss-Legendre-Quadrature'. The integration routine was tested with different numbers of nodes and compared to analytic solutions of multipole expansions to verify their accuracy. To verify the accuracy for real problems, the multipole expansion for the analytical solution^[24] for the potential between two spherical conductors was compared to the multipole expansion coefficients for the calculations using the axis symmetrical BEM method as a function of number line elements. Table 4.4 compares the first 10 multipole coefficients for the analytic and numeric solution for the axis symmetrical calculations for 36, 156 and 316 line elements.

multipole	analytical	36	156	316
1	-0,357065	-0,356819	-0,357007	-0,357051
3	-0,229501	-0,229364	-0,229469	-0,229493
5	-0,147533	-0,147473	-0,147520	-0,147530
7	-0,094856	-0,094850	-0,094856	-0,094856
9	-0,060998	-0,061031	-0,061008	-0,061000

Table 4.4: The table compares the analytically and numerically calculated multipole coefficients for the two spherical conductor problem. Obviously, the more elements, the higher the accuracy.

As expected, the accuracy of the calculated coefficients ($\approx \pm 2 \cdot 10^{-4}$) is in the same range as the relative error which has been calculated before.

Chapter 5

Simulations of Different Types of Ion Traps

In this chapter, an overview of different types of ion traps will be given. Based on numerical simulations of electrical potentials, different properties will be discussed in detail. First the approximation of hyperbolic shaped electrodes with circular rods will be investigated. Also the consequences of the finite structure and mechanical misalignments of the electrodes will be presented. Furthermore, the Split-Ring-Electrode-Trap (SRET) as an approximation for a spherical Paul-Trap will be discussed and the linear 22 pole trap will be investigated in detail. After this a new type of a 24-pole multipole trap is introduced, based on a numerical simulations. Finally space charge effects will be studied, with special focus given to the 22 pole trap.

5.1 Approximation of Hyperbolic Shaped Electrodes

Due to manufacturing difficulties like machine precision or high costs of fabricating hyperbolic rods, often circular rods (low manufacturing costs and relative high precession) are used to build linear multipole traps, quadrupole mass filters or ion beam guides. This approximation of the hyperbolic electrode structure will result in higher order multipole components of the electrical field^[25]. These higher multipole components can affect significantly the guiding, trapping or mass selection properties of the device^[15,26]. To overcome such problems, it is important to find the optimum parameters like the ratio of the radius of the trapping field r_0 and the diameter of the circular rods R to get the best possible approximation of an hyperbolic electrical potential Φ .

5.1.1 The Ideal Ratio R/r_0 of a Linear Multipole Trap

The optimum choice of the ratio R/r_0 for linear multipole devices with circular rods, where r_0 is the inscribed circle between the electrodes and R is the radius of the rods (see Fig. 5.1) are discussed in a lot of publications^[15,25–28]. In this section the ratio of R/r_0 for all linear multipole traps up to order $\tilde{n} = 11$ will be presented where the next higher order component of the field is vanishing. The order \tilde{n} of the multipole is defined as:

$$\tilde{n} = \frac{\text{number of rods}}{2}. \quad (5.1)$$

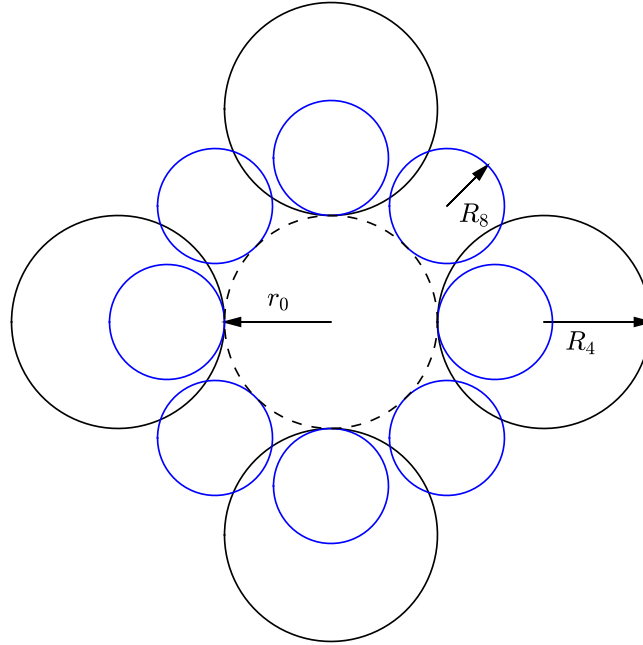


Figure 5.1: The sketch shows a quadrupole and a octopole (black and blue lines) with circular rods. The dashed lines indicates the inscribed circle r_0 . R_4 and R_8 indicates the radius of the rods for the quadrupole and octopole, respectively

To evaluate the approximation of the hyperbolic multipole field it is appropriate to express the electric potential Φ via a multipole expansion (Eq. 4.4). The amplitude of coefficients a_n and b_n in this expansion provides the information of the higher order multipole components of the field. In the following only symmetric alignments of the electrodes around the center of the device will be discussed. For symmetry reasons, only a_n with $n = \tilde{n}(2k + 1)$ ($k = 0, 1, 2, \dots$) will appear in this expansion. Here \tilde{n} denotes the order of the linear multipole. This means e.g. for a quadrupole where $\tilde{n} = 2$ only $a_2, a_6, a_{10}, a_{14}, \dots$ will appear in this expansion. One criterion for a good approximation is that the first higher order component of the field is zero (for a quadrupole $a_6 = 0$ and a hexapole $a_9 = 0$, and so on). For a quadrupole

mass filter it was presumed that this criterion will lead to the best performance. Therefore several groups have calculated different values for R/r_0 where a_6 reaches zero using different methods.

Dayton [29] calculated that a ratio of $R/r_0 = 1.148$ results in $a_6 = 0$. Denison [27] calculated a value of 1.1468. Reuban [15] and Douglas [25] give a value of $R/r_0 = 1.145111$ resulting in $a_6 = 0$. For higher order multipoles Douglas^[25] gives different values for R/r_0 for different optimization criteria.

In the following, values for R/r_0 for which the next appearing higher order multipole component vanishes, are calculated. The electric potential and their multipole expansions are computed with the two dimensional BEM method as described in the previous chapters.

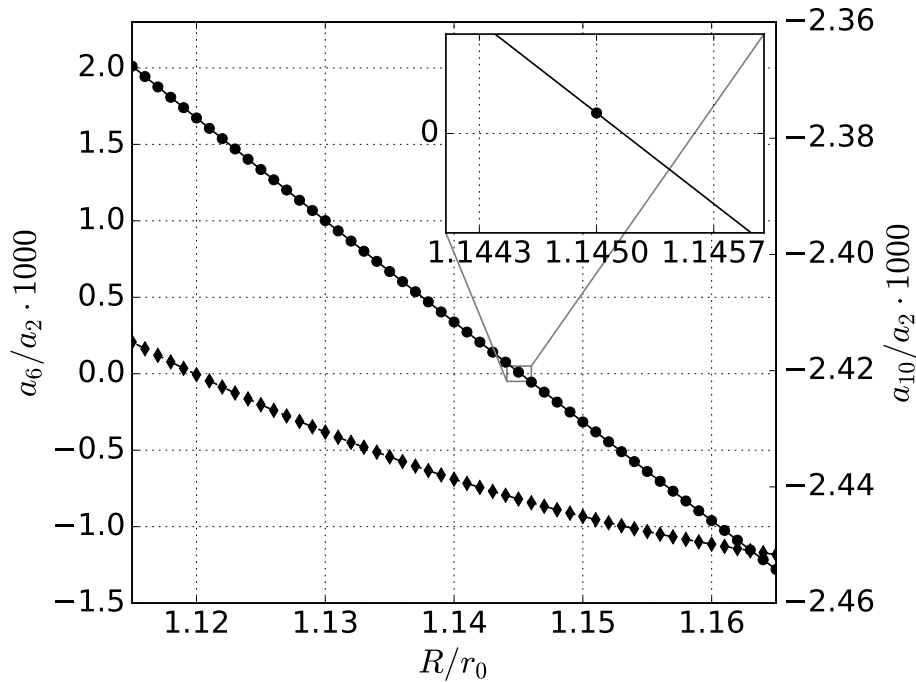


Figure 5.2: This plot shows the higher order multipole components a_6, a_{10} in the case of a quadrupole with circular rods. The left/right axis shows a_6 / a_{10} scaled with the value of the quadrupole component of the field and multiplied by a factor of 1000 to see the small influence. The inlay shows a zoom in the region where a_6/a_2 is vanishing.

Figure 5.2 shows a plot for a quadrupole where the two following non vanishing higher order multipole coefficients are plotted as a function of R/r_0 . The root of the next higher order component leads to the values where this component is vanishing. From this one calculate a value of $R/r_0 = 1.145158$ which is in good agreement with the value from Reuban [15] and Douglas [25].

Figure 5.3 shows the ratio of R/r_0 where the next higher multipole component is vanishing up to order $\tilde{n} = 11$. The numerically calculated values are given in Tab. 5.1.

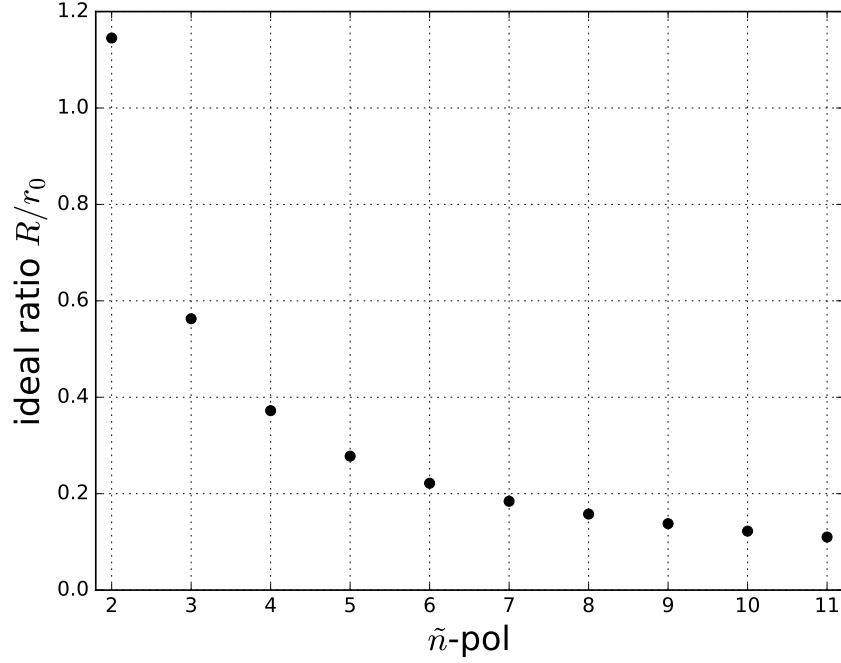


Figure 5.3: The plot shows the the ratio R/r_0 , for which the next higher order multipole component vanishes ($a_{3\tilde{n}} = 0$) as a function of the multipole order \tilde{n} up to 11.

\tilde{n}	this work R/r_0	Douglas [25] R/r_0
2	1.145158	1.14511
3	0.562876	0.5628
4	0.3722019	0.3721
5	0.2778222	0.2778
6	0.2215821	0.2215
7	0.1842312	-
8	0.1576886	-
9	0.1377635	-
10	0.1223321	-
11	0.1100043	-

Table 5.1: The table shows the numerically calculated values for $a_{3\tilde{n}} = 0$ corresponding to Fig. 5.3.

5.1.2 Influence of Higher Order Multipole Components on a Quadrupole

For the transmission of a QMF it is necessary to find a reasonable criterion for a good approximation for a quadrupole field which is created with circular rods instead of hyperbolic shaped rods. Mass selection properties can be significantly influenced by higher order components of the field. One theory for a possible criterion for an optimum ratio of R/r_0 is that the next appearing higher order multipole component a_6 has the largest influence on the mass selective properties of the QMF. For a value of $R/r_0 \approx 1.109$ the amplitudes of the components a_6 and a_{10} compensate each other. This could also be a good criterion for the best choice of R/r_0 . In order to optimize the mass selective properties of a QMF it is indispensable to investigate the influence of higher order multipole contributions of the field to the ion motion. Unfortunately it is not possible to find a stability diagram or regions of stability for higher order inhomogeneous multipole fields. This is only possible for a pure quadrupole field Eq. 4.6 (see section 3.1). In this case the equations of motion are uncoupled for each direction. For inhomogeneous multipole fields it is possible to find a heuristic parameter ($\eta^{[5]}$, see Section 3.3). They provide to some extent a stability criterion of the ion motion inside an ion trap or ion guide. To get an impression or a statistical statement of the influence of higher order multipole contributions on the ion motion in a QMF it is possible to simulate the ion motion for an appropriate number of randomly distributed ions and compare them relative to the motion of an ion in an ideal quadrupole field. For an infinitely long linear quadrupole with circular rods the equations of motion can be written in the following form:

$$\begin{aligned}\ddot{x}(t) &= -\frac{q}{m}(U - V \cos(\Omega t)) \frac{\partial \Phi}{\partial x} \\ \ddot{y}(t) &= -\frac{q}{m}(U - V \cos(\Omega t)) \frac{\partial \Phi}{\partial y}\end{aligned}\tag{5.2}$$

with

$$\begin{aligned}\frac{\partial \Phi}{\partial x} &= \sum_{k=2}^{\infty} a_k k \frac{r^{k-1}}{r_0^k} \cos(\phi(k-1)) \\ \frac{\partial \Phi}{\partial y} &= -\sum_{k=2}^{\infty} a_k k \frac{r^{k-1}}{r_0^k} \sin(\phi(k-1)).\end{aligned}\tag{5.3}$$

For the electric field which is produced by circular rods, the quadrupole component of the field a_2 differs from '1' for different radii R of the rods. Therefore, to compare the influence of higher order multipole components of the field, which arise from a circular rod geometry to a pure quadrupole field it is necessary to introduce a so called effective distance $r_{0,eff}$. This is used to scale the quadrupole component a_2 of the electric field to 1. This can be done in the following way:

Step 1: calculate the multipole expansion coefficients (Eq. 4.4) for a certain ratio of R/r_0 as described with r_0 for a pure quadrupole field

Step 2: calculate the effective distance $r_{0,eff} = \frac{r_0}{\sqrt{a_2}}$

With the reduced parameters $a = -\frac{8eU_0}{m\Omega^2 r_{0,eff}^2}$, $q = \frac{4eV_0}{m\Omega^2 r_{0,eff}^2}$ and $\xi = \frac{\Omega t}{2}$ mentioned in section 3.1 it is possible to rewrite Eq.5.2 in the following form.

$$\begin{aligned}\ddot{x}(\xi) &= -(a - 2q \cos(2(\xi - \xi_0))) \frac{\partial \tilde{\Phi}}{\partial x} \\ \ddot{y}(\xi) &= -(a - 2q \cos(2(\xi - \xi_0))) \frac{\partial \tilde{\Phi}}{\partial y}\end{aligned}\tag{5.4}$$

and

$$\begin{aligned}\frac{\partial \tilde{\Phi}}{\partial x} &= \sum_{k=2}^{\infty} \frac{a_k}{a_2^{k/2}} k \frac{r^{k-1}}{r_{0,eff}^{k-2}} \cos(\phi(k-1)) \\ \frac{\partial \tilde{\Phi}}{\partial y} &= - \sum_{k=2}^{\infty} \frac{a_k}{a_2^{k/2}} k \frac{r^{k-1}}{r_{0,eff}^{k-2}} \sin(\phi(k-1))\end{aligned}\tag{5.5}$$

With Eq. 5.4 and Eq. 5.5 it is possible to investigate the stability of the ion motion independent of the angular rf frequency Ω and the mass of the ion as a function of a and q . To see the small influence of the next higher order multipole contributions to the motion it is necessary to integrate the equations of motions Eq. 5.4 numerically very precisely. This was done with the previous mentioned Runge-Kutta-Nystroem-method of fourth order with a step size of $h = \pi/60$. To evaluate the influence of higher multipoles, the value a as a function of q with $a = 2 \cdot \mu \cdot q$ (see Fig.5.4) was varied. Here μ denotes the slope of the 'load-line' for different mass-resolutions $M = m/\Delta m$ of the QMF. For the calculation only the next two higher multi-pole components (a_6, a_{10}) of the electric field were used. The variation of the ratio R/r_0 shows, that the change of a_{14} is not significant, therefore higher order components (see Tab. 5.2) were neglected in the simulations.

$a_k/a_2^{k/2}$ see Eq. 5.5	$R/r_0 = 1.109$	$R/r_0 = 1.121$	$R/r_0 = 1.128$	$R/r_0 = 1.145$
a_6/a_2^3	0.00242	0.00160	0.00113	0.00001
a_{10}/a_2^5	-0.00240	-0.00241	-0.00241	-0.00242

Table 5.2: The table shows the different multipole contributions up to order $k = 10$ for different ratios of R/r_0 .

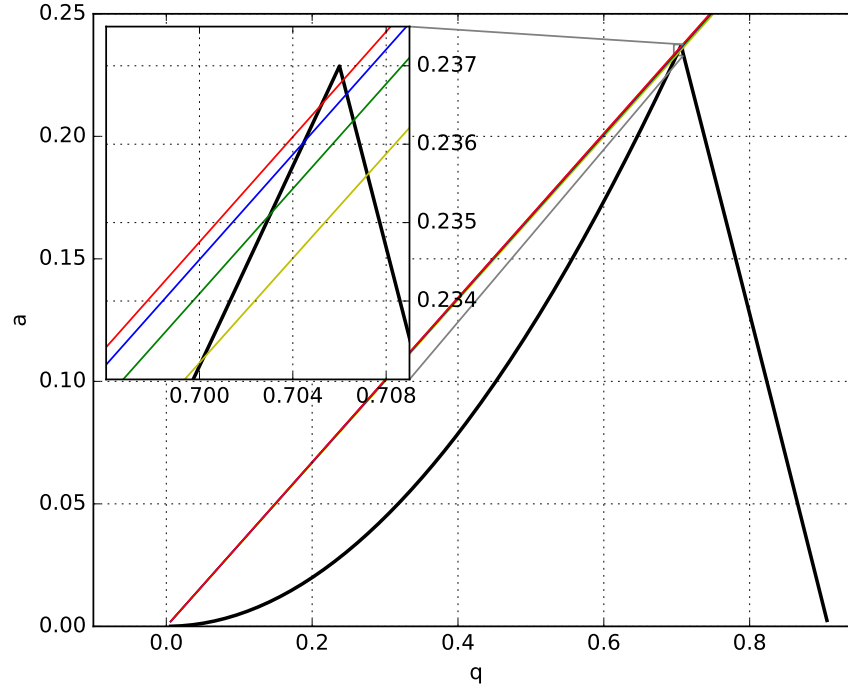


Figure 5.4: The plot shows the stability diagram for the first stability region of a QMF. The black lines are the boundaries of the stable regions for x and y direction. The red, blue, green and yellow lines are the different 'load-lines' for $(\mu = 0.16768, M = 800)$, $(\mu = 0.16752, M = 400)$, $(\mu = 0.16721, M = 200)$ and $(\mu = 0.16658, M = 100)$, respectively.

The simulations were performed with four different sets of rod diameters R with a fixed closest distance r_0 to the trap center (see Tab. 5.2) and four different mass-resolutions $M = m/\Delta m$ (see Fig.5.4). Similar simulations of mass spectra were also performed by Douglas and Konenkov [26]. In contrast to Douglas and Konenkov the number of simulated ions was increased by a factor of 25 to 50000 ions for each value of a and q and the number of rf cycles for the ions in the rf field was increased by a factor of 10 to 2000 cycles. The value of q was increased by a step size of $\Delta q = 0.00005$ in the range of $q \in [0.68, 0.715]$, the initial phase ξ_0 was randomly distributed $\xi_0 \in [0, \pi/2]$ and the initial position of the ion x_0, y_0 randomly distributed within a radius of $r_0 \in [0, 0.2 \cdot r_0]$. For simplicity, the initial velocity (v_x, v_y) was chosen to be 0.

The transmission $T(q)$ of the QMF was estimated in the following way:

- if the amplitude of the ion motion $r_{ion} = \sqrt{x_{ion}^2 + y_{ion}^2} < r_0 \Rightarrow$ transmitted
- if the amplitude of the ion motion $r_{ion} = \sqrt{x_{ion}^2 + y_{ion}^2} \geq r_0 \Rightarrow$ not transmitted

Based on these simulations one can get an impression of the influence of higher order multipole components to the transmission of the ions. Figure 5.6 shows that higher

order multipole components have a significant influence on the transmission of the ions. The simulations with hyperbolic rods show an almost perfect peak shape. For the circular rods, some special features like dips and small plateaus can be seen. Probably these features are a consequence of nonlinear resonances. In particular the higher mass-resolution $M = m/\Delta m$ has a strong impact on the width of the transmission peak. A shift of the peak positions to higher values of q with an increase of R/r_0 is visible (see Fig. 5.5 and Figs. A.1, A.2 and A.3).

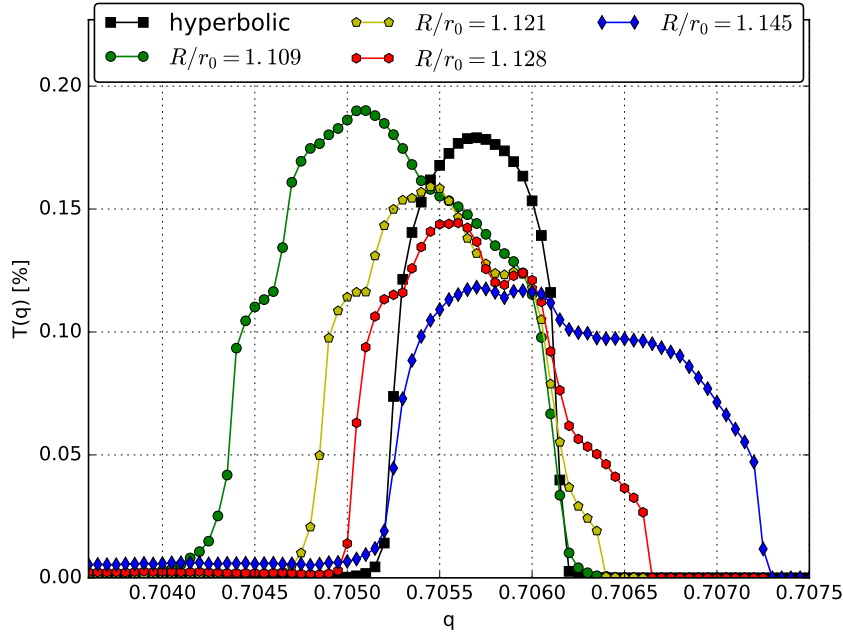


Figure 5.5: The plot shows transmission curves $T(q)$ for $M = 800$

Furthermore, the transmission is decreasing with higher values of R/r_0 (see Figs. A.1, A.2, A.3, 5.5). These effects increase with an increase of the mass-resolution M . The simulations also show that the criterion of a vanishing a_6 component does not lead to an optimum performance of a QMF. This criterion shifted the peaks to higher values of q and broadened the peak. The criterion $a_6 \approx -a_{10}$ leads also to a peak shift to lower values of q and also broadened the peak. The width of the peak is almost the same, but the transmission decreases for the first criterion. Therefore one can say that the second criterion is in this sense the better one. If all results are compared (see Fig. 5.6), one can say that a ratio of $R/r_0 \approx 1.13$ leads to the best performance of a QMF with circular rods.

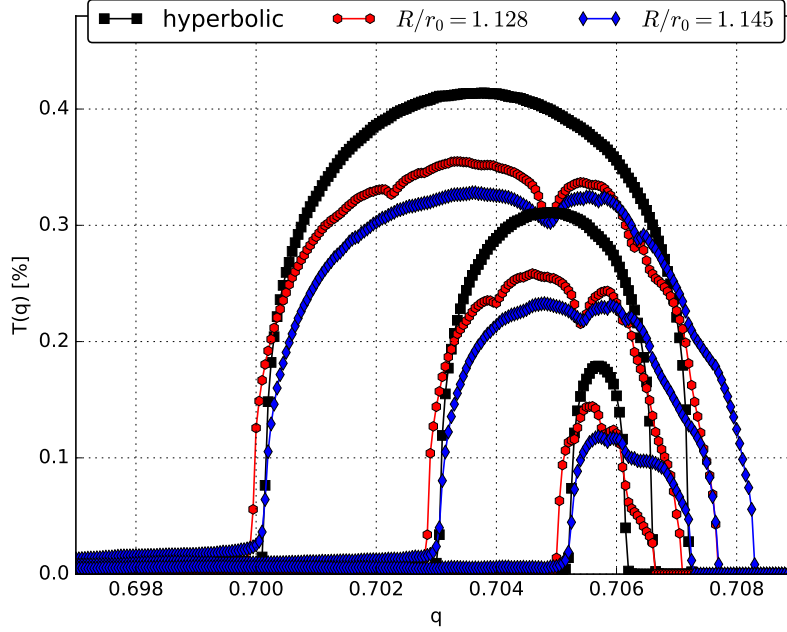


Figure 5.6: The plot shows transmission curves $T(q)$ for $M = 100$, $M = 200$ and $M = 800$

This result agrees well with the result of Douglas and Konenkov [26]. They found that a rod set geometry with $R/r_0 = 1.145111$ does not lead to optimum performance of a quadrupole mass filter. It would be better if the amplitudes of a_6 and a_{10} are about the same to compensate each other which leads to a value of $R/r_0 \approx 1.13$. A possible explanation for this would be, if one considers only a radial force \mathbf{F}_r Eq. 5.6 (neglecting the contribution from the angle ϕ in Eq. 5.3) which arise from higher order components (a_6, a_{10}) of the field and calculate their strength as a function of the radial distance r .

$$\mathbf{F}_r \propto \frac{6 \cdot a_6}{r_0} \left(\frac{r}{r_0} \right)^5 + \frac{10 \cdot a_{10}}{r_0} \left(\frac{r}{r_0} \right)^9 \quad (5.6)$$

This Force can be calculated for different ratios of R/r_0 . The results of this calculation show (Figs. 5.7 and 5.8), that for $R/r_0 \approx 1.13$ \mathbf{F}_r is smaller than for $R/r_0 \approx 1.109$ and $R/r_0 \approx 1.145$. This approximation would also provide that a ratio of $R/r_0 \approx 1.13$ is better than choosing $R/r_0 \approx 1.145$ or $R/r_0 \approx 1.109$ to remove the a_6 component or to compensate a_6 and a_{10} .

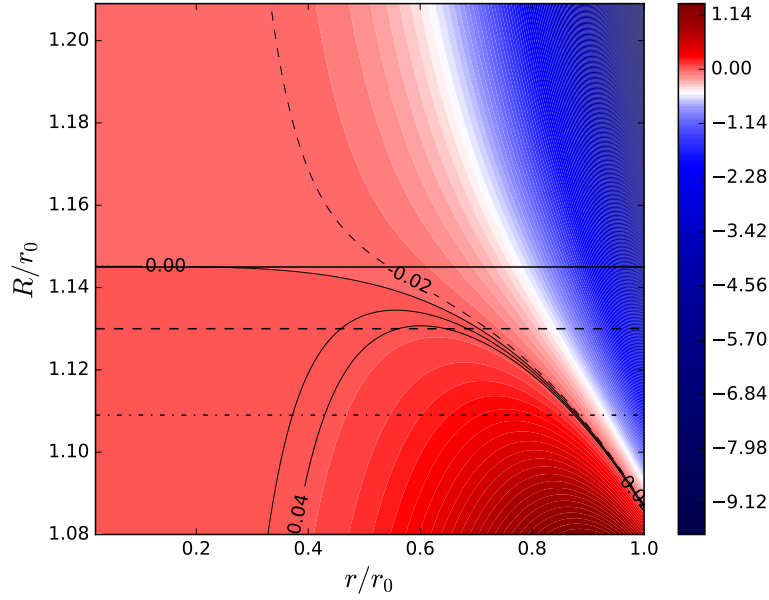


Figure 5.7: The contour plot shows \mathbf{F}_r (in arbitrary units) as a function of the ratio R/r_0 and the spatial distance from the center of the QMF. The solid, dashed and dashed-dot lines indicates the ratios R/r_0 for 1.145, 1.13, 1.109, respectively

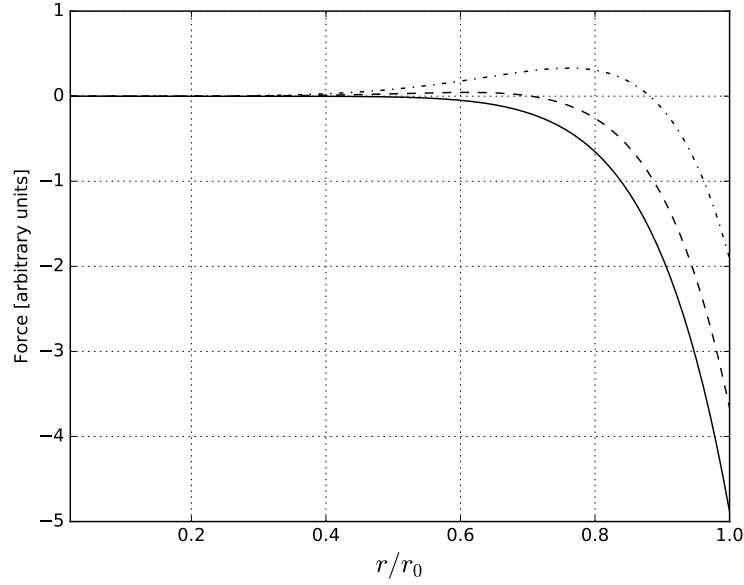


Figure 5.8: The plot shows \mathbf{F}_r (in arbitrary units) as a function of the spatial distance from the center of the QMF. The solid, dashed and dashed-dot lines indicate the ratios R/r_0 for 1.145, 1.13, 1.109, respectively (see Fig.5.7).

5.2 Influence of the Finite Size of Hyperbolic Electrodes

To overcome the problems of higher order multipole contributions, which are due to the usage of circular rods, one can use hyperbolic shaped electrodes. But even there higher order multipole contributions due to the finite size of the electrodes are obtained. To see the influence of the finite size systematic calculations of the electric potential for different sizes of the electrodes were performed. The size was chosen by truncating the electrodes at a radius R_{tr} . Figure 5.9 demonstrates the truncation of the electrodes.

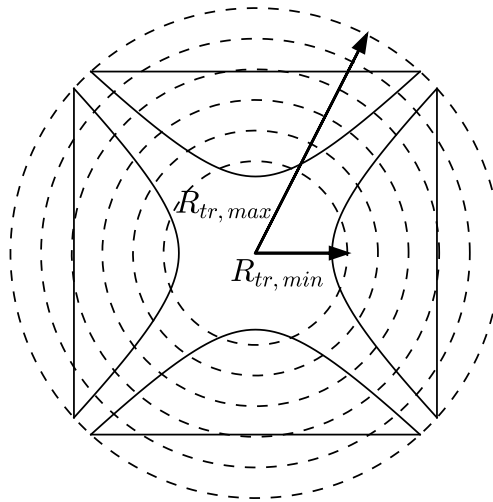


Figure 5.9: The solid lines show a hyperbolic electrode structure for a finite size QMF in two dimensions. The dashed lines show the six different radii where the electrodes are truncated. The arrows indicate the minimum and maximum radius of the truncation R_{tr} .

Table 5.3 shows the influence of the finite size in terms of the next higher order multipole contributions as a function of the radius where the electrodes are truncated. a_6 can be reduced, almost to zero for a ratio of R_{tr}/r_0 between 2 and 2.4. However, then a_{10} will increase. A large influence is visible if the truncation of the electrodes becomes $R_{tr}/r_0 < 1.6$. This means, R_{tr}/r_0 should not be smaller than 1.6 in order to avoid anharmonicities of the trapping field. For values of $R_{tr}/r_0 \geq 2.4$ the finite size has no significant effect on the higher order multipole contributions. These calculations also show that it is not possible to reduce higher order components of the field to zero. This is a consequence of the plane surface of the backside of the

electrodes. This will have always a non negligible contribution to the field within the electrodes. This effect is in competition to the total size of the electrodes.

R_{tr}/r_0	a_2	a_6	a_{10}
1.2	0.970651	$4.4235 \cdot 10^{-2}$	$-1.4894 \cdot 10^{-2}$
1.6	0.999479	$7.2669 \cdot 10^{-4}$	$-3.6115 \cdot 10^{-4}$
2.0	0.999922	$-5.9054 \cdot 10^{-7}$	$-4.2580 \cdot 10^{-6}$
2.4	0.999926	$-6.6849 \cdot 10^{-6}$	$-1.2455 \cdot 10^{-6}$
2.8	0.999926	$-6.6757 \cdot 10^{-6}$	$-1.2302 \cdot 10^{-6}$
3.2	0.999926	$-6.6956 \cdot 10^{-6}$	$-1.2347 \cdot 10^{-6}$

Table 5.3: Shown are the numerically calculated values for a_n for $n = (2, 6, 10)$ as a function of the truncation radius. In contrast to the calculations in section 5.1, the multipole contributions are not scaled to the quadrupole component to show that a_2 approaches 1 with increasing R_{tr} .

One option to reduce this effect could be a grounded housing aligned around the electrodes. But this will also have consequences to the field inside the QMF. This effect, of a grounded cylindrical housing around the electrodes, was discussed in Fanghänel et al. [30] and Denison [27]. It was shown that the ratio R/r_0 has a larger influence of the amplitudes of higher order multipole components than a grounded housing. Fanghänel et al. [30] reported that there is no ideal radius for the housing to reduce higher order multipole components. Instead, the calculations show that the overall influence of the housing is insignificantly small. To minimize a_6 and a_{10} anyway, the radius R_a of the cylindrical housing should be as small as possible.

5.3 The Split Ring Electrode Trap

The following was partly published in the paper 'Optimization of RF multipole ion trap geometries' by Fanghänel et al. [30].

The next example is a re-design of a Paul trap (3D quadrupole) which allows an open access to the trap center for a non-destructive detection of an isolated nanoparticle. The limited optical access to the trapping volume at a Paul trap (see CAD-model Fig.4.2a) was one reason for designing a spherical quadrupole trap with non ideal hyperbolic shaped electrodes, which still have an almost perfect harmonic potential near the trap center. Based on this, Gerlich and Decker have designed a split ring electrode trap (SRET)^[31] which allowed for example the detection of thermal radiation from hot trapped C_{60}^+ ^[32]. The fundamentals of such measurements can be found in Schlemmer et al. citetestscl01. They derived, using the effective potential approximation (sec 3.2.1) that the motion of an ion along the axial direction is well described by an harmonic oscillator with the frequency ω_z

$$\omega_z = \frac{e}{m} \cdot \frac{\sqrt{2}V}{r_0^2 \Omega}. \quad (5.7)$$

One can show that this frequency is identical to the frequency of the secular motion which dominates the spectrum of the motion of the ion. By measuring the eigenfrequencies ω_z , using optical, non-destructive methods, it is possible to determine highly accurately the charge-to-mass ($\frac{e}{m}$) of a single charged particle^[33–35]. Other groups adopted the design from Gerlich and Decker [31] to further develop the SRET for single nanoparticle mass spectrometry^[36–38]. A new version of such a SRET will be described in a forthcoming publication by Esser et al. [36]. A cross sectional view of the electrode geometry is shown in Fig. 5.10. This trap consists of three lower electrodes and three upper electrodes which are symmetrical aligned around the trap axis (z-direction) and have a mirror symmetry around the r-direction. The two inner electrodes are kept at the same potential and have a similar function as the ring electrode of the classical Paul trap. The splitting of the ring electrode into two symmetrical pieces allows an optical access to the center of the trap to observe the stored ion. The base of these electrodes is separated by $2 Z_i$ as shown in Fig. 5.10. The outer electrodes with their bases being separated by $2 Z_o$ resemble the two cap electrodes of the Paul trap and are also kept at the same voltage. The outer electrodes can be used as steering electrodes.

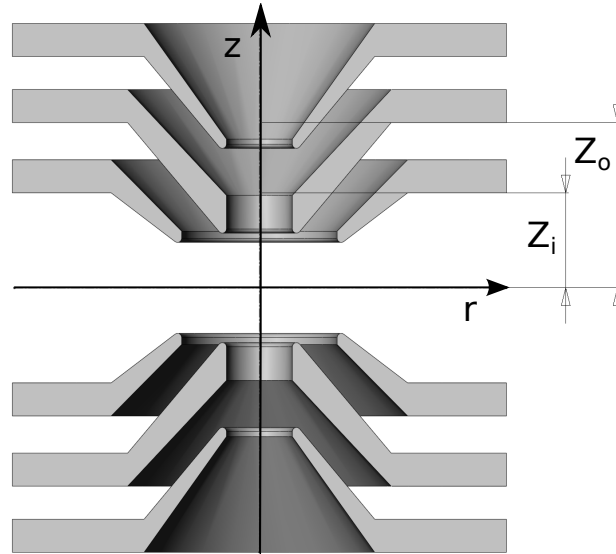


Figure 5.10: Cross sectional view of the set of electrodes comprising a split ring electrode trap (SRET). The mechanical model for the BEM potential calculation is taken from the CAD program Pro Engineer. The original ring electrode of the Paul trap is split into the inner most pair of conical electrodes (potential $+\Phi_{rf}$). The lower and upper cap electrodes of the Paul trap are replaced by the middle electrodes (potential $-\Phi_{rf}$). A third pair of electrodes (potential $\Phi = 0$) is used for additional steering options. (This figure is reproduced from Fanghänel et al. [30]).

The main assumption in order to determine accurately the charge-to-mass by measuring the eigenfrequencies is based on the fact, that one has an approximately harmonic potential near the trap center in the axial direction. Furthermore, a pre-

cise knowledge of the rf voltage V , the angular frequency Ω and the parameter r_0 is required. The first one implies, in terms of a multipole expansion (section 4.1, Eq. 4.7), that the quadrupole contribution (c_2) of the field have to dominate and all other higher order contributions should be negligibly small. Since only hyperbolic shaped electrodes can fulfill this requirement properly, the task is to find an electrode arrangement (geometry and alignment) that is as harmonic as possible near the trap center. For the following simulations the electrode geometry from Esser et al. [36] was used. To optimize a trap w.r.t. to requirement of an potential as harmonic as possible, the distance Z_i and Z_o were systematically varied to minimize the c_0 and the next higher order appearing multipole component c_4 of the. Once finding an optimum geometry for a given set of parameters one has to determine an effective parameter or characteristic length of the trap $r_{0,eff}$ which scales the c_2 coefficient to an absolute value of one¹. This characteristic length of the trap $r_{0,eff}$ can be used as the parameter r_0 in Eq. 5.7. Fig. 5.11 shows the result of a systematic analysis of the multipole coefficients as a function of the distances of the inner (Z_i , x-abscissa) and the outer (Z_o , y-ordinate) electrodes. (Z_i and Z_o are only changed by 0.3 mm and 0.1 mm, respectively, compared to the original design by Esser et al. [36].)

The change in the c_4 coefficient is shown as a colored contour plot as function of the shifts ΔZ_i and ΔZ_o . Also curves for $c_4 = 0$ and $c_4 = \pm 0.002$ are marked by solid and dashed lines. These lines are almost parallel to the abscissa which shows that the c_4 contribution of the field of the trap is only changed when the outer electrodes are displaced with respect to the inner electrodes. Also the curves for $c_0 = 0$ and $c_0 = \pm 0.001$ are marked by lines which are tilted at an angle showing that the dc potential (c_0) changes by both displacements but due to the scale of the plot much more by the displacement of the outer electrodes. This indicates that by a combined change of both displacements Z_i and Z_o it is possible to operate the trap without a persistent dc contribution ($c_0 = 0$). The case where $c_4 = c_0 = 0$ can be found at the intersection point of both solid lines. This variation of only two parameters shows how a desired geometry can be found once some general design criteria have been defined. The small changes in c_4 and c_0 also show that the electrodes displayed in Fig. 5.10 represent a good approximation for a 3D Paul trap.

¹Since the electrode arrangement of the SRET deviates from a perfect hyperbolic shaped electrode arrangement, the parameter r_0 has to be adjusted.

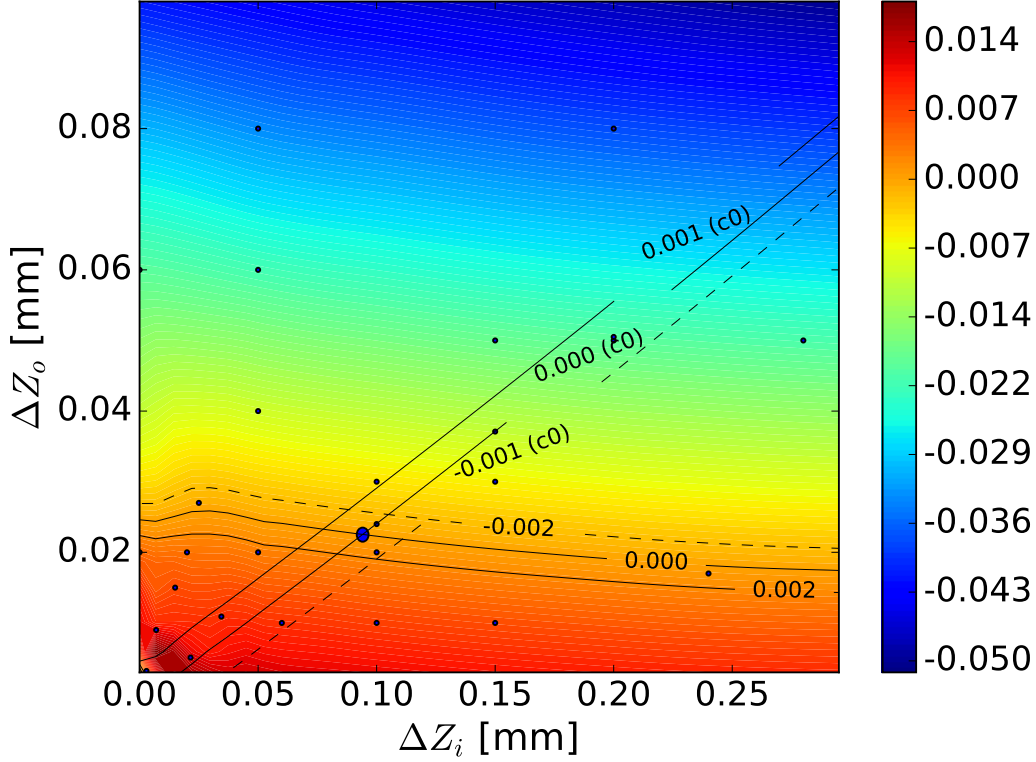


Figure 5.11: Multipole coefficient c_4 of the SRET as a function of the displacement of the inner and outer electrodes, see Fig. 5.10 for details. The small displacements are relative to the original design^[36]. The desired conditions $c_4 = 0$ and $c_0 = 0$ are found by the crossing lines. (This figure is reproduced from Fanghänel et al^[30]).

Please note, that this electrode configuration also produces higher order multipole contribution ($c_6, c_8, c_{10} \dots$). The calculated multipole components up to order $n = 8$ for the case of a vanishing c_0 and c_4 are $c_2 = -1, c_6 = 1.078454, c_8 = 0.581607$. Fig. 5.13 shows the relative deviation of the square of the electric field of pure quadrupole field to the field what is generated by the electrode arrangement of the SRET

$$\frac{\mathbf{E}_{Paultrap}^2 - \mathbf{E}_{SRET}^2}{\mathbf{E}_{Paultrap}^2}. \quad (5.8)$$

As can be seen in Fig. 5.13, within a radius of $r/r_{0,eff} \lesssim 2\%$ the deviations are smaller than 0.001%. For larger radii the deviation grows rapidly due to higher order components of the field. This higher order components of the field have an influence on the frequency of the secular motion, which becomes more dominant for larger amplitudes of the ion motion. As a consequence, the eigenfrequencies of the secular motion can slightly change as function of the axial and radial amplitude (see Fig. 5.14). These frequency shift due to higher order multipole contributions will be analyzed in the following.

As a first approach, these shifts will be numerically analyzed using the effective potential approximation. The effective potential ($V^* \propto \mathbf{E}^2$) can be written, including

the above mentioned higher order multipole components as

$$\mathbf{E}^2 = \frac{\left(2c_2r_0^6z + c_6r_0^2\left(\frac{45r^4z}{4} - 30r^2z^3 + 6z^5\right) + c_8\left(-\frac{35r^6z}{2} + 105r^4z^3 - 84r^2z^5 + 8z^7\right)\right)^2}{r_0^{16}} + \frac{r^2(7c_8(5r^6 - 120r^4z^2 + 240r^2z^4 - 64z^6) - 2r_0^2(8c_2r_0^4 + 15c_6(r^4 - 12r^2z^2 + 8z^4)))^2}{256r_0^{16}} \quad (5.9)$$

with $r = \sqrt{x^2 + y^2}$. A first order approximation for evaluating frequency shifts due to higher order field components can be done by neglecting all coupling terms ($r^n z^m$) in Eq. 5.9. This leads to the following Equation

$$\mathbf{E}^2(z) = \frac{4c_2^2z^2}{r_0^4} + \frac{24c_2c_6z^6}{r_0^8} + \frac{32c_2c_8z^8}{r_0^{10}} + \frac{36c_6^2z^{10}}{r_0^{12}} + \frac{96c_6c_8z^{12}}{r_0^{14}} + \frac{64c_8^2z^{14}}{r_0^{16}}. \quad (5.10)$$

With the relation of the secular motion of an ion in an effective potential (Eq. 3.20), Eq. 5.10 can be transformed in a equation for an anharmonic oscillator.

$$-\frac{m}{e} \frac{d^2z}{dt^2} = \frac{8c_2^2z}{r_0^4} + \frac{144c_2c_6z^5}{r_0^8} + \frac{256c_2c_8z^7}{r_0^{10}} + \frac{360c_6^2z^9}{r_0^{12}} + \frac{1152c_6c_8z^{11}}{r_0^{14}} + \frac{896c_8^2z^{13}}{r_0^{16}} \quad (5.11)$$

In order to evaluate frequency shifts $\Delta\omega/\omega_0$ as a function of the amplitude, this equation was solved using numerical routines and compared to the solution of a harmonic oscillator. Figure 5.12 shows the frequency shifts, calculated by the use of the effective potential approximation and for full numerically calculated trajectories as a function of different initial positions r_i, z_i . For the calculations a value of $q_z = -\frac{4eV}{m\Omega^2r_0^2} = 0.078$ was chosen².

Frequency shifts due to higher order anharmonicities can also be calculated analytically if one neglects all coupling terms (Eq. 5.10). Such calculations are known from the shift of the eigenfrequencies of ions in Penning traps^[6]. If one assumes that the ions move in a harmonic potential with anharmonic perturbations, frequency shifts can, according to the principle of averaging, approximated. Such formulas are given in the Book from Major, Gheorghe and Werth [6]. In order to use these formulas one has to normalize Eq. 5.10 in the following form.

$$\mathbf{E}^2(z) = \frac{z^2}{r_0^2} + \frac{\tilde{c}_6z^6}{r_0^6} + \frac{\tilde{c}_8z^8}{r_0^8} + \frac{\tilde{c}_{10}z^{10}}{r_0^{10}} + \frac{\tilde{c}_{12}z^{12}}{r_0^{12}} + \frac{\tilde{c}_{14}z^{14}}{r_0^{14}} \quad (5.12)$$

with $\tilde{c}_6 = \frac{24c_2c_6}{r_0^2} \cdot \frac{r_0^2}{4c_2^2}$ and so on. From this, frequency shifts for each higher order anharmonicity can be calculated as a function of the axial amplitude (blue line in

²This value coincides with the parameters used by Gerlich and Decker [31] in the experiment.

Fig.5.12). The frequency shifts up to the order of 14, following Eq. 5.12, can be obtained by the following expression:

$$\Delta\omega/\omega_0(z) = \tilde{c}_4 \frac{3z^2}{4r_0^2} + \tilde{c}_6 \frac{15z^4}{16r_0^4} + \tilde{c}_8 \frac{35z^6}{32r_0^6} + \tilde{c}_{10} \frac{315z^8}{256r_0^8} + \tilde{c}_{12} \frac{693z^{10}}{512r_0^{10}} + \tilde{c}_{14} \frac{3003z^{12}}{2048r_0^{12}} \quad (5.13)$$

The frequency shifts calculated for the different methods are summarized in Fig. 5.12.

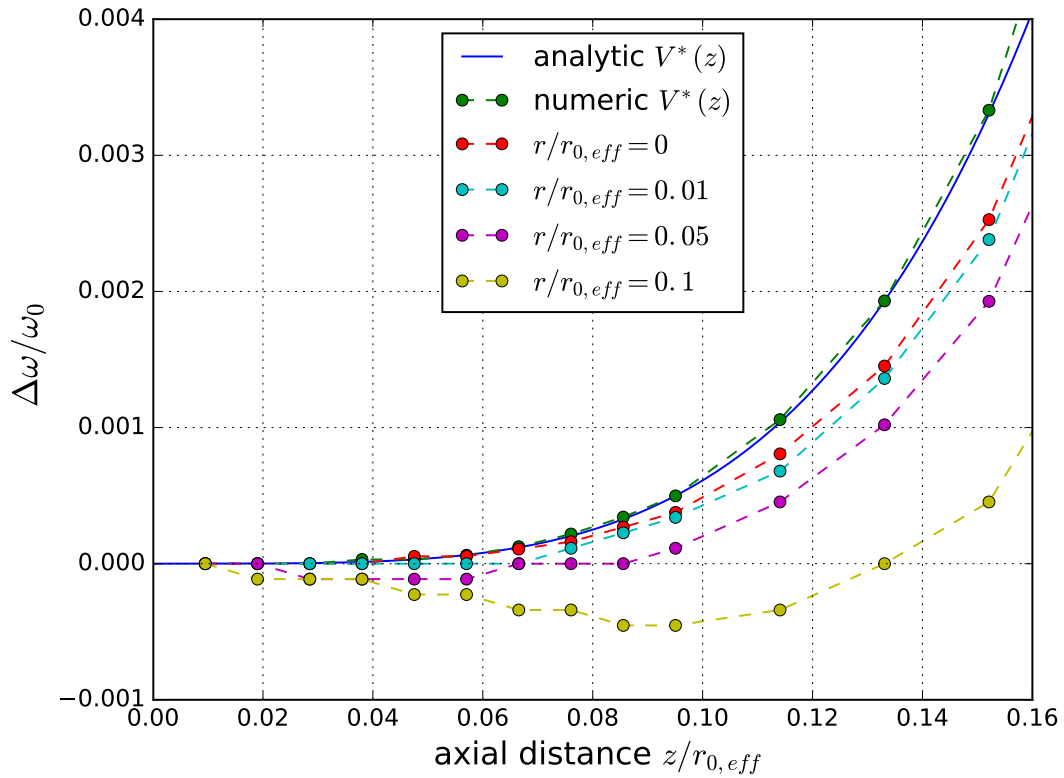


Figure 5.12: This plot shows frequency shifts $\Delta\omega/\omega_0$ calculated in the effective potential approximation $V^*(z)$ (assuming no coupling terms) and the frequency shifts for full 3 dimensional calculations under influence of the rf field for different initial positions r_i, z_i . For the calculation of the trajectories in the oscillating field q was set to $q = 0.078$. The blue line shows the frequency shifts analytically calculated within the effective potential approximation.

The simulations show, that frequency shifts calculated within the effective potential approximation are comparable to the 'real' calculated shifts within a radius of $\rho = \sqrt{x^2 + y^2 + z^2} \leq 3\%$ around the center of the trap. For larger axial amplitudes the deviation of $\Delta\omega/\omega_0(SRET)$ to $\Delta\omega/\omega_0(V^*)$ increases rapidly. The sign of the deviation depends on the radial amplitude r of the ion motion. This results from the neglected coupling terms in Eq. 5.9. For radii $\rho \leq 3\%$ the frequency shifts influenced by higher order field components are negligibly small. The shifts calculated with the analytic expression (Eq. 5.13) coincide almost perfectly with the numerically calculated shifts within the effective potential approximation. Therefore shifts due

to higher order anharmonicities can be predicted with the formula Eq. 5.13. For axial amplitudes $z/r_{0,eff} < 0.015$ the simulation of trajectories does not provide accurate frequency information, but the analytically calculated shifts are smaller than $\Delta\omega/\omega_0 < 4 \cdot 10^{-7}$ in this area. Figure 5.14 shows the shift of the frequency, if the axial and radial amplitude of the ion is too large. This implies, that in experiments for the determination of a highly accurate charge to mass ratio^[33–38], the amplitudes of the ion should be less than 2% of the effective radius $r_{0,eff}$ to guarantee no significant influence of higher order anharmonicities of the field to the secular frequency. Schlemmer et al.^[33] reported a maximal axial amplitude of $z_{max}/z_0 = 0.013$, where $z_0 = \frac{r_0}{\sqrt{2}}$ is small enough that frequency shifts due to anharmonicities can be neglected. This coincides with the results found in this work.

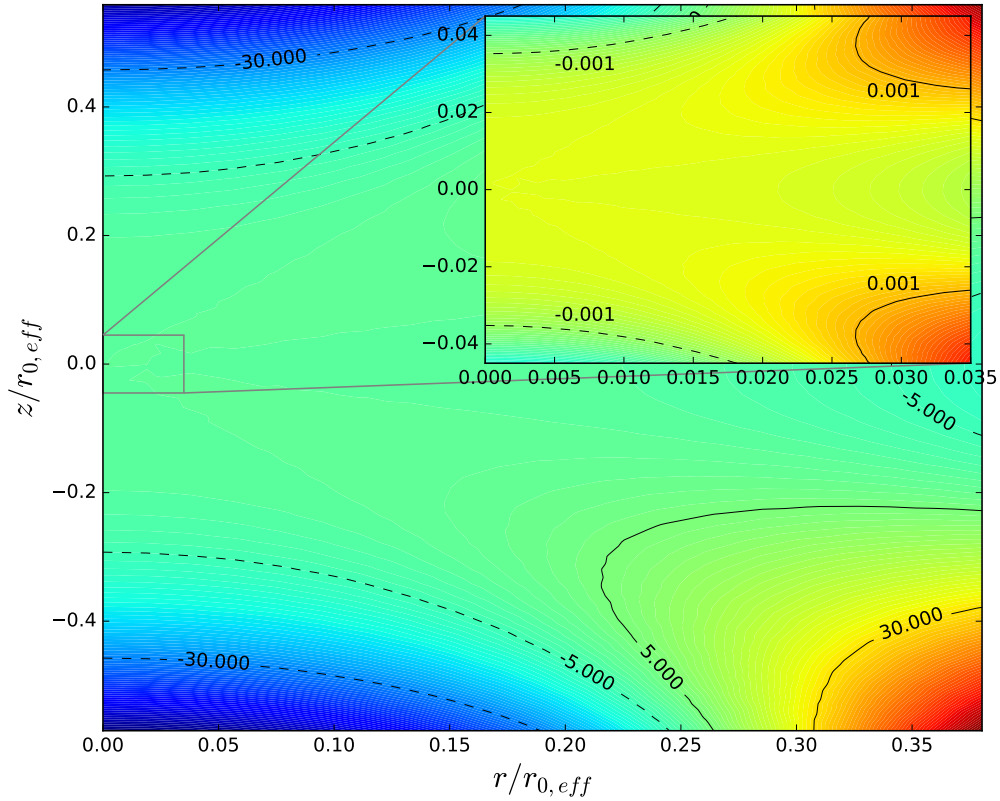


Figure 5.13: The plot shows the relative deviation of the square of the electric field of a pure quadrupole field to the field which is generated from the above described SRET for the region of the trap center in %. Please note: The color scale in the inset was changed in order to see small differences in the relative deviation .

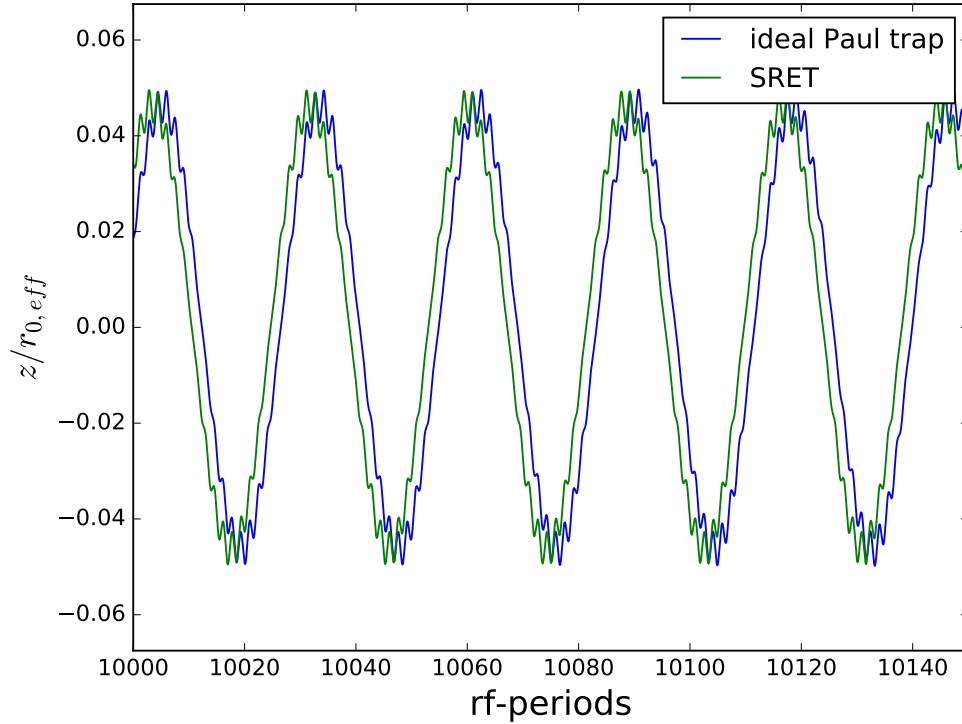


Figure 5.14: The plot shows the calculated trajectories of an ion moving in an ideal Paul trap (blue) and in the SRET (green) with the initial conditions $q = 0.078$, $z = 0.05 \cdot r_{0,eff}$ and $r = 0.1 \cdot r_{0,eff}$ after 10000 periods in the rf field.

5.4 The 22 Pole Ion Trap

The following part was partly published in the paper 'Optimization of RF multipole ion trap geometries' by Fanghänel et al. [30].

The 22-pole ion trap developed by Gerlich [5, 39] is used today in several laboratories to study ion molecule reactions^[40–46] as well as to observe spectra of atomic and molecular ions and clusters^[47–53]. The advantage of higher order multipole traps compared to the more frequently used quadrupole traps is the large electric field free region (see Fig. 5.15) of the trap which allows for efficient buffer gas cooling^[39] as demonstrated recently by several experiments^[53–55]. The lower part of Fig. 5.16 shows a simplified 3 dimensional CAD model of a 22-pole trap. The main parts are the 22 rods aligned as a cylinder with an inner radius of r_0 and the two electrostatic einzel-lenses at the exit and entrance of the trap.

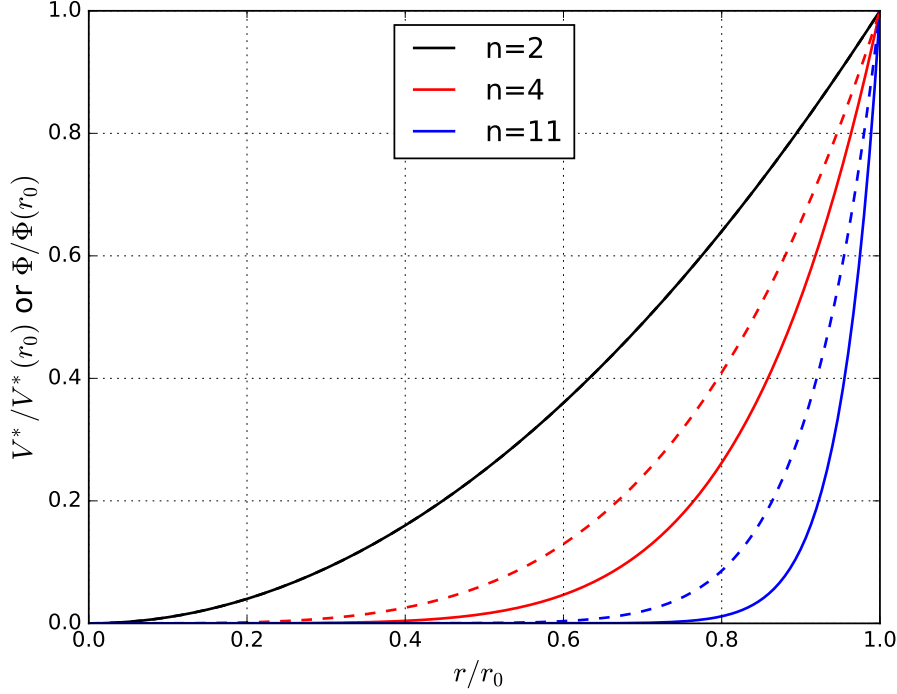


Figure 5.15: The plot shows the effective potential V^* (solid) and the electrical potential Φ (dashed) as a function of the radial distance for different orders of linear multipole traps. For the case of a quadrupole field the effective potential V^* and the electrical potential Φ are identical.

Since $\Phi(\mathbf{r}) \propto \mathbf{r}^n$ and $V^*(\mathbf{r}) \propto \mathbf{E}^2(\mathbf{r}) \propto \mathbf{r}^{2n-2}$, where n denotes the number of RF electrodes divided by two, the large electrical field free region is a consequence of the 22 electrodes on which a radio frequency (RF) voltage is applied. The electrical potential Φ for a 22-pole trap produced by 22 hyperbolic shaped rods is given by Eq. 4.4 with $n = 11$

$$\Phi_{rf}(\mathbf{r}, \phi) = \left(\frac{\mathbf{r}}{r_0} \right)^{11} \cos(11\phi) \quad (5.14)$$

The use of circular rods instead of hyperbolic ones will lead to higher order multipole contributions of the radial trapping field. Due to symmetry the next two higher order multipole components are a_{33} and a_{55} (see Eq. 4.4). By setting R/r_0 to 0.11, where R is the radius of the rods (see Tab. 5.1), the a_{33} component vanishes. The remaining multipole component $a_{55}/a_{11} \approx 0.0027$, has no significant influence on the trapping potential. If the case of the vanishing a_{33} is disregarded, e.g. using $R = 0.0005$ m and $r_0 = 0.005$ m ($\Rightarrow R/r_0 = 0.10$) then a_{11}/a_{33} becomes ≈ 0.0013 . Also in this case the influence on the trapping potential is negligible small. This shows that Eq. 5.14 is still a very good approximation for the electric potential which is produced by 22 circular rods.

As mentioned, the flat potential in radial direction allows for an efficient buffer gas cooling of the ions. Furthermore, due to the large field free region the ions

can largely interact with a reaction gas without the influence of the force from the radial trapping field. For an axial confinement, a static voltage U_{dc} is applied on the entrance end exit lenses, shown as hollow cylinders in figure 5.16 (lower part).

As mentioned in section 3.2.1, the effective potential approximation is an appropriate tool to describe the behavior of charged particles in inhomogeneous fast oscillating electrical fields. In the following this approximation is used to investigate different aspects of a 22-pole trap. For the calculations of the effective potential a voltage of $V_{rf} = 15$ V at a frequency of $\Omega = 2\pi \cdot 17$ MHz is applied to the rods. The dc voltage at the 22-rods was set $U_{dc,22} = 0$ V. For trapping positively charged ions, e.g. mass = 16 u and $q = +e$, a positive dc voltage (U_{dc}) is applied to the trap entrance and exit electrodes. Typical values for U_{dc} are a few Volts although less than 0.1 eV are needed to keep ions at thermal energies. For demonstration purposes $U_{dc} = 1$ V was chosen. The resulting effective potential for these conditions is shown in Fig. 5.16 (upper part) in a x-z cut, where z is the trap axis. Equipotential lines are given for a few, non-equidistant values to characterize the potential well in regions of interest. This result can be interpreted by the fact that ions with a few meV of energy can explore a considerable fraction of the trap volume (several mm in the radial (x) direction and more than 10 mm along the trap axis).

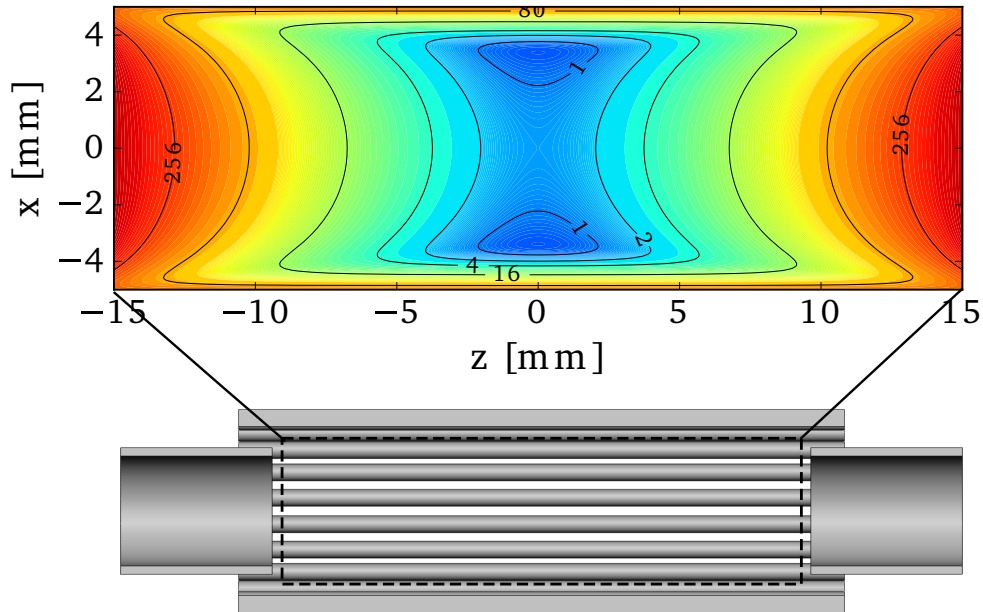


Figure 5.16: Lower part: Cross section of a CAD-model of a 22-pole trap including cylindrical end electrodes. Upper part: Effective potential in the x-z-plane. Equipotential values are given in meV. (This figure is reproduced from Fanghänel et al^[30]).

Figure 5.17 gives a closer look at the effective potential at the axial position $z=0$ for two different applied dc voltages at the end electrodes. The minimum of the effective potential is not at the radial position $x = 0$ as desired. The minimum is

shifted to $x \approx 3.4$ mm for the case of $U_{dc} = 1$ V. and $x \approx 3.7$ mm for 4 V. This shift, which is also seen in Fig. 5.18 is due to the fact that a dc voltages is applied to the end electrodes. This leads to a saddle point of the electrical potential at the center of the trap. Because of the symmetry of the trap in radial direction, a so called 'mexican-hat' potential is formed. This potential leads to a force which pushes the ions towards the 22 rods of the trap. The dashed lines in Fig. 5.17 and 5.18 indicate this dc part of the potential (Φ_{st} in Eq.3.19) alone, the solid lines show the resulting effective potential as a superposition of the rf and the dc parts. The shift of the minima in radial direction, will push cold ions (≈ 1 meV ≈ 10 K) away from the center of the trap. This fact is interesting for spectroscopy studies as done in many recent experiments^[53,55–57]. Since cold ions will be pushed away from the center of the trap a decrease of the overlap with irradiating light which is passed along the trap axis can be expected. Such an effect has been seen in photodetachment experiments of OH^- ^[58] as well as in ion trap simulations from Asvany et al.^[59]. To avoid the effect of a decreasing overlap, the voltage applied on the end electrodes should be well below 1V. This can be done by trapping the ions with appropriate voltages and lowering this voltage to a few mV during the thermalisation process of the ions with a buffer gas.

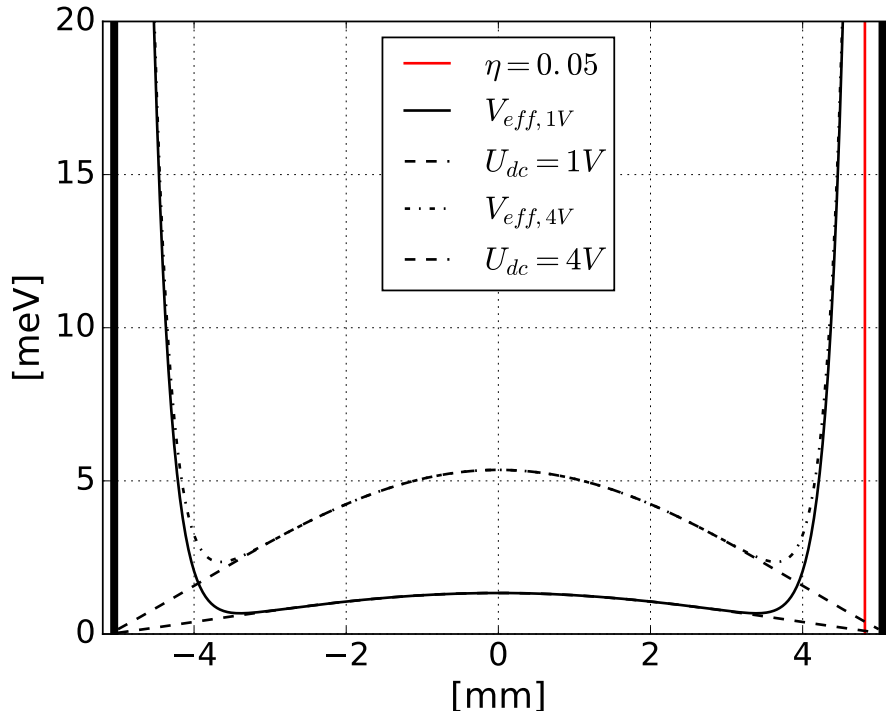


Figure 5.17: Effective potential in radial direction for $z = 0$ in a 22-pole ion trap taking into account the effect of the end electrodes (dc end electrode voltage 1 V and 4 V). The position for the adiabaticity parameter $\eta = 0.05$ is indicated as a red vertical bar. The thick vertical solid lines left and right indicate the position of the rods. (This figure is reproduced from Fanghänel et al.^[30]).

The effective potentials drawn in Fig. 5.17 and 5.18 show another important aspect of low temperature trapping. Since the minimum of the effective potential is not at the center of the trap, the ions will be kept in close distance to the rf electrodes. The ions will always experience a micro-motion, because the rf potential is non-vanishing around the minimum of the effective potential. The amount of energy stored in this micro-motion therefore is the minimum kinetic energy of the ions which is characterized by the energy difference between the dashed line (dc only) and the solid line (full effective potential), shown as vertical bars in Fig. 5.18. Therefore, the ions will not be fully thermalized under these conditions, an issue discussed in several recent publications^[59,60]. This effect increases with increasing the amplitude of voltages on the exit and entrance electrodes.

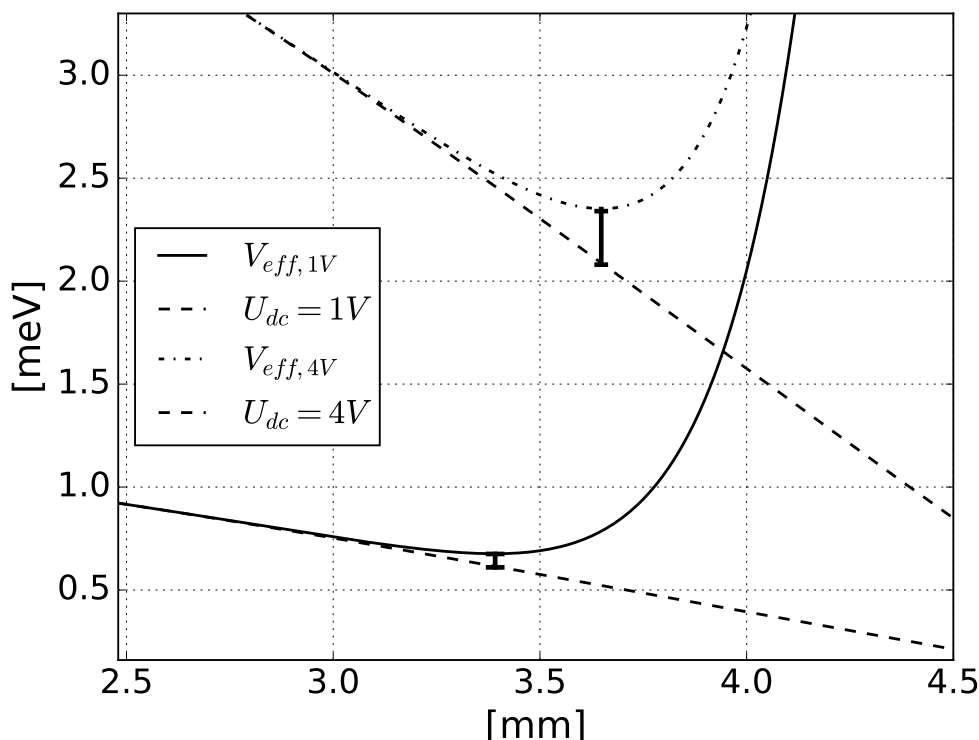


Figure 5.18: Zoom-in view of the minima of the effective potentials of Fig. 5.17. Vertical bars indicate energy of persistent micromotion at the minimum of the effective potential. (This figure is reproduced from Fanghänel et al^[30]).

5.4.1 The Kinetic Energy Distribution

Since the evaluation of experimental data e.g. measuring kinetic reaction rates of ion-molecule reactions is based on the assumption of an ensemble in a thermodynamic equilibrium, the influence of electrical rf-fields to the kinetic energy distribution of the ions is important. It is well known that ions can gain kinetic energy from electrical rf-fields which is named rf heating. Therefore the assumption of a strict

thermodynamic equilibrium is not completely given. To estimate the influence of electrical rf-fields to the kinetic energy distribution of ions simulations of trajectories in an ideal 2 dimensional 22-pol trap under influence of buffer gas collisions were performed. By neglecting space charge effects each ion trajectory can be simulated individually. The simulations were performed in the following way:

1. Create an ion at a random position inside the 22-pole trap with random velocities for both directions which are given from a Maxwell-Boltzmann distribution at around 300 K.
2. Perform random collisions with a buffer gas at a specific temperature given from a Maxwell-Boltzmann distribution. Here, the collisions were treated as elastic collisions, calculated via transformation into the center of mass frame^[59].
3. After around 1500 collisions the buffer gas collisions were stopped and the position and the velocities of the ions were tracked until the mean velocity does not change further.

From this procedure one gets the velocity distribution of each individual ion. The parameters are the same as used above with $U_{dc} = 0$ and a mass of the ions $m = 16$ amu. To get a better insight, the calculations of the trajectories were performed within the effective potential approximation³ (see section 3.2.1). The advantage of using the mathematical construct of the effective potential approximation is the separation of the micro-motion and the macro-motion of the ions, which allows to evaluate their influence to the kinetic energy distribution. Figure 5.19 shows the kinetic energy distribution relative to the initial energy of a single ion moving in an ideal 2 dimensional 22 pole trap separated in different contributions from the micro and the macro-motion of the ions. The velocity of an ion is defined as the time derivative of Eq. 3.7 and the whole kinetic energy is defined as:

$$E_{kin}(t) = \frac{1}{2}m \left(\dot{\mathbf{R}}_0^2(t) + 2 \cdot \dot{\mathbf{R}}_0(t) \cdot \dot{\mathbf{R}}_1(t) + \dot{\mathbf{R}}_1^2(t) \right) \quad (5.15)$$

where $\dot{\mathbf{R}}_0(t)$ and $\dot{\mathbf{R}}_1(t)$ denote the macro and micro motion of the ion. Figure 5.19 (a) shows the energy distribution of the whole kinetic energy. As can be seen in this figure a relative sharp peak appears in the distribution and the energy can reach a maximum of three times the initial energy E_0 . As already known, this sharp peak is almost independent from the initial conditions of the ions^[5]. Figure 5.19 (b) shows the energy distribution accounting for only $\frac{1}{2}m \left(\dot{\mathbf{R}}_0^2(t) + \dot{\mathbf{R}}_1^2(t) \right)$. Figure 5.19 (c) and (d) shows the energy distribution for the macro and micro motion, respectively. Since the last three contributions ((b), (c) and (d)) cannot gain three times the initial energy E_0 , the high energy part arises from the coupling of the micro motion and macro motion (middle term Eq. 5.15). This means the rf-heating effects are

³The results of these calculations are identical with the exact numerically calculated trajectories

a consequence of the micro motion arising from the rf-field which couples to the macro motion of the ions. Figures 5.19 (b) and (c) demonstrate that the sharp defined peak is a feature of the macro motion of the ion. This proves the assumption that the ions will move most of the time in a field free region. The shape of the kinetic energy distribution becomes more narrow, when increasing the order of the multipole trap ($n > 11$)^[5,59]. This means that shape of a velocity distribution of an ensemble of ions becomes a real Maxwell-Boltzmann distribution if one increases the order of multipole. In contrary the velocity distribution of a lower order multipole trap ($n < 8$) is far away from a Maxwell-Boltzmann distribution. In order to calculate rf-heating effects to an ensemble such individual simulations were done for different temperatures of the collisional buffer gas. For each temperature 20000 ions were simulated and the individual energy distributions were accumulated.

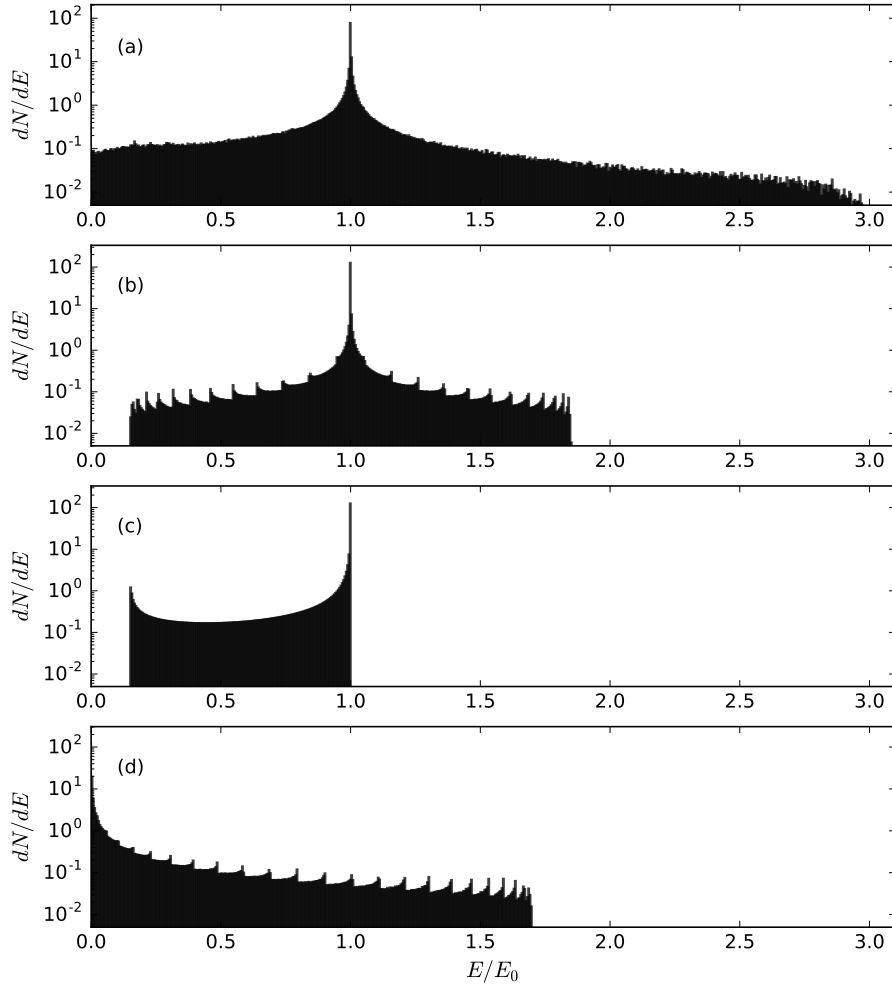


Figure 5.19: The plot shows the kinetic energy distribution relative to the initial energy of a single ion moving in an ideal 2-dimensional 22 pole trap, where figure (a) shows the whole kinetic energy distribution Eq. 5.15. Figures (b), (c) and (d) show the energy distributions of $\frac{1}{2}m(\dot{\mathbf{R}}_0^2(t) + \dot{\mathbf{R}}_1^2(t))$, only the macro motion and only the micro motion, respectively.

Figure 5.20 shows the accumulated energy distributions for a buffer gas with $m = 4$ amu and a temperature of 10 K, separated for individual contributions as before.

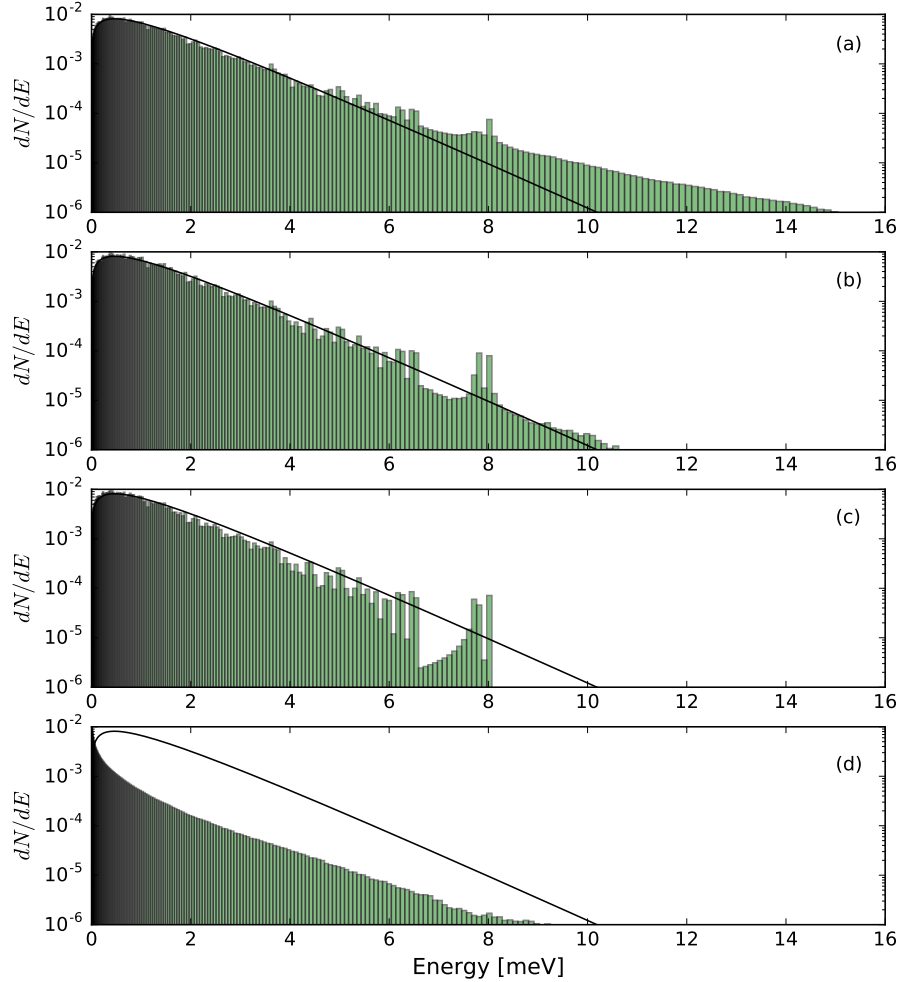


Figure 5.20: The plot shows the accumulated kinetic energy distribution of 20000 ions moving in an ideal 2 dimensional 22-pol trap where figure (a) shows the whole kinetic energy Eq. 5.15. Figures (b), (c) and (d) show the energy distributions of $\frac{1}{2}m(\dot{\mathbf{R}}_0^2(t) + \dot{\mathbf{R}}_1^2(t))$, only the macro motion and only the micro motion, respectively. The black solid lines in this figure indicate a Maxwell-Boltzmann distribution for 10 K.

The black solid lines in this figure indicate a Maxwell-Boltzmann distributions for 10 K. As can be seen clearly in Fig. 5.20 (a), a deviation from a Maxwell-Boltzmann distribution for 10 K towards higher energies. This high energy tail is well known. As can be seen in Fig. 5.20 (b) the sum of the energy from micro and macro motion match well to the Maxwell-Boltzmann distributions for 10 K. Therefore one could assume the whole energy distribution can be separated in two parts. First part is the sum of the energy from micro and macro motion, which are following the Maxwell-Boltzmann distributions for the buffer gas temperature and a second one for a higher temperature part, which derive from the coupling between the micro

and macro motion. Figure 5.21 shows a fit of the weighted sum of two Maxwell-Boltzmann distributions for a buffer gas temperature of 10 K, 20 K and 30 K. As can be seen in this figure a sum of two Maxwell-Boltzmann distributions fits the simulated energy distribution very good. The ratio of T_2 and T_1 is roughly 2.2 and the fraction of the energy contribution from T_1 is $\approx 95\%$. It is an interesting question to what extent the remaining 5% of the higher energy distribution can influence e.g. the measurements of ion-molecule reaction rates.

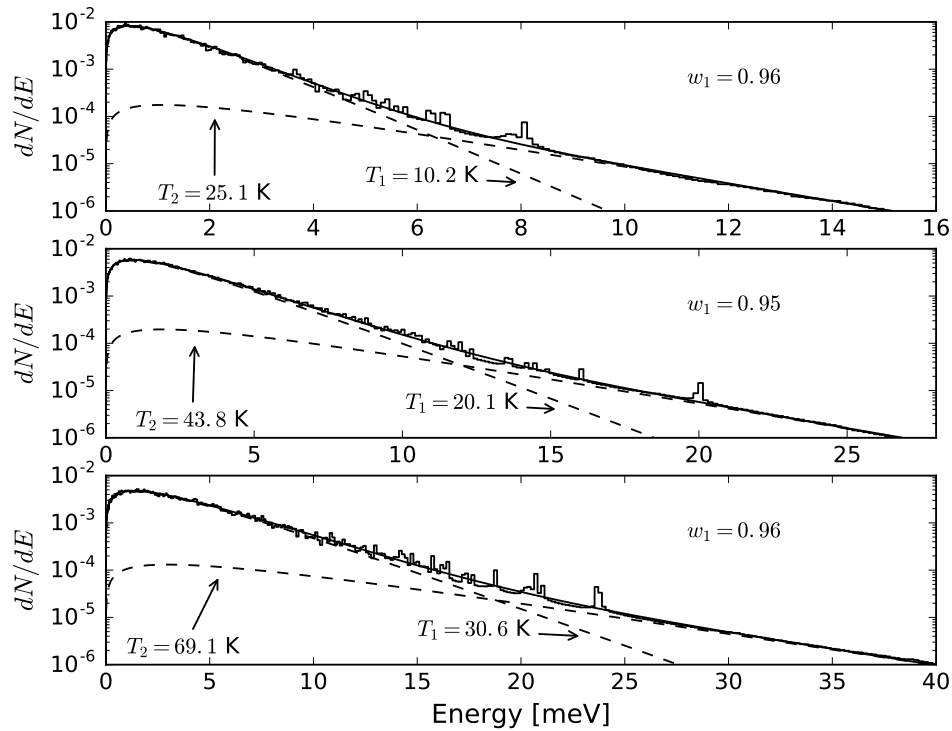


Figure 5.21: The plot shows a fit of a weighted sum of two Maxwell-Boltzmann distributions for a buffer gas temperature of 10 K, 20 K and 30 K from the upper to the lower plot. The two fitted temperatures are indicated by T_1 and T_2 . The weighting factors are indicated by w_1 with $w_2 = 1 - w_1$.

Simulations of a realistic 22-pole trap ($U_{dc} \neq 0$) shows that the shape kinetic energy distribution depends in contrast to the ideal case strongly on the initial conditions of the ions. (Here no buffer gas collisions were taken into account, since this is not necessary in order to demonstrate the above mentioned dependency on the initial conditions.) Figure 5.22 illustrates this for a single ion with different initial conditions. The energy is measured relative to the mean kinetic energy $\langle E \rangle$. The sharp edge for low initial kinetic energies (red and blue lines) are a consequence from the shifted minima in the effective potential. The ions can not overcome the barrier of a few meV in the center of the trap (see Fig. 5.17) and therefore they will only move in a circle w.r.t. the minima. As mentioned above, here, the ions will undergo a permanent micro motion, which can lead to additional rf-heating. With a higher initial kinetic energy (green and black lines in Fig. 5.22), the additional static field

E_{st} is negligible and the kinetic energy distribution converges to the 'ideal' case. This means, for low temperatures (around 4-15 K) the role of the additional static field E_{st} , as a consequence of the axial trapping field, becomes more and more relevant in terms of the translational energy distribution of the ions.

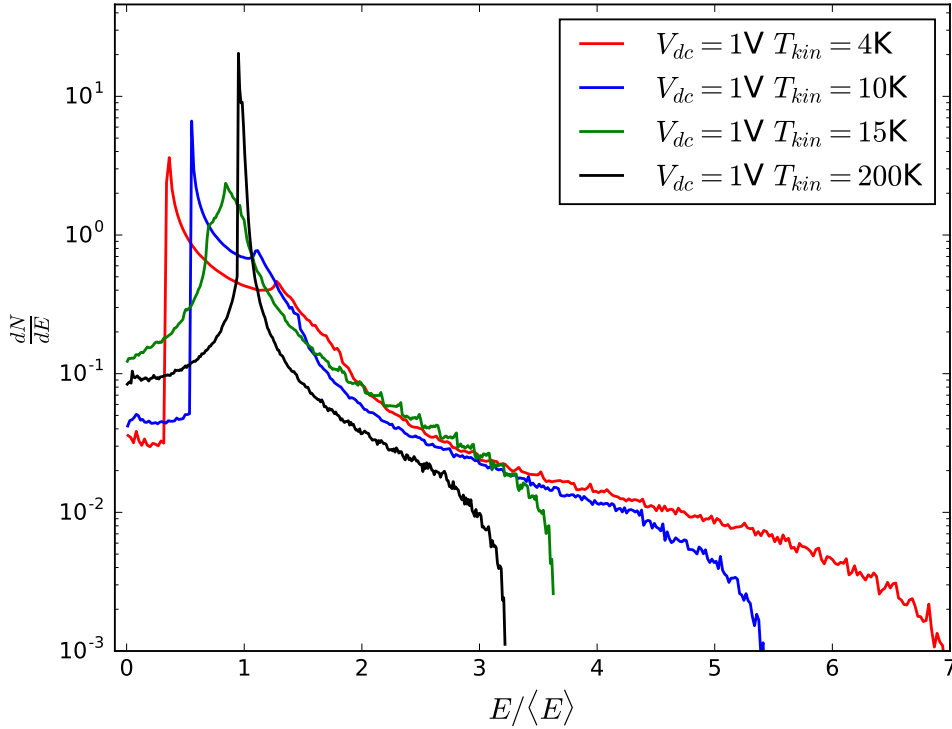


Figure 5.22: The plot shows the kinetic energy distribution of one ion moving in a real 22 pole trap with different initial conditions w.r.t their initial position and velocity. For this simulations no buffergas collisions were taken into account.

Another aspect, essential for spectroscopy studies, is the above mentioned overlap of an axial incoming laser radiation and the ion cloud in the trapping volume. One way to reduce the effects of a decrease of the overlap is the use of ring electrodes surrounding the multipole ion trap. The purpose and use of such ring electrodes has been described extensively by Gerlich^[5]. Figure 5.25 shows a CAD model of such ring electrodes aligned around the rf rods. Figure 5.23 shows a direct comparison for the effective potential formed with normal exit and entrance lenses (lower plot) kept at a voltage of $U_{dc} = 0.5$ V and the effective potential which is formed by two ring electrodes (upper plot) located at $z = \pm 14$ mm w.r.t the trap center with an applied voltage of $U_{dc} = 10$ V. The calculations show, that also with the use of ring electrodes, a 'mexican-hat' potential surface will appear around the center of the trap. The field of these electrodes change the trap potential only by penetration. The advantage of this is, that, by changing the applied voltage on rings in the Volt regime (tens of Volts), the change inside the trap is on a meV scale. Therefore using

ring electrodes as control electrodes leads to highly reproducible trapping potentials. For further calculations one ring electrode has been located near the exit of the 22 pole ion trap ($z = 10$ mm w.r.t. the center of the trap). To evaluate the influence of the size of the ring electrodes two alternative rings with thickness of 0.5 mm and 0.15 mm and a height of 0.8 mm and 2.5 mm have been considered. Fig. 5.24 shows the result of the static potential along the z -axis of the trap. In the upper part the potential barrier is shown along the trap axis ($z, x = 0$). In the lower part equipotential lines are drawn for the two thicknesses in a x - z cut. The 22 rods of the trap and the end electrodes are all kept at 0 V. Applying a DC voltage of 1 V to the ring electrode results in a barrier height of some 0.6 mV on the trap axis.

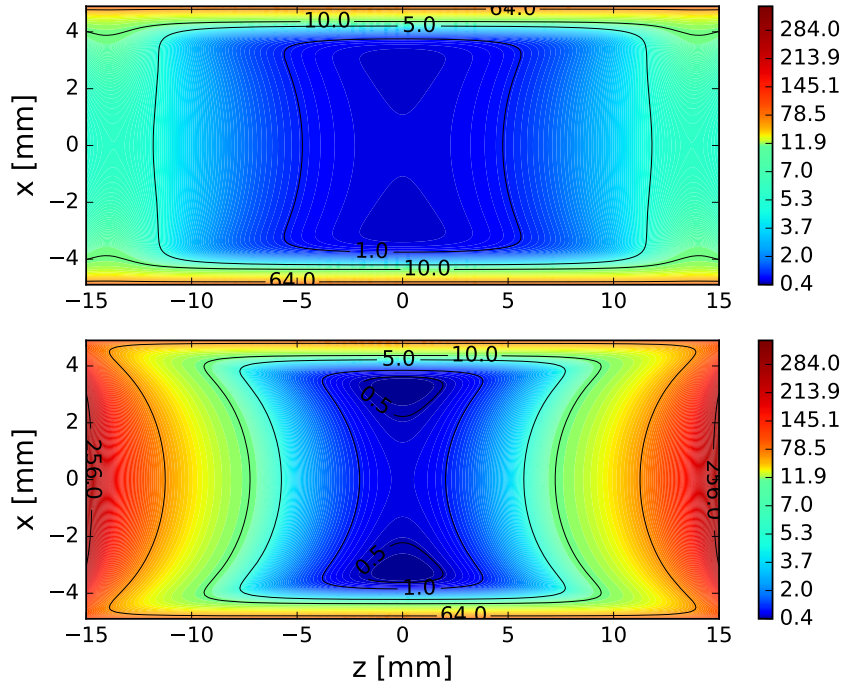


Figure 5.23: The plot shows a comparison between the effective potential which is formed with two ring electrodes located at $z = \pm 14$ mm w.r.t. the trap center with an applied voltage of $V_{dc} = 10$ V (upper) and the effective potential formed with normal exit and entrance lenses (lower) with a voltage of $V_{dc} = 0.5$ V.

The penetration of the 0.5 mm thick ring is about $6 \cdot 10^{-4}$ and somewhat less for the thinner ring. Therefore the height of the penetration depends on the thickness of the ring. These values compare very favorably to previous finite element calculations by Haufler who simulated the effect of ring electrodes and tested the resulting fields by means of ion reflection measurements^[61]. Increasing the distance between the 22 rods and the ring by a factor of two reduces the penetration to some $4.5 \cdot 10^{-4}$. These results suggest that geometrical changes on the ring electrodes lead to substantial changes in the effective potential. Therefore the ring electrodes have to

be manufactured and mounted with considerable mechanical accuracy. Due to the small penetration of the ring electrodes, trapping potentials can be shaped properly for low energy storage of ions. In fact, a small barrier as shown in Fig. 5.24 can be used to leak out ions with excess kinetic energy, e.g. for product ions from a chemical reaction where part of the reaction energy is converted into ion kinetic energy. However, great care has to be taken to calibrate the energy scale of such a setup. Ion reflection measurements as shown by Gerlich^[5] demonstrate that such a calibration is feasible. The combination of both the ring and exit and entrance electrodes can also be practicable. With such a configuration it is conceivable to extract ions which overcome the barrier of the ring electrode. In this case the negative voltage at the exit electrode penetrates the trapping potential. The upper part of Fig. 5.24 shows the effective potential along the trapping axis with conditions for the 22-pole with one ring electrode and a voltage of -0.1 V at the exit electrode. The potential barrier from the ring electrodes practically vanishes. Therefore much higher potentials on the ring electrode are needed to reestablish the desired barrier.

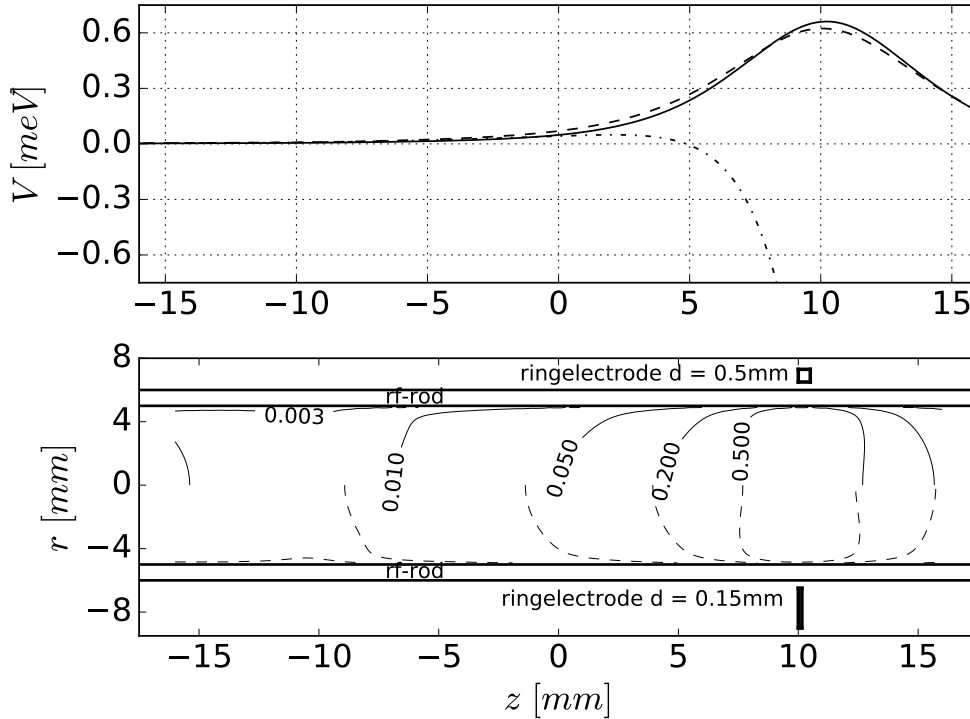


Figure 5.24: Effective potential for a 22-pole ion trap with one ring electrode at $z = 10$ mm. Upper part: Effective potential along the axial direction ($z, r = 0$). Solid line and dashed lines indicate the effective potential for ring electrodes with thickness of 0.5 mm and 0.15 mm and an applied voltage of 0V at the end electrode. The dashed dotted line indicates the effective potential with a 0.15 mm thick ring electrode and a voltage of -0.1V at the end electrode. Lower part: Effective potential as contour lines for a 0.15 mm thick ring electrode (lower half part) and a 0.5 mm thick ring electrode (upper half part). (This figure is reproduced from Fanghänel et al.^[30]).

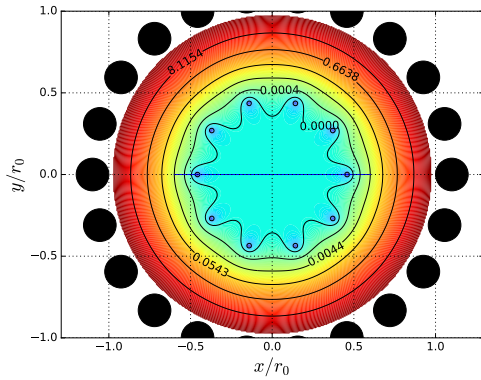


Figure 5.25: The plot shows a CAD model for a 22-pole trap with two ring electrodes aligned around the rf rods

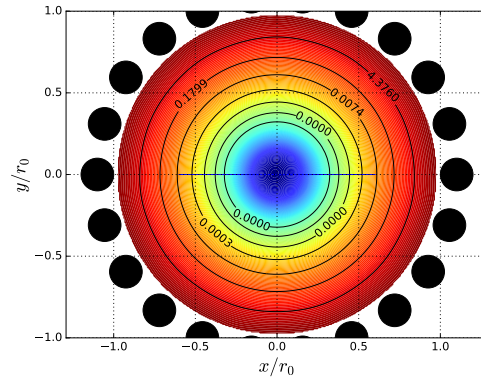
5.4.2 Mechanical Misalignments of the RF Electrodes

At last the influence of a mechanical misalignment of the rf electrodes will be discussed in this section. For sake of simplicity only two cases will be discussed and the results will be shown in terms of the effective potential. The first misalignments is a translational shift of every second rf-rod in positive x-direction for 0.1% of r_0 ($50\mu m$). The second case is a rotational shift of every second rod counterclockwise by one degree. Furthermore, both cases for only a single rod were calculated. The results are shown in Fig. 5.26. Figure 5.27 shows a closer look at the effective potential along the blue lines in Fig. 5.26. The effects from misalignments are in the order of $10^{-2} \mu eV$ for the above used operating parameter for the 22 pole trap. Such small potential distortions become relevant if one works in a kinetic ion temperatures regime of mK. For a kinetic ion temperature regime in the range of kelvin this effects should be negligible compared to the effect of an static potential due to axial confinement from the entrance and exit lenses. Obviously the relevance of such distortions becomes more important if one change the operating parameter of the trap or we increase mechanical misalignments. An effect which is caused by such mechanical misalignments was reported by R. Otto et al.^[62] who finds 10 local minima in the effective potential. They measured the column density distribution of trapped OH^- ions in a 22-pole ion trap which was obtained from position-dependent photodetachment rate measurements. Figure 5.26 ((a),(c) and (d)) shows 10 minima which appear as an consequence of a mechanical misalignment. Figure 5.28 shows the effective potential for their reported operating parameters (mass = 17 amu, $f = 5$ MHz, $V_{rf} = 160$ V and $V_{dc} = -2$ V). In order to match their measured distortion of the effective potential, a misalignment was chosen for one rod with a rotational shift of 1 degree counterclockwise and a translational shift of 1% of r_0 marked with the arrows in Fig.5.28. As can be seen in Fig.5.28, one possibility of the appearance of 10 local minima in the effective potential derived from the density distribution can

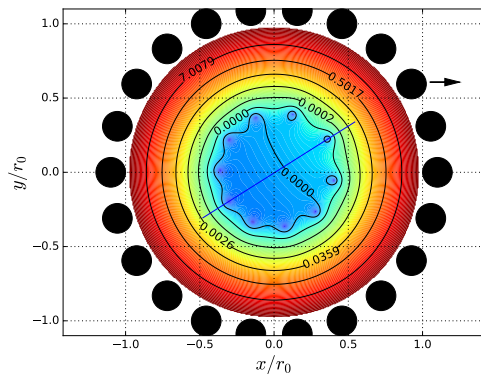
be a misalignment of a single rod. This was also concluded by R. Otto et al^[62] as a possible reason. The calculations demonstrate, that small mechanical misalignments together with inappropriate operating parameters of a 22 pole trap could influence the trapping properties of the device.



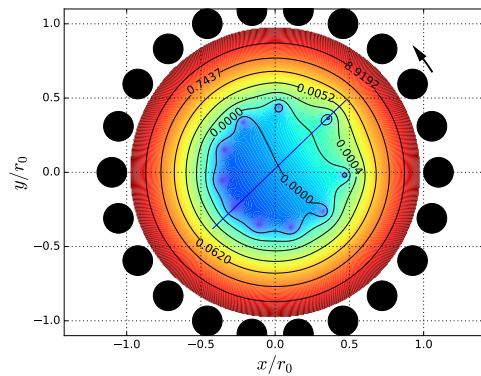
(a) translational misalignment of every second rod



(b) rotational misalignment of every second rod



(c) translational misalignment of one rod (see arrow)



(d) rotational misalignment of one rod (see arrow)

Figure 5.26: The plots show the effect of different forms of misalignments of the rods in terms of the effective potential [meV].

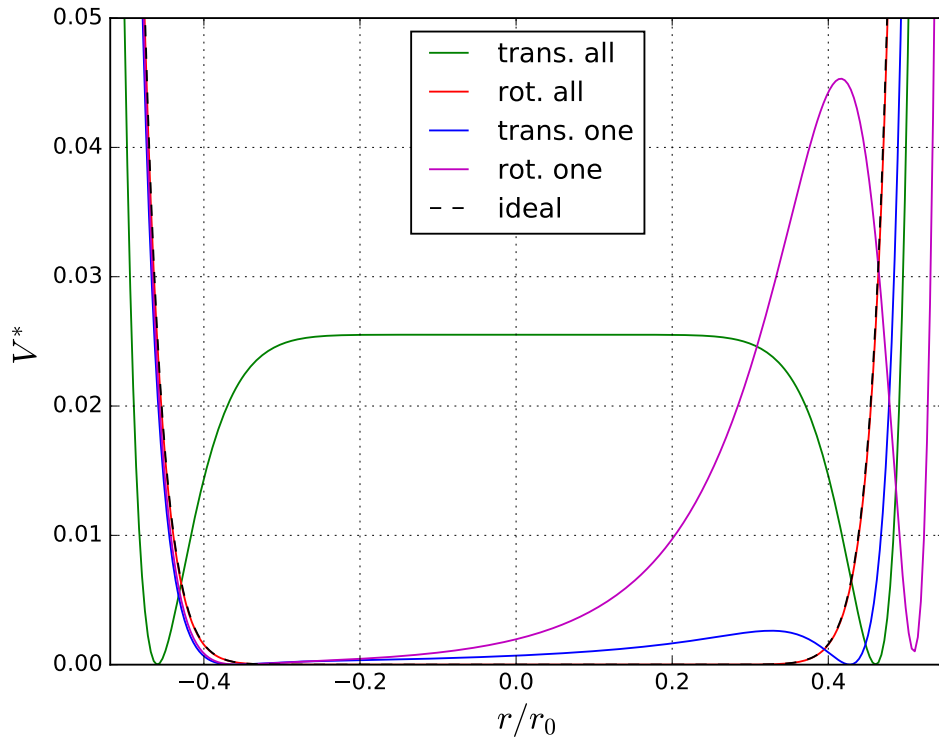


Figure 5.27: The plot shows the effective potentials meV along the blue lines in figure 5.26.

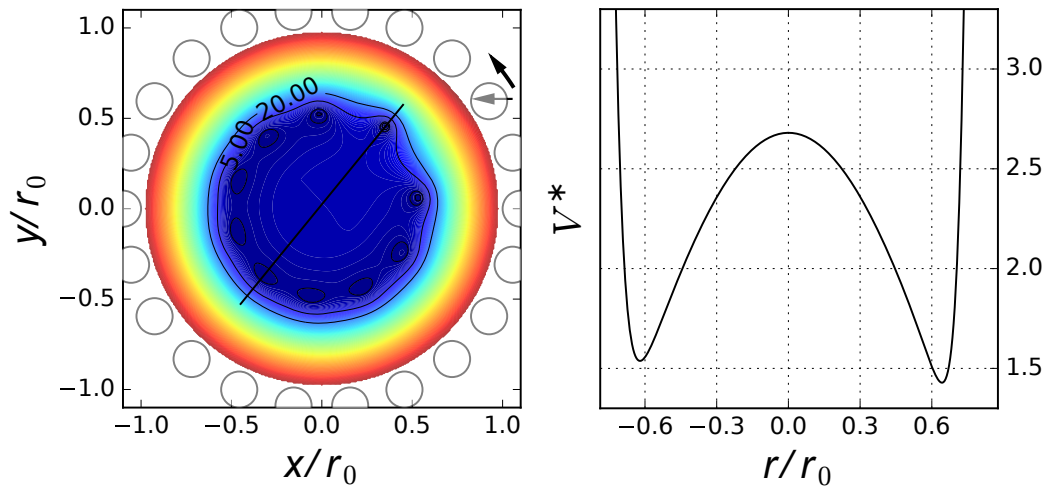


Figure 5.28: The left plot shows the effective potential in meV as a contourplot. The right plot shows the effective potential in meV along the blue line.

5.5 A Linear 24 Pole Quadrupole Trap

As mentioned before, the BEM method is well suited to develop and optimize new trap designs for more sophisticated experiments. In the following a new type of linear multipole trap will be described which allows to trap the ions in a multipole field to cool the ions efficiently to low temperatures and also to mass select them directly in the trap. The benefit of such a trap will be shown based on the following experiment. Figure 5.29 illustrates how such a trap in connection with the method of predissociation spectroscopy of $\text{C}_3\text{H}_3^+ - \text{He}$ can be used to get a spectrum with a good signal to noise ratio. Until now, the experimental procedure in the cologne 22-pole trap looks as follow:

1. trapping of the C_3H_3^+ ions and thermalization with Helium buffer gas. The total number of trapped primary C_3H_3^+ ions is around ≈ 100000 . If the temperature is low enough (≤ 10 K) different complexes of $\text{C}_3\text{H}_3^+ - \text{He}$, $\text{C}_3\text{H}_3^+ - \text{He}_2$ or $\text{C}_3\text{H}_3^+ - \text{He}_3$ etc. will form in the trap (see upper left part Fig. 5.29). From this one will have an approximately constant amount of C_3H_3^+ and $\text{C}_3\text{H}_3^+ - \text{He}$ ions in the trap.
2. dissociate with a laser the $\text{C}_3\text{H}_3^+ - \text{He}$ complex and count the decrease of the number of trapped $\text{C}_3\text{H}_3^+ - \text{He}$ or the increase of C_3H_3^+ ions (blue and red curves upper right part Fig. 5.29).

For statistical reasons it is preferable to count the decrease of the number of trapped $\text{C}_3\text{H}_3^+ - \text{He}$ because the increase of C_3H_3^+ ions (around a few thousand) are in the order of the noise level of the trapped C_3H_3^+ ions.

The above mentioned new trap design allows the following measurement scheme:

1. trapping of the C_3H_3^+ ions and thermalization with Helium buffer gas in the multipole trapping mode. For low temperatures also different complexes of $\text{C}_3\text{H}_3^+ - \text{He}$, $\text{C}_3\text{H}_3^+ - \text{He}_2$ or $\text{C}_3\text{H}_3^+ - \text{He}_3$ etc. will formed in the trap (upper left part Fig. 5.29).
2. switch the trap to a mass selective mode and remove all ion species out of the trap (cleaning the trap) except the $\text{C}_3\text{H}_3^+ - \text{He}$ complex (middle left part Fig. 5.29).
3. dissociate with a laser the $\text{C}_3\text{H}_3^+ - \text{He}$ complex and count the increase of C_3H_3^+ ions (lower part right Fig. 5.29).

Such an experiment can provide better statistical results because the cleaning of the trap leaves no background counts (C_3H_3^+ ions) in the trap.

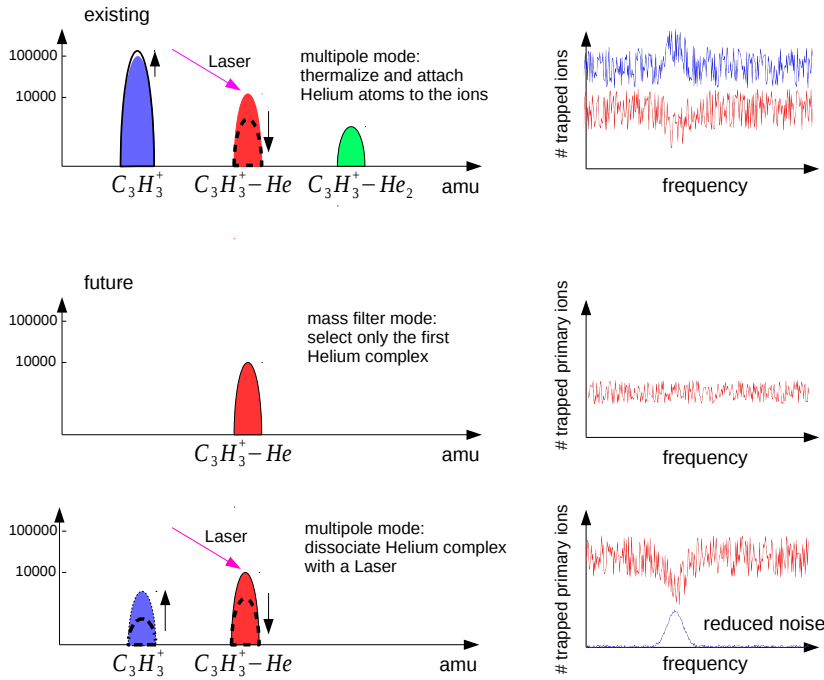


Figure 5.29: The sketch compares an existing and possible future experiment for a new kind of ion trap.

From this the new trap design has to fulfill multiple requirements:

1. a preferably flat trapping potential in the multipole mode to thermalize efficiently the ions to low temperatures
2. an approximate quadrupole potential to select masses with a difference of 4 atomic mass units

A straight forward way to get a near quadrupole potential is to build a so called wire quadrupole. The trap then consists of thin rods (wires) geometrically arranged as a linear quadrupole. Such a linear wired quadrupole has been used in the group of Jana Roithová in Prague^[63] for IRPD spectroscopy of small hydrocarbon dication, $C_7H_6^{2+}$. A cross section (x-y-plane) of such a trap with 24 wires is shown in Fig. 5.30. The effective potential which is produced by this wire arrangement is plotted in Fig. 5.31. The effective potential shows clearly that such an arrangement does not lead to an ideal quadrupole field. With increasing distance away from the trap center anharmonicities of the field becomes more and relevant. This can also be seen in terms of the multipole coefficients (see table 5.4). For the above mentioned experiment the mass resolution $M = m/\Delta m$ of the mass filtering mode has to be in the order of $\approx 39/3 = 13$. For this purpose the deviations from the ideal quadrupole field are negligible.

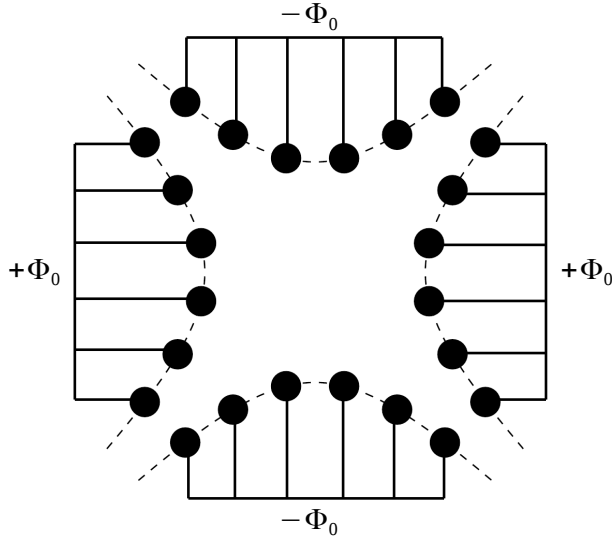


Figure 5.30: Cross section of a 24 wire quadrupole wired as a quadrupole. The wires are arranged along hyperbolic lines (dashed lines).

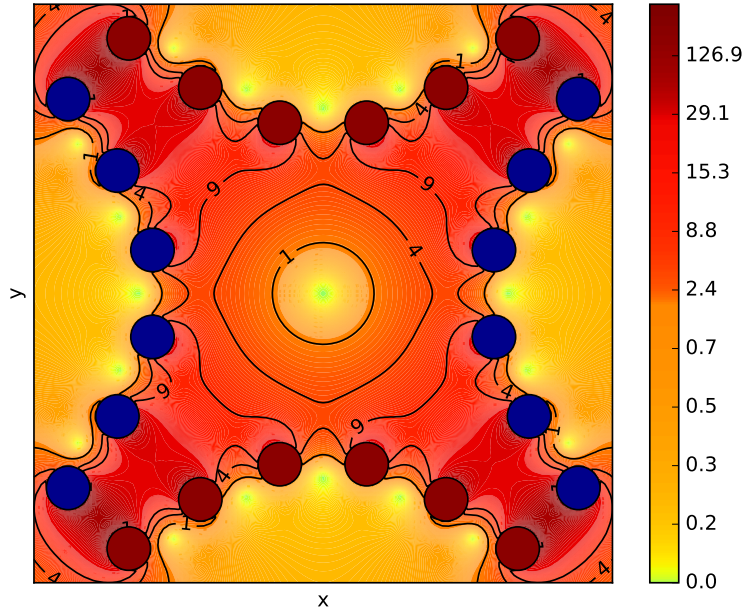


Figure 5.31: The plot shows the effective potential of the rod arrangement as a pure quadrupole. For the calculations of the effective potential the following values are used: mass = 50 [amu], $f = 10$ [Mhz], $V_{rf} = 15$ [V]. The resulting effective potential is given in meV. The blue and red circles mark the rods and their polarity.

To use this trap also as a multipole trap, different possible wirings are shown in Figure 5.34. To thermalize efficiently the ions to low temperatures the effective

potential in the multipole mode should be as flat as possible. The BEM method can now be used to calculate the electric potential, the electric field and so on for different wirings. Figure 5.31 show the resulting effective potentials for the different types of wiring the rods. For all cases of wiring additional minima appear in the effective potential. For case a and d the effective potential is the most flattest. This can be seen in Figure 5.32. This plot shows all effective potentials at a line at 45 degrees w.r.t. x-axis compared to an ideal effective potential from 10-pol and 12-pol multipole trap. The depth of the appearing minima can be seen in figure 5.33. These calculations demonstrate, that ions with a kinetic temperature higher as ≈ 30 K (2.5 meV) can explore these additional minima for these trap settings. To evaluate the different versions of wirings the multipole coefficients are an appropriate tool. These coefficients are listed in Tab. 5.4.

a_k/b_k	quadrupole	version a	version b	version c	version d	version e
2	1.0	0	-0.548369	-0.976445	0.010756	0.526858
4	0	-0.699053	0	0	0.698806	0
6	-0.056243	0	-0.546436	-0.367455	-0.00496	0.556357
8	0	-0.312419	0	0	0.312624	0
10	-0.061112	0	-0.127138	-0.124499	0.000554	0.12603
12	0	-0.029753	0	0	0.029706	0
14	-0.024707	0	0.010883	-0.015576	0.000356	-0.011594
16	0	0.024729	0	0	-0.024758	0
18	0.003237	0	0.022099	0.016734	0.000145	-0.02239
20	0	0.017083	0	0	-0.01708	0
22	0.008119	0	0.010274	0.014206	-6.4e-05	-0.010145

Table 5.4: The table shows the calculated multipole coefficients using Eq.4.4 up to order 22. For the quadrupole wiring only the a_k coefficients appear in the expansion. For the multipole wiring only b_k coefficients appear in the expansion.

The coefficients for version (a) and (d) show, that the potential is nearly the same for distances $r/r_0 \leq 0.9$ away from the trap center. This can be clearly seen at the effective potentials (see Fig. 5.34). Both versions are comparable with an ideal deca (n=5) or dodeca (n= 6) multipole field (plotted as dashed lines in Fig. 5.32) for $r/r_0 \leq 0.6$. To look for stability an η -map can be calculated using the derived multipole coefficients for each wiring type. Keep in mind that this expansion coefficients are only valid for $r \leq r_{0,eff}$. For $r > r_{0,eff}$ the results from the multipole expansion deviate from the real (full numeric) results. All η -maps shows nearly the same regions of stability inside the convergence radius $r_{0,eff}$. Therefore, based on these results (see Fig. 5.32) version (a) and (d) should be the preferred ones. Another question, what will not be answered here, is the used electrical circuit to connect both kinds, the quadrupole and the multipole trap.

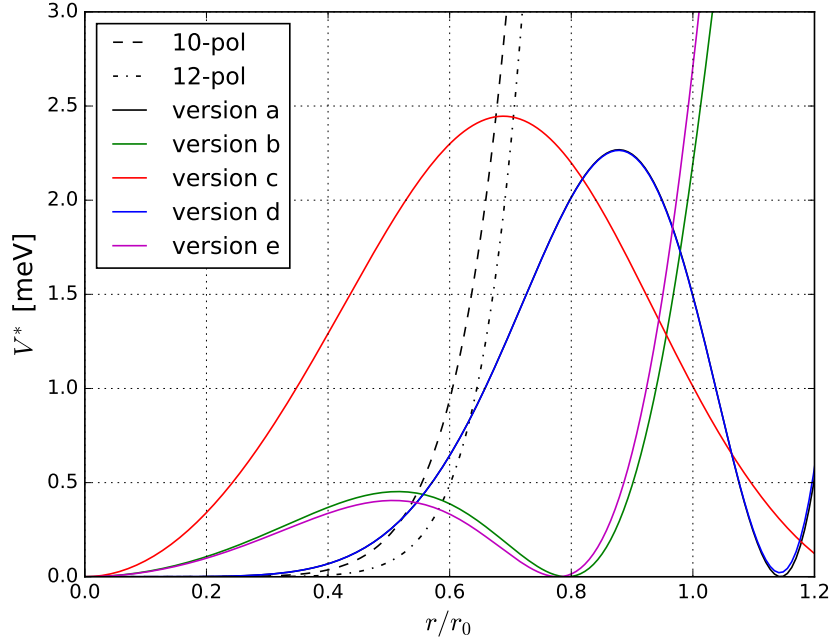


Figure 5.32: The plot compares the effective potential of the five different types of rod wirings at an angle of 45 degree (w.r.t the x-axis) to an ideal deca and dodeca-pol. For the calculations of the effective potential the following values are used: mass = 50 [amu], $f = 10$ [Mhz], $V_{rf} = 15$ [V]. The resulting effective potential is given in meV

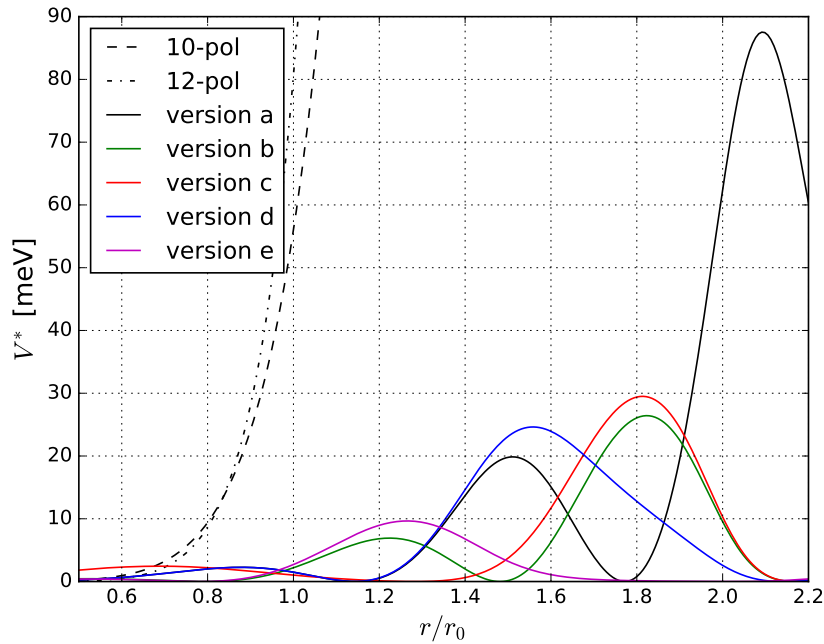


Figure 5.33: Same as Fig. 5.32, different scale.

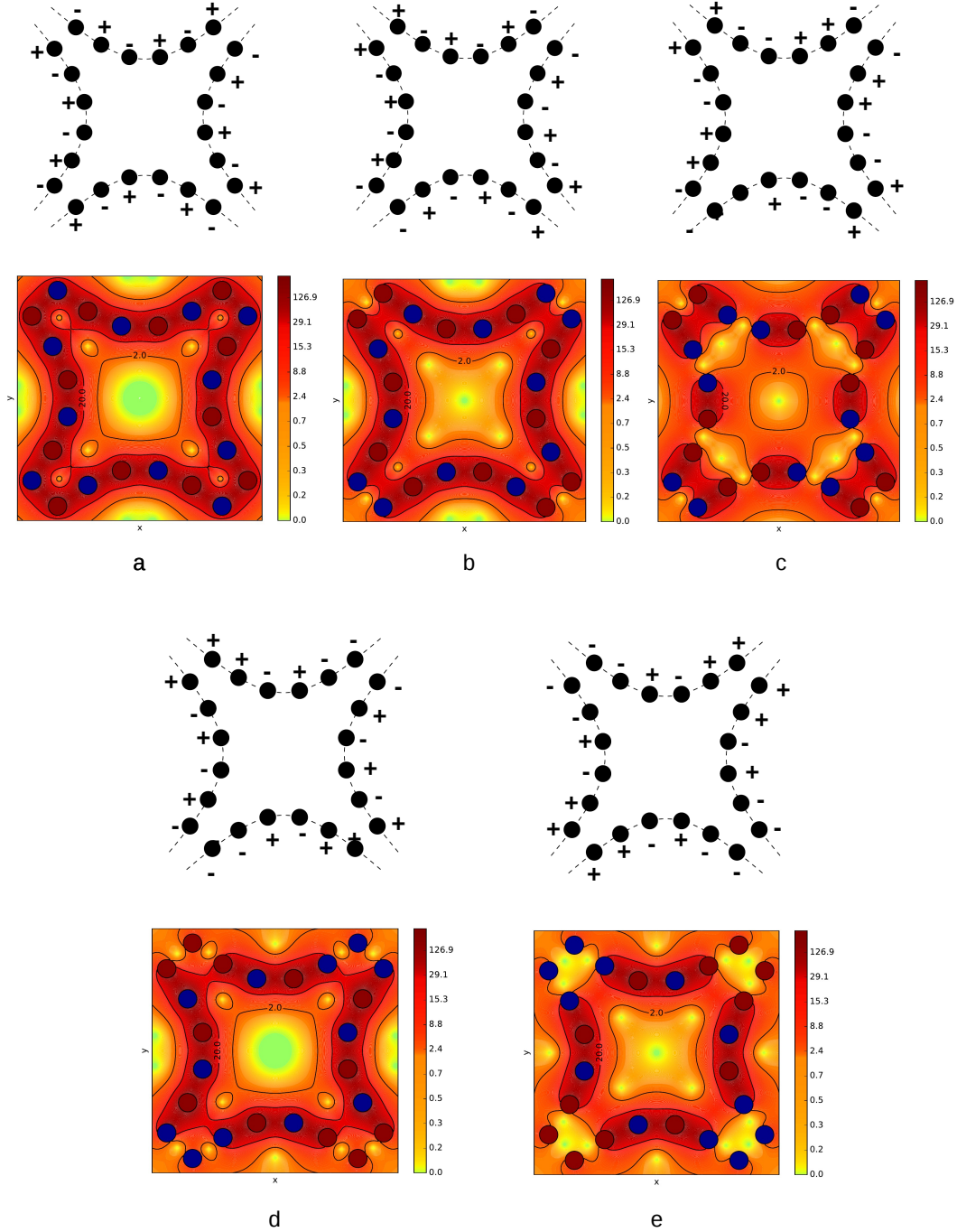


Figure 5.34: The sketch shows five different possible wirings for a 24 wire quadrupole as a multipole. The '+' and '-' signs mark the different polarity of the rods. The lower plots show the effective potential which is produced by the respective wirings. The red ('+') and blue ('-') circles mark the rods and the polarity of the wiring. For the calculations of the effective potential the following values are used: mass = 50 [amu], $f = 10$ [Mhz], $V_{rf} = 15$ [V]. The resulting effective potential is given in meV.

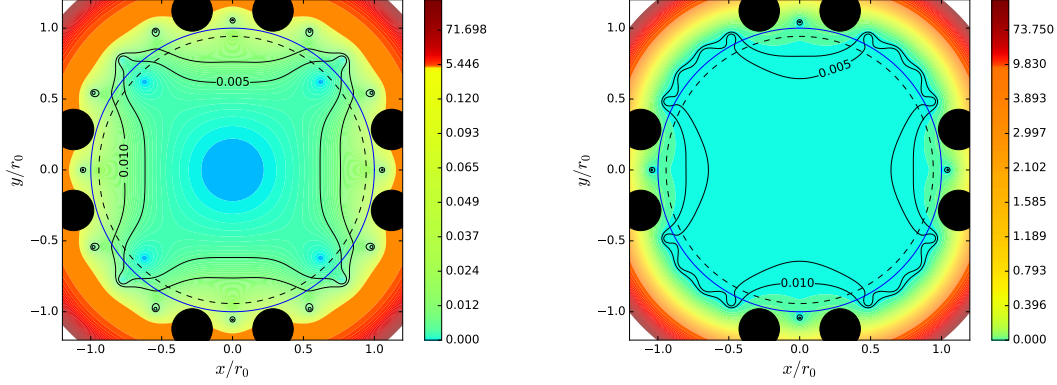


Figure 5.35: The plot shows the scalar field $\eta(\mathbf{r})$ for version wiring (a) and (c) of the 24-multipole. The blue circle marks the effective radius $r_{0,eff}$ and also the edge of the convergence radius for the multipole expansion. The black dashed line indicates $\eta(\mathbf{r}) = 0.02$ for an ideal decapole trap.

5.6 Space Charge Effects

Due to a high ion number density the Coulomb interaction between ions can become significant to influence the motion of ions in an ion trap by an additional time dependent space charge potential. In order to get an impression of the influence of the number density on the ions inside a certain volume one may use the following first order approximation which compares the thermal energy $E_{therm} \sim k_b T$ of the ions with the average energy from the Coulomb repulsion $E_{coulomb} \sim \frac{e^2}{4\pi\epsilon_0 r_{ws}}$ between ions. Here r_{ws} is the Wigner-Seitz radius which is defined as follows:

$$r_{ws} = \left(\frac{3V}{4\pi N}\right)^{1/3} = \left(\frac{3}{4\pi n}\right)^{1/3} \quad (5.16)$$

with being V the trapping volume, N the number of particles or n the number density of the ions. Base thereupon, the following expression is obtained

$$\Gamma = \frac{E_{coulomb}}{E_{therm}} = \frac{e^2}{4\pi\epsilon_0 r_{ws} k_b T}. \quad (5.17)$$

The ratio Γ describes the average nearest-neighbor Coulomb repulsion energy w.r.t. the thermal energy. If $\Gamma \ll 1$ space-charge effects can be neglected. In the following an example will be given to evaluate space charge effects in a 22 pole trap using Eq. 5.17. In order to estimate the Wigner-Seitz radius r_{ws} the effective potential can be used. The effective potential of a real 22 pole trap with the trapping parameters $f = 17\text{MHz}$, $m = 16\text{amu}$, $V_{rf} = 15\text{V}$ and $V_{dc} = 1\text{V}$ on the entrance and exit lenses is shown in the upper part of Fig. 5.16. For a kinetic temperature of 20K ($\approx 2\text{ meV}$) the ions can roughly explore an axial length of $l \approx \pm 3\text{ mm}$ and a radial distance of $r \approx \pm 3.5\text{ mm}$. These assumption results in a trapping volume

of $V = 2l\pi r^2 \approx 2.31 \cdot 10^{-7} m^3$. For simplicity it is assumed that the ions are equally spaced from each other. Figure 5.36 shows Γ as a function of the number of particles for three different temperatures. Unfortunately, it is not possible based on quantity Γ to evaluate to what extent space charge effects can influence the dynamics of ions in a trap. One almost gets the impression that for less than 10000 ions space charge effects can be neglected in a 22 pole trap. The following considerations demonstrate qualitatively the consequences of space charge effects. Assuming an reasonable amount of ions equally spaced around the center of an ideal trap. As a consequence the ion ensemble will create a space charge potential. The electric field created by this space charge potential will push the ions away from the center of the trap. This effect is in competition with the strength of the confining effective potential. Therefore, an equilibrium ion distribution between the space charge potential and the confining effective potential will be formed. As a result, the ions can not be equally spaced within the trapping volume. Since the field free region of an ion trap will increase with the number of multipoles, this effect will also increase with the order of the multipole trap. Therefore a space charge potential created by an ion cloud has the same effect of pushing the ions towards to the rf electrodes as the static voltage U_{dc} from the axial confining entrance and exit lenses of the 22-pole trap (see section 5.4). This has important consequences for the spectroscopy in higher order multipole traps, because one option to increase the signal is increasing the number of trapped ions. This will result in an increase of the above mentioned effect, especially at low temperature. The discussed effect was also experimentally confirmed by Walz et al^[64] for measurements of the spatial distribution of a stored ion cloud in an octupole trap.

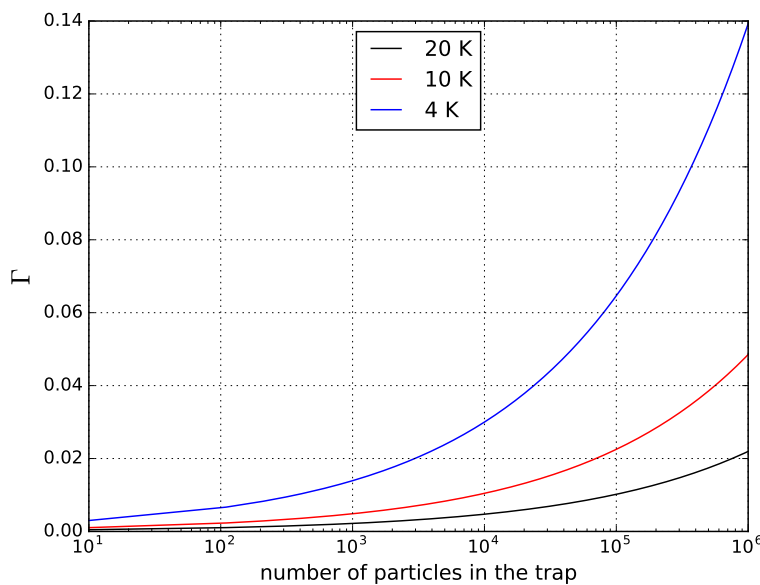


Figure 5.36: The plot shows Γ as a function of the number of particles in a 22 pole trap using the in the text mentioned simplistic assumptions for temperatures of 20K, 10K and 4K.

In order to calculate the density distribution of an ion cloud at a given temperature inside an ion trap one can make use of the so called mean field approach. Since the macro motion of ions is well defined in a time independent effective potential, this approach can be used to describe the global behavior of an ion cloud confined in such an effective potential^[65,66]. Assuming a thermal equilibrium state of an ensemble of N -particles than the number density $n(\mathbf{r})$ is given, according to Dubin^[67] by:

$$n(\mathbf{r}) = N \frac{\exp(-\frac{e}{k_b T} [V_{rf}^*(\mathbf{r})/e + \Phi_{dc}(\mathbf{r}) + \Phi_{sc}(\mathbf{r})])}{\int d^3\mathbf{r} \exp(-\frac{e}{k_b T} [V_{rf}^*(\mathbf{r})/e + \Phi_{dc}(\mathbf{r}) + \Phi_{sc}(\mathbf{r})])} \quad (5.18)$$

where N is the total number of ions, $V_{rf}^*(\mathbf{r})/e + \Phi_{dc}(\mathbf{r})$ is the effective trap potential and $\Phi_{sc}(\mathbf{r})$ is the space charge potential created by the ions. The space charge potential and the density distribution are related by the 'Poisson equation' 2.5, 5.19.

$$\Delta\Phi_{sc} = -\frac{\rho(\mathbf{r})}{\epsilon_0} = -\frac{e \cdot n(\mathbf{r})}{\epsilon_0}. \quad (5.19)$$

Since the number density $n(\mathbf{r})$ is a function of the space charge potential Φ_{sc} (see Eq. 5.18) and Φ_{sc} is determined by the number density (see Eq. 5.19), the space charge potential $\Phi_{sc} = F[n(\mathbf{r})]$ can be expressed as a functional of the number density $n(\mathbf{r})$. As a consequence one can rewrite Eq. 5.18 in the following form

$$n(\mathbf{r}) = c \cdot \exp(-\frac{e}{k_b T} [V_{rf}^*/e + \Phi_{dc} + F[n(\mathbf{r})]]) \quad (5.20)$$

with $c = \frac{N}{\int d^3\mathbf{r} \exp(-\frac{e}{k_b T} [V_{rf}^*/e + \Phi_{dc} + \Phi_{sc}])}$.

This equation can be solved iteratively via 'Fixed-point-iteration' in the following way:

1. Assume an initial number density $n_0(\mathbf{r})$
2. Calculate the corresponding space charge potential $\Phi_{sc,0}$ by the use of Eq. 5.19
3. Calculate the new number density $n_1(\mathbf{r})$ by inserting $\Phi_{sc,0}$ in Eq. 5.18
4. Repeat steps 1.-3. until the difference $\max\{abs(n_i(\mathbf{r}) - n_{i+1}(\mathbf{r}))\}$ reaches an appropriate limit.

In order to perform step 2. a numerical algorithm was developed to solve the Poisson equation in cylindrical coordinates by the use of the finite difference method (see section 4.2.1). Since a knowledge on the static potential $\Phi_{dc}(\mathbf{r})$ is required (see Eq. 5.18) an analytical expression for Φ_{dc} was calculated. This can be done by the following approximation. First, the potential of the 22 rods for $\cos(\Omega t) = 0$ is approximated as a cylinder of a radius $r_{0,cy}$ and a voltage of $\Phi_{dc}(r = r_{0,cy}, z) = 0$, where $r = r_{0,cy}$, z is defined as the shell surface. At the bottom and the top of the cylinder a voltage of $\Phi_{dc}(\tilde{r}, z = \pm l) \neq 0$ is applied, where \tilde{r} is a function which

satisfied the geometry of the exit and entrance lenses. This boundary value problem can be expressed by the following expression^[24].

$$\Phi_{dc}(r, z) = \sum_{n=1}^k f_n J_0 \left(x_n \frac{r}{r_{0,cy}} \right) \frac{\cosh(x_n \frac{z}{r_{0,cy}})}{\cosh(x_n \frac{l}{r_{0,cy}})} \quad (5.21)$$

Here J_0 denotes the Bessel function of the first kind and zero order while x_n is the n-th root of the Bessel function. l is the half length to the lenses (w.r.t. the trap center) and k is an appropriate order to fit the potential. f_n is constant which satisfies the Laplace problem with the given boundary conditions and is defined as follows:

$$f_n = \frac{2}{r_{0,cy}^2 J_1^2(x_n)} \int_0^{r_0} r F(r) j_0 \left(x_n \frac{r}{r_{0,cy}} \right) dr \quad (5.22)$$

$$F(r) = \Phi_{dc}(r, \pm l)$$

J_1 are the Bessel functions of the first kind and first order and $F(r)$ is a function which represents the static potential for $\Phi_{dc}(r, \pm l)$. A comparison of the numerically calculated potential⁴ to the analytic evaluated potential is show in Fig. A.4. The error of the approximation is $L_{2,error} = 5.84 \cdot 10^{-06}$. Since this error is small, the analytical approximation can also be used for a fast integration of the equation of motions in order to simulate ion trajectories in realistic 3-dimensional 22 pole traps. Figures 5.37 - 5.39 show the calculated number density of an ion cloud inside a 22-pole trap for different parameters. For the simulation the same parameters (mass = 16 amu and q = +e, $V_{rf} = 15V$, $f = 17Mhz$) as given section 5.4 were used. These plots nicely shows the above mentioned effect of the shifted ion cloud in radial direction towards to the rf electrodes. Calculations from Champenois et al. [68] who neglects an additional axial static voltage show a similar behavior. Fig. 5.37 (upper plot) shows the increase of the number density in radial with an increasing number of stored ions.

⁴The static potential can be derived with the BEM method (see section 4.2).

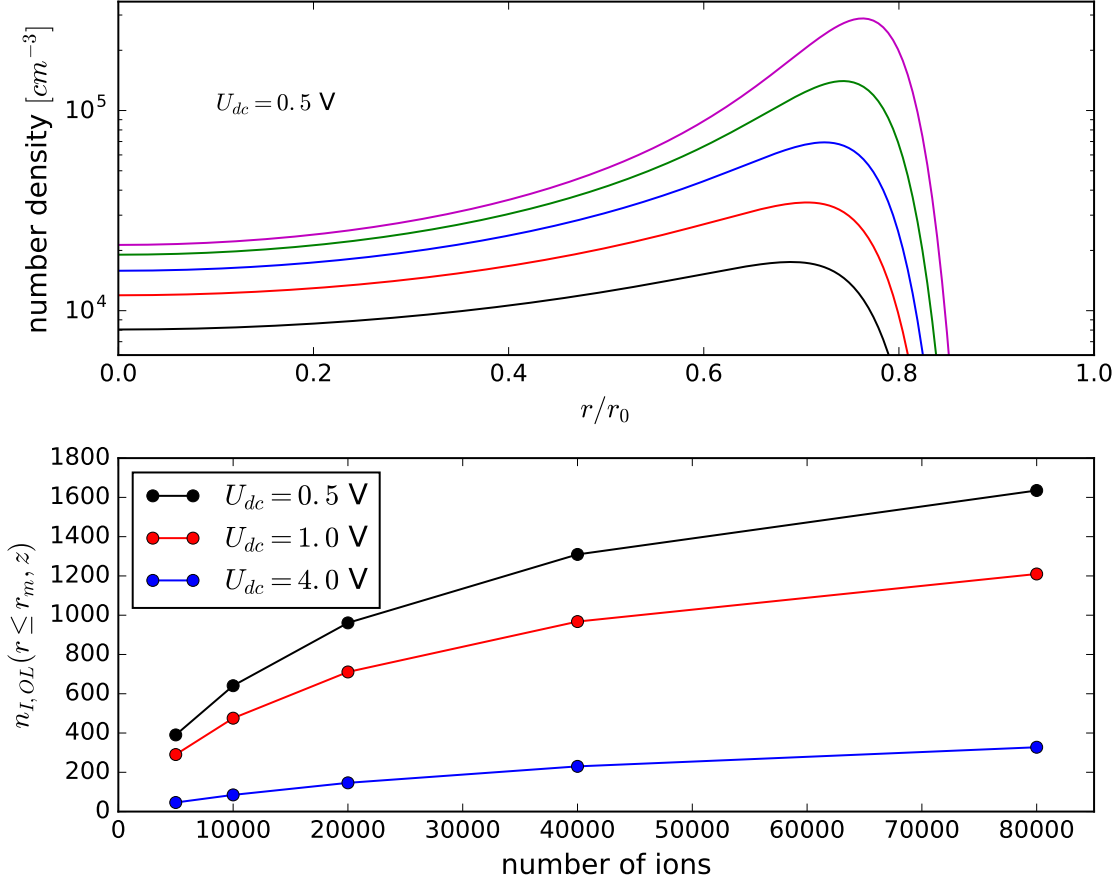


Figure 5.37: The upper plot shows the number density $n(\mathbf{r})$ in ions/cm^3 as a function of the radial direction at $z = 0$ in a 22-pol trap for different numbers of trapped ions at a temperature of 10 K ($U_{dc} = 0.5$ V). The number of trapped ions correspond to the circles in the lower plot. The lower plot illustrates the calculated overlap (see Eq. 5.23) of a radiation source (beam radius of $r_m = 1.5$ mm) with the ion cloud in 22 pole trap as a function of the total number of stored ions for 10 K with $V_{dc} = 0.5, 1, 4$ V.

As can be seen in this figure, the more ions will be stored, more ions will be pushed towards the rf electrodes. By means of spectroscopy in a 22 pole trap, the overlap between light and the ion cloud around the center determine the strength of our signal if all other parameters are constant. For a mean laser beam radius of $r_m \approx 1.5$ mm the lower plot in Fig. 5.37 shows the calculated overlap

$$n_{I,OL} = 2\pi \int_{-z_0}^{z_0} \int_0^{r_m} n(r, z) r dr dz \quad (5.23)$$

of the laser with the ion cloud as a function of the total number of stored ions (10K and $U_{dc} = 0.5, 1, 4$ V). One can see the expected decrease of the overlap with decreasing number of stored ions. Furthermore, the calculations show the as suggested in section 5.4 decrease of the overlap with an increase of the applied voltage U_{dc} at

the exit and entrance lenses. Figures 5.38 and 5.39 show the number density as function of the radial and axial directions. Figure 5.39 shows that the ion cloud widens in axial direction with an increase of the total number of stored ions. This is a consequences of the electric field which is created by the ion competing with the effective potential in radial and axial direction. Figure 5.38 shows that with a decreasing temperature the electric field which is created by the ion cloud becomes more and more relevant, since the thermal energy becomes smaller than the energy stemming from the coulomb repulsion (see Eq. 5.17). The calculation done within the mean-field approach demonstrates the influence of the size of the ion ensemble w.r.t. the the local density distribution. The results shows also that space charge effects can not be neglected a priori in 22 pole ion traps for a reasonable amount of stored ions.

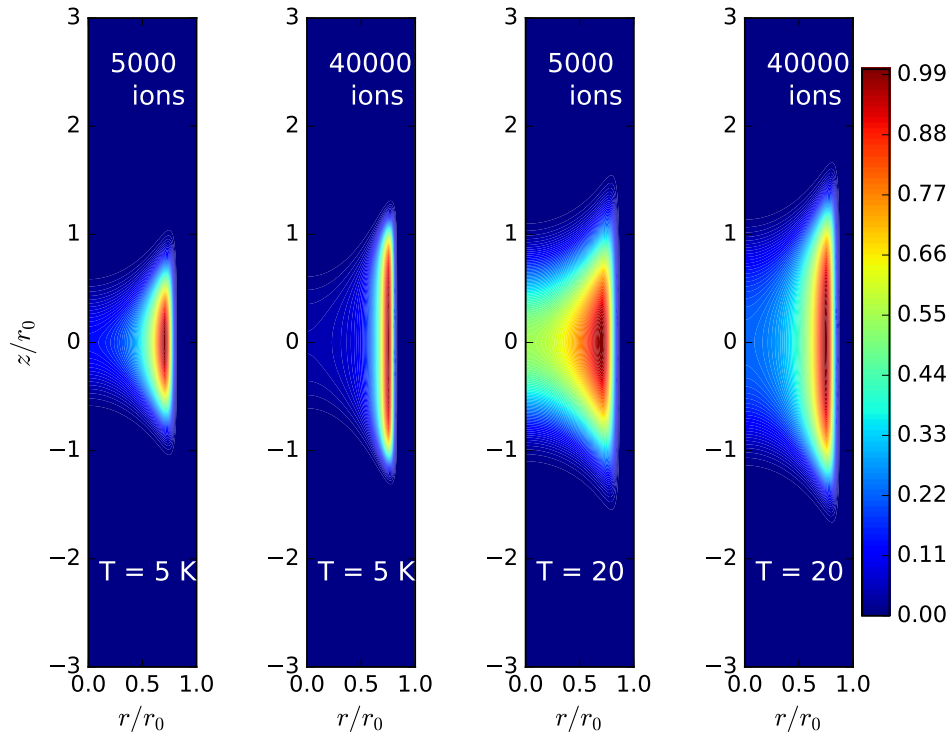


Figure 5.38: The plots show the number density $n(\mathbf{r})$ as a function of the radial and axial direction of a 22-pol trap for different numbers of trapped ions at 5 K and 20 K. For reason of comparability, all distributions are scaled to their maximum value.

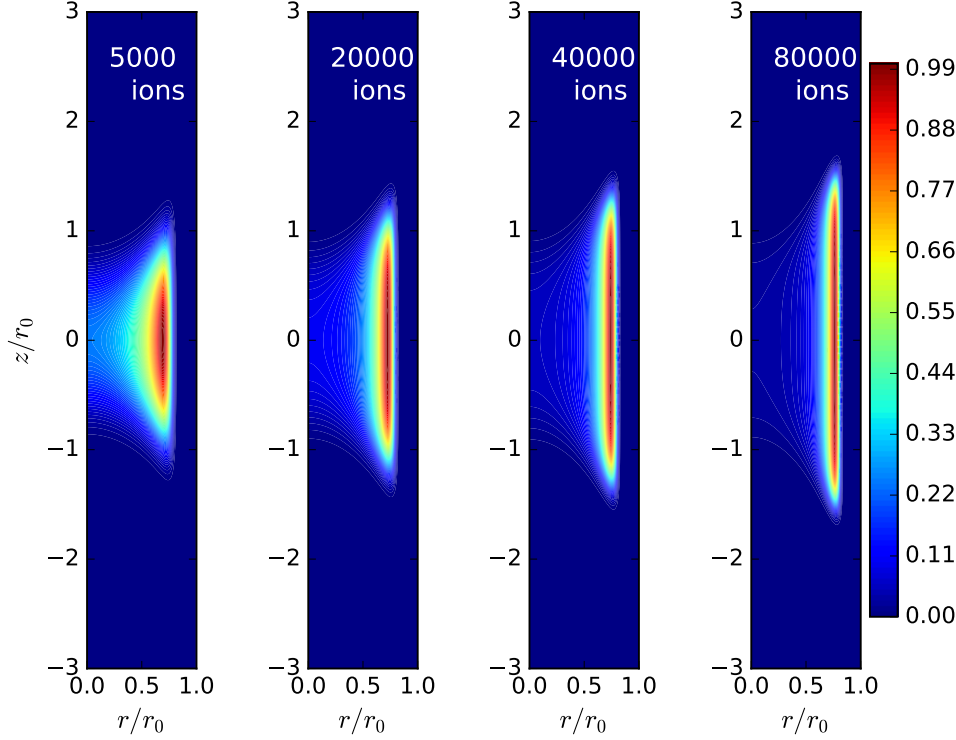


Figure 5.39: The plots show the number density $n(\mathbf{r})$ as a function of the radial and axial direction of 22-pol trap for different numbers of trapped ions at a temperature of 5 K and an axial trapping voltage of 0.5 V. For reason of comparability, all distributions are scaled to their maximum value.

Furthermore, these calculations can be used to calculate rf heating effects in a first order as a function of the number of stored ions. As can be seen in Fig. 5.37 the ions will be pushed towards the rf electrodes with an increasing number of ions. As a result, more ions will undergo a 'higher' permanent micro-motion. In order to calculate first order heating effects, one can make use of the time averaged kinetic energy of the oscillating motion. Within the effective potential approximation this can be expressed by:

$$\langle E_{kin,osc}(t) \rangle = \frac{1}{2} m \langle \dot{\mathbf{R}}_1^2(t) \rangle = V_{rf}^*(\mathbf{R}_0(t)). \quad (5.24)$$

with $\dot{\mathbf{R}}_0(t)$, $\dot{\mathbf{R}}_1(t)$ the macro and micro motion of the ion. The calculation of the number density in the mean field approach depends on the temperature of an ion cloud (in a thermal dynamic equilibrium) and the time independent effective potential. The latter represents the kinetic energy of the macro-motion. For the total kinetic energy the additional micro-motion has to be taken into account. To calculate this additional energy one may take into account that the number density represents the probability-distribution $p(\mathbf{r})$ that an ion is on average at position \mathbf{r} in the trapping volume. With Eq. 5.24, the additional kinetic energy from the micro-motion can be estimated as follows:

$$\langle E_{kin,micro} \rangle = \sum_i p(\mathbf{R}_{0,i}) \cdot V_{rf}^*(\mathbf{R}_{0,i}) \quad (5.25)$$

The effective temperature of the ion ensemble can be calculated as follows:

$$T_{eff} = T_{macro} + \frac{2}{3k_b} \cdot \langle E_{kin,micro} \rangle \quad (5.26)$$

with T_{macro} the temperature in a thermal dynamic equilibrium. As can be seen in Fig. 5.40, the temperature increases with the number of stored ions and with an increase of the applied dc voltage at the exit and entrance lenses. At small numbers of stored ions the effective temperature tends to the temperature of the ensemble in a thermal dynamic equilibrium. Here, increase is mainly determined by the axial trapping voltage which pushes the ions towards the rf electrodes. With an increase of the number of trapped ions space charge effects dominates the temperature increase. This is caused by the large field free region of a 22-pole trap. This approximation of first order heating effects in connection with the simulations done within the meanfield approach reveals that rf-heating is stronger as lower the nominal trap temperature, as higher the total number of stored ions and as higher the axial trapping voltage is. For multipole traps of order smaller than $n = 11$, the effect of pushing the ions toward to the rf electrodes will decrease but to the same extent the ions will undergo a longer time period in a not field free region which will result also in an effective temperature increase.

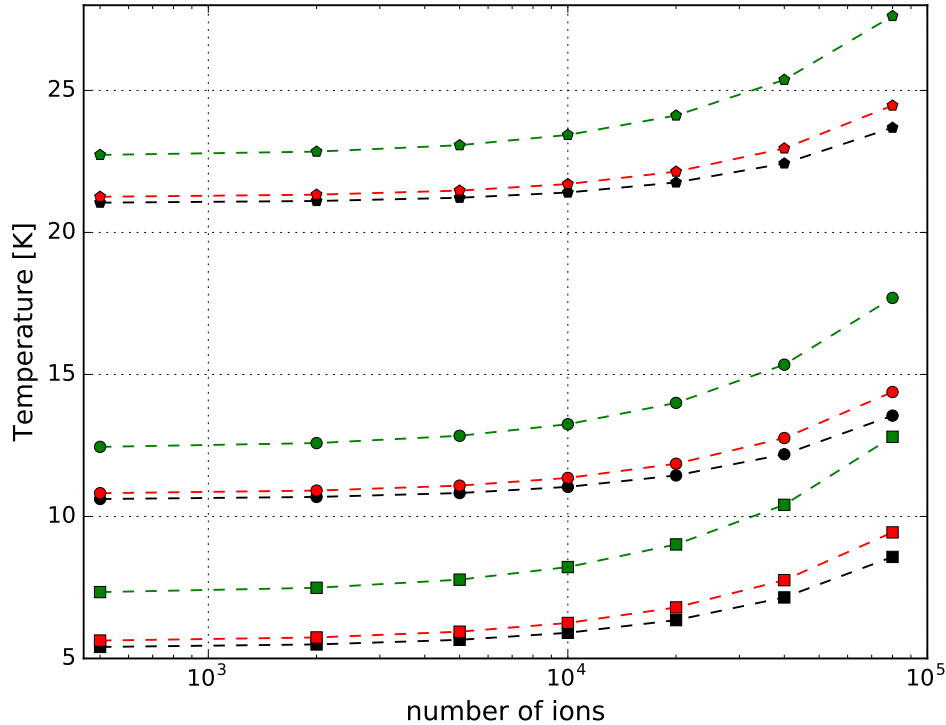


Figure 5.40: The plots show the effective kinetic temperature (see Eq. 5.26) of an ion ensemble as a function of the number of stored ions (x-axis) and the applied dc voltage (color coded) at the entrance and exit lenses of a 22-pole trap. Black, red and green indicates $V_{dc} = 0.5, 1$ and 4 V.

Additionally, ion trajectories in a 22-pole trap under the influence of collisions and

coulomb repulsion due to space charge effects were simulated to verify the mean field approach. The developed numerical algorithm to solve the Poisson equation in cylindrical coordinates with use of the finite difference method was used in order to calculate the space charge effects. As a collision model a simple elastic hard sphere collision model was used^[59]. Therefore, the velocity of both colliding particles were transformed in the center of mass frame. The velocity of the buffer gas particle was chosen randomly from a Maxwell Boltzmann velocity distribution at the simulated trap temperature. The collisional impact position of the buffer gas particle was chosen randomly around the ion. From this, the velocity of the ion after the collision in the center of mass frame was calculated. The resulting velocity of the ion is obtained by transforming back into the laboratory frame. The electric field of the 22 pole trap was calculated using the superposition of an ideal radial trapping potential (Eq. 5.14) and the axial electric potential given in Eq. 5.21. Together with Eq. 3.1 the Equations of Motion (Eq. 5.27) can be integrated very efficiently

$$\begin{aligned}\ddot{x} &= \frac{e}{m} \left(\cos(\Omega t) \cdot E_x + \frac{\partial \Phi_{dc}(r, z)}{\partial x} + E_{x,sc} \right) \\ \ddot{y} &= \frac{e}{m} \left(\cos(\Omega t) \cdot E_y + \frac{\partial \Phi_{dc}(r, z)}{\partial y} + E_{y,sc} \right) \\ \ddot{z} &= \frac{e}{m} \left(\frac{\partial \Phi_{dc}(r, z)}{\partial z} + E_{z,sc} \right)\end{aligned}\tag{5.27}$$

where E_i denotes the electric field of the rf part and $\frac{\partial \Phi_{dc}(r, z)}{\partial i}$ ($i = x, y$) the static electric field of the trap. $E_{i,sc}$ ($i = x, y, z$) is the electric field from the ion cloud. The integration was done with the beforehand mentioned Runge-Kutta-Nystroem-method. The simulations were performed with an cloud size of 5000, 10000, 20000, 40000 and 80000 ions. In order to reduce the calculation time the simulation was separated in two phases, an initial and final phase. In the first phase a certain number of ions were randomly distributed within the trapping volume with a Maxwell Boltzmann distribution of 300 K. Furthermore, the integration time step was increased and the calculation of \mathbf{E}_{sc} was only performed for every 20 th. period of oscillation. Additionally random collision processes with the buffer gas were performed. For the final phase, the integration time step has been reduced. The calculation of the electric field due to space charge effects \mathbf{E}_{sc} was performed for every second period of oscillation. This can be done, because the spatial change of the position of the ion ensemble is very slow, so that the electric field due to space charge effects is not significantly changing within one period of oscillation. In agreement to the experiments, the frequency of the collisions with buffer gas was following an exponential decay. After a certain number of integration steps the velocities were stored in a 1-dimensional histogram ($\mathbf{v} = \sqrt{v_x^2 + v_y^2 + v_z^2}$) and the positions were stored in a 2-dimensional histogram (\mathbf{r}, z components) in order to reduce the memory effort for saving the positions and velocities of the ions. The histograms were accumulated until the change of the position histogram did not change significantly anymore. Furthermore, the velocity component v_z , parallel to a laser beam, was extracted for

all ions at position $r \leq 0.0015$ mm. From this the Doppler broadening can be calculated to determine the translational temperature of the ions within the overlap of the laser beam.

Fig. 5.41 shows the calculated density distribution from the simulation of an ensemble of 5000, 20000, 40000 and 80000 ions at a nominal trap temperature of 5 K and an axial trapping voltage of 0.5 V. The results of the full numerical approach are quiet similar to the results from the mean field approach (see Fig. 5.39). A closer in look on Fig. 5.42 shows that the number density calculated with both methods differs for $r/r_0 \lesssim 0.4$. This means that the calculated overlap of a laser with the ion cloud in Fig. 5.37 is probably smaller than predicted by the mean field approach. Nevertheless, the calculations show that the mean field approach is an appropriate and efficient tool to calculate the number density as a function of the size of the ion cloud.

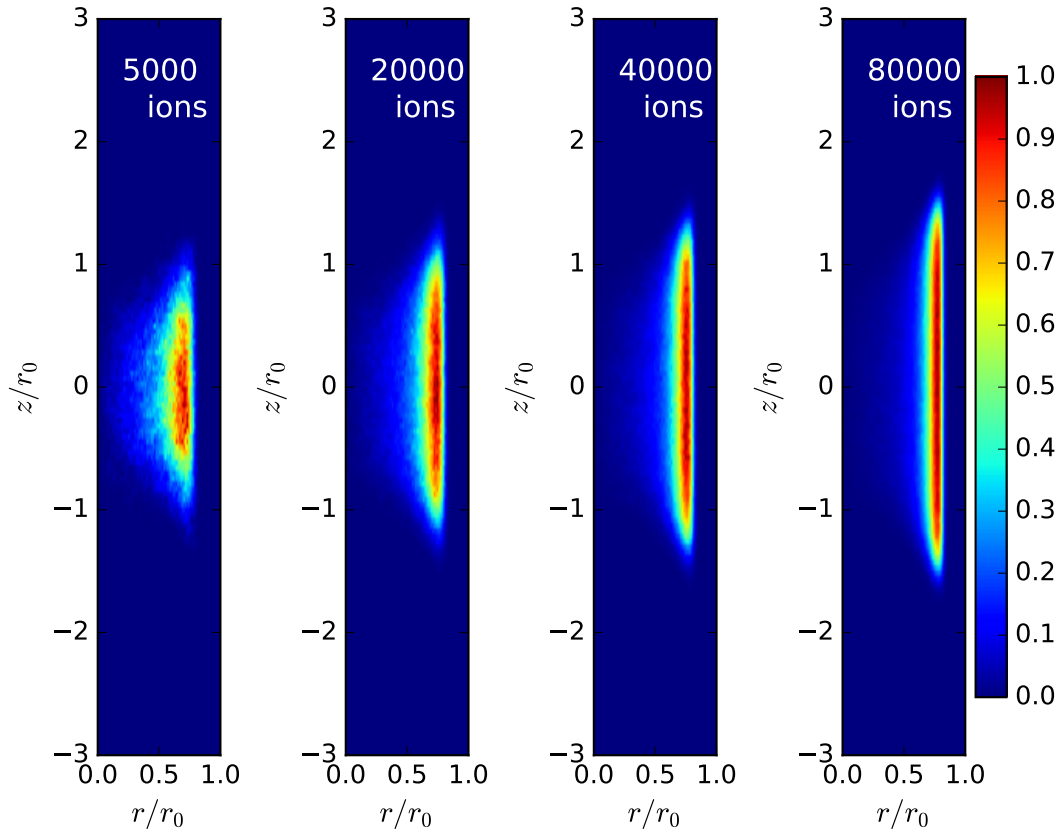


Figure 5.41: The plots show the number density $n(\mathbf{r})$ as a function of the radial and axial direction of 22-pol trap of an ensemble of 5000, 20000, 40000 and 80000 ions at a nominal trap temperature of 5 K and an axial trapping voltage of 0.5 V. For reason of comparability, all distributions are scaled to their maximum value.

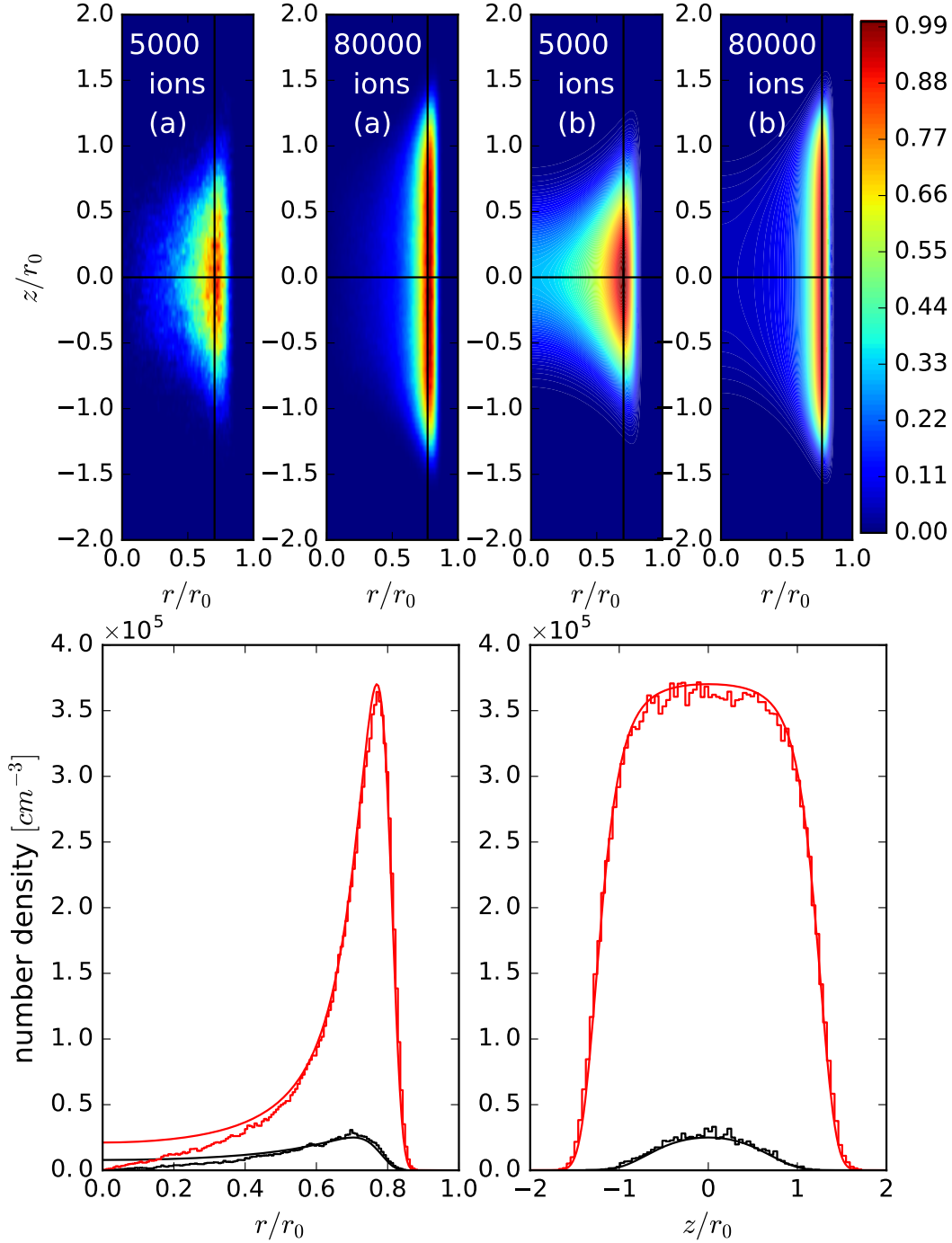


Figure 5.42: The plots show a comparison of the number density $n(\mathbf{r})$ as a function of the radial and axial direction of a 22 pol trap for an ensemble of 5000 and 80000 ions at a nominal trap temperature of 10 K and an axial trapping voltage of 1 V calculated with the full numerical approach (a) and the mean field approach (b). For reason of comparability, all distributions in the upper plots are scaled to their maximum value. The lower plots show the number density at a cut in radial and axial direction at the positions indicated by the black lines in the upper plots. The solid lines indicate the number density calculated with the mean field approach and the histogram with the the full numerical approach.

As described above, in the full numerical simulations, the velocities were recorded in terms of accumulation of velocity histograms. Figure 5.43 shows a histogram for 5000 and 80000 ions at a buffer gas temperature of 5 K and an axial trapping voltage of 0.5 V. Different temperatures could be calculated from the velocity distributions. As can be seen in Fig. 5.43(right panel) the velocity distributions for v_z within $r \leq 0.0015$ mm can be well described with a Maxwell-Boltzmann distributions at $T \approx 5.2$ K. The number of trapped ions has no significant influence on the temperature in the axial direction. The velocity distribution of the whole ion ensemble (left panel) deviates with increasing of the number of ions from a Maxwell-Boltzmann distribution, where the temperature increases with an increasing number of ions. Therefore the mean speed v_{avg} and root mean square speed v_{rms} (green vertical line and red vertical line Fig. 5.43) were calculated. From this quantities also a temperature could be calculated which differs from the temperature fitted with a Maxwell-Boltzmann distribution. This serves to prove once again, as shown in section 5.4.1, that the ion ensemble is not in a thermo-dynamic equilibrium.

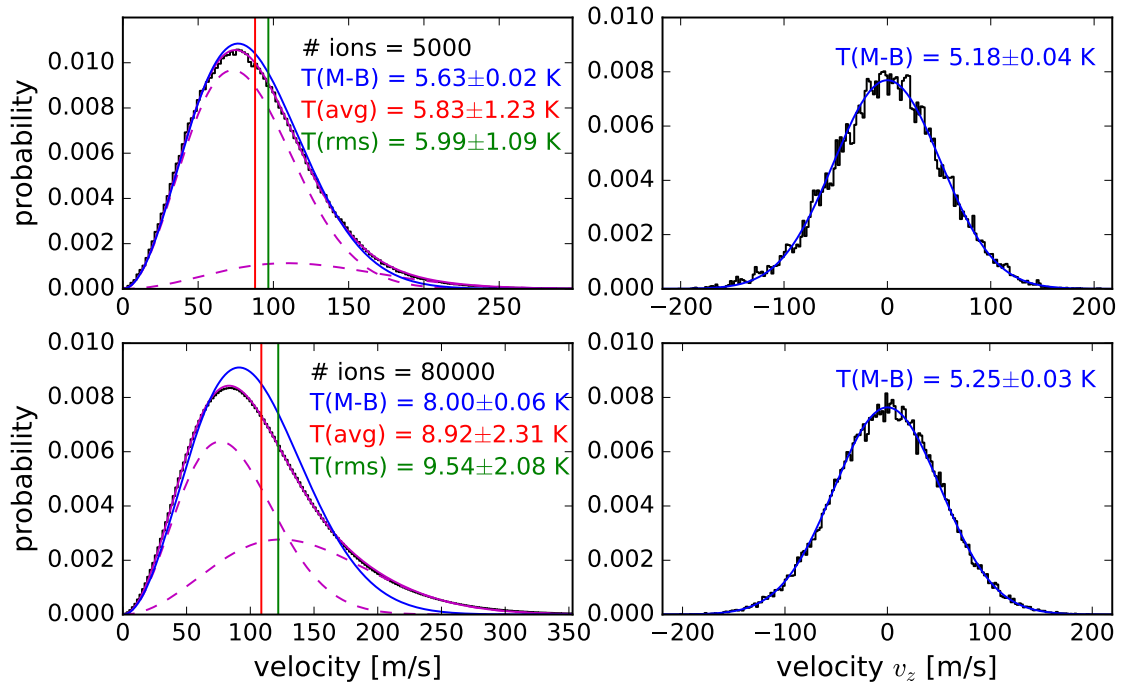


Figure 5.43: The plots show the calculated velocity distributions for an ion ensemble of 5000 and 80000 as indicated for a nominal trap temperature of 5 K and an axial trapping voltage of 0.5 V. The left panel shows the velocity distribution for $\mathbf{v} = \sqrt{v_x^2 + v_y^2 + v_z^2}$ and the right panel the corresponding velocity distribution for v_z within $r \leq 0.0015$ mm. The blue solid lines indicates the fitted temperatures assuming a Maxwell-Boltzmann distribution (M-B). The vertical red and green line indicate the mean ($T(\text{avg})$) and root mean square ($T(\text{rms})$) speed of the velocity distributions. The magenta solid and dashed lines in the left panel shows the fit of a weighted sum of two Maxwell-Boltzmann distributions and their individual contributions with $T_1 = 5.1$ K, $T_2 = 11.0$ K and weighting factors $w_1 = 0.83$ and $w_2 = 1 - w_1$ for 5000 ions.

The magenta solid and dashed lines in Fig. 5.43 (left plots) show that the velocity distribution can be well described with a weighted sum of two Maxwell-Boltzmann distributions. The individual contributions are $T_1 = 5.1$ K, $T_2 = 11.0$ K and weighting factors of $w_1 = 0.83$ and $w_2 = 1 - w_1$ for 5000 ions and $T_1 = 5.62$ K, $T_2 = 14.81$ K and $w_1 = 0.58$ for 80000 ions. From this, a weighted temperature

$$T_{weight} = w_1 \cdot T_1 + (1 - w_1) \cdot T_2 \quad (5.28)$$

of $T_{weight}(5000) = 6.06$ K and $T_{weight}(80000) = 9.41$ K can be calculated. A comparison to the quantities $T(v_{avg})$ and $T(v_{rms})$ shown that the temperature calculated from the root mean square speed v_{rms} is appropriate to describe the temperature of the ion ensemble. Figure 5.44 compares the effective temperature calculated with the mean field approach and the the weighted temperature calculated from the full 3-dimensional numerical simulations of the ion trajectories as a function of number of trapped ions and the axial trapping voltage. As can be seen in this figure, the first order calculation of the effective temperature T_{eff} (Eq. 5.26) with the mean field approach underestimates the temperature of the ion ensemble calculated by the full simulations. This is due to the fact (as mentioned in section 5.4.1) that the energy of the micro motion is only a part of the energy which is stored in the ion motion. The other part of the energy is stored in the coupling between the micro and macro motion (middle term Eq. 5.15). Therefore the first order effective temperature T_{eff} is only a lower limit of the temperature of the ion ensemble.

Conclusion

The number density of an ion ensemble moving in 22-pole trap were calculated within the mean field approach and compared to full 3-dimensional calculations of trajectories. The mean field approach is an appropriate tool to evaluate the influence of coulomb repulsion to the density distribution of an ion cloud inside a ion trap. The validity of this approach is guaranteed as long as the the effective potential approximation is applicable. It could be demonstrated that the ions are not equally spaced in between the trapping volume and that space charge effects can become relevant for ion cloud sizes of more than $\gtrsim 5000$ ions. For spectroscopy experiments in a 22-pole trap the axial trapping voltage and the number of stored ions determine the overlap of radiation with the ion cloud. It would be interesting to measure the increase or decrease of the overlap as a function of the axial trapping voltage or the number of stored ions to evaluate the validity of the used numerical approaches. The simulation additionally shows that the velocity component of the ion ensemble in axial direction, in between the laser overlap, has a translational temperature slightly higher as the temperature of the buffer gas. Therefore, the Doppler temperature measured in experiments in 22-pole traps^[54], which is always higher than the buffer gas temperature, can not be explained within this calculations. The overall velocity distributions of the ion ensemble can be well described by a weight sum of two Maxwell-Boltzmann distributions. Depending on the axial trapping voltage

and the size of the ion cloud the weighted temperature can increase up to 50% of the temperature of the buffer gas. The effective temperature T_{eff} can be used as a lower limit of the temperature of the ion cloud.

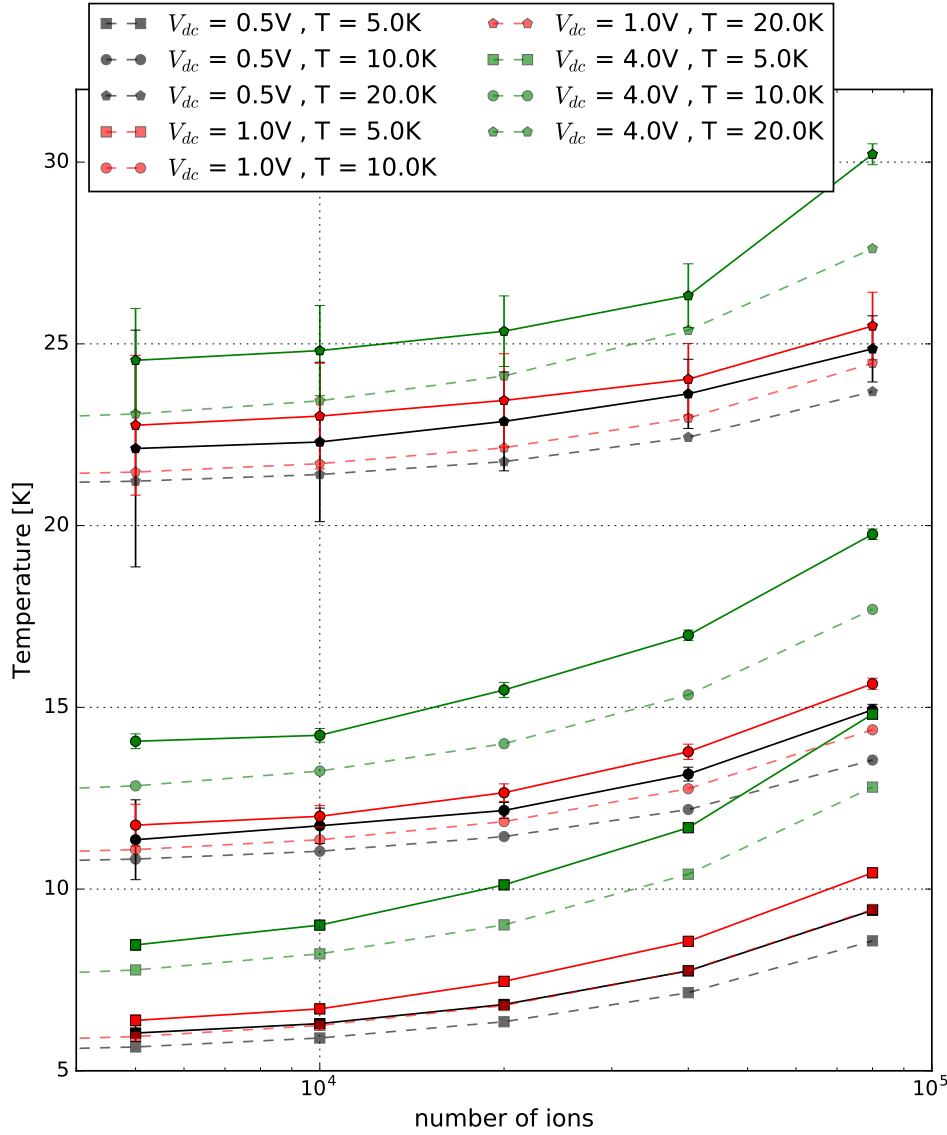


Figure 5.44: The plot is the same as Fig. 5.40 (dashed lines). The solid lines indicated the calculated weighted temperatures (Eq. 5.28) via a fit of the sum of two weighted Maxwell-Boltzmann distributions as function of the number of stored ions and the axial trapping voltage as indicated in the legend

Chapter 6

Experimental Work

The experimental part of this thesis is structured as follows. First, an overview about the experimental setup and techniques will be given in section 6.1.1.

Next, the accuracy and the reproducibility of measured ion molecule reaction rate coefficients using the LIRtrap setup will be discussed. Here, various tests will be presented to investigate the influence of different experimental parameters on the determined rate coefficients.

Afterwards, the reaction of $\text{N}^+ + \text{H}_2 \rightarrow \text{NH}^+ + \text{H}$ and its dependence on the fine-structure state of the nitrogen ions and the nuclear-spin state of the hydrogen molecules will be analyzed in detail. Besides this, the influence of helium buffer gas and ternary cluster effects of helium and nitrogen ions to this reaction will be examined. Additionally, the whole hydrogen abstraction reactions, starting with $\text{N}^+ + \text{H}_2$ will be investigated and rate coefficients will be given. Moreover, this work provides a characterization of a piezoelectric valve which is used to control the reaction gas flow into the 22 pole trap.

6.1 Experimental Setup and Techniques

Figure 6.1 shows a schematic setup of the LIRTrap (laser induced reactions LIR) trapping apparatus. The main parts are the storage ion-source, the first and second quadrupole mass filter (QMF), the 22-pole trap and the Daly-detector. A detailed description of all parts can be found in [69],[5] and [70]. The latest version of the LIRTrap setup is described in [71]. The data acquisition system was modified by using National Instruments Labview 2012 in connection with a National Instruments CompactRIO¹ controller.

This ion trap apparatus can be used to measure reactions between cations and neutral molecules as a function of the time, temperature and reaction gas density. Additionally, a laser can be coupled to the setup to measure laser induced reactions. Details of the LIR-technique can be found in [72].

¹NI cRIO-9022 controller attached to an 8-slot cRIO-9114 chassis

In the following, a general procedure to measure reaction rate coefficients in the 22-pole trap (LIRtrap) will be given and some of their limitations will be shown. To produce the desired ion species, neutral gas is constantly admitted to the storage ion-source. The ions are produced via electron impact ionization. The ionization energy can be varied by several eV. It should be noted that the neutral gas flow to the ion-source results in increase of the pressure of the whole apparatus. The reached equilibrium pressure is used as the background pressure (p_{back}) and has to be taken into account for the determination of the density of the neutral reaction gas. After a certain storage time, the ion source will be opened for a few ms via an electrostatic einzel lens to inject the ions into the first QMF to select the desired ions and guide them to the 22-pole trap. Because of the residual gas pressure of the whole apparatus, the ion source will produce different species of ions and therefore this selection process is necessary. Nevertheless it is possible that also undesired ions-species can reach the 22-pole trap, because the QMF can only select the ions by their charge to mass ratio. To trap the ions, the voltage applied at the entrance lens is lowered in this way that the ions can pass the entrance of the 22-pole trap while at the exit lens, a static voltage is applied that the incoming ions will be reflected at this barrier. After a few microseconds (this roughly corresponds to the traveling time of the ions through the trap) the voltage at the entrance lens will be increased so that the ions can not leave the trap. To ensure that no more ions can enter the trap during the storing time, an additional set of einzel lenses will deflect all following ions. To increase the trapping efficiency, a short ($\approx 0.1 - 10$ ms) and intense ($\approx 10^{16}$ molecules/ cm^3) Helium pulse is injected via a pulsed piezo valve to the trap before the ions arrive. The function of the buffer gas pulse is to decelerate and thermalize the incoming ions to the nominal trap temperature via collisions. During the measurement, the neutral reaction gas is usually constantly admitted to the trap. Due to collisions with the inner walls of the housing of the trap, it can be thermalize to the nominal trap temperature. The time for storing the ions in the presence of the reaction gas can varied from milliseconds to several seconds. After this time, the exit lens will open and all product ions can leave the trap. With the second QMF all product ions can be mass selected and separately detected/counted with the detector. Unfortunately only cations can be detected with the used Daly detector. A detailed description detecting cations via a Daly-detector can be found in [69]. This procedure will then be repeated at several storage times for each product ion to record a time evolution of an ion-neutral reaction. The pressure of the ion-source and the chamber is monitored during the whole measurement by two hot cathode ion gauges². The temperature of the trap itself is measured by a silicon diode³.

To perform the experiments at variable temperatures, the copper housing of the trap itself is mounted on a 10 Kelvin Leybold cold-head. This enables to measure in a temperature range from 300-10 Kelvin. To hold the temperature of the trap

²ARUN Microelectronics

³Lake Shore Cryotronics Silicon diode DT-470

constant for long periods of time, heating elements⁴ are mounted around the cold-head. The maximum achievable heating power is limited by the connection between the heating elements and the cold head and their maximum heating power. Here, the temperature should not exceed ≈ 330 K to prevent damage on the cold head. Unfortunately, the current LIRtrap setup allows a stable temperature controlling only between 10 K and 30 K.

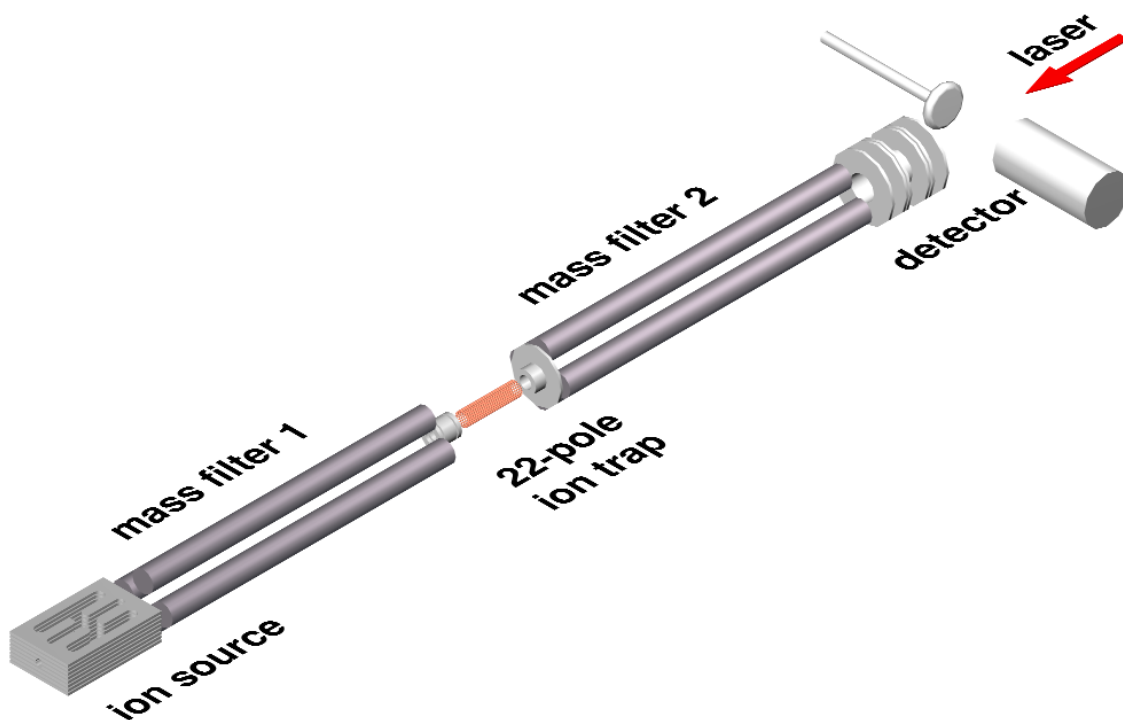


Figure 6.1: Schematic of the 22-pole trap setup^[72]. The storage ion source is used to produce ions by electron impact ionization with neutral gas and store them by a rapidly oscillating voltage applied to the electrodes of the source. The first QMF selects and guides the desired ions. The einzel-lenses are used for guiding and focusing the ion beam. The ions are trapped in the 22-pole trap, which is mounted on a 10 Kelvin cold-head (Leybold), together with a neutral reaction and buffer-gas to cool the ions and perform experiments. The second QMF selects the product ions from the reaction to count them at the Daly-detector.

6.1.1 Determination of the Reaction Gas Density

The number density of the reaction gas inside the trap can be calculated with the following relation^[73]

$$n(\text{cm}^{-3}) = 4.18 \cdot 10^{17} \cdot \frac{f_{\text{cal}} \cdot p_{\text{trap}}(\text{mbar})}{\sqrt{T_{\text{trap}}(\text{K})}}, \quad (6.1)$$

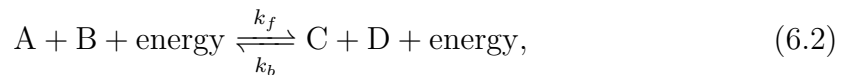
where f_{cal} is a gas specific calibration factor which depends on the used pressure gauge. (The calibration for the LIRTrap apparatus was done with a hot cathode

⁴MINCO Heating elements

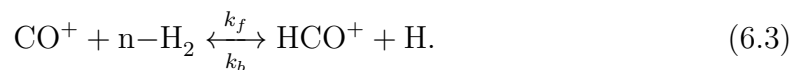
ion gauge from ARUN Microelectronics and a Spinning Rotor Gauge System from MKS). T_{trap} is the nominal temperature of the trap measured with a silicon diode (Lake Shore Cryotronics Silicon diode DT-470) and p_{trap} is the pressure difference between the background pressure (p_{back} see sec. 6.1.1) and the resulting pressure due to the continuous flow of neutral reaction gas into the trap, measured with the ion gauge outside the trap. Further information about the determination of the calibration factor f_{cal} can be found in Gaertner [73]. For LIRTrap the factors for hydrogen $f_{H_2,cal} = 84.69$ and helium $f_{He,cal} = 299.26$ were estimated.

6.2 Time Evolution of Chemical Reactions

In general, each chemical reaction can be described as follows:



where A and B are the reactants and C and D are the products. Also a certain amount of energy can be required to promote a reaction or can be released due to the reaction. k_f and k_b are the rates of the forward and the backward reaction. In order to determine these rates, the time evolution of a chemical reaction has to be measured. The time dependence of ion-molecule reactions can be measured in ion traps by varying the storage time of the ions in the trap in presence of the neutral reaction gas. The procedure for such a measurement is described in section 6.1.1. A measurement of the time evolution of the reaction of CO^+ ions with $n - \text{H}_2$ molecules were n stands for normal hydrogen with an ortho/para ratio of 3:1 is shown in Fig. 6.2. This ion-neutral reaction can be modeled as follows



If the number of the neutral reaction gas is much higher than the number of the ions, then such an ion-neutral reaction can be described as an pseudo first order reaction^[74]. Under the assumption of no other reaction channels, the change of the number of primary ions (CO^+) and product ions (HCO^+) as a function of the storage time can be modeled as,

$$\begin{aligned} \frac{d\text{CO}^+}{dt} &= -k_f[\text{H}_2]\text{CO}^+ \\ \frac{d\text{HCO}^+}{dt} &= k_f[\text{H}_2]\text{CO}^+ \end{aligned} \quad (6.4)$$

where $[\text{H}_2]$ is the number density of the neutral reactant. Because of the small amount of H atoms in the trap (each single reaction event forms one H atom and gets lost in the trap) and the continuously admitted H_2 , the backward reaction k_b

can be neglected. This system of first order coupled differential equations is solved by the following equations.

$$\begin{aligned} \text{CO}^+(t) &= \text{CO}_{t=0}^+ \cdot \exp(-\tilde{k}_f t) \\ \text{HCO}^+(t) &= \text{CO}_{t=0}^+ \cdot \left(1 - \exp(-\tilde{k}_f t)\right). \end{aligned} \quad (6.5)$$

This system of equations can now be fitted to the measured time evolution to determine the rate of the reaction \tilde{k}_f . The rate coefficient k_f is connected to the rate in the following

$$k_f = \frac{\tilde{k}_f}{[\text{H}_2]}. \quad (6.6)$$

In order to calculate an absolute rate coefficient (Eq. 6.6), the knowledge of the number density is essential.

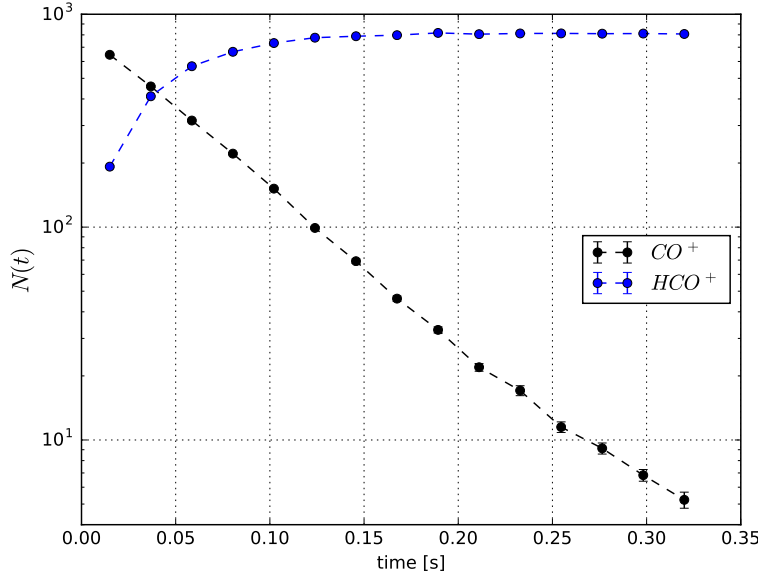


Figure 6.2: The plot shows the time evolution of the reaction of CO^+ ions (black dots) with $n - \text{H}_2$ molecules in a 22-pole trap at a temperature of 23 K (nominal trap temperature) and a constant H_2 pressure of $1.99 \cdot 10^{-7}$ [mBar].

6.3 Testing the LIRtrap Setup

Aim of this PhD thesis was to continue the work of S. Gärtner who was previously working on the LIRTrap apparatus on the $\text{N}^+ + \text{H}_2$ reaction system. In her thesis [75] she elaborated on some experimental parameters e.g. the cycle-time (time for each individual measurement), amplitude of the rf trapping voltage, pressure of the primary ionization gas in the ion-source or electrical potentials of the ion

trap apparatus, that have an influence on the reproducibility of the measured rate coefficient for the reaction



She comes to the conclusion that as far as the cycle time, the electric guiding and trapping potentials are not changing the reproducibility could be improved. Since the rate coefficient should be largely independent from these parameters, as long as the values of these parameters are chosen within a suitable range, the reaction 6.7 was measured again as a function of the temperature. Figure 6.3 shows an Arrhenius type plot of the repeated measured rate coefficients for reaction 6.7. This plot shows a comparison of the measured rate coefficients at the beginning of this thesis (black circles) and the measured rates after improving the measurement procedure and determination of the relevant parameters (blue squares).

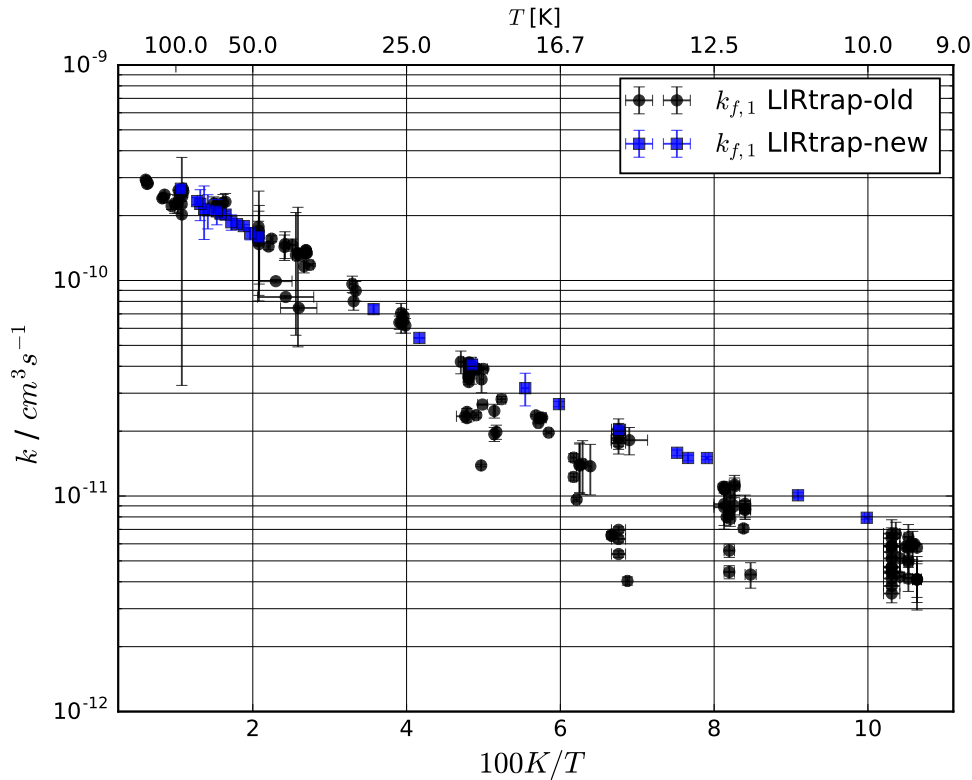


Figure 6.3: The plot shows the initial (black circles) and final (blue squares) measurements of the temperature dependence of rate coefficient $k_{f,1}$ for the reaction $\text{N}^+ + \text{n-H}_2$. These measurements were recorded within a period of ≈ 2 years.

It is clearly evident that the first measured rates have large fluctuations which increase below 25 Kelvin. The absolute value of the rates is almost the same for temperatures above 20 Kelvin. Below 20 Kelvin the rates measured at the beginning of this thesis deviate significantly up to a factor of 3 from the measurements

performed after improving the setup. To identify the reasons for the large fluctuations in the measured rate coefficients, the LIRtrap setup and the measurement procedure were tested w.r.t. all relevant experimental parameters.

In the following section, the results of these tests will be summarized.

6.3.1 Tests to Improve the LIRtrap Setup

In this section the results of all tests in order to improve the LIRtrap setup will be summarized. The details of the necessary measurements for these tests can be found in the appendix A.3. Furthermore, an experimental procedure will be described in order to get reliable and reproducible results for ion-molecule reaction rates coefficients in the LIRtrap apparatus.

The following list gives an overview about all performed tests:

1. The stability of guiding and trapping the ions
2. Saturation effects of the ion detection system
3. Temperature behavior of the calibration of the neutral reaction gas
4. The number density of the reaction gas at low temperatures
5. Measuring rate coefficients during the cool down phase of the apparatus
6. The equilibrium between the number density inside and the pressure outside of the trap

1. The Stability of Guiding and Trapping the Ions

The main reason for the observed periodic instabilities in the number of counted ions, as also reported by S. Gärtner, could be identified and largely improved. Due to the wrong applied heating voltage (a AC-voltage with a frequency of 50 Hz) for the tubes of the rf-frequency generator, the amplification of the rf-voltage was modulated by a 50 Hz signal, which caused this periodic instabilities.

The stability of trapping the ions was investigated w.r.t. the accumulated number of trapped ions for different storage times in the 22 pole trap. If the number of accumulated measurements is chosen too small, statistical deviations of the assumed normal distributed number of trapped ions can also lead to fluctuations in the determined rate coefficients. Further details of these measurements can be found in the appendix A.3.1.

2. Saturation Effects of the Ion Detection System

By measuring the number of ions detected by the photomultiplier ⁵ (PMT) and

⁵HAMAMATSU R647-01

comparing them to the number of converted PMT-signals from the discriminator ⁶, saturation effects of the detection system could be observed (Fig. 6.4). Due to the detection limit of the discriminator (300 MHz), very rapid sequentially arriving ions signals from the PMT can get lost at this stage and cannot be counted. These effects can systematically influence the determined rate coefficients to lower values up to 5%. To reduce saturation effects, the number of stored ions should be limited to $\lesssim 1000$ and the voltage of the exit lens should be lowered as a function of time (to eject the product ions out of the 22 pole trap) to spread the ion cloud.

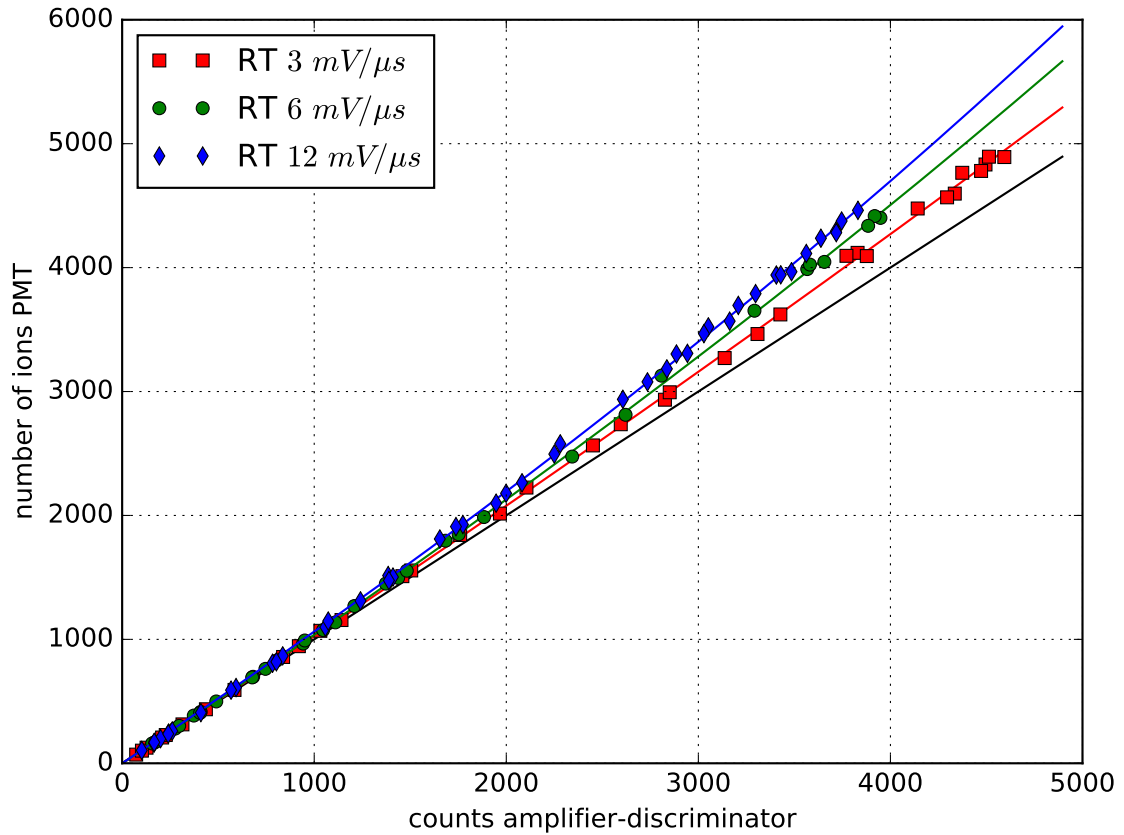


Figure 6.4: The plot shows the relation between detected N^+ ions (PMT-signals) and discriminator-signals as a function of the ramp-time (RT). With increasing the number of ions and the ramp-time saturation effects becomes visible. The black solid line indicates a perfect one to one relation. The colored solid line shows the fitted lines for different ramp-voltages.

For the latter, a lowering speed or a ramp-time (RT) of $6 \text{ mV}/\mu\text{s}$ was found to be sufficient. Further details of these measurements can be found in the appendix A.3.2.

3. Temperature Behavior of the Calibration of the Reaction gas

Since calibration of the neutral reaction gas density (see section 6.1.1) can only

⁶Philips Scientific 300 MHz Discriminator Model 6904

be performed at room temperature ⁷, the validity of this calibration w.r.t. lower temperatures was tested. Therefore an exothermic reaction where the rate coefficient is expected to be independent from the temperature was used. Here, the following reaction was chosen:



In terms of a constant determined rate coefficient of $k_1 = 1.50 \cdot 10^{-9} \text{ cm}^3 \text{ s}^{-1}$ as a function of the temperature, it could be shown that the temperature behavior of the calibration is correct. Figure 6.5 shows the Arrhenius-curve of the estimated rate coefficients for this reaction.

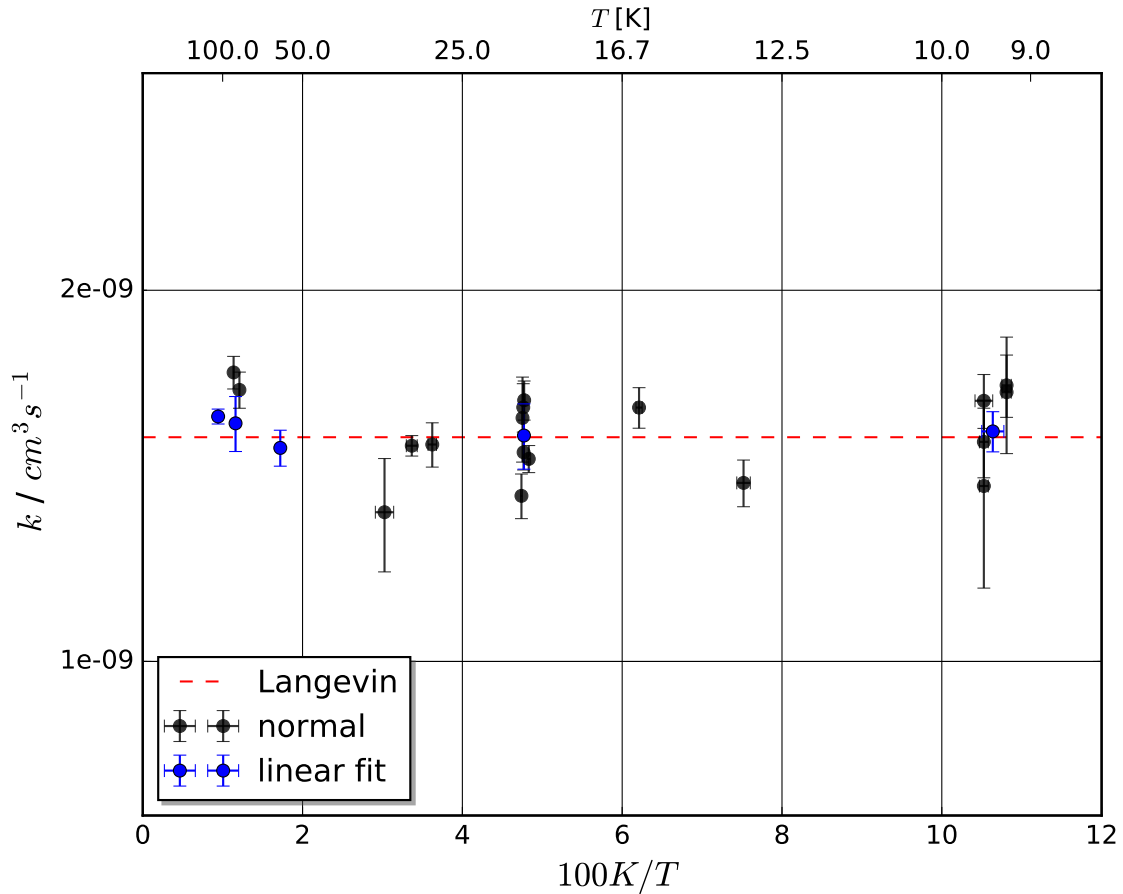


Figure 6.5: The plot shows the Arrhenius curve for the reaction of $\text{N}_2^+ + \text{H}_2$. The black dots indicate the rate-coefficients calculated directly with the number density of H_2 estimated via Eq. 6.1. The blue dots indicate the estimated rate-coefficients from measurements with different H_2 pressures in the trap at a certain temperature. The rate-coefficients are calculated from the slope of the linear dependence of the H_2 number density and the rate \tilde{k} Eq. 6.6. The red dashed line indicates the theoretic calculated Langevin-rate of $k_L = 1.52 \cdot 10^{-9} [\text{cm}^3/\text{s}^{-1}]$.

⁷The used Spinning Rotor Gauge System from MKS for the calibration is operating outside from the trap at room temperature.

To verify the correctness of the absolute value of the number density with this method the rate coefficient for this reaction has to be known precisely.

Furthermore, during these measurements also the CO^+ ion which has the same mass as the N_2^+ ion could be identified based on the reaction dynamics with H_2 . The occurrence of the CO^+ ion in the residual gas is probably caused by some deposits from old experiments with methane e.g. CH_5^+ or the one broken filament of the ion source. Because of the high temperature inside the source it is also entirely possible that the amount of carbon comes from the stainless steel parts of the ion-source. A contamination due to a leak in the vacuum system could largely be excluded using a leak detector. The fluctuation between the rates at equal temperatures (black dots Fig. 6.5) revealed a further problem, which arises from the calculated number density of the reaction gas in the 22-pole trap. This problem will be discussed in the next paragraphs.

Further details of these measurements and all determined rate coefficient also for the reactions of $\text{N}_2^+ + \text{H}_2 \xrightarrow{k_2} \text{H}_2^+ + \text{N}_2$ and $\text{H}_2^+ + \text{H}_2 \xrightarrow{k_3} \text{H}_3^+ + \text{H}$ can be found in the appendix A.3.2.

4. The Number Density of the Reaction Gas at Low Temperatures

At low temperatures the effect of cryosorption^[76] in particular the adsorption or the freezing out of the reaction gas on the inner walls of the copper trap housing has been taken into account. It could be shown that the effect of adsorption together with small fluctuations of the trap temperature ($\Delta T \leq 1\text{K}$), caused by instabilities of the heating system of the trap⁸, can significantly influence the measured rate coefficients (see Fig. A.12 appendix). This effect becomes more relevant for rather fast reactions. As can be seen, a change in temperature of $\Delta T \approx 1\text{K}$ can result in a temporarily change of pressure p_{trap} up to 70%.

Additional factors which have been taken into account in order to determine the number density of the reaction gas reliable and details of these measurements can be found in the appendix A.3.4. Figure 6.6 illustrates this effect in terms of the measured pressures at the ion-gauges and the simultaneous measured trap temperature.

⁸This instabilities are caused by problems in the thermal contact of the heating wires around the coldhead.

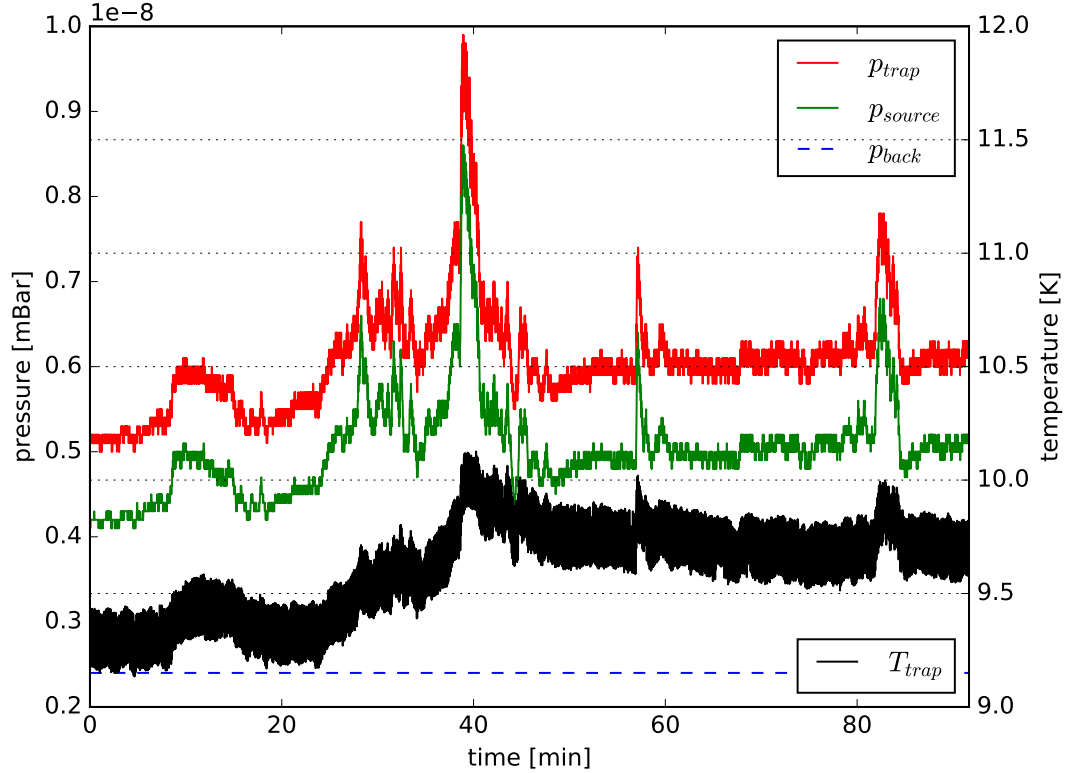


Figure 6.6: The plot shows a measurement of the temperature (black) and the pressure measured at the first QMF (p_{source} , green) and in the main chamber (p_{trap} , red) at 10 K. The blue dashed line marks the residual pressure of the apparatus. One can see that each variations in the temperature correlates to the measured pressure at both ion-gauges.

5. Measuring Rate Coefficients During the Cool Down Phase of the Apparatus

In order to determine rate coefficients efficiently as a function of the trap temperature, it is proposed to measure the reaction rates during the cool down phase of the apparatus. Due to the above mentioned effect of the adsorption of the reaction gas as well as the residual gas on the inner walls of the trap housing, this technique can lead to large errors. This fact can be seen nicely in Fig. 6.7.

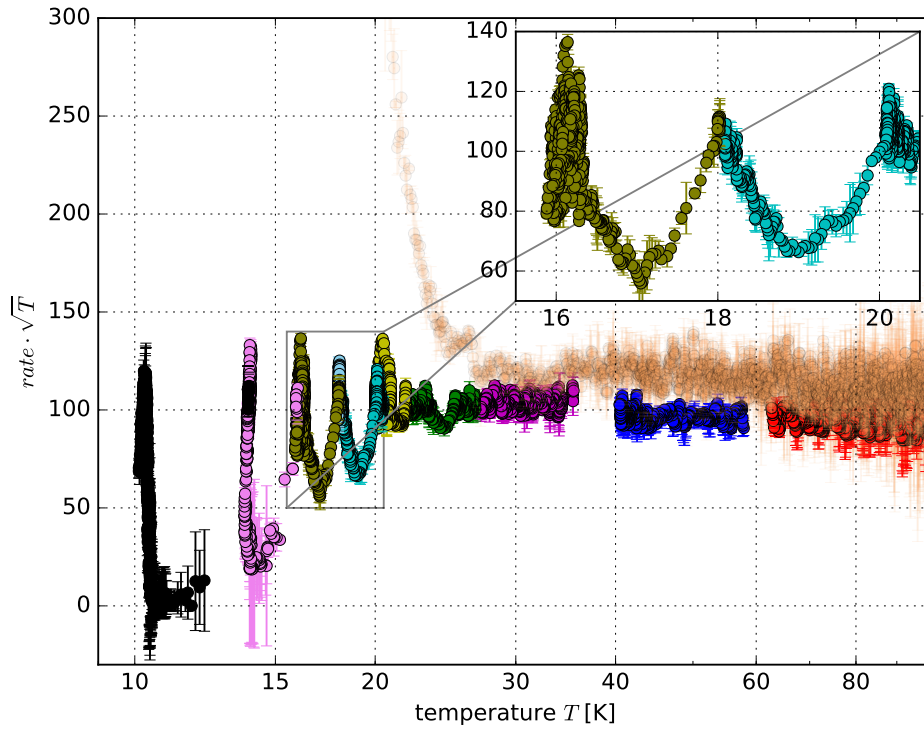


Figure 6.7: The plot shows the results of 10 measurements in term of the calculated rates for the reaction $\text{CO}^+ + \text{H}_2 \rightarrow \text{HCO}^+ + \text{H}$ in range from 10-100 Kelvin. These measurements were performed during the cooling down phase of the apparatus. A heating current to slow down the rate of cooling the trap was applied. The measurement indicated with the sandbrown dots in the range from 20 to 100 Kelvin is a measurement after stopping the cooling of the trap.

Further details of these measurements can be found in the appendix A.3.5.

6. The Equilibrium Between the Number Density Inside and the Pressure Outside of the Trap

By measuring the decay of the N^+ ions, using the reaction $\text{N}^+ + \text{n-H}_2 \rightarrow \text{NH}^+ + \text{H}$, and simultaneously measuring the reaction gas pressure of the ion-gauge in the main chamber (p_{trap}) it was tested, how long one has to wait until an equilibrium between the number density inside and the pressure outside of the trap is achieved. It could be shown in terms of the determined reaction rates that although the measured pressure at the ion-gauge is almost constant, the pressure inside the trap is increasing. As can be seen in Fig. 6.8 an equilibrium between inside and outside of the trap is reached after ≈ 2 hour with respect to the time since opening the valve for the neutral reactant. As a result of this, the determined rates are systematically smaller if the experiment is performed in a time interval of 0.5-1.5 hour after opening the neutral gas valve.

Further details of these measurements can be found in the appendix A.3.6.

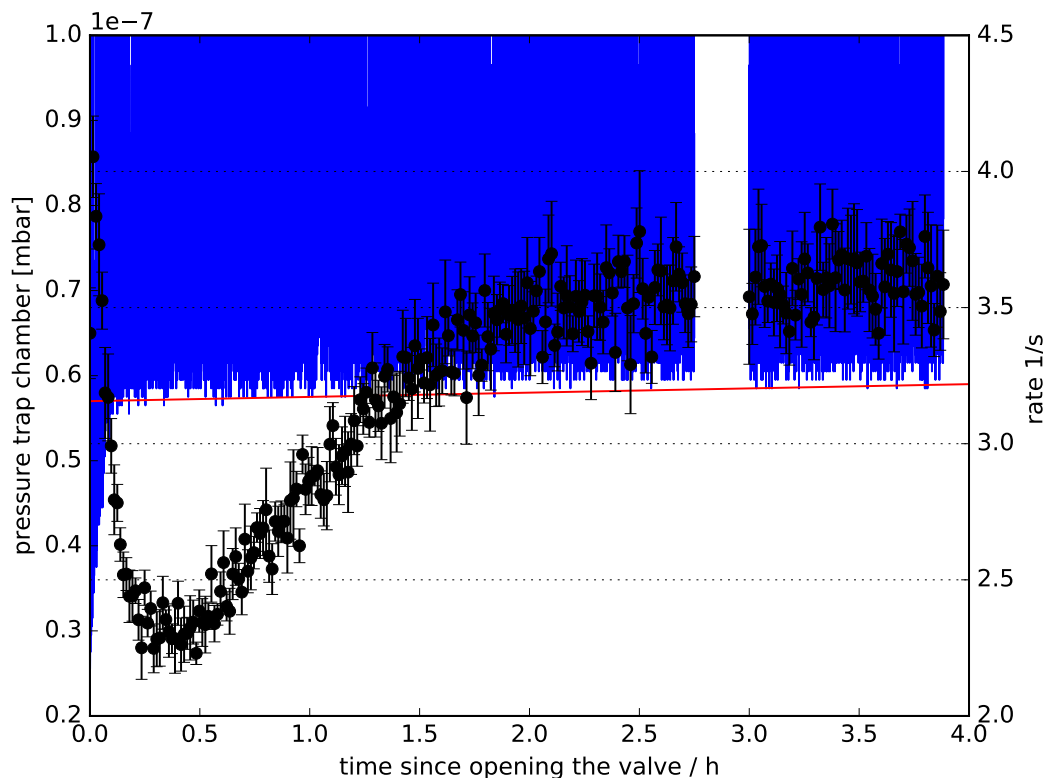


Figure 6.8: The plot shows a measurement of the depletion of the N^+ ions in terms of the calculated rates (black dots) as a function of the time since opening the valve for the neutral reactant H_2 at 10 K. The baseline (red) of the blue lines shows the correspondent H_2 pressure measured outside of the trap. The spikes, which are cut, at the blue curve result from the Helium piezo pulse at the begin of each single measured point to thermalize the incoming N^+ ions.

Conclusion

The measurements described in this section have shown, that various experimental parameters have an influence on the reproducibility and the accuracy of the determined rate coefficients. The following list summarizes these parameters.

1. The number of accumulated measurements can statistically influence the results.
2. The ion-counting process can influence systematically the results to lower rates if the number of trapped ions is significant larger than 1000.
3. The speed for lowering the voltage of the entrance lens of the trap in order to eject the ions should be chosen around $6 \text{ mV}/\mu\text{s}$, to avoid saturation effects of the detection system.
4. For temperatures below $\approx 25 \text{ K}$ and/or low reaction gas pressures, one has

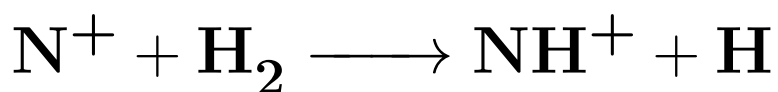
- to be very careful in order to avoid a temporarily rising of the reaction gas pressure as a consequence of adsorption effects.
5. Measuring rate coefficients during the cool down phase of the apparatus can result in errors of the rate coefficients, especially at low temperatures.
 6. An equilibrium between the number density inside and the pressure outside of the trap can not be assumed for a constant pressure measured outside by the ion-gauges. Measurements performed too early w.r.t. the time since opening the valve for the neutral reactant can result in systematically smaller rate coefficients.

Based on this list, the measurement procedure could be optimized in order to reduce the fluctuations and to guarantee the reproducibility of the measured rate coefficients. A detailed description for an optimized measurement procedure w.r.t. the listed experimental parameters can be found in the appendix A.3.7.

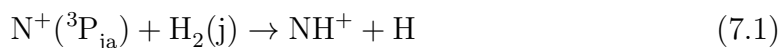
All problems discussed above show that the calculation of the neutral reaction gas density is the most difficult part in determining absolute ion-molecule reaction rate coefficients.

The finally calculated effective rate coefficients $k_{f,1}$ for the initialization of the ammonia synthesis (Eq. 6.7) are shown in the Arrhenius type plot Fig. 6.3 (blue squares). Despite the continuing uncertainties, the fluctuations in the measured rates could be reduced and the reproducibility could be improved. This demonstrates that the strategy described in section A.3.7 is appropriate for a reliable measuring of reaction rates as a function of temperature using the LIRTrap apparatus.

Chapter 7



As was mentioned in the introduction, until today, it is not clear, if the formation of NH^+ is endothermic or hindered by a barrier. A lot of experimental data suggests that the title reaction is slightly endothermic by a few tens of meV. A step towards to answering the question, how different forms of energies (thermal energy, electronic energy of $\text{N}^+(\text{}^3\text{P}_{\text{ja}})$ and rotational energy of H_2) can help to promote this reaction was done by Marquette et al.^[77]. They have shown, using the CRESU technique, that the rotational energy of the hydrogen molecule ($j = 0, 1$) is as efficient as the thermal energy in promoting the reaction $\text{N}^+(\text{}^3\text{P}_0) + \text{H}_2(j=0) \rightarrow \text{NH}^+ + \text{H}$ with an endothermicity of $\Delta H = 18 \pm 2$ meV. The influence of the fine structure population of the nitrogen ion on the reaction



was investigated in Cologne in 2008 with LIRtrap and 2017 with COLtrap^[78] using spectroscopic methods. The aim of these experiments was to depopulate the $\text{}^3\text{P}_0$ state of the nitrogen ion via THz-radiation at $\nu = 1.461$ THz^[79] to observe a change in the reaction rate with para-hydrogen (2008 LIRtrap) or to prevent the formation of weakly bound $(\text{N}-\text{He})^+$ cluster at 4 K (2017 COLtrap^[78]). Since the power of the used radiation source is in the range of μW and the Einstein A coefficient for this transition ($\text{}^3\text{P}_0 \rightarrow \text{}^3\text{P}_1$, $A \approx 3.5 \cdot 10^{-6} \text{ s}^{-1}$ ^[80,81]) is three order of magnitude smaller compared to other experiments with rotational transitions, no effect could be observed. Therefore, these results remained unpublished.

First information on state specific rate coefficients for the reaction 7.1 are given in the latest results of Zymak et al. [46]. Based on measurements of the title reaction as a function of temperature and the ortho/para fraction of the hydrogen in a 22-pole trap they were able to extract, assuming strict adiabatic behavior, state specific rate coefficients for the first time. They concluded that there are still uncertainties, how the energy of the fine-structure states of nitrogen is available for driving this reaction. In addition to the experiments, reaction 7.1 has been the object of some theoretical studies (Nyman and Wilhelmsson [82], Russell and Manolopoulos [83]). Nyman and Wilhelmsson applied a model based on strictly

adiabatic behavior excluding reactions of nitrogen ions in the $\text{N}^+(\text{}^3\text{P}_2)$ state as well as collision induced changes of fine structure state populations. Thus, only initial population of the two lowest fine structure states $\text{N}^+(\text{}^3\text{P}_0)$ and $\text{N}^+(\text{}^3\text{P}_1)$ is taken into account. A comprehensive summary of previous theoretical treatments and further experiments concerning the role of the fine-structure of nitrogen can be found in Zymak et al. [46].

In the following sections, a detailed analysis of the $\text{N}^+(\text{}^3\text{P}_{\text{ja}}) + \text{H}_2(\text{j}) \rightarrow \text{NH}^+ + \text{H}$ will be given.

7.1 The $\text{N}^+(\text{}^3\text{P}_{\text{ja}}) + \text{H}_2(\text{j})$ Reaction

In this section state specific rate coefficients for the title reaction will be derived using a non-adiabatic approach. In order to motivate the non-adiabatic approach, first the adiabatic approach, based on Nyman and Wilhelmsson^[82], will be used for evaluating the measurements. Here, limitations and conflicts of the adiabatic approach w.r.t the observed measurements will be discussed. Furthermore, two rather easy approaches for a quantitative analysis of the effective rate coefficients will be described. The first approach describes the temperature dependence of the rate coefficients using a simple Arrhenius function

$$k(T) = k_A \cdot \exp(-T_A/T) \quad (7.2)$$

where $T_A = E_A/k_b$ is the activation temperature, E_A is the activation energy and k_b is the Boltzmann constant. The second approach is to evaluate the temperature dependence by a weighted sum of two Arrhenius functions

$$k_{eff}(T, f) = f k_o \exp(T_{A,o}/T) + (1 - f) k_p \exp(T_{A,p}/T). \quad (7.3)$$

Here, k_o and k_p are the rate coefficients for a high temperature and $T_{A,o}$, $T_{A,p}$ are the activation temperatures for the reaction with ortho and the para, respectively. $f = \frac{[o-\text{H}_2]}{[\text{H}_2]}$ denotes the fraction of ortho-hydrogen in the sample. In addition to the temperature dependence, the second approach allows the evaluation of effective rate coefficients in dependence on the rotational state of the hydrogen molecule. The appendix A.4.1 contains detailed results of this calculations. Before going into details of the adiabatic and non-adiabatic approach, the results of the performed measurements will be compared to previous works. Figure 7.1 shows an Arrhenius plot of the experimental thermal rate coefficients for the title reaction with normal- H_2 and para- H_2 from the actual measurements and for previous experiments. The rate coefficients determined by Zymak^[46] for the reaction with $n - \text{H}_2$ ($f = 0.75$) deviates towards lower temperatures up to three times to the actual measurements. The values measured by Gerlich^[84] are in better agreement with our data. In comparison to Marquette 88, our rates are inbetween. The reason for the differences is unclear, but they illustrate the challenge of measuring absolute reaction rate coefficients.

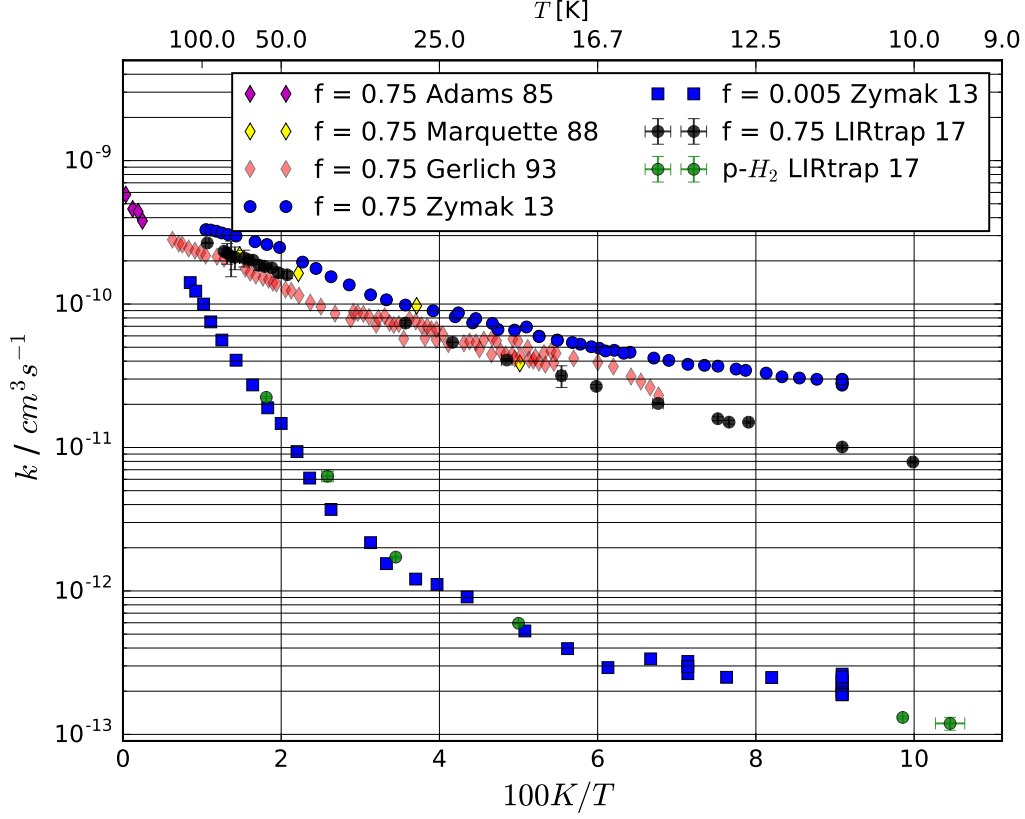


Figure 7.1: Arrhenius plot of the effective rate coefficients for the title reaction with $n - \text{H}_2$ and $p - \text{H}_2$ from the actual measurements and previous works (see legend).

7.1.1 The Adiabatic Model

Nyman and Wilhelmsson^[82] applied a theoretical model for the reaction 7.1 which was also used by Russell and Manolopoulos [83]) to study this reaction. This approach, based on strictly adiabatic behavior, excludes reactions of nitrogen ions in the $\text{N}^+(\text{}^3\text{P}_2)$ state as well as collision induced changes of fine structure state populations. Thus, only the initial population of the two lowest fine structure states $\text{N}^+(\text{}^3\text{P}_0)$ and $\text{N}^+(\text{}^3\text{P}_1)$ is taken into account. In order to apply this approach to evaluate our measurements, a model mentioned by Marquette et al. [77] will be used. This model includes the thermal population of the fine structure states of the $\text{N}^+(\text{}^3\text{P}_{ja})$ ($ja = 0, 1, 2$) with their state specific rate coefficients and the rotational states ($j = 0, 1$) of the hydrogen molecule. Following this ansatz an effective or thermal rate coefficient can be written as:

$$k_{eff}(T) = f \cdot \sum_{ja=0}^2 \xi_{ja}(T) k_{1,ja}(T) + (1 - f) \cdot \sum_{ja=0}^2 \xi_{ja}(T) k_{0,ja}(T). \quad (7.4)$$

The coefficients $\xi_{ja}(T)$ account for the thermal population of the fine structure states of $\text{N}^+(\text{}^3\text{P}_{ja})$ with $ja = 0, 1, 2$

$$\xi_{ja}(T) = \frac{g_{ja}}{Z(T)} \exp\left(-\frac{E_{ja}}{k_b T}\right) \quad (7.5)$$

where $Z(T)$ is the partition function, g_{ja} are the degeneracies and E_{ja} the energies of the three fine structure states (see Tab.7.1).

$\text{N}^+(\text{}^3\text{P}_{ja})$	g_{ja}	E_{ja} [meV]
$\text{N}^+(\text{}^3\text{P}_0)$	1	0
$\text{N}^+(\text{}^3\text{P}_1)$	3	6.1
$\text{N}^+(\text{}^3\text{P}_2)$	5	16.2

Table 7.1: Degeneracies g_{ja} and the energies E_{ja} for the three lowest fine structure states of the nitrogen ion [79].

$k_{j,ja}(T)$ are the state specific rate coefficients each defined as Arrhenius function

$$k_{j,ja}(T) = k_{j,ja}^A \exp\left(\frac{-T_{j,ja}^A}{T}\right). \quad (7.6)$$

The coefficients $k_{j,ja}^A$ describe the reaction rates for high temperatures and $T_{j,ja}^A$ is the activation temperature. Including the strict adiabatic behavior into this model¹, the effective rate coefficient is obtained by

$$k_{eff}(T) = f \cdot \sum_{ja=0}^1 \xi_{ja}(T) k_{1,ja}(T) + (1-f) \cdot \sum_{ja=0}^1 \xi_{ja}(T) k_{0,ja}(T). \quad (7.7)$$

Zymak et al. [46] initially used this approach in order to determine state specific rate coefficients for the title reaction. A consequence of strict adiabatic behavior would be that N^+ ions in the $\text{}^3\text{P}_2$ state are completely insensitive to collisions with H_2 [46]. These assumptions are in contrast with our experimental results where all N^+ ions sooner or later depleted. In order to compare our results to the results of Zymak [46] the same model is used. In accordance with Zymak, we also disregarded the fact of the forbidden fine state changing collisions. This means, the evaluation of the experimental data is based on the assumption that the fine structure is thermally populated according to the trap temperature due to collisions with the helium buffer gas within a few ms. Additionally, one must assume that the remaining nitrogen ions in the $\text{N}^+(\text{}^3\text{P}_2)$ state at high temperatures (see Fig. 7.12), can be neglected or relax

¹Only the initial population of the two lowest fine structure states $\text{N}^+(\text{}^3\text{P}_0)$ and $\text{N}^+(\text{}^3\text{P}_1)$ is taken into account

rather fast, due to collisions with He or H_2 , and that only the two lowest reactive fine structure states remain². The results are shown in Figure 7.2 together with results of a global fit of Equation 7.7, using the same set of state specific rate coefficients across the whole data set (Table 7.2), varying only f as appropriate. The obtained best fit value $f = 0.0114$ agrees with the ortho contamination of $f = 0.015 \pm 0.005$ determined via Eq. 7.3 (see A.3.7).

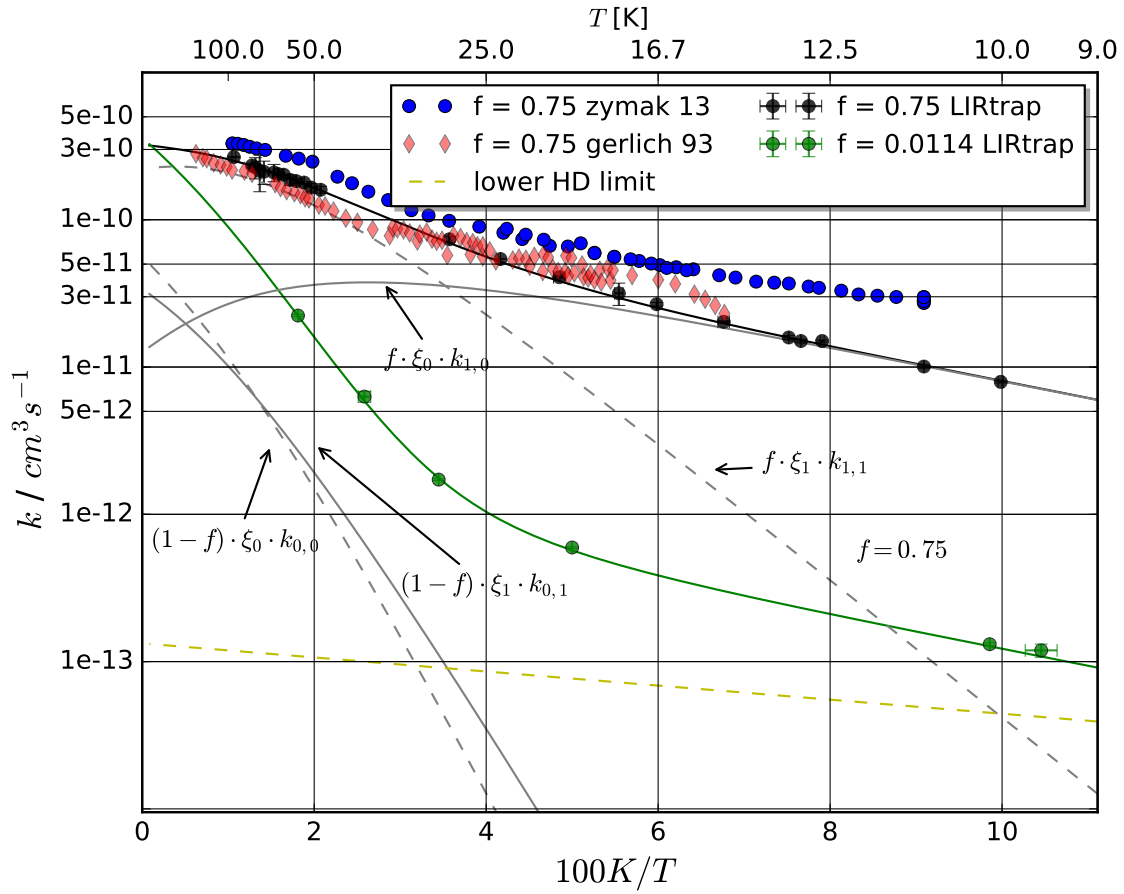


Figure 7.2: The plot shows determined effective rate coefficients from actual measurements of p- H_2 (green circles) and n- H_2 (black circles). For comparability the rate coefficients from Gerlich^[84] and Zymak^[46] for n- H_2 are plotted. The black and green solid lines show the global fit of the thermal rate coefficient via Eq. 7.7 for n- H_2 and p- H_2 . The individual thermal weighted contribution of the state specific rates $k_{j,ja}(T)$ for n- H_2 are plotted as gray solid and dashed lines indicated with arrows. The dashed yellow line indicates the lower detection limit, scaled to highest possible ratio of HD- H_2 of $3.8 \cdot 10^{-4}$, by reactions with the amount of HD in the H_2 gas^[75].

²Please note that the evaluation does not include any time and temperature depended relaxation rates for fine structure state changing collisions.

j, ja	$k_A [10^{-10} \cdot cm^3/s]$	$T_A [K]$	Reference
$k_{0,0}$	12.22	222.75	this work
$k_{1,0}$	1.51	26.47	
$k_{0,1}$	6.74	189.73	
$k_{1,1}$	8.83	36.88	
$k_{0,0}$	12	230	Zymak et al. [46]
$k_{1,0}$	1.9	18	
$k_{0,1}$	14	230	
$k_{1,1}$	12	40	
$k_{0,2}$	0.51	53.4	rates for kinetic reaction model
$k_{1,2}$	1.44	18.4	Zymak et al. [46]
kr_{2-1}	0.58	37.0	rates for relaxation
kr_{1-0}			

Table 7.2: The table shows the state specific rate coefficients for the title reaction used to fit the data in this work and the set which was used by Zymak et al. [46]. Also given are state specific rate and relaxation coefficients used by Zymak for the non-adiabatic model.

7.1.2 The Non-Adiabatic Model

As mentioned above, the evaluation of the measurements using the adiabatic approach^[82] (Eq. 7.7) is internally inconsistent w.r.t. the experimentally observed depletion of all N^+ ions. Consequently, the calculated state specific rate coefficients via Eq. 7.7 (Tab. 7.2) must be incorrect. Figure 7.3 shows the reproduction of the measured mono exponential decay of the N^+ ions as a function of the trapping time, assuming the correctness of the calculated state specific rate coefficients via Eq. 7.7 (Tab. 7.2). It can be seen that this set of rate coefficients can not reproduce a mono exponential decay for different temperatures. In the first 100 ms the decay looks almost the same. For longer trapping times the decay deviates strongly from the expected decay (yellow dots). Only the curve for 10 K follows the expected decay, because the population of the 3P_2 and 3P_1 state is at 10 K close to zero and the effective rate for the 3P_0 population is dominated by $f \cdot k_{1,0}$ ($f = 0.75$) which is the expected thermal rate. This behavior is due to the fact that no fine structure state changing collisions and reactivity of the 3P_2 state is included in this model. This means Eq. 7.7 is appropriate to describe the thermal rates as function of the temperature in terms of state specific rate coefficients, whereby these state specific rates coefficients are only a first order approximation of state specific rate coefficients for reaction 7.1.

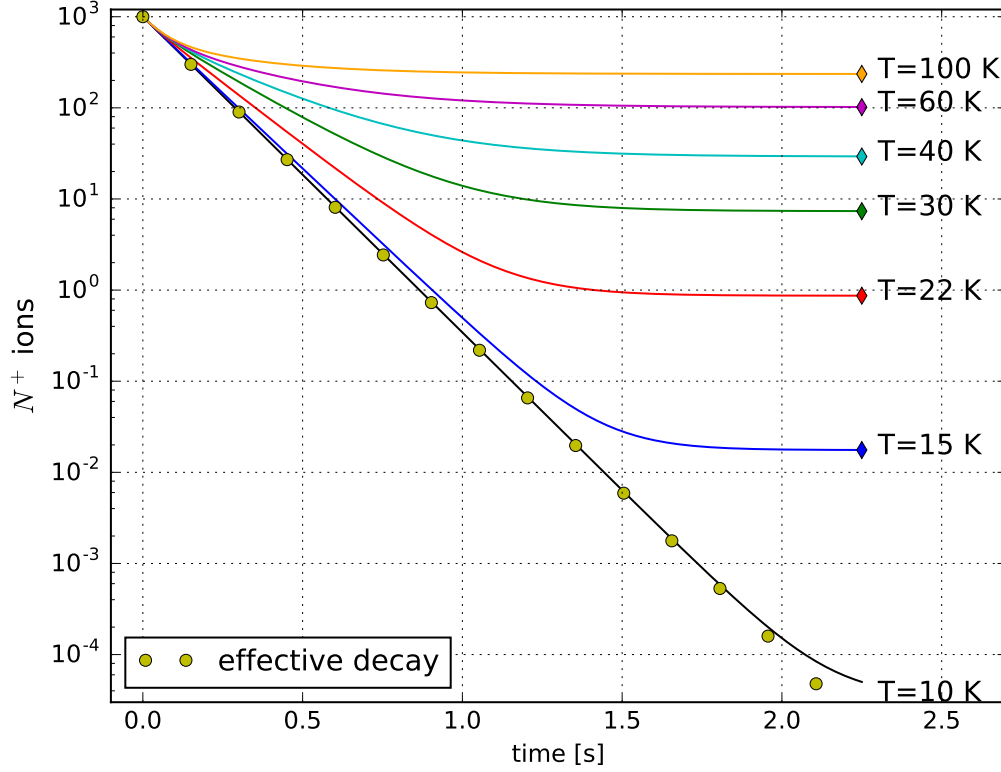
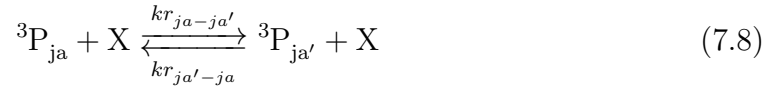


Figure 7.3: The plot shows the hypothetical decay of the N^+ ions as a function of the trapping time for different temperatures as indicated, following the adiabatic model of Nyman and Wilhelmsson [82], and using the state specific rate coefficients in Tab. 7.2. The hydrogen number density is chosen that the measured rate $k = 8 \text{ s}^{-1}$ from the experiment would be equal for all temperatures. The yellow dots indicate the expected mono exponential decay. The diamonds at the end of each curve indicate the non reacting nitrogen ions which are populated in the $^3\text{P}_2$ state.

In order to achieve a mono exponential decay as observed in the measurements the non-adiabatic model can be applied. Within the non-adiabatic approach, fine structure state changing collisions



where X denotes the collision partner, and/or reactivity of the $^3\text{P}_2$ state are taken into account. Figure 7.4 shows a scheme of a time depended non-adiabatic model, introduced by Zymak et al. [46] which assumes reactions and collisional relaxations of the $^3\text{P}_2$ state. The state specific reaction and relaxation rate coefficients are assumed to follow a simple Arrhenius temperature behavior (Eq. A.14). The backward relaxation rates are related to the principle of the detailed balance³

$$\frac{kr_{f \rightarrow i}(T)}{kr_{i \rightarrow f}(T)} = \frac{(2ja_i + 1)}{(2ja_f + 1)} \exp(\Delta E/k_b T) \quad (7.9)$$

³micro reversibility

where i and f denotes the initial and final state and ja the state of the Nitrogen ion and ΔE denotes the difference of the internal energy of the fine structure states (Tab. 7.1). This non-adiabatic model results in a system of three coupled differential equations, which are able to describe the decay of the N^+ ions as a function of time.

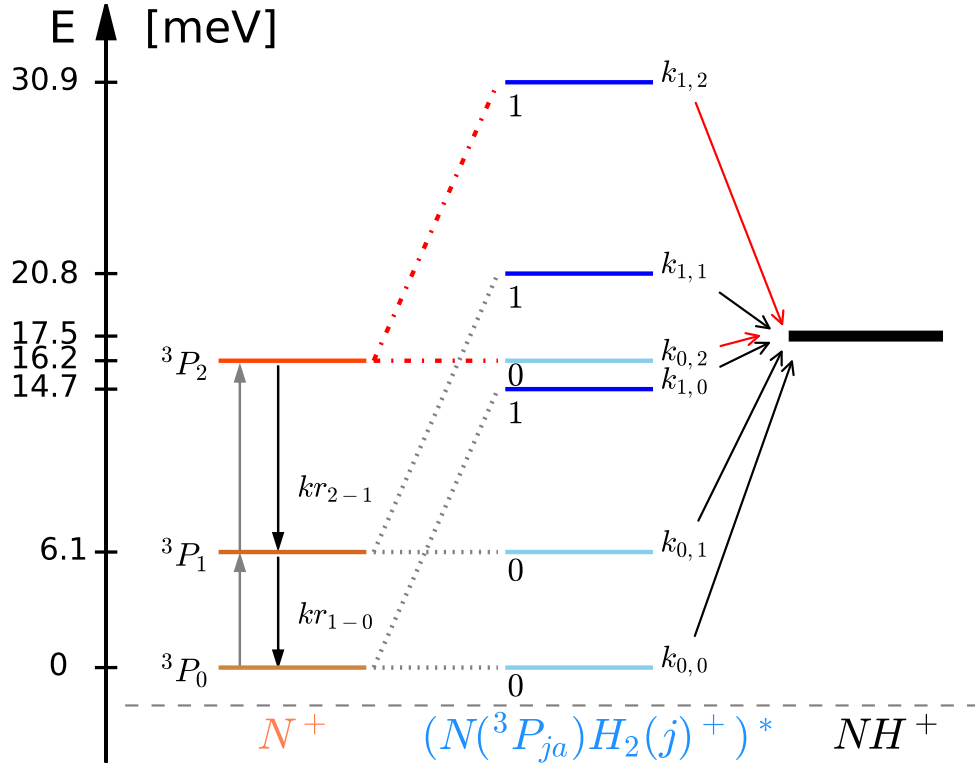


Figure 7.4: Energy scheme of the state specific the title reaction introduced by Zymak et al [46]. The gray dotted lines indicate, following the adiabatic model, the allowed paths to form a $(N(^3P_{ja=0,1,2})H(j=0,1)_2^+)^*$ complex and react to the NH^+ ion. The red dashed dotted lines indicate the forbidden path to form the $(N(^3P_2)H(j=0,1)_2^+)^*$ complex, which is considered to be non reactive. The black and red arrows (pointing to the NH^+ ion) show the state specific reaction rates, where red indicates a forbidden reaction (strict adiabatic model). Additionally relaxation rates for fine state changing collisions kr_{2-1} and kr_{1-0} are marked with black arrows. The gray arrows show the reverse relaxation rates. Remark: The adiabatic model of Nyman and Wilhelmsson [82] inhibits also fine state changing collisions from $^3P_2 \xrightarrow{kr_{2-ja}} ^3P_{ja}$ ($ja = 1, 0$).

Since collisional relaxation of the fine structure is allowed within the non-adiabatic model, an obvious assumption is that collisions of N^+ with helium or hydrogen can change the population of the fine structure states which could result in change in the observed rate coefficient. An influence of the helium and hydrogen number density to the rate coefficients could be a first hint at the role of the energy of the fine structure states of the N^+ ions in promoting this reaction. Motivated by these hypothesis, experiments to evaluate a possible change of the rate coefficients as a function of helium buffer gas and hydrogen number density were performed. These measurements and its results will be presented in the next paragraph.

Influence of the Buffer Gas Density on the Rate Coefficients

For testing the influence of the helium and hydrogen density on the effective reaction rate coefficient, experiments at 29 K and 10 K nominal trap temperature with p- H_2 with additional helium during the whole reaction were performed. Due to experimental limitations (temperature can be held constant for long periods of time only below 30 K, see section 6.1.1) these two temperatures were selected. The measurements were performed as follows:

1. Cool down of the apparatus to the desired temperature.
2. Confirming the stability of trapping the ions in presence of a helium buffer gas pulse and an additional constant amount of helium over several seconds.
3. Admitting the neutral reaction gas p- H_2 into the trap.
4. Performing a 4-point measurement, using only an initial buffer gas pulse in order to trap the ions efficiently and thermalize them.
5. Performing a 4-point measurement with different amounts of additional helium in the trap at the same p- H_2 density as before (still using the initial buffer gas pulse).
6. Performing a final 4-point measurement, using only an initial buffer gas pulse in order ensure that the p- H_2 density had remained constant.
7. Increasing or decreasing successively the p- H_2 density and perform steps 5-7 again.

The number of accumulated measurements⁴ at a specific hydrogen and helium number density was 30 and 40 for 10 K and 29 K, respectively. Figure 7.5 shows four typical measurements at 10.15 K and 29 K using only an initial helium buffer gas pulse (black) and additionally to the buffer gas pulse a constant amount of helium during the reaction (red). As can be seen in Fig. 7.5, the rate of the decay of the N^+ ions increases in presence of helium during the reaction. Since a reasonably amount of helium ($\approx 10^{14} \text{ cm}^{-3}$) was used, possible contamination with n- H_2 and $(\text{NHe})_n^+$ ($n = 1, 2, 3, \dots$) clusters has been taken into account, resulting in larger effective reaction rates. The possible n- H_2 contamination of the helium has been evaluated using the exothermic reaction of N_2^+ with H_2 (section A.2). The observed decrease of N_2^+ ions and the increase of N_2H^+ ions was monitored in presence of helium and the contamination was derived based on the expected rate coefficient for reaction A.2 (Tab. A.2). As helium clustering with the nitrogen ion at low temperature would further complicate the analysis, these measurements were performed at

⁴Number of measured depletion curves of the N^+ ions at a certain hydrogen and helium number density.

16 K (Fig. A.19). A contamination of $\frac{[H_2]}{[He]} = (1.2 \pm 5.5) \cdot 10^{-7}$ was derived, which is in line with the maximum expectable contamination of 0.5 ppm for helium 6.0⁵.

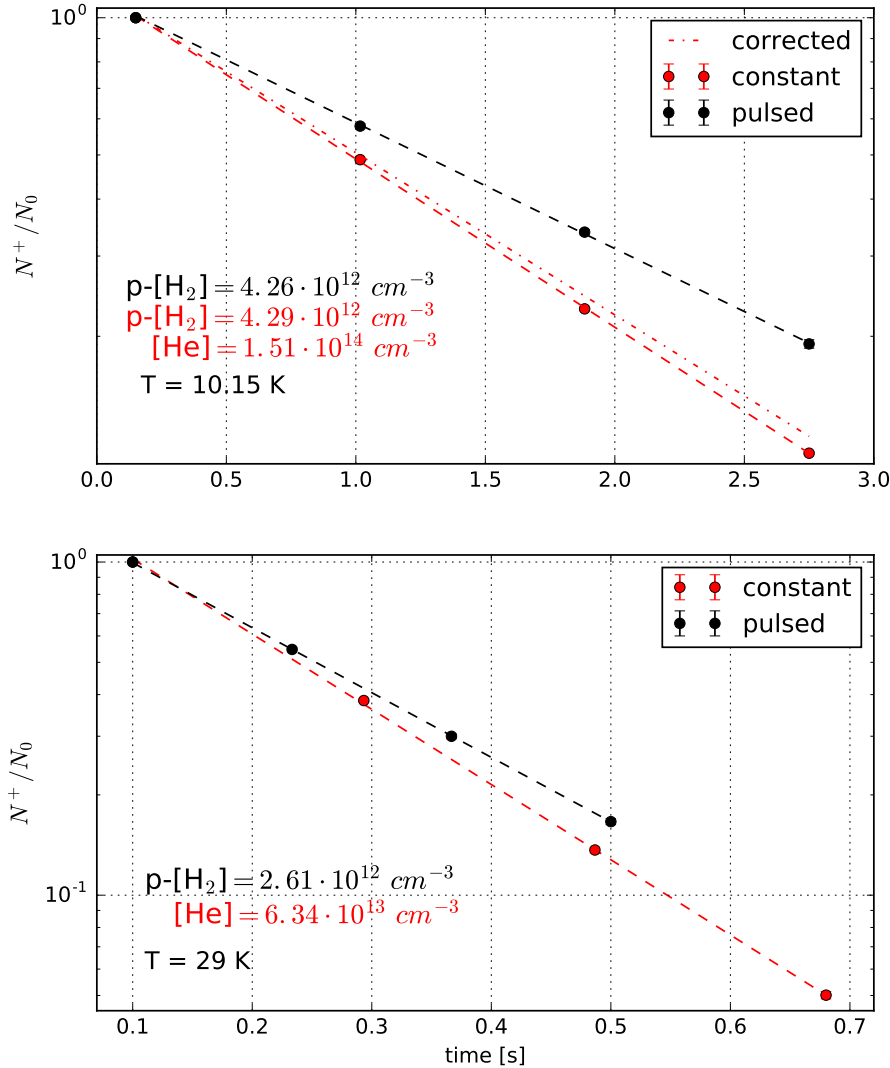


Figure 7.5: The plot shows four measurements at 10.15 K and 29 K using only an initial helium buffer gas pulse (black) and additionally to the buffer gas pulse a constant amount of helium during the reaction (red). The dashed lines indicate a mono-exponential fit of the data. The red dashed-dotted line in the upper plot indicates a correction, assuming a helium cluster formation with a ternary rate coefficient of $k_1 = 1.5 \cdot 10^{-30} \text{ cm}^6/\text{s}$ and a contamination of hydrogen in the helium of $\frac{[H_2]}{[He]} = 7 \cdot 10^{-7}$.

The influence of $(N-He)_n^+$ ($n = 1, 2, 3, \dots$) cluster effects is described in section 9.1. It has been shown that these effects have to be taken into account for temperatures below 15 K. The influence of a contamination of hydrogen in the helium and a cluster formation is shown in Fig. 7.5 (upper plot) as the red dashed-dotted line. Assuming

⁵https://produkte.linde-gase.de/laserbetriebsgase/helium_6.0.html

a worst case with $\frac{[\text{H}_2]}{[\text{He}]} = 7 \cdot 10^{-7}$ and a ternary rate coefficient of $k_1 = 1.5 \cdot 10^{-30} \text{ cm}^6/\text{s}$ (Tab 9.1) for the $(\text{N}-\text{He})_n^+$ cluster formation, the effective rate decreases by $\approx 3\%$, where the contamination of hydrogen in the helium is negligible.

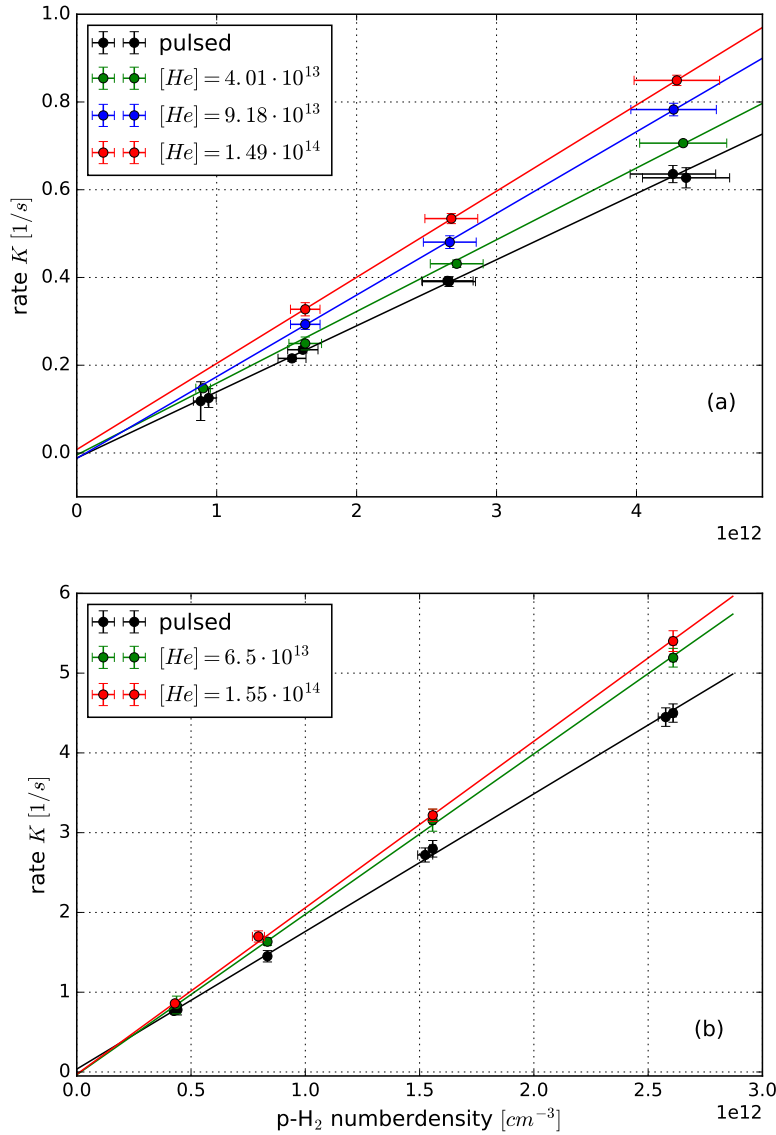


Figure 7.6: The plot shows the rate calculated from the decay of the N^+ ion as a function of the para hydrogen number density for 10.15 K (a) and 29 K (b) for different amounts of helium during the reaction. The label 'pulsed' denotes the measurements using only an initial helium buffer gas pulse. The large error bars in the upper plot are the consequence of operating the cold head. Due to this operation the temperature varies periodically (slightly), which causes fluctuations in the hydrogen pressure by cryosorption effects.

Figure 7.6 shows the rate calculated from the decay of the N^+ ions as a function of the para hydrogen number density for 10.15 K and 29 K for different amounts of helium.

From the linear fit via Eq. A.12 the effective rate coefficient was calculated. A trend to larger rate coefficients with increasing the helium density is clearly visible. Figure 7.7 shows the effective rate coefficient as a function of the Helium number density. As can be seen in Fig. 7.7 and Fig. 7.6 the rate coefficient increases linear with the helium number density. The red and black dots in Fig. 7.6 indicate measurements with p- H_2 mixtures from two different days. The rate coefficients for the measurements indicated by the black dots are by a factor of 1.15 larger than by the measurements indicated by the red dots. The reason for this is probably a different p- H_2 mixture, caused by different evaporation temperatures at the production of the para-hydrogen.

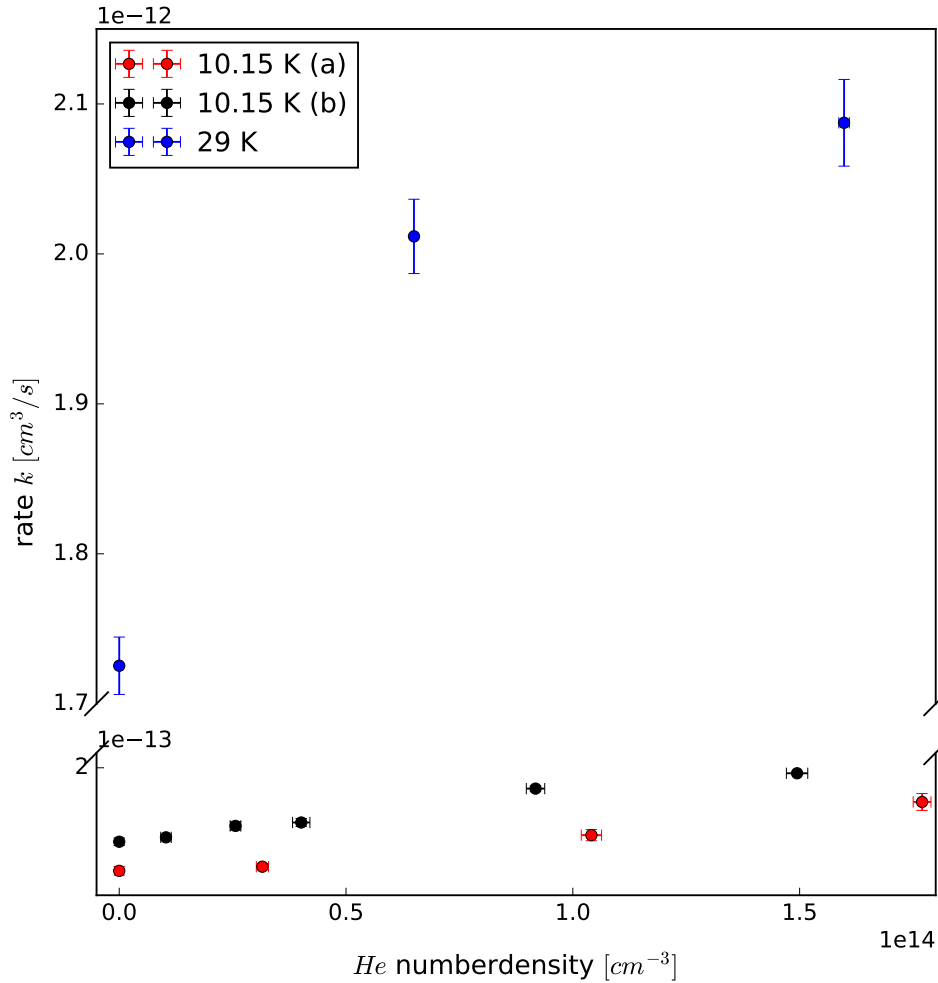


Figure 7.7: The plot shows the effective rate coefficient as a function of the helium number density. The red and black dots indicate measurements with p- H_2 mixtures from two different days.

Analysis of the Data using the Non-Adiabatic Model

In this section, a quantitative analysis of the experimental results, based on the non-adiabatic model (Fig. 7.4) will be presented.

As mentioned, the non-adiabatic model (Fig. 7.4) is represented by a set of three coupled differential equations. This system will be used in the following to evaluate the time dependent decay of the N^+ -ions as a function of the hydrogen and helium number density. Since an analytic solution can not be calculated for this system, numerical routines will be used.

All experiments showed a nearly exponential decay in the number of N^+ ions, which can be described by an effective thermal rate via Eq. 7.7 and Tab. 7.2. This observed fact was used to produce synthetic experimental data for arbitrary temperatures and hydrogen number densities (using $f = 0.75$ or $f = 0.0114$). Using this synthetic data, a global fit over a temperature range from 10 K to 100 K with different hydrogen and helium number densities were performed in order to calculate the rates which can reproduce the experimental measured mono exponential decay. In this fit, 16 parameters (12 for the reaction and 4 for the relaxation) were taken into account. The initial distribution across the fine structure states ($\text{N}^+(t = 0)$ -ions), resulting from the ionization processes in the ion source, are assumed to be 5/9, 3/9 and 1/9 in the $^3\text{P}_2$, $^3\text{P}_1$ and $^3\text{P}_0$ state, respectively. The initial helium buffer gas pulse at the beginning of the thermalization process was modeled following A. Sorgefrei [70] (see Fig. A.18). As no rates for relaxation of the fine structure states of $\text{N}^+(^3\text{P}_{\text{ja}})$ with hydrogen and helium are available, these rates were constrained using the Langevin rate coefficients as upper limits ($k_{L,(\text{N}^+, \text{H}_2)} = 1.57 \cdot 10^{-9} \text{ cm}^3/\text{s}$ and $k_{L,(\text{N}^+, \text{He})} = 6.05 \cdot 10^{-10} \text{ cm}^3/\text{s}$), considering five different situations:

1. No relaxation with hydrogen and helium
2. Only reactions of the $^3\text{P}_1$ and $^3\text{P}_0$ state but no restriction for the relaxation
3. Slow ($kr \leq 8 \cdot 10^{-12} \text{ cm}^3/\text{s}$) relaxation rate coefficients for hydrogen and helium
4. Relaxation ratio helium to hydrogen $kr_{\text{Helium}}/kr_{\text{Hydrogen}} = 10^{-4}$
5. Relaxation ratio helium to hydrogen $kr_{\text{Helium}}/kr_{\text{Hydrogen}} = 0.3$

A genetic algorithm from the Magix fitting engine of T. Möller [85] was used initially to identify suitable local minima within the large parameter space. Following this, the Levenberg–Marquardt algorithm was used to find an appropriate set of parameters.

1. In the simulation, assuming no relaxation of the fine structure, no set of parameters could be found that can fit the mono exponential decay over the whole temperature range satisfactorily.
2. Allowing only reactions of the two lower fine structure states $^3\text{P}_1$ and $^3\text{P}_0$ with no restrictions for the relaxation \Rightarrow No appropriate set of parameters could be found.

3. For the case of the restriction of the relaxation rates ($kr \leq 8 \cdot 10^{-12} \text{ cm}^3/\text{s}$), no suitable set of parameters could be found (see Fig. 7.8).

For the simulated situations using different relaxation efficiencies ($kr_{\text{Helium}}/kr_{\text{Hydrogen}} = 10^{-4}$ or 0.3), sets of parameters could be found in order to reproduce the mono exponential decay quite well.

4. The assumption of an efficiency of $kr_{\text{Helium}}/kr_{\text{Hydrogen}} = 10^{-4}$ for the relaxation process, predicts an increase of the rates up to 22% (see Fig. 7.8 upper plot) for the case of an additional amount of constant helium ($[He] = 1.6 \cdot 10^{14} \text{ cm}^{-3}$) during the reaction for $f = 0.75$ and $T > 50 \text{ K}$. The rates for $f = 0.0114$ remain unchanged under the influence of constant helium. Since such an increase of the rates was never observed experimentally for normal hydrogen above 50 K, we can exclude the assumption that the efficiency using hydrogen is much larger as for helium.

5. The assumption of an relaxation efficiency of $kr_{\text{Helium}}/kr_{\text{Hydrogen}} = 0.3$ leads to the best agreement with the observed mono exponential decay over the whole temperature range. The change in the effective rates, using an additional amount of constant helium is negligible (see Fig. 7.8).

The global fit confirms that both, relaxation processes and the reaction of the 3P_2 state, must be taken into account to accurately reproduce the observed mono exponential decay of N^+ ions. Furthermore, the efficiency of relaxation with hydrogen and helium must be in the same order magnitude. Figure 7.8 (lower plot) demonstrate that an increase of the reaction rates by increasing the number density of the buffer gas at 29 K and 10.15 K with para hydrogen ($f = 0.0114$) can not be expected. In order to achieve the experimentally observed increase of the rate coefficients due to relaxation processes with helium and hydrogen (Fig. 7.5 and 7.7), it has been shown that the relaxation rates must be lowered by at least three orders of magnitude w.r.t to the relaxation rates calculated by the global fit (Tab. 7.3). This is caused by the facts:

- that for a fast relaxation process, the majority of the nitrogen ions are thermally populated in the fine structure states after a few ms according to the trap temperature (Fig. 7.12). Towards lower temperatures, more and more N^+ ions will be populated in the 3P_0 state where the effective rate coefficient will be dominated by the $k_{j,0}$ reaction rate (Eq. 7.6). Therefore no change in the rate due to additional helium can be expected.
- Since the reverse relaxation kr_{0-1} or kr_{1-2} defined by Eq. 7.9 decreases tremendously with decreasing temperature (for $T = 30 \text{ K}$ $\frac{kr_{0-1}}{kr_{1-0}} = 0.28$ and $\frac{kr_{1-2}}{kr_{2-1}} = 0.034$), an increase of the effective rate coefficient via back population of the 3P_1 state (assuming $k_{j,1} > k_{j,0}$) at low temperatures is very unlikely.

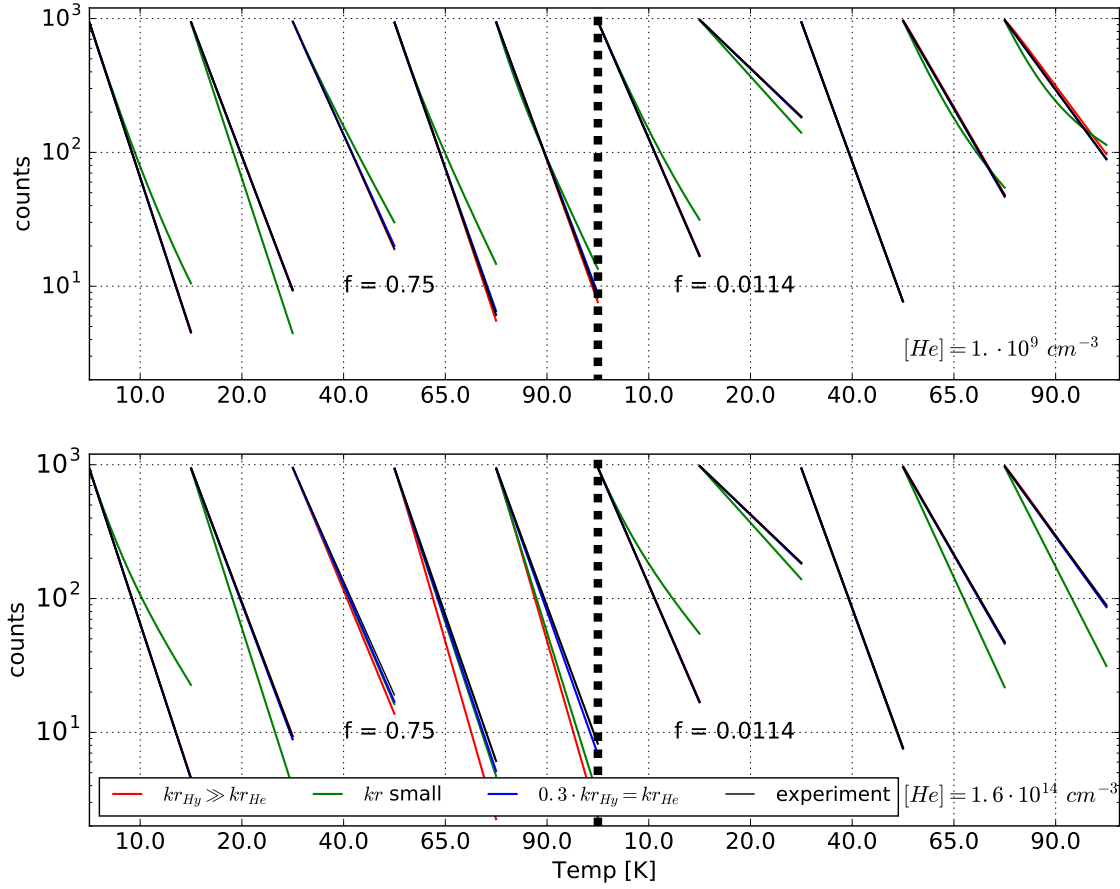


Figure 7.8: The plot compares the experimentally observed mono-exponential decay of the N^+ ions (black solid lines) (reproduced from the fitted parameters Tab. 7.2 using the adiabatic model) to the calculated decay using the non-adiabatic model (green, blue and red solid lines), for different assumptions w.r.t. the efficiency of the relaxation process as indicated. For the calculations shown in the upper plot only an initial helium buffer gas pulse was taken into account and a negligible small helium background as indicated in the plot. For the lower plot a constant helium density of ($[\text{He}] = 1.5 \cdot 10^{14} \text{ cm}^{-3}$) during the reaction has been considered. The vertical black dashed line separates the simulation in $f = 0.75$ and $f = 0.0114$. Please note: The time information (x-axis) was replaced by the temperature in this plot. The hydrogen number densities were chosen randomly.

Figure 7.9 demonstrates (via simulation of the non-adiabatic model) the increase of the reaction rate at 29 K under the influence of three different amounts of helium and using para-hydrogen ($f = 0.0114$). The efficiency of the relaxation process was assumed to be $kr_{\text{He}}/kr_{\text{H}_2} = 0.05^6$. For low helium number densities together with an initial helium buffer gas pulse the reaction rate is equal to the measured rate, where the rate is mainly defined by $k_{j,2}$ (upper plot). An increase of the helium leads to a faster relaxation process of the fine structure, where the population of the $^3\text{P}_0$ state (Fig. 7.12) becomes dominant and the effective reaction rate is defined by $k_{j,0}$.

⁶In order to reproduce experimentally the observed increase of the reaction rates for different helium number densities.

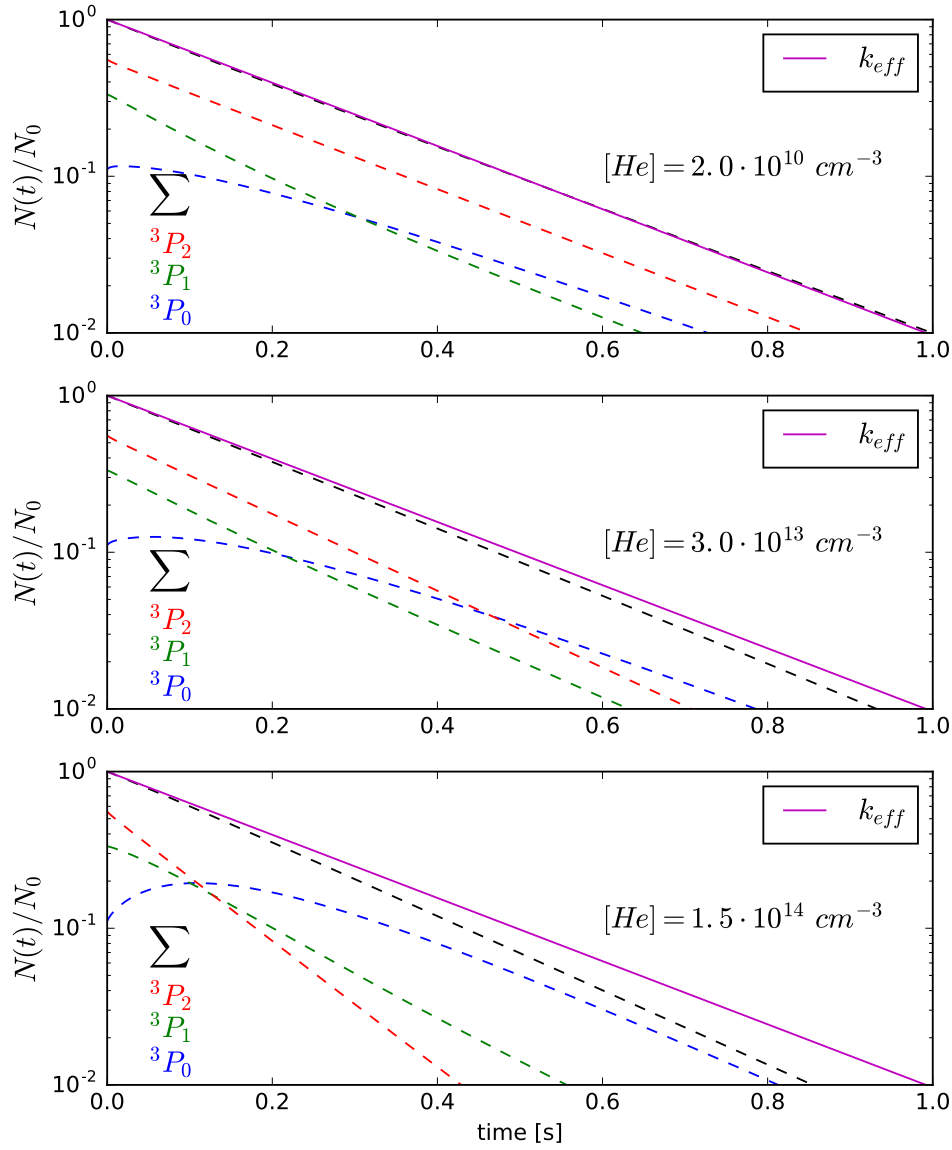


Figure 7.9: The plot shows the simulated decay using the non-adiabatic model of the N^+ ions for three different number densities of constant helium during the reaction at 29 K for the reaction with p-hydrogen ($f = 0.0114$, $[H_2] = 2.6 \cdot 10^{12} \text{ cm}^{-3}$). The rates for the relaxations are $kr_{2-1}(T = 29K) = 6.46 \cdot 10^{-13} \text{ cm}^3/\text{s}$ and $kr_{1-0}(T = 29K) = 7.19 \cdot 10^{-13} \text{ cm}^3/\text{s}$. The magenta solid line indicates the measured effective decay using only an initial helium buffer gas pulse. The dashed lines indicate the three different decays of the fine structure population and the sum of all. The sum corresponds to the experimentally observed increase of the decay of the N^+ ions in the presence of helium. The efficiency of the relaxation process was chosen as $kr_{He}/kr_{H_2} = 0.05$.

This simulation shows also that for slow relaxation rates, the fine structure is not thermalized to the ambient trap temperature after 800 ms. As mentioned, restriction of the global fit to such small relaxation rates, result in a non reproducibility of the observed thermal rates. Therefore, assuming that the non-adiabatic model is appropriate to describe reaction 7.1, the case of slow relaxation of the fine structure

states can be excluded.

The intensive analysis of the non-adiabatic model leads to the conclusion that relaxation processes under the influence of helium buffer gas and hydrogen are not able to increase the effective rate coefficients.

7.1.3 Results

The applied method and the large number of free parameters mean that more than one set of parameter choices will yield fits of comparable quality. Two examples are provided in Table 7.3 and are compared to the results of fitting Eq. 7.7. As expected, the state specific reaction rates differ from the rates fitted via Eq. 7.7 (Tab.7.2). The exception here are the rates for the $^3\text{P}_{ja}$ state with $ja = 0, 1$ and o-hydrogen which are in a good agreement. Within uncertainties, most values agree between the two parameter sets, the only exception being the activation temperatures for the rates $k_{0,2}$ and $k_{1,2}$, which both are associated with a reaction from level $^3\text{P}_2$. As these also show large uncertainties, they must have only minor contributions to the reaction. Relaxation rates on the other hand are large compared to reaction rates ($kr_{\text{He}} \lesssim 0.4 \cdot k_{L,(\text{N}^+, \text{He})}$ and $kr_{\text{H}_2} \lesssim 0.5 \cdot k_{L,(\text{N}^+, \text{H}_2)}$), implying that ions initially populating the upper state contribute to the reaction by relaxation to the lower fine structure states and subsequent reaction, rather than by direct reaction from the $^3\text{P}_2$ state.

j, ja	first set k_A	T_A	second set k_A	T_A	adiabatic model k_A	T_A
$k_{0,0}$	$10.60^{+0.46}_{-0.46}$	$234.82^{+2.88}_{-1.92}$	$10.36^{+0.01}_{-0.01}$	$232.40^{+0.49}_{-0.26}$	12.22	222.75
$k_{0,1}$	$6.68^{+0.22}_{-0.18}$	$169.92^{+1.35}_{-1.35}$	$6.57^{+0.01}_{-0.00}$	$170.87^{+0.26}_{-0.09}$	6.74	189.73
$k_{0,2}$	$0.06^{+0.05}_{-0.04}$	$208.31^{+46.69}_{-25.14}$	$0.11^{+0.06}_{-0.03}$	$73.29^{+3.94}_{-5.91}$		
$k_{1,0}$	$1.50^{+0.02}_{-0.02}$	$26.39^{+0.10}_{-0.14}$	$1.49^{+0.00}_{-0.00}$	$26.37^{+0.01}_{-0.01}$	1.51	26.47
$k_{1,1}$	$9.09^{+0.04}_{-0.04}$	$36.17^{+0.33}_{-0.40}$	$9.04^{+0.02}_{-0.01}$	$36.07^{+0.11}_{-0.13}$	8.83	36.88
$k_{1,2}$	$0.98^{+0.11}_{-0.09}$	$162.35^{+12.15}_{-6.54}$	$0.44^{+0.12}_{-0.15}$	$78.47^{+12.95}_{-10.59}$		
kr_{2-1}	$8.49^{+0.03}_{-0.14}$	$1.05^{+0.37}_{-0.07}$	$8.47^{+0.02}_{-0.17}$	$0.86^{+1.28}_{-0.00}$		
kr_{1-0}	$8.37^{+0.05}_{-0.11}$	$1.29^{+0.63}_{-0.02}$	$8.38^{+0.02}_{-0.11}$	$0.80^{+0.82}_{-0.03}$		

Table 7.3: Two sets of fitted state specific rate coefficients for non-adiabatic model Fig. 7.4 for reaction 7.1 k_A are given in units of $10^{-10} \cdot \text{cm}^3/\text{s}$ and T_A in Kelvin. The last two rows show the state specific rate coefficients using the adiabatic model (Tab. 7.2). The rates for the relaxation are given for hydrogen. The rates for the relaxation with helium are smaller by a fraction of $\frac{3}{10}$. Remark: The errors were calculated with the Error estimation using Markov chain Monte Carlo (MCMC)^[85] algorithm which is able to calculate asymmetric errors.

Figure 7.10 shows the timescales for fine structure relaxation at several typical experimental conditions. At the lowest temperatures and f values (lower right plot),

the relaxation process is finished within the first few ms, implying that the thermalization of the kinetic temperature of the ions must be at least in the same order. This is supported by simulations of ion trajectories.

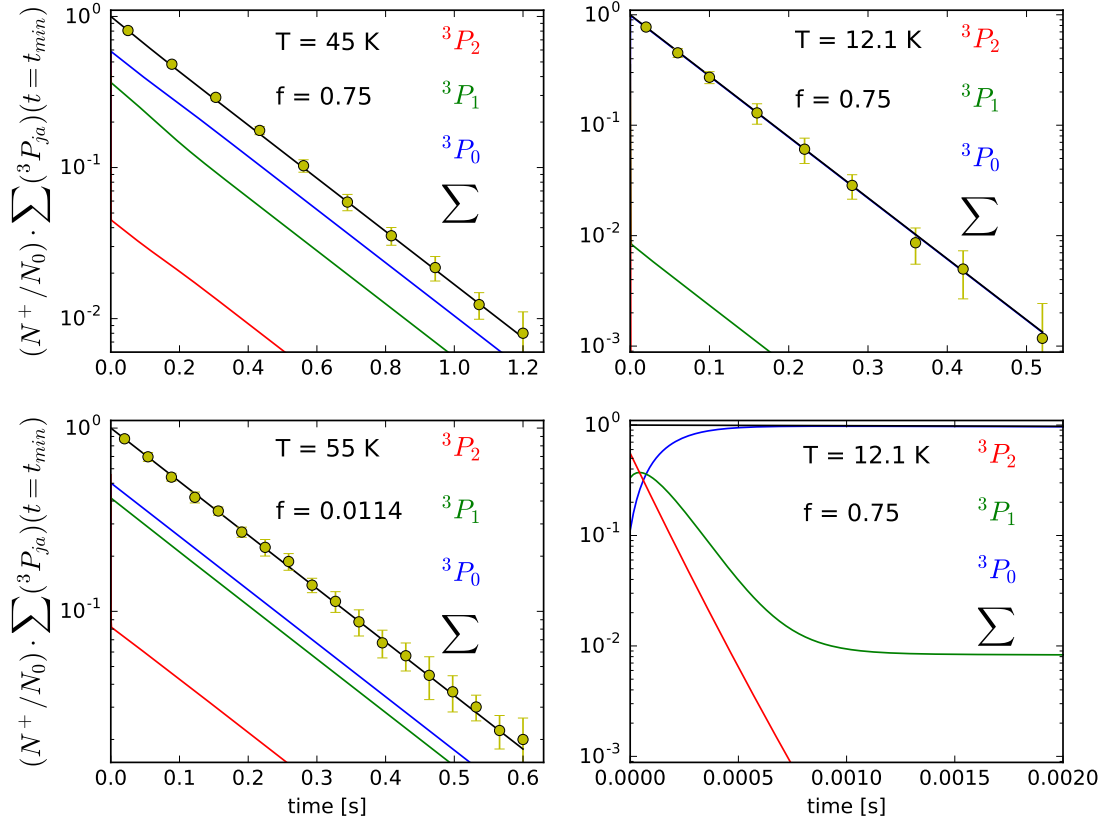


Figure 7.10: The plots show relaxation and reaction of N^+ ions at typical experimental conditions. The yellow dots show the experimentally measured decay of N^+ ions at the indicated temperatures and ortho fraction f . The lower right plot is a zoom into the first ms of the upper right plot to demonstrate the timescale of relaxation process of the fine structure states. The three thin colored lines indicates the change of the different $^3P_{ja}(ja=0,1,2)$ states using the kinetic reaction-relaxation model with the first set of fitted parameter Tab. 7.3.

Ions of mass 14 with an initial Maxwell-Boltzmann distribution of 10000 K⁷ thermalize to 10 K within 25 collisions in an ideal 22-pole trap, filled with helium buffer gas, in agreement with Asvany and Schlemmer [59]. An estimation, using a helium buffer gas pulse modeled following A. Sorgefrei [70], shows that the time for translational thermalization to a nominal trap temperature of 10 K is about 0.6 ms⁸. This demonstrate that the rather large relaxation rates are possible.

As mentioned, the weak influence of the reaction rates for the 3P_2 state at low temperatures is a consequence of the fast relaxation process. For temperatures below

⁷comparable with the energy of the incoming ions with an initial fine state population of 5/9, 3/9 and 1/9

⁸ $num_{collision} = \int_0^{t_{therm}} [He](t) \cdot k_{L,(N^+,He)} dt > 35$

100 K the population of the $^3\text{P}_2$ state decreases rapidly (Fig. 7.12). At 40 K only a fraction of the N^+ ions is populated in the $^3\text{P}_2$ state, where the reaction rates are dominated by the rates $k_{1,0}$ and $k_{1,1}$ (Fig. 7.11). Both these facts explain, why the influence of the reaction rates for the $^3\text{P}_2$ states is rather weak and can therefore not accurately be determined. In order to verify the calculated set of parameters, especially the rates for the $^3\text{P}_2$ state, more measurements at different temperatures with well known ortho-para mixtures of the Hydrogen are necessary.

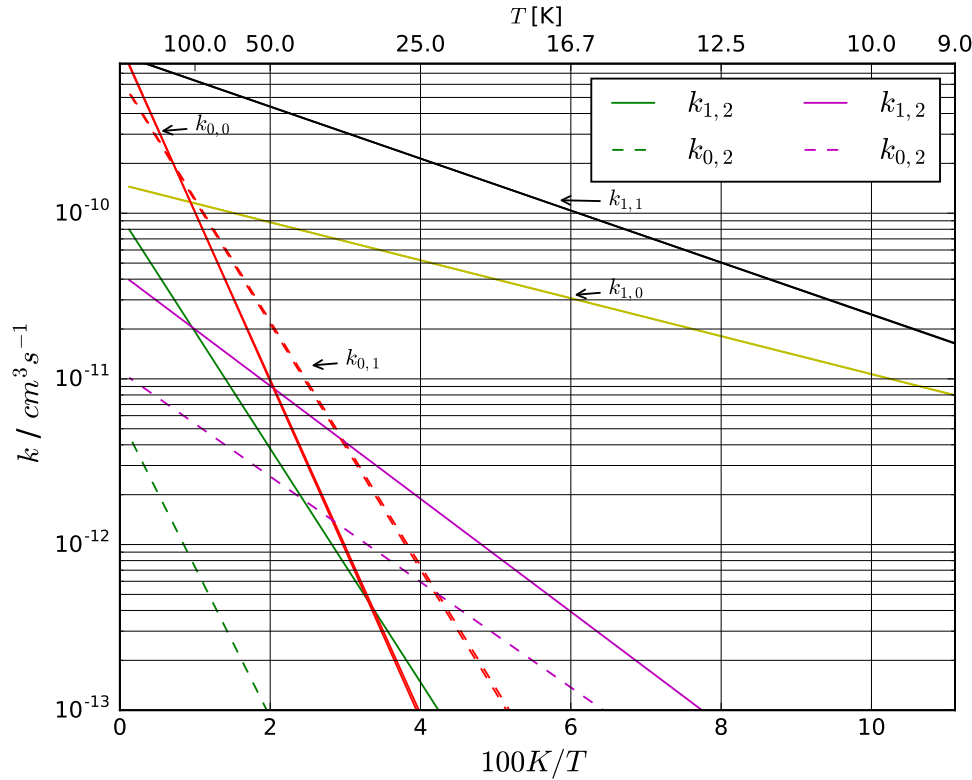


Figure 7.11: The Arrhenius plot shows both sets of the fitted state specific rate coefficients $k_{j,ja}(T)$ with $ja = 0, 1, 2$ and $j = 0, 1$. The rates for both sets with $k_{j,ja}(T)$ with $ja = 0, 1$ and $j = 0, 1$ can not be distinguished from each other. The green lines indicate the first set of parameters and the magenta lines for the second set of the $k_{j,2}(T)$ with $j = 0, 1$ rates. The used sets of parameters can be found in Tab.7.3

Conclusions

The reaction 7.1 has been examined with different methods over a temperature range from 100 K -10 K with normal and para-hydrogen ($f \approx 0.0114$). State specific rate coefficients for the reaction and relaxation (with hydrogen and helium) could be extracted using a non-adiabatic reaction model (section 7.1.2) in connection with a global fit over the whole measured temperature range. The global fit was based on the assumption of the experimentally observed mono-exponential decay of the N^+ ions and the determined temperature dependent effective rate coefficients. The

contribution of the 3P_2 state via direct reactions was found to be negligible, leaving high uncertainties on the associated rates. The main contribution of this state is via relaxation to lower states and subsequent reaction. The reaction rates for the $^3P_{ja}$ state with $ja = 0, 1$ could be calculated quite good using a global fit. Furthermore, it could be demonstrated that relaxation processes due to a large amount of helium within this model are not able to increase the rate of the reaction significantly. In contrast to the predicted strict adiabatic model of Nyman and Wilhelmsson [82] the experimental results cannot be reproduced without taking into account the reactivity and relaxation of the 3P_2 state. Nevertheless, due to the large parameter space of the non-adiabatic model there are still uncertainties concerning the role of the fine states in promoting the reaction 7.1.

The purity of the used para hydrogen is approximately one order of magnitude greater than theoretically expected at an evaporation temperature of ≈ 18 -19 K (see Fig. 7.13). J. Gerke [86] has shown using Raman spectroscopy and the same equipment as used in this measurements, that the purity of p-Hydrogen should be better than $f = 0.0007$ or $f = 0.0018$ for evaporation temperatures of 18.2 K or 20.15 K, respectively. In comparison to S. Gärtner [75], who estimates lowest thermal rates of $k(10K) \approx 5 \cdot 10^{-14} \text{ cm}^3/\text{s}$ for the reaction 8.3 with para hydrogen, the actual rates are larger by a factor of ≈ 2 (see Fig. 7.2). Ongoing experiments reevaluating the back conversion of the produced para hydrogen point to a much faster back conversion than expected from previous measurements performed by J. Gerke [86]. This could indicate a contamination in the Teflon bottle or a leak in the gas inlet between the Teflon bottle and the leakage valve for the neutral gas of the trap. These issues need to be addressed, before additional ortho fractions can be feasibly investigated, as required for a full understanding of the reaction system.

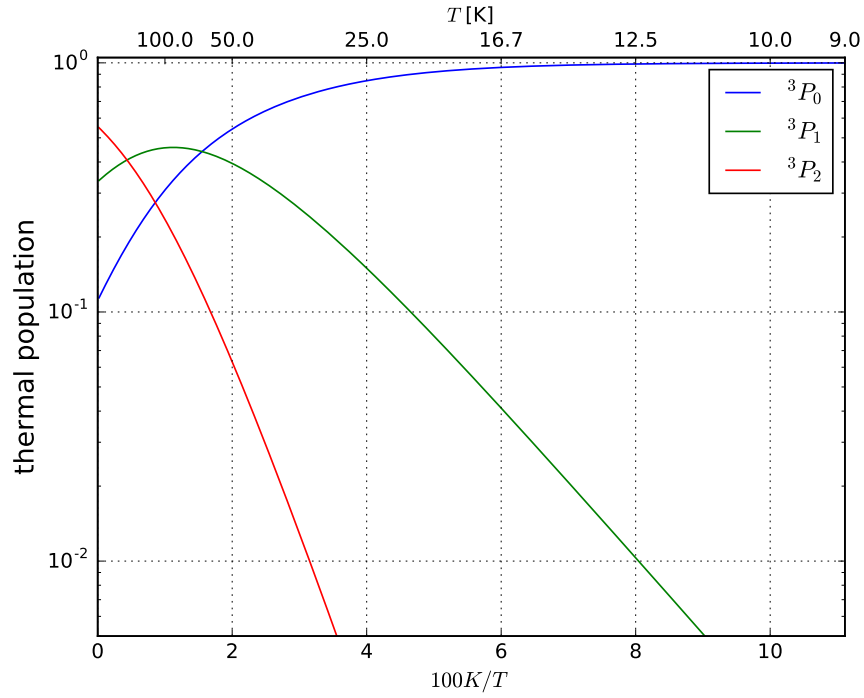


Figure 7.12: Thermal population of the nitrogen fine structure states $\text{N}^+(^3P_0)$, $\text{N}^+(^3P_1)$ and $\text{N}^+(^3P_2)$ as a function of temperature.

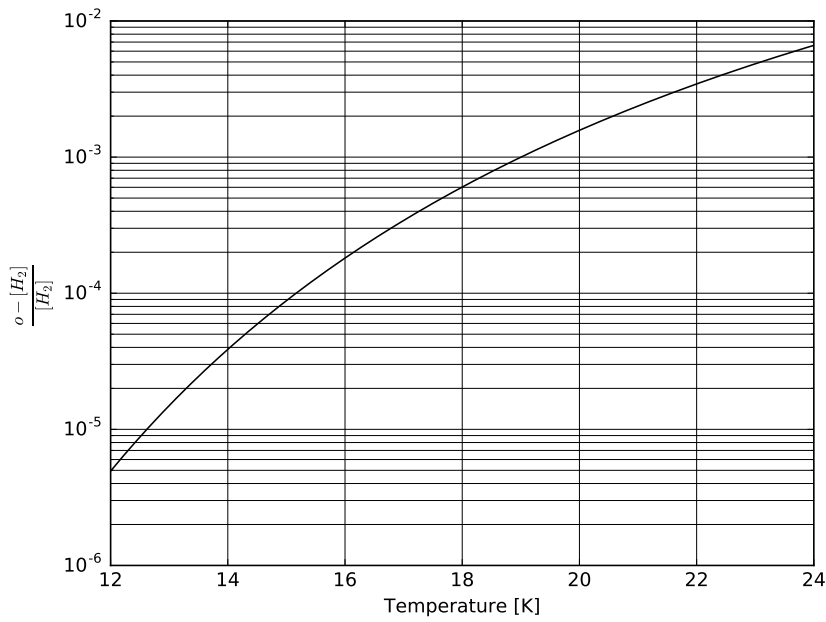


Figure 7.13: Temperature dependence of the ortho fraction $f = \frac{o-[\text{H}_2]}{[\text{H}_2]}$.

Chapter 8

The $\text{N}^+ + \text{H}_2$ Reaction Chain

Through the presence of ammonia NH_3 in interstellar clouds, its formation is of great astro chemical interest. It is supposed that ammonia is formed by the following reaction sequence^[87]:



where in a next step ammonia is produced by dissociative recombination



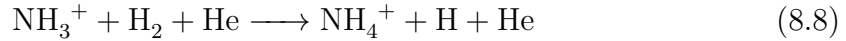
Over the last 30 years the initialization reaction of this chain $\text{N}^+ + \text{H}_2 \rightarrow \text{NH}^+ + \text{H}$ and the formation of NH_4^+ via reaction $\text{NH}_3^+ + \text{H}_2 \rightarrow \text{NH}_4^+ + \text{H}$ have been investigated with different methods in several groups.

The hydrogen abstraction reaction chain starting with N^+ and ending with NH_4^+ can be described via



$k_{f,i}$ and $k_{b,i}$ are rate coefficients for the forward and backward reactions. Reaction 8.5 was included as H_3 is a significant by-product of the NH_4^+ formation chain. Reaction 8.3 is assumed to be slightly endothermic or hindered by a barrier, while reactions 8.4 and 8.6 are assumed to be exothermic. Smith and Adams^[88] estimated

a rate coefficient of $k_{f,2} = 1.5 \cdot 10^{-9} \text{ cm}^3/\text{s}^{-1}$ and branching ratio of 0.85 and 0.15 for reaction 8.4 and 8.5 respectively at room temperature in a Selected Ion Flow Tube (SIFT) experiment. They also estimated a rate of $k_{f,3} = 2.7 \cdot 10^{-10} \text{ cm}^3/\text{s}^{-1}$ for reaction 8.6 in the same experiment at room temperature. J.K. Kim et al. [89] reported a value of $k_{f,3} = 1.2 \cdot 10^{-10} \text{ cm}^3/\text{s}^{-1}$ for this reaction measured in Ion Cyclotron Resonance Mass Spectrometry experiments at room temperature. Investigations by Fehsenfeld et al.^[90] showed that reaction 8.4 is quite slow at room temperature with a rate coefficient of $k_{f,4} = 5 \cdot 10^{-13} \text{ cm}^3/\text{s}^{-1}$. Smith and Adams [91] have been measured this reaction from 510 Kelvin down to 85 Kelvin in a SIFT experiment. They found that the rapid decrease of $k_{f,4}$ with decreasing temperature does not continue below temperatures of 298 Kelvin. The later work of Luine and Dunn^[92] and Bohringer^[93] showed, that the rate coefficient increases at lower temperatures. These authors assume that initially a complex $(\text{NH}_4^+\text{H}_2)^*$ forms, from which tunneling could then occur. They mentioned that at low temperatures, the lifetime of the complex is long and even a small tunneling probability could be important. In addition to the two-body reaction 8.7, Bohringer^[93] observed a three-body process



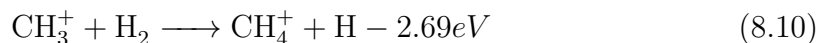
at temperatures below 150 Kelvin. Theoretical calculations by Herbst et al.^[94] confirmed the temperature dependence for reaction 8.7.

The rate coefficients $k_{f,i}$ were measured in a temperature range of 9.5 - 97 K. In our case, the backward rate coefficients $k_{b,i}$ can be neglected, as the number of hydrogen molecules and nitrogen atoms inside the 22-pole trap not significantly promote the backward reaction. For fitting of the forward reaction rate coefficients $k_{f,2-5}$, the effective (thermal) rate coefficient $k_{f,1}$ for the initialization reaction 8.3 was taken from the measurements discussed in section 7.1. If this rate is fixed, then the number density of the hydrogen can be estimated from the mono-exponential decay of the N^+ ions. Figure 8.1 and 8.2 show typical measurements and the fitted time evolution curves of the hydrogen abstraction reactions 8.3-8.7 at 24 Kelvin and 92 Kelvin respectively. The fit was done using a numerical integration routine and was adjusted manually.

At each temperature, the number of product ions levels off after a certain storage time (Figure 8.1 and 8.2), suggesting that some other ion species of mass 15 [amu] is involved, which is not reactive with H_2 . A non-negligible amount of carbon in the ion source (see section 6.3.1 and A.3.3) would form hydrocarbon ions with H_2 . One candidate that will pass the first QMF and is reactive with H_2 is the CH_2^+ ion. The reaction



is known to be fast with a rate coefficient at the Langevin limit of $k_r = 1.57 \cdot 10^{-9} \text{ cm}^3 \text{ s}^{-1}$ ^[95]. The following hydrogen abstraction reaction



is highly endothermic^[96] and should not take place under cryogenic conditions which would explain the constant amount at mass 15 [amu]. Therefore, the following rate equations

$$\begin{aligned}\frac{d\text{CH}_2^+}{dt} &= -k_r[\text{H}_2]\text{CH}_2^+ \\ \frac{d\text{CH}_3^+}{dt} &= k_r[\text{H}_2]\text{CH}_2^+\end{aligned}\tag{8.11}$$

were additionally taken into account to fit the experimental results.

Figure 8.3 shows the rate coefficients $k_{f,2-5}$ as a function of the inverse temperature together with results from previous works, averaged at each temperature.

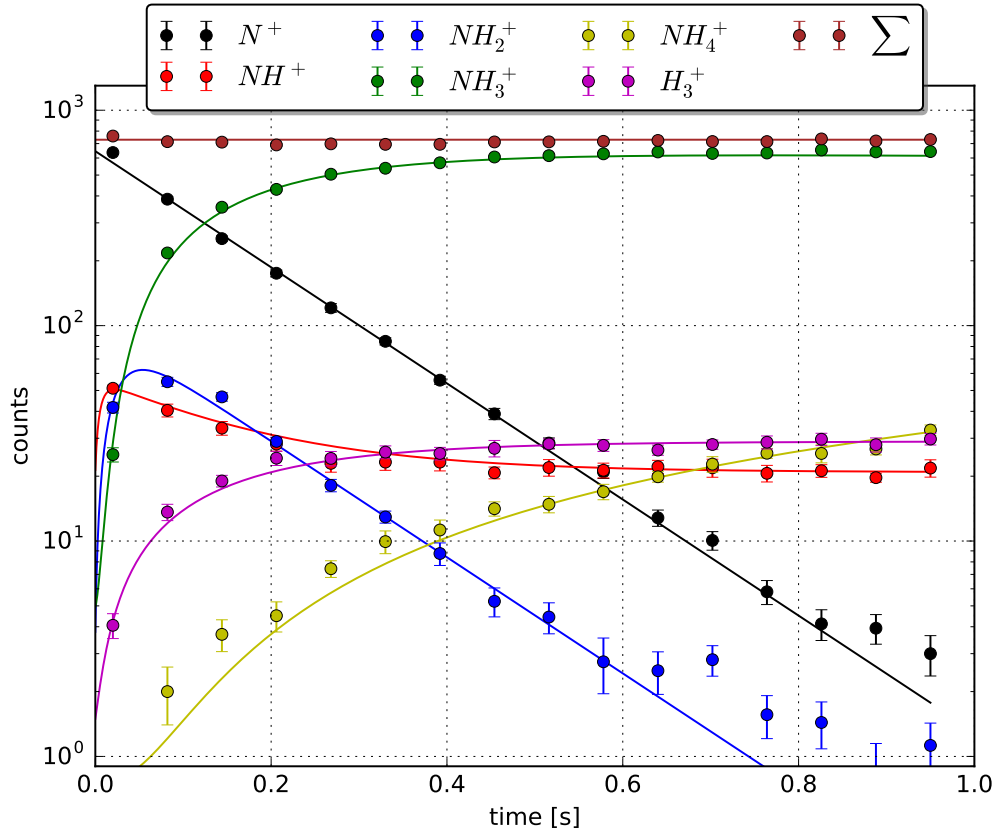


Figure 8.1: Time evolution of reactions 8.3 - 8.7 at 24 Kelvin nominal trap temperature and a hydrogen number density of $[n\text{-H}_2] = 1.2 \cdot 10^{11} \text{ cm}^{-3}$. Solid curves show numerical fits to the data.

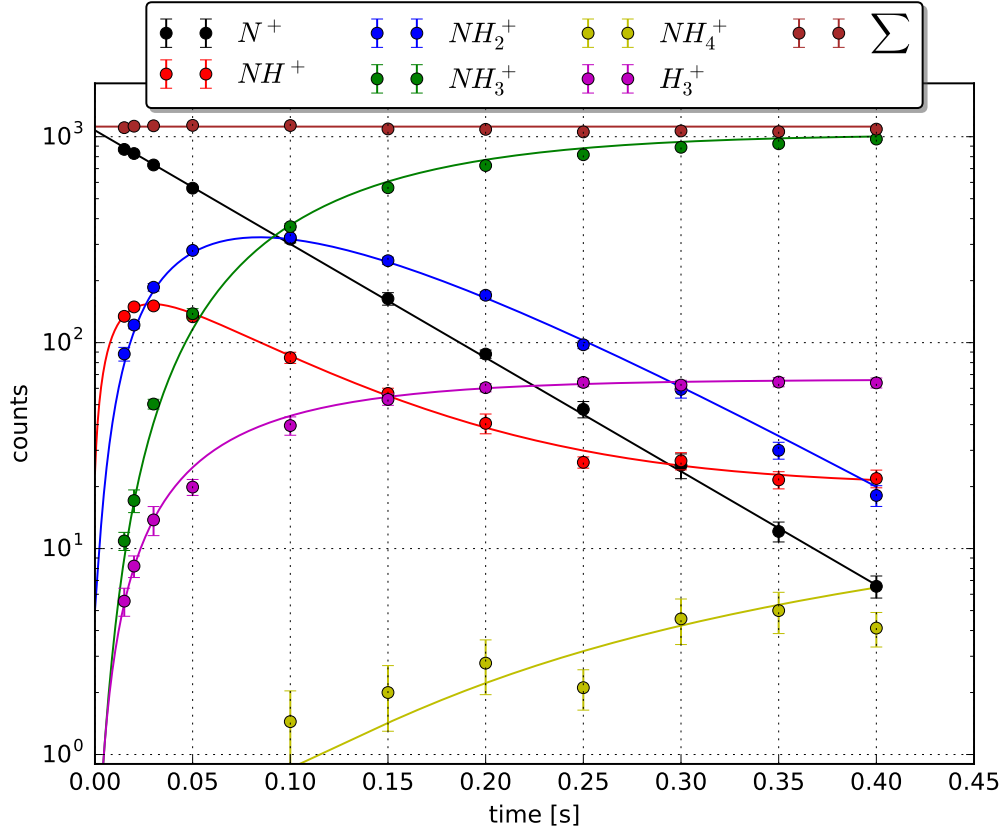


Figure 8.2: Time evolution of reaction 8.3 - 8.7 at 92 Kelvin nominal trap temperature and a hydrogen number density of $[n-H_2] = 5.1 \cdot 10^{10} \text{ cm}^{-3}$. Solid curves show numerical fits to the data.

Both rates, $k_{f,2}$ (reaction 8.4) and $k_{f,5}$ (reaction 8.5), decrease with decreasing temperature, showing Arrhenius type behavior. The results from these Arrhenius fits are summarized in table 8.1 and can be extrapolated to a value of $k_{f,2} = 1.7 \cdot 10^9 \text{ cm}^3/\text{s}^{-1}$ at 300 K, in good agreement with the results of Smith and Adams^[88]. Reaction 8.6 shows an approximately constant rate coefficient $k_{f,3} = (4.16 \pm 0.20) \cdot 10^{10} \text{ cm}^3/\text{s}^{-1}$ as a function of temperature, confirming the exothermic behavior assumed by Smith and Adams, although at a slightly slower rate. The branching ratio of $br = 0.15$ between reaction 8.4 and reaction 8.5 derived by Smith and Adams^[88] is three times larger than the value $br \approx 0.05$ measurement in this experiment. The temperature behavior of reaction 8.7 can also be confirmed. The calculated rate coefficients slightly differ from the values estimated in previous experiments.

$k_{f,i}$	$k_A [\text{cm}^3/\text{s}^{-1}]$	$T_A [\text{K}]$
$k_{f,2}$	$(1.79 \pm 0.17) \cdot 10^{-9}$	(15.98 ± 1.51)
$k_{f,5}$	$(8.89 \pm 1.17) \cdot 10^{-11}$	(15.78 ± 2.15)

Table 8.1: Parameters of a fit of simple Arrhenius-type function for reaction 8.4 and 8.5

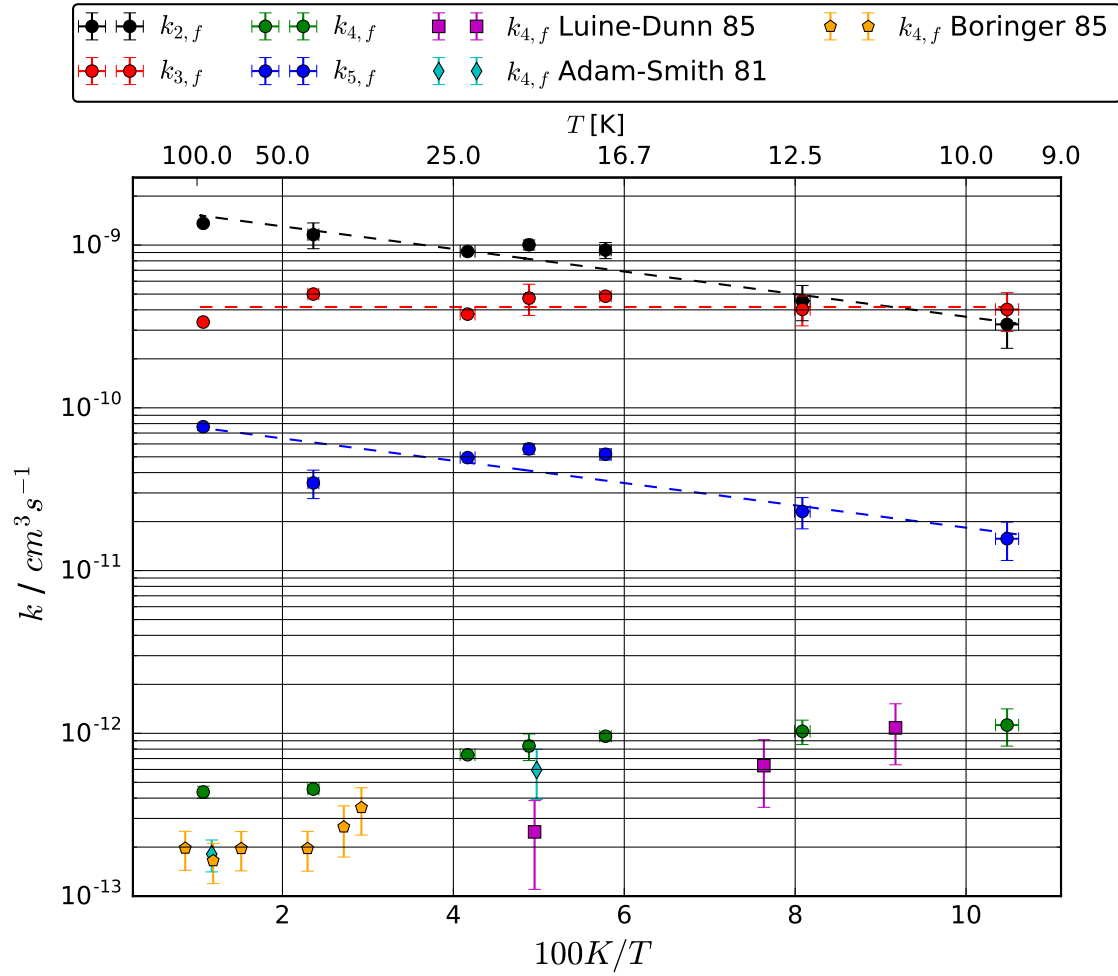


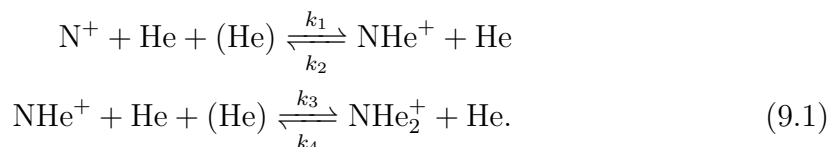
Figure 8.3: The plot shows the rate coefficients $k_{f,2-5}$ (reactions 8.3 - 8.7) as a function of inverse temperature. Uncertainties show the standard deviation of the mean for different measurements at the same temperature. Dashed lines show the average rate $k_{f,3} = (4.16 \pm 0.20) \cdot 10^{10} \text{ cm}^3/\text{s}^{-1}$ for reaction 8.6 (red) and Arrhenius fits for reactions 8.4 (blue) and 8.5 (black).

Chapter 9

Ternary Reaction Processes

9.1 (N–He_n)⁺ Cluster

At low temperatures the formation of weakly bound molecules or clusters via ternary processes can occur. At temperatures around 10 K the association of N⁺ with He to (N–He_n)⁺ was observed. For temperatures above 15 K no clusters were observed. In order to evaluate ternary reaction processes which can impede the determination of the rate coefficients of the reaction N⁺ + H₂ in this temperature region, the formation of helium-nitrogen clusters was investigated. Figure 9.1 shows a mass spectrum of trapped N⁺ ions in presence of helium ([He] = 4.0 · 10¹⁴ cm⁻³) at 9.8 K¹. Such cluster effects, if not taken into account in the reaction model, can lead to apparently larger rate coefficients for reaction 7.1 because they will also result in a depletion of the N⁺ ions. The influence of cluster effects can be taken into account in terms of their ternary cluster formation rate coefficients. Since the (N–He₃)⁺ cluster is two orders of magnitude smaller than the (N–He₂)⁺ cluster and was only observed at 9.8 K and for helium number densities [He] > 3.5 · 10¹⁴ cm⁻³, this component was neglected in the following. Therefore, the formation of (NHe_n)⁺ (n = 1, 2) cluster can be described by the following reaction scheme:



¹Interesting is the fact that the relative intensities of the mass peaks of the (NHe₃)⁺ cluster is by one order of magnitude smaller as expected. Maybe that could be hint at the structure of the nitrogen-helium complex.

Here k_1 and k_3 denote the ternary forward rate coefficients and k_2 and k_4 the backward rate coefficients. The corresponding rate equation system looks as follows

$$\begin{aligned}\frac{dN^+}{dt} &= -k_1[\text{He}]^2N^+ + k_2N\text{He}^+[\text{He}] \\ \frac{dN\text{He}^+}{dt} &= k_1[\text{He}]^2N^+ - k_2N\text{He}^+[\text{He}] - k_3[\text{He}]^2N\text{He}^+ + k_4N\text{He}_2^+[\text{He}] \\ \frac{dN\text{He}_2^+}{dt} &= k_3[\text{He}]^2N\text{He}^+ - k_4N\text{He}_2^+[\text{He}],\end{aligned}\quad (9.2)$$

where $[\text{He}]$ is the helium number density. For this system a non trivial analytic solution is available². Here, in order to fit the rate constants for the system (Eq. 9.2) a numerical routine was used. Figure 9.2 shows a measurement at 9.8 K. The solid lines indicate the fitted curves. The calculated rate coefficients for the helium cluster formation for 9.8 K and 12.85 K are listed in Table 9.1.

T [K]	k_1	k_2	k_3	k_4
9.8(0.1)	1.37(0.18)	4.10(2.35)	2.41(1.72)	6.55(10.62)
12.85(0.05)	1.28(0.06)	3.81(0.81)	1.68(0.36)	1.77(14.2)

Table 9.1: The table shows the calculated rate coefficients for reaction 9.1 via Eq.9.2. The values for k_1 and k_3 are in units of $10^{-30} \text{ cm}^6 \text{ s}^{-1}$. The values for k_2 and k_4 are in units of $10^{-16} \text{ cm}^3 \text{ s}^{-1}$. The uncertainties are derived from the errors of the helium pressure.

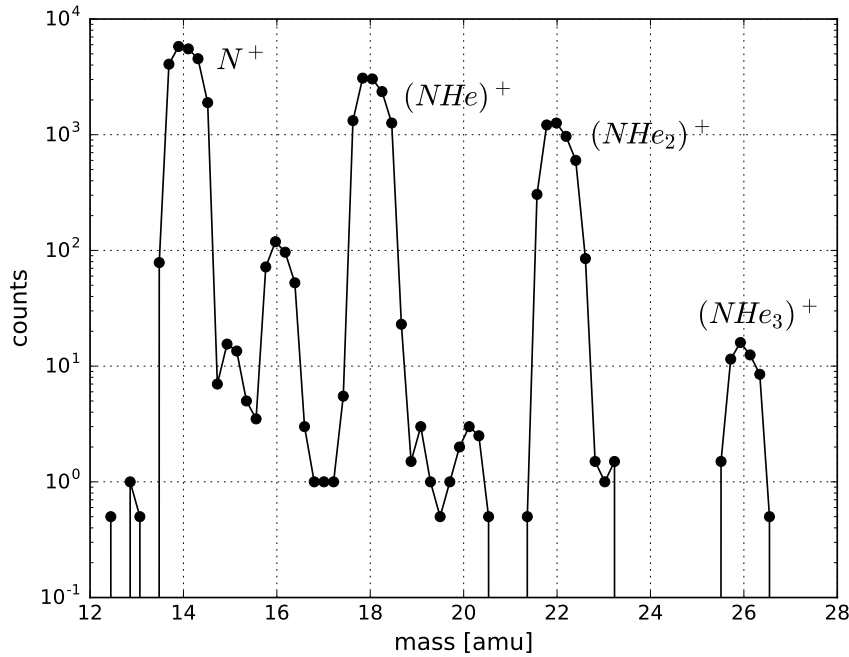


Figure 9.1: The plot shows a mass spectrum of trapped N⁺ ions in presence of helium ($[\text{He}] = 4.0 \cdot 10^{14} \text{ cm}^{-3}$ at 9.8 K.

²using Mathematica

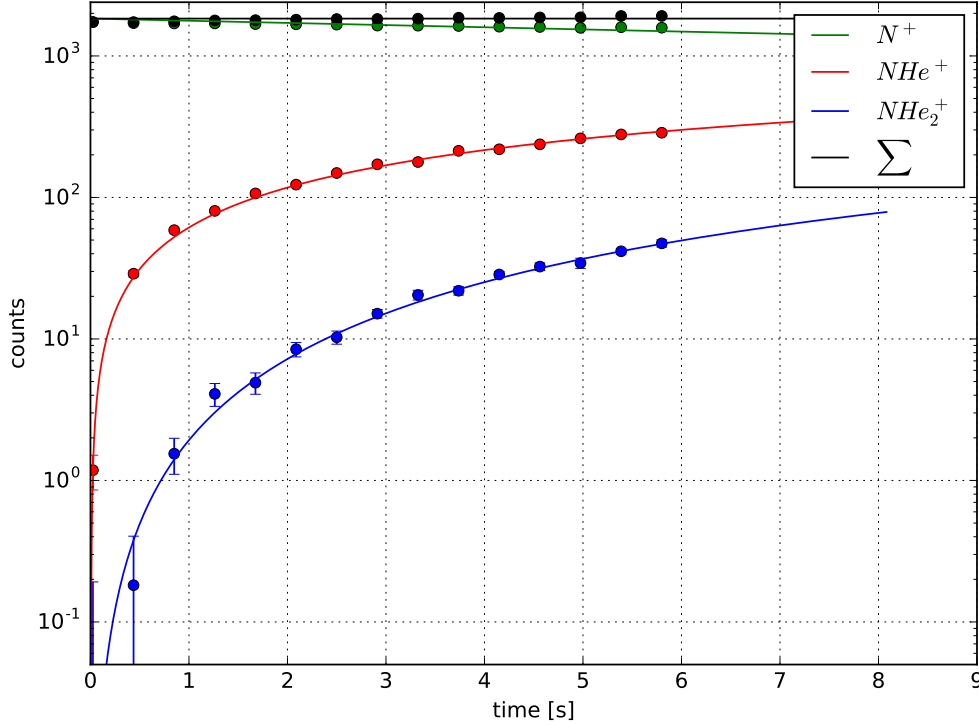


Figure 9.2: The plot shows a measurement of N^+ with He to $(NHe_n)^+$ ($n = 1, 2$) at $T = 9.8K$ and a number density of $[He] = 1.52 \cdot 10^{14} cm^{-3}$. The solid lines indicate the fitted curves via Eq. 9.2.

Conclusion

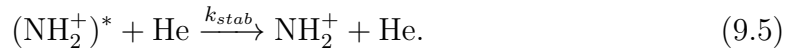
Ternary rate coefficients for the formation of $(N-He_n)^+$ ($n = 1, 2$) clusters could be determined for temperatures between 9.8 and 13 K. Gerlich^[84] calculated a ternary rate coefficient for the formation of the $(N-He)^+$ cluster of $4.6 \cdot 10^{-31} cm^6 s^{-1}$ at 15 K in a 22 pole trap. Taking into account the slightly higher temperature and the smaller rate coefficient, the present results are in good agreement with Gerlich. Furthermore, these ternary rate coefficients can be used to correct the determined rate coefficients for reaction 7.1 under the influence of a huge amount of helium during the reaction.

9.2 The Ternary Reaction of

$$N^+ + H_2 + He \rightarrow NH_2^+ + He$$

Since the increase of the effective rate coefficient of reaction $N^+ + H_2(j=0) \rightarrow NH^+ + H$ as consequence of relaxation processes of the fine structure population of the N^+ ion can be excluded, possible ternary reactions will be investigated in this section. The roughly linear dependence of the rate coefficient in presence of the helium (Fig.7.7 could suggest a ternary reaction process which is in competition with the

reaction to NH^+ . The electronic state correlation diagram for the $\text{N}^+ - \text{H}_2$ system (see Zymak et. al [46] figure 1) shows, starting from the collisional $\text{N}^+ - \text{H}_2$ complex, that a formation of a strongly bound NH_2^+ complex is possible under the influence of a third stabilizing collision partner. The competition between reaction to NH^+ and the strongly bound NH_2^+ complex can be modeled as follows.



In the first step both collision partners, the N^+ ion and H_2 molecule, form a weakly bound complex with a rate coefficient k_c . This rate can be assumed to be proportional to the Langevin rate coefficient^[40] k_L (Eq. A.3):

$$k_c = f \cdot k_{L,AB} \quad (9.6)$$

where A and B indicate the involved collision partners and f denotes the fraction of the collisions leading to complex formation. Here $k_{L,\text{N}^+\text{H}_2} = 1.56 \cdot 10^{-9} \text{ cm}^3/\text{s}$ was used. Typical values for f range from 0.5 to 0.1^[40]. For this calculations a value $f_B = 0.25$ is chosen in the following. The weakly bound complex can either redissociate into reactants with rate coefficient k_{red} or can dissociate into products with rate k_{dis} . Stabilization requires quenching of the excess energy, either in radiative or in collisional processes. Therefore, the rate coefficient for stabilization is composed of a radiative and a collisional part via equation

$$k_{stab} = k_{rad} + k_{coll}[\text{He}]. \quad (9.7)$$

Since $k_{rad} \ll k_{coll}$ the radiative part can be neglected. In the steady state approximation (Lindemann mechanism) the overall measured rate k as a function of the hydrogen and helium number density can be given in the form

$$k([\text{H}_2], [\text{He}]) = \frac{k_c k_{dis} [\text{H}_2]}{k_{red} + k_{dis} + k_{coll}[\text{He}]} + \frac{k_c k_{coll} [\text{He}] [\text{H}_2]}{k_{red} + k_{dis} + k_{coll}[\text{He}]} \quad (9.8)$$

where the last term describes the ternary rate coefficient.

$$k_{ter} = \frac{k_c k_{coll}}{k_{red} + k_{dis} + k_{coll}[\text{He}]} \quad (9.9)$$

Taking into account that $k_{red} \gg k_{coll}[\text{He}]$, the ternary rate coefficient is independent of the helium density. At temperatures below 15 K cluster formation (e.g. $(\text{NHe})_n^+$ ($n = 1, 2$)) can not be neglected, thus an additional rate $k_{cluster}$ needs to be considered, resulting in

$$k([\text{H}_2], [\text{He}]) = k_1[\text{H}_2] + k_{ter}[\text{H}_2][\text{He}] + (k_{cluster}[\text{He}]^2), \quad (9.10)$$

where $k_1 = \frac{k_c k_{dis}}{k_{red} + k_{dis}}$ is the effective two body rate coefficient. Figure 9.3 shows the fit of the experimental data at 10.15 K with the model Eq. 9.10 (red surface). Model Eq. 9.10 reproduces the experimental data well, as shown in Figure 9.3 and A.20, A.21 in the appendix.

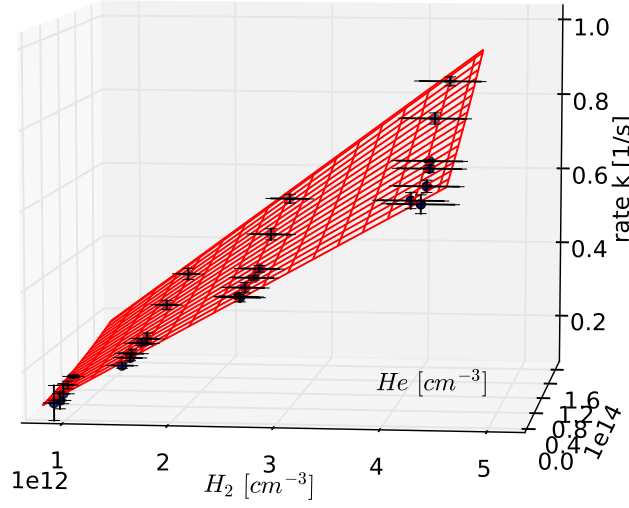


Figure 9.3: The plot shows the measured rates k as a function of the hydrogen and helium number density at 10.15 K. The red surface shows the fit via Eq. 9.10. The fitted rates can be found in Tab. 9.2.

Table 9.2 summarizes fit results for two different temperatures and two different p-H₂ mixtures at the same temperature. At 29 K the ternary rate is one order of magnitude larger than at 10 K, which is unexpected for ternary reactions. Interestingly, the rate coefficient k_1 between two similar p-H₂ mixtures at 10 K deviates. The rate of measurement (b) is 16% larger as for measurement (a). Furthermore, the calculated ternary rate for the measurement (b) is 53% larger as for measurement (a). The reason for the differences in k_1 at 10 K can be caused by a slightly different p-H₂ mixture, implying that the ortho fraction in measurement (a) is smaller than in (b). Paul et al. [97] showed for the cluster formation of H₃⁺ with para-H₂ that the ternary rate coefficient increases with decreasing the ortho fraction of the hydrogen. With respect to their results the deviation in the ternary rates at 10 K of $\approx 53\%$ which tends in the opposite direction are rather unexpected³. Nevertheless, the in-

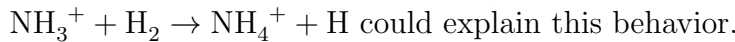
³The relevance of this result in relation to our observation is not clear since we do not form

crease of the ternary rate by one order of magnitude with increasing temperature is surprisingly. With respect to results from other authors, one would expect that ternary ion molecule reaction rate coefficients decrease with increasing temperatures, because of the higher thermal energy ($3/2k_bT$) of the ions which would reduce the lifetime of the short living complex.

T [K]	k_1 [$10^{-13}\text{cm}^3/\text{s}$]	k_{ter} [$10^{-28}\text{cm}^6/\text{s}$]	Remarks
10.15	1.27 ± 0.03	1.93 ± 0.19	(a)
10.15	1.48 ± 0.02	2.96 ± 0.13	(b)
29	17.75 ± 0.38	19.71 ± 2.58	

Table 9.2: Rate coefficients for the reaction system 9.5. (a) and (b) denote two different para- H_2 mixtures in the experiments. Uncertainties are derived from the least squares fit.

A contamination of the used helium⁴ with n- H_2 could be associated with the observed temperature dependence of the ternary rate coefficient. The purity of the helium was measured to be $\frac{[\text{H}_2]}{[\text{He}]} = (1.2 \pm 5.5) \cdot 10^{-7}$. The stability of trapping the N^+ ions, using a huge amount of helium, was confirmed over several seconds before the experiments were performed. Thus, an increase of the ternary rate due to hydrogen contamination can be excluded.⁵ In order to explain the unusual temperature dependence of the ternary rate coefficient, maybe tunnel effects, as mentioned by other authors^[91–93] for the reaction,



could explain this behavior. For a better understanding of the influence of helium with respect to ternary processes, all possible reaction channels of the reaction



should be investigated. Figure 9.4 compares two measurements using only an initial helium pulse (solid lines) and additional helium (dashed lines).

cluster.

⁴helium 5.0

⁵A large contamination would result in a constant offset of the rate coefficient k_1 . Such an offset was never observed.

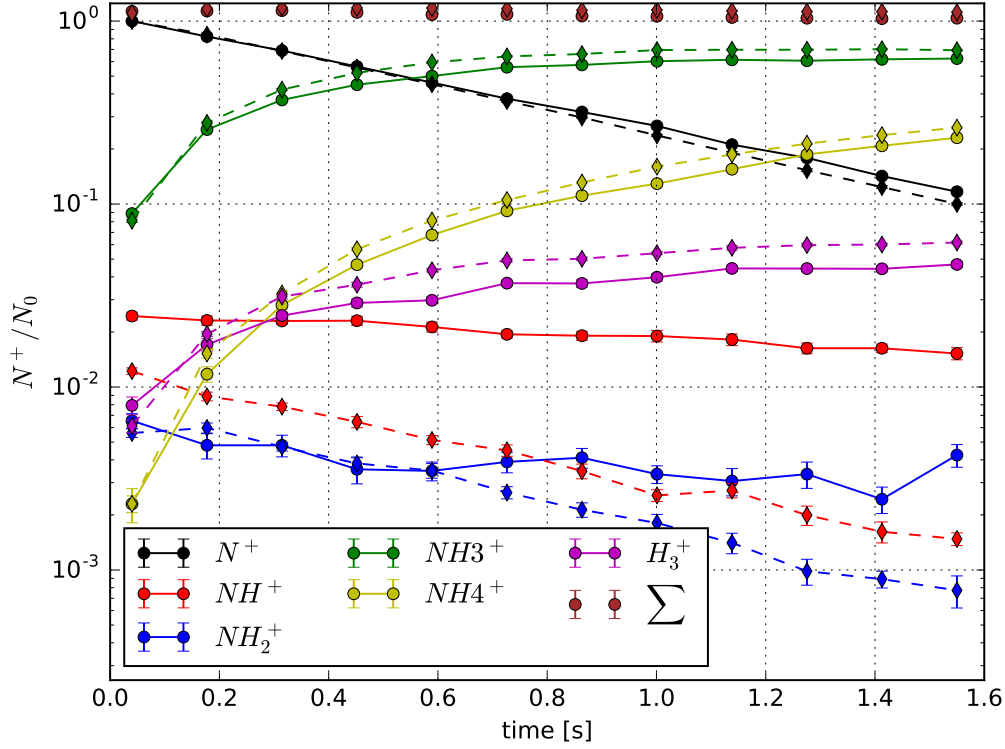
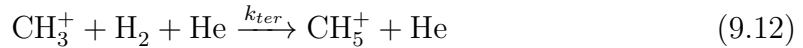


Figure 9.4: The plot shows a comparison between the full reaction chain 8.3 - 8.7 at 29 K with (dashed lines) and without (solid lines) constant flux of Helium after the initial buffering pulse. The Helium number density is $[\text{He}] = 4.5 \cdot 10^{13} \text{ cm}^{-3}$.

In contrast to the measurements using only an initial helium pulse the NH^+ ions are largely depleted and also their initial number is smaller. Furthermore, the depletion of the NH_2^+ ions is slightly stronger using helium. The number of detected NH_3^+ , NH_4^+ and H_3^+ increases slightly towards larger storage times. The depletion of the NH^+ and the lower initial amount of NH^+ in presence of helium suggests that maybe an additional ternary effect is involved.

The depletion and the smaller initial number of NH^+ ions in presence of helium could indicate an additional ternary effect. As mentioned in section 8, the flattening of the number of ions at mass 15 [amu] (see Fig. 8.1 and 8.2) could be caused by a non-negligible amount of carbon in the ion source which would form hydrocarbon ions with H_2 . The depletion of mass 15 [amu] under the influence of helium could be explained by the well known ternary reaction



with a rate coefficient of $k_{\text{ter}} = (0.8 - 1.5) \cdot 10^{-27} \text{ cm}^3/\text{s}$ ^[98] (at 80 K). This third body process would support the assumption of the contamination of the ion source with some carbon. The depletion of the mass 16 [amu] and the small increase of the rates at masses 3, 17 and 18 [amu] could also indicate some unknown ternary reactions.

In order to investigate unusual temperature dependence of the ternary rate coefficient, the change in the number of NH_2^+ ions as a function of the helium number density must be measured. Since the rate coefficient for the subsequent reaction $\text{NH}_2^+ + \text{H}_2 \rightarrow \text{NH}_3^+ + \text{H}$ ($k_{3,f} \approx 1.0 \cdot 10^{-9} \text{ cm}^3/\text{s}$) is large compared to the ternary rate, it would be difficult to observe a significant change in the number of NH_2^+ ions as a function of the helium number density. Due to this fact and the above mentioned other ternary reaction channels, a detailed investigation of ternary processes in the presence of helium seems to be very difficult.

Concluding this, the calculated ternary rates at 10.15 K are consistent with ternary rates measured by other authors^[98]. The ternary rates at 29 k are larger than expected and research into this is ongoing. Care was taken to minimize systematic errors caused by experimental drifts (section 6.3.1), thus the most likely explanations for the faster than expected loss of N^+ ions in the presence of helium are a) unknown experimental artifacts and/or b) mis-assumptions w.r.t. the ternary reaction mechanisms.

Chapter 10

Characterization of a Piezoelectric Valve

For a better understanding of the role of the fine structure states of nitrogen in promoting reaction $\text{N}^+(\text{}^3\text{P}_{\text{ja}}) + \text{H}_2(\text{j}) \rightarrow \text{NH}^+ + \text{H}$ it would be favorable to distinguish between relaxation and thermalization processes and reaction processes.

Until now, the measurements of rate coefficients of ion-molecule reactions in the LIRTrap setup were performed under the influence of collisions with a short ($\approx 100 \mu\text{s}$) pulse of helium buffer gas at the beginning of the storage cycle. in order to increase the trapping efficiency and to thermalize the ions to the ambient trap temperature. After the initial pulse the number density is exponentially decaying in the first $\approx 80 \text{ ms}$ (see Fig. A.18). Meanwhile the neutral reaction gas is flowing continuously into the trap. Therefore, it is not possible to distinguish between the thermalization/relaxation processes of the reactants and the reaction processes. Especially for the determination of state specific rate coefficients of reaction 7.1, this problem could lead to false interpretations of the measurements. “It is an open question to what extent relaxation processes can influence the reaction $\text{N}^+(\text{}^3\text{P}_{\text{ja}}) + \text{H}_2(\text{j}) \rightarrow \text{NH}^+ + \text{H}$ [46].”

To investigate the influence of relaxation to the state specific reaction rate coefficients, it is necessary to separate the thermalization process from the reaction process. One possibility is to use two piezo electric valves to separate in time the buffer gas flow from reaction gas flow. The operating principles and the functionality of such a valve can be found in the bachelor thesis of C.Konietzko [99]. One such piezo electric valve is currently used to inject a short intense helium buffer gas into the trap. Therefore, a short but large voltage pulse (about 100 V and 100 μs) is applied to the piezo element to open it. Applying the same method to the reaction gas will lead to some difficulties. Since the determination of reaction rate coefficients requires a rather good knowledge of the number density of the reaction gas, the short pulsed mode is not practicable to inject the reaction gas into the trap, because the pulsing leads in to a time dependent number density of the reaction gas in the trap (see Fig. A.18). Due to the fact that we measure the pressure outside the

trap with an ion-gauge, and that the repetition rate of such pressure measurements is rather slow (max. 4 Hz), the absolute determination of the number density as a function of the time is very inaccurate.

Another mode to operate such a piezo valve is to resonantly excite it at its resonance frequency to open it, using a periodic oscillating voltage (tickling mode). The operation in this modus can lead to a constant gas flow into the trap if the frequency of the periodic oscillating voltage applied to the piezo element agrees with the resonance frequency of the piezo cantilever system it self. This frequency depends on the size of the piezo element and the cantilever is in the range of a few kHz. This method has the advantage that after a time constant Δt_1 , an equilibrium between the flow in and flow out of the trap will be reached. Due to the difference in volumes of the trap housing and main chamber, after a second time constant Δt_2 also the measured pressure outside of the trap will be constant and can be used to determine the equilibrium reaction gas number density inside the trap. This mode allows a temporal separation of thermalization and relaxation processes and the accurate determination of the reaction gas density for the calculation of the rate coefficients. The operation mode of the piezo valve in the tickling mode is illustrated in Fig. 10.1. As mentioned, the bottleneck of this method is that pressure can not be directly measured as a function of time inside the trap to determine the time constant Δt_1 of the reaction gas flow. To overcome this problem, one can make use of a rather fast ion-molecule reaction with a well known reaction cross section σ to characterize implicitly the time dependence of the number density inside the trap as a function of different parameters as follows:

1. A constant beam of primary ions is guided through the 22 pole trap.
2. At a certain time, the piezo valve is opened using the tickling mode and an increase of the product ions and a decrease of the primary ion as a function of time could be observed.

This procedure is shown in Fig. 10.1 (lower right).

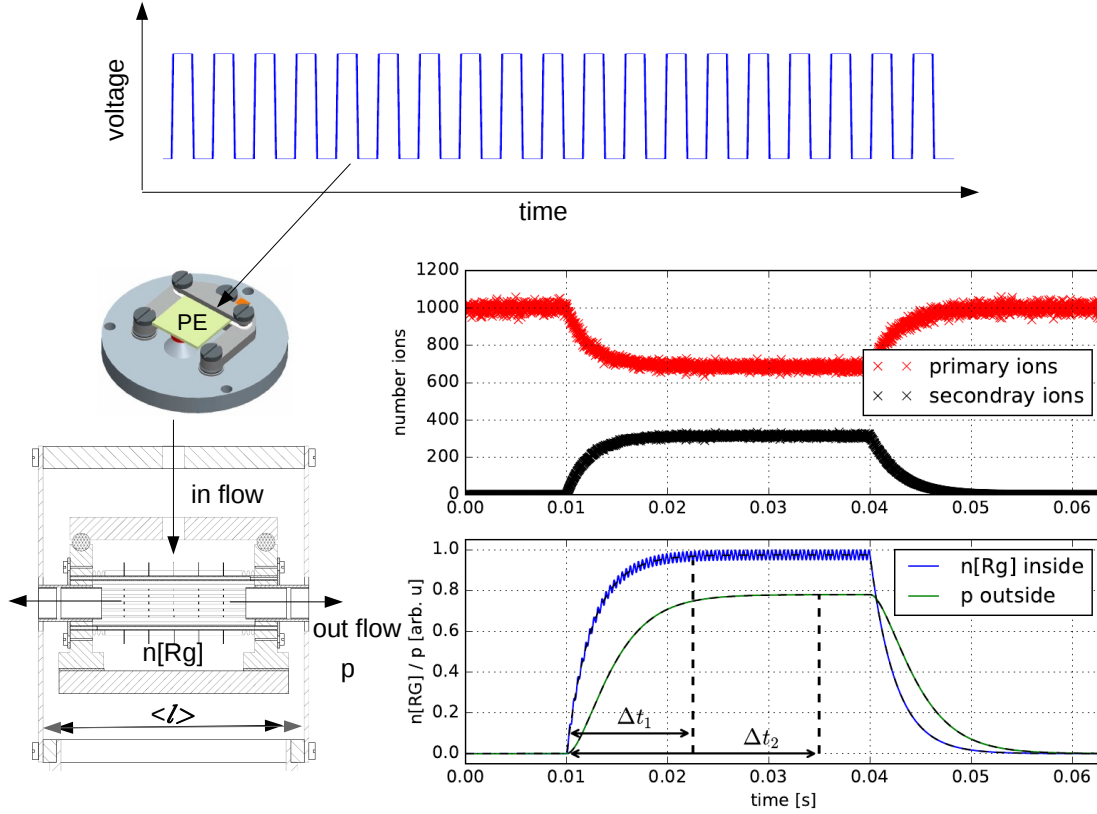
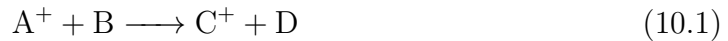


Figure 10.1: The plot illustrates the operation of a piezo valve in the tickling mode. The upper plot shows periodic oscillating voltage which is applied to the piezo element (PE). The lower left figure shows a cross section of the 22 pole trap. Arrows indicates the gas flow into to the trap and out of the trap. $n[\text{Rg}]$ denotes the number density of reaction gas (Rg) inside the trap. p denotes the measured pressure outside of the trap. The arrow marked with $\langle l \rangle$ indicates the effective interaction path length (and its uncertainty) of the ion beam with a reaction gas. The lower right plot (lower panel) shows the number density inside the the trap (blue) and the pressure outside the trap as a function of time, assuming an ideal behavior. The units at the y-axis were chosen arbitrarily for demonstration purposes. The upper right plot (upper panel) shows an ideal time dependent behavior of the primary ions (red dots) and the secondary ions (black dots) as a function of a reaction gas pulse shown in the lower panel using the tickling mode. (The number of primary ions was chosen randomly distributed around a value of 1000)

For an ion-molecule reaction



where A^+ represents the primary ion, B is the neutral reactant, C^+ and D are the products, the decrease of the primary ion and increase of the product ion as a function of time can be described, following the pseudo-first order approximation^[74], similar to Eq. 6.4. Using $t = \frac{\langle l \rangle}{v}$ and $dt = \frac{dl}{v}$, where v denotes relative velocity of the reactants and $\langle l \rangle$ the effective interaction path length for the reaction, the increase and decrease of the primary and product ions, can be written as a function of the

effective interaction path length $\langle l \rangle$ with the following equation,

$$A^+(\langle l \rangle) = A_0^+ \cdot e^{-\frac{k \cdot [Rg] \cdot \langle l \rangle}{v}} \quad (10.2)$$

$$B^+(\langle l \rangle) = A_0^+ \cdot (1 - e^{-\frac{k \cdot [Rg] \cdot \langle l \rangle}{v}}). \quad (10.3)$$

Here k is the rate coefficient, $[Rg]$ is the number density of the neutral reaction gas and A_0^+ is number of primary ions for $l = 0$. Using that the rate coefficient can be written as

$$k = \langle v \cdot \sigma(v) \rangle, \quad (10.4)$$

where σ is the reaction cross section^[59], and assuming that the cross section $\sigma(v) \approx \sigma$ Eq. 10.3 can be written as:

$$B^+(\langle l \rangle) = A_0^+ \cdot (1 - e^{-\langle l \rangle \cdot \sigma \cdot [Rg]}). \quad (10.5)$$

Introducing now the time dependence of the reaction gas $Rg(t)$, the increase of the product ion (see Fig. 10.1 lower right) as a function of the time can be written as:

$$B^+(t) = A_0^+ \cdot (1 - e^{-\langle l \rangle \cdot \sigma \cdot [Rg(t)]}) \quad (10.6)$$

To get a model for the reaction gas density $Rg(t)$ one can assume in first order that one has a gas flow rate a [$N/(cm^3s)$] into a volume V (trapping volume) and flow b [$1/(cm^3s)$] out from volume V . The flow rate a corresponds to a number of particles \tilde{a} [N/s] that flow in a certain time interval into volume V and b corresponds to the number of particles which flow out from trapping volume V with a rate \tilde{b} [$1/s$]. With this the time dependent gas flow can be expressed with the following first order differential equation.

$$\frac{dN(t)}{dt} = \tilde{a} - \tilde{b} \cdot N(t) \quad (10.7)$$

Dividing equation 10.7 by the volume V leads to the differential equation for the number density evolution inside the trapping volume.

$$\frac{1}{V} \frac{dN(t)}{dt} = \frac{dn(t)}{dt} = a - \tilde{b} \cdot n(t) \quad (10.8)$$

Under the operating conditions $p \lesssim 10^{-4}$ mbar in the experiments one can assume a molecular flow. Therefore, the constant \tilde{b} should be proportional to the mean velocity of the particle ensemble and the area of the orifice of the trapping volume. Thus, \tilde{b} should be dependent on the square root of the temperature. Furthermore, this model requires that the flow from the piezo valve inside the trap is constant¹ and the suction capacity of the turbo pumps outside of the trapping volume is large compared to the outflow of the trap to prevent a significant flow back through the orifice into the trapping volume. The suction capacity of the used turbo pumps

¹Calculations of an oscillating flow rate a in Eq. 10.8 show (see Fig. 10.1 lower right), that in time average a constant flow a can be assumed.

(Pfeiffer UHD 400) outside of the trapping volume is in the range of $S = (280000 - 400000) \text{ cm}^3/\text{s}$ dependent on the type of the gas. The effusion volume flow q_V out of the trapping volume can be approximated with

$$q_V = \frac{\bar{v} \cdot A}{4} \quad (10.9)$$

where \bar{v} is the mean velocity of the particle ensemble at a certain temperature and A is the area of the orifice. If one assumes hydrogen molecules at a temperature of 300 K and two orifices with radii of 0.33 cm the effusion volume flow is about $q_V = 30500 \text{ cm}^3/\text{s}$. This shows that the suction capacity of the used turbo pumps is large compared to the outflow of the trap. To summarize this, the above mentioned assumption can be done in order to model time dependent number density with Eq. 10.8. The solution of Eq. 10.8 with $n(t_0) = 0$ is:

$$n(t) = -\frac{a \cdot (-1 + e^{\tilde{b} \cdot (t_0 - t)})}{\tilde{b}} \quad (10.10)$$

For a sufficient time t the number density inside the trapping volume reaches a constant n_0 (see blue line Fig. 10.1 lower right), therefore the ratio of flow inside and the effusion volume flow can be written as $\frac{a}{\tilde{b}} = n_0$, the reached equilibrium number density of the reaction gas which can be calculated using the constant pressure measured outside of the trap and Eq. 6.1. Equation 10.10 can now be simplified to:

$$n(t) = n_0 \cdot (1 - e^{\tilde{b} \cdot (t_0 - t)}) \quad (10.11)$$

Substitution Eq. 10.11 in Eq 10.6 leads to the function of the time depended change of the product ions for reaction eq. 10.1.

$$B^+(t) = A_0^+ \cdot (1 - e^{-\langle l \rangle \cdot \sigma \cdot n(t)}) = A_0^+ \cdot (1 - e^{-\langle l \rangle \cdot \sigma \cdot n_0 \cdot (1 - e^{\tilde{b} \cdot (t_0 - t)})}) \quad (10.12)$$

With the knowledge of $\langle l \rangle$, the effective length, and σ , the reaction cross section for reaction 10.1, formula Eq. 10.12 can be used to characterize the reaction gas flow of the piezo valve.

One possible reaction for this calibration is the ion-molecule reaction of Argon ions with hydrogen. This reaction was studied by several authors^[100–102]. The following products can be formed by this reaction.



Due to a three body collision process



also the formation of H_3^+ is possible. The cross section σ for reaction 10.13 was measured by Ervin and Armentrout [100] in a guided ion beam tandem mass spectrometer. They determined a cross section for energies in the laboratory frame of about 1eV for the product $\text{ArH}^+ + \text{H}$ of $\sigma = (5.0 \pm 1) \cdot 10^{-15} \text{ cm}^2$. For the charge transfer reaction (10.14) the measured cross sections ranges from $\sigma = (2 - 15) \cdot 10^{-16} \text{ cm}^2$ [100].

Experimental

The experimental procedure to use reaction cross sections to calibrate the reaction gas number density as a function of time is quiet similar to the experiment from Ervin and Armentrout [100]. The creation of the ions, mass selection and guiding them through the apparatus is the same as described in the previous sections. The translational energy of the Ar^+ ions is defined by the potential difference between the ion source and the interaction region area in the 22-pole trap. The ion energy determined from this potential difference can differ by a few electron volts from the nominal laboratory energy of the ions. This difference arises from effects due to the ionization process in the ion source. To determine the translational energy of the Ar^+ ions the technique of a retarding potential analysis described by Ervin and Armentrout [100] was used. Therefore, the bias voltage of the 22-pol trap was varied to obtain a retardation curve. The same was done with the bias voltage of the exit lens of the 22-pole trap. Both tests were unsuccessful w.r.t. the rather worse observed retardation curves. It seems that this was caused by the complex geometry of the electrostatic einzel-lenses to focus and guide the ions through the setup, where small changes in the applied voltages of these lenses lead to a change of the focus and guiding properties of the ion beam. In order to get a rough estimate of the translational energy of the ions the following technique was used. The continuous Ar^+ ion beam was hindered by applying a rather high voltage ($\approx 6 - 8 \text{ V}$ w.r.t. the bias voltage of the 22-pole trap) to the electrostatic einzel-lens at the entrance of the 22-pole. After a certain time the voltage at these electrostatic einzel-lens was dropped and the incoming ions were measured using a multiscaler analyzer ² as a function of time. The same procedure was done with the exit lens of the 22-pole trap. As a result, a small time difference Δt (see Fig. 10.2) in the arrival time of the ions time can be observed.

²MSC6A FAST ComTec

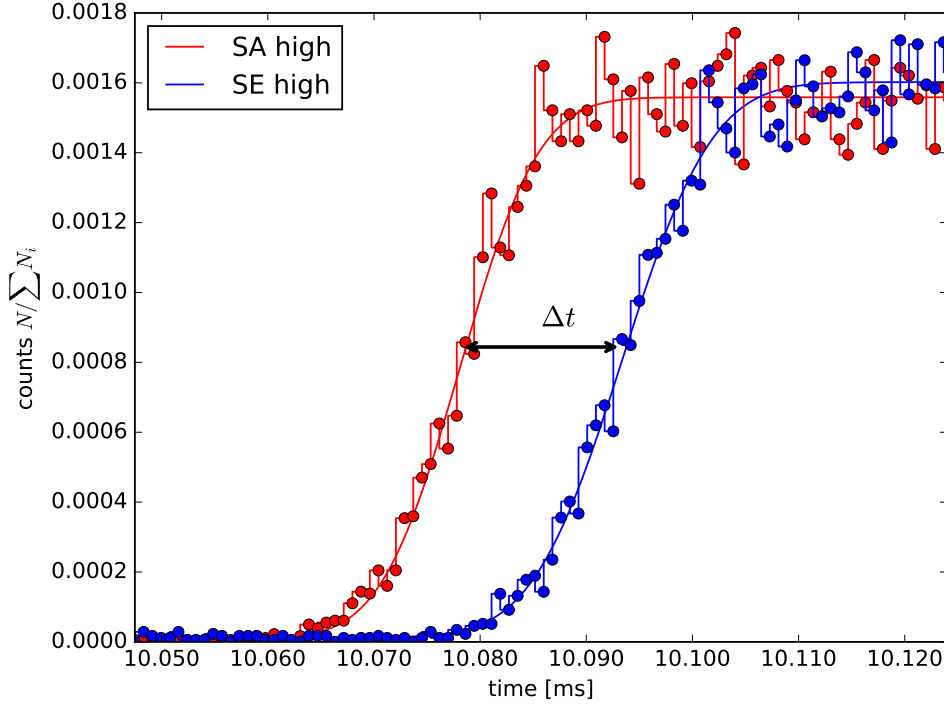


Figure 10.2: The plot shows the measurement of the translational energy of the ions. The red line indicates the measurements where the ion beam is hindered by an electrostatic barrier at the exit lens of the 22 pole. The blue line indicates the measurements where the ion beam is hindered at the entrance lens to pass the 22 pole. After a certain time the barrier will be dropped and the ion can pass. The small indicated time difference Δt can be interpreted as the flight time through the 22 pole trap.

Form the difference in the incoming time Δt of the ions and length L between entrance and exit lens the mean velocity of the ions could be calculated. The geometrical distance between the entrance and exit is $d = 44$ mm. Since the ions will be stopped due to a potential well the real path length L through the trap can differ from the geometrical distance. To determine a more realistic path L a simulation was performed. For this the static part of electrical field for the situations where,

1. the ions were stopped at the entrance lens
2. the ions were stopped at the exit lens

were calculated using the BEM method. With this, the trajectories for 5000 incoming ions were calculated and the effective path was calculated from the difference of the mean turning points of the ions. Figure 10.3 illustrates this for 100 incoming ions. The effective length calculated from the simulations is $L_{eff} = 39.5$ mm. As mentioned before this value differs from the mean geometrical distance $d = 44$ mm. For the calibration the value from the simulation was used. The translational energy in eV of the ions was calculated as

$$E_{ion} = \frac{1}{2e} m \left(\frac{L_{eff}}{\Delta t} \right)^2, \quad (10.17)$$

with m the mass of the ions and e the elementary charge. From several measurements a translational energy of $E_{ion} = 1.00 \pm 0.27$ eV could be calculated. The potential difference between the ion source and the potential of the 22 pole trap was about 1.1 eV for all measurements. This shows that the above mentioned assumption that the energy of the ions is determined by the potential difference between the ion source and interaction region is quite good. Smear out effects of the collisional energy due to the energy distribution of the H_2 reaction gas were neglected, because the thermal energy of the H_2 (≈ 25 meV at 300 K) is only a fraction of the translational energy of the Ar^+ beam. For further calculations a value of $E_{ion} = 1.00 \pm 0.27$ eV will be used.

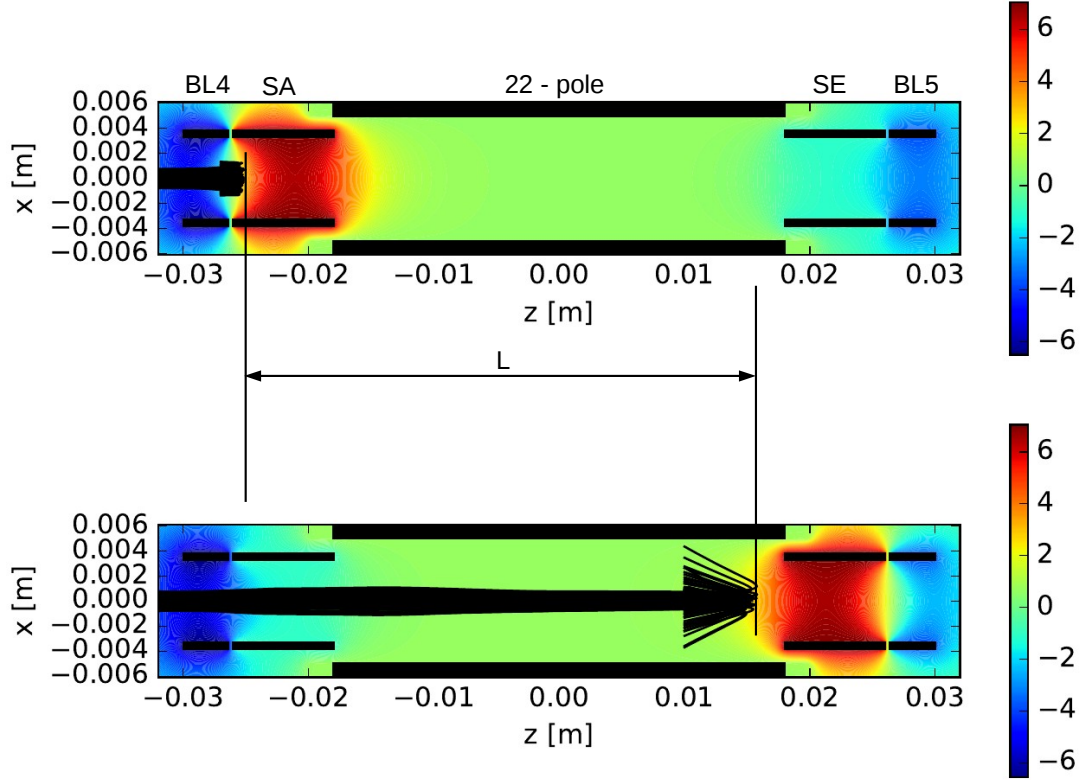


Figure 10.3: The plot illustrates the determination of the effective path length L which is used for the calibration of the ion energies in z - x plane. The applied voltages for the simulation was the same as used in the experiment w.r.t. to the potential difference between the bias voltage of the ion source and the bias voltage of the trap it self. The straight black solid lines indicate the cross sections of the different einzel-lenses (BL4, SE, SA, BL5) and the 22-pol where SE and SA are the entrance and exit lenses and BL4 and BL5 are einzel-lenses to focus the ion beam into the trap. The upper plot shows the situation where the incoming ions are blocked with a high potential applied at the entrance lens. The static voltages for BL4, SE, 22-pol, SA, BL5 are -6.5V, 7V, 0.7V, -1V and -3.7 respectively. The lower plot shows the situation where the incoming ions are blocked with a high potential applied at the exit lens. The static voltages for BL4, SE, 22-pol, SA, BL5 are -6.5V, -1V, 0.7V, 7V and -3.7 respectively. The thin black lines indicate the ion trajectories.

Adjustment of the Piezo-Frequency

During the time of the measurements it was found that the reaction gas flow is very sensible to small changes in the frequency of the applied oscillating voltage of the piezo element. The resonance frequency of the used piezo valve is $f = 3.5$ kHz. Due to a kind of wear and temperature effects this frequency can slightly change w.r.t. the operating time of the piezo valve. To adjust the frequency correctly an oscilloscope should be connected in order to read the roughly applied frequency. Furthermore a bias voltage should be applied in a way that the piezo valve barely closed. Following this a small oscillating voltage should be applied to the piezo till a gas flow can be seen at ion gauge controllers. Now the frequency can be fine tuned till the maximum pressure is measured at ion gauge controllers.

To test the 'collection' efficiency of the experiment, which means, testing if the sum of all reaction channels is equal to the initial amount of the Ar^+ ions, measurements at 275 K and 300 K were performed. As can be seen in Fig. 10.4 (upper plot), the sum of all reaction channels (blue) is not equal to number of the Ar^+ ions without reaction gas (black). The reason for this is probably that many scattering events take place in the interaction volume, where scattered ions can change easily their direction. Compared to an octopole ion guide as used by other authors^[100], the large field free region of a 22 pole trap will not strongly focus scattered ions back to the central axis in axial direction. Therefore, scattered ions can easily hit some electrodes and get lost. Especially the exit lenses are predestined for such events due to their smaller radii compared to the inner radii r_0 of the trap. Also back scattering events can not be excluded. Furthermore, the number of Ar^+ ions under the influence of reaction gas (red Fig. 10.4 upper plot), decreases as long as H_2 is tickled into the trap, whereas the number of ArH^+ ions stays constant after ≈ 500 ms. This could be caused by H_2 , which is leaving the trap through the electrostatic lenses and by an increase of the effective lengths $\langle l \rangle$ of the interaction volume. Here a time depended number density gradient along the axial trap axis can occur. Due to the large volume of the main chamber compared to the volume of the trap itself other reactions processes outside the trap are very unlikely. It seems that the main uncertainties are the rather low collection efficiency caused by a lot of scattering events and the effective lengths $\langle l \rangle$. To evaluate the consequences of these uncertainties w.r.t. to the calculated cross section, measurements of all reaction channels were performed for different H_2 number densities at 300 K and 275 K. The reaction

network of $\text{Ar}^+ + \text{H}_2$ to their products can be written as:

$$\begin{aligned}
 \frac{d\text{Ar}^+}{dl} &= -\sigma_1[\text{H}_2]\text{Ar}^+ - \sigma_2[\text{H}_2]\text{Ar}^+ \\
 \frac{d\text{ArH}^+}{dl} &= \sigma_1[\text{H}_2]\text{Ar}^+ - \sigma_3[\text{H}_2]\text{ArH}^+ \\
 \frac{d\text{H}_2^+}{dl} &= \sigma_2[\text{H}_2]\text{Ar}^+ - \sigma_4[\text{H}_2]\text{H}_2^+ \\
 \frac{d\text{H}_2^+}{dl} &= \sigma_3[\text{H}_2]\text{ArH}^+ + \sigma_4[\text{H}_2]\text{H}_2^+
 \end{aligned} \tag{10.18}$$

with the cross sections σ_i $i = 1 - 4$. This system can be solved analytically using Mathematica or a similar software. For further calculations the solution for the second equation in system 10.18 is given by:

$$\text{ArH}^+(\langle l \rangle) = -\frac{\text{Ar}_0^+ \sigma_1 e^{-[\text{H}_2]\sigma_3 \langle l \rangle} (e^{[\text{H}_2]\langle l \rangle(-\sigma_1 - \sigma_2) + [\text{H}_2]\sigma_3 \langle l \rangle} - 1)}{\sigma_1 + \sigma_2 - \sigma_3} \tag{10.19}$$

A least squares fit of this system to the measurements at 275 ± 10 K is shown in Fig. 10.5. An effective reaction path length of 4.4 cm was assumed which is identical to the geometrical distance (see Fig. 10.3). The determined cross sections are listed in table 10.1. As can be seen the determined values are of the same order of magnitude as measured by Ervin and Armentrout [100] ($\sigma_1 = (5.0 \pm 1) \cdot 10^{-15} \text{ cm}^2$ and $\sigma_2 = (2 - 15) \cdot 10^{-16} \text{ cm}^2$). The ion-product ratio of σ_1 and σ_2 at 300 K of 0.93 and 0.7 is in excellent agreement with the ratio measured by D.K. Bedford and D. Smith [102]. The value of σ_1 is smaller by a factor of $\approx 1.5 \pm 0.1$ than as the value measured by Ervin and Armentrout. The H_3^+ intensities show the expected quadratic dependence of a secondary process on the number density of H_2 . The smaller values of σ_1 agrees with the considered rather large scattering effects of the Argon ions within the interaction area. The deviation between 300 K and 275 K for σ_1 can raise due to a difference in the translational energies of the Argon ions. Due to the large scattering effects as discussed above and the uncertainty of the effective reaction path length, which scales exponentially with the cross section, the results seems to be quite good. Therefore, this method seems to be working and to be accurate enough for calibrating the number densities as a function of time.

T [K]	σ_1	σ_2	σ_3	σ_4
300 ± 5	3.06 ± 0.05	0.24 ± 0.03	1.50 ± 0.53	0.09 ± 0.51
275 ± 10	3.57 ± 0.05	0.63 ± 0.04	2.39 ± 2.13	0.04 ± 0.51

Table 10.1: Calculated cross sections of reaction 10.18 are given in units of 10^{-15} cm^2 . The errors are the statistical errors from the least squares fit.

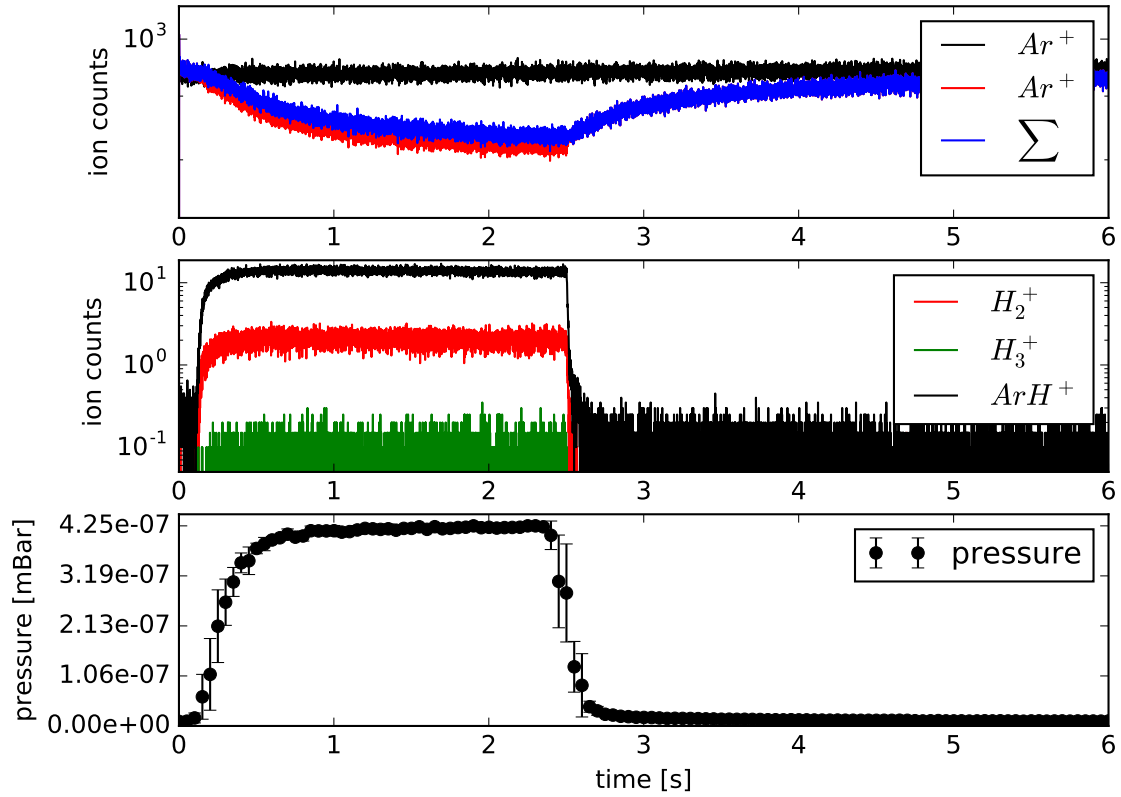


Figure 10.4: The plot shows an accumulation of 20 measurements of the reaction $Ar^+ + H_2$ using an Argon ion beam at an energy of $E_{ion} = 1.00 \pm 0.27$ eV and a hydrogen number density of $[H_2] = 8.7 \cdot 10^{11} \text{ cm}^{-3}$ at a temperature of 275 K. The black line in the upper plot shows the Argon ion beam without hydrogen in the trap. The red line shows the Argon ion beam with hydrogen and the blue line the sum of all product ions. The middle plot shows the number of H_2^+ , H_3^+ and ArH^+ product ions as indicated. The upper plot shows the mean values of the measured pressure outside of the trap.

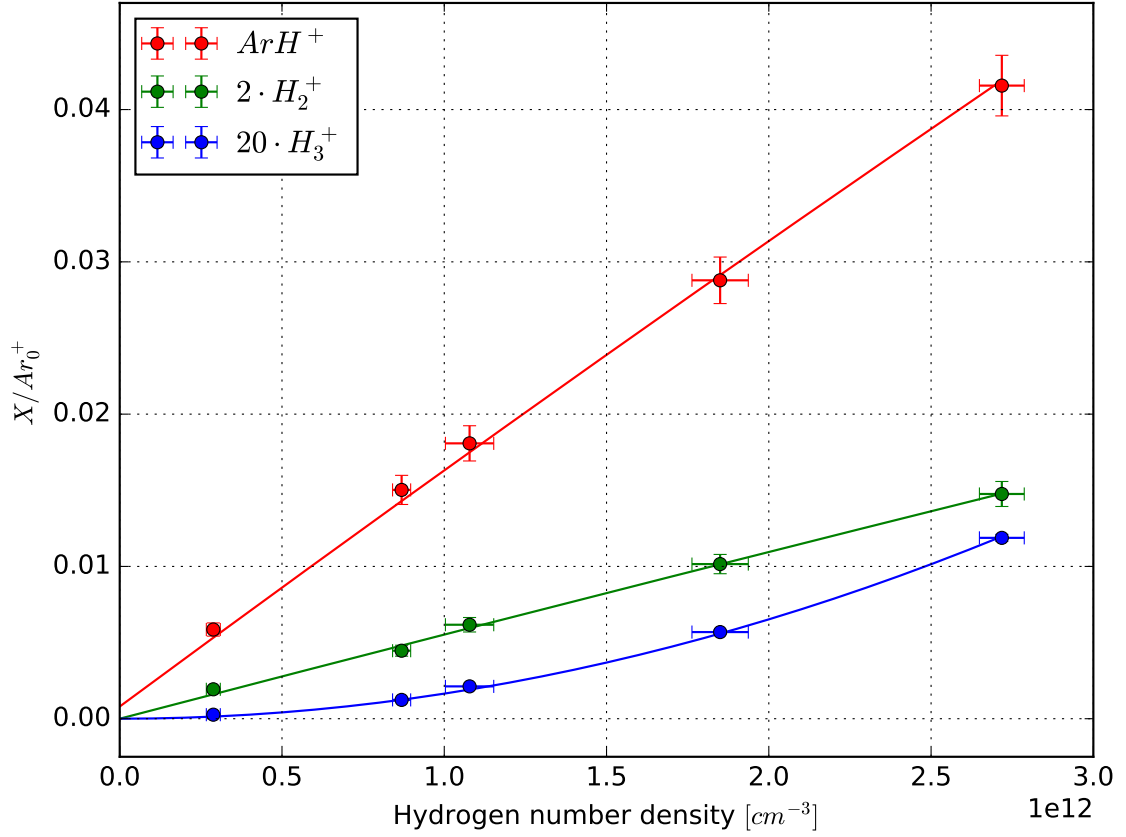


Figure 10.5: The plot shows the ratio of product ion intensity to Argon ion intensity without H_2 as a function of the hydrogen number density at 275 ± 10 K with an energy of $E_{ion} = 1.00 \pm 0.27$ eV. The lines indicate fit of the equation system 10.18. An effective reaction path length of 4.4 cm is assumed.

Figure A.22 compares the increase of the ArH^+ ions $\tilde{b} = 10 \text{ s}^{-1}$ (see Eq. 10.12) and substituting Eq. 10.11 for the reaction gas flow $[Rg(t)]$ in the simple reaction model Eq. 10.6 (solid lines) and into the more sophisticated reaction model 10.19 (dashed lines). The values for the cross sections are taken from Tab. 10.1. The results of both models look quite similar. Above a hydrogen number density of $[H_2] = 1.0 \cdot 10^{12} \text{ cm}^{-3}$ small deviations due to secondary effects are visible. To ensure an, as far as possible, accurate determination of \tilde{b} as a function of the temperature of the reaction gas, the more sophisticated reaction model 10.19 will be used in the following. Figure 10.6 shows \tilde{b} determined from the increase of the ArH^+ ions for different temperatures. In contrast to the expected behavior \tilde{b} depends not only on the temperature but also increases with the absolute pressure $p = p_{RG} - p_{background}$. For temperatures above $\approx 30 \text{ K}$ \tilde{b} can be more or less described with the following function (see red surface Fig. 10.6):

$$\tilde{b}(p, T) = c_1 \sqrt{T} \cdot (1 - e^{-c_2 p / T^{c_3}} + c_4) \quad (10.20)$$

with $c_1 = 11.6 \pm 2.1$, $c_2 = (8.7 \pm 2.1) \cdot 10^5$, $c_3 = 0.33 \pm 0.03$ and $c_4 = 6.46 \pm 0.68$. The errors are the statistical errors of the least squares fit. For temperatures below 23 K

\tilde{b} becomes very small and can not be described within the model function Eq. 10.20.

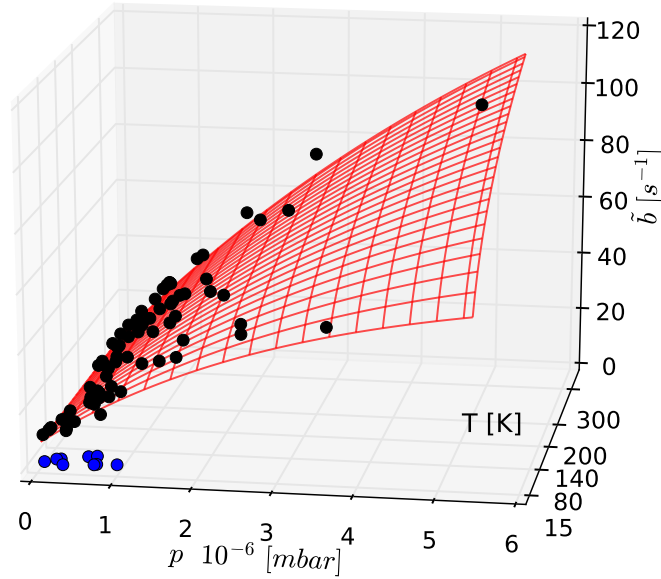


Figure 10.6: The plot shows \tilde{b} as a function of temperature and absolute pressure p . The black dots are the measurements with $T > 30$ K and the blue dots for $T < 23$ K. \tilde{b} was determined from the increase of the Ar^+ ion, substituting Eq. 10.11 for the reaction gas flow $[Rg(t)]$ into the reaction model 10.19. The gray surface indicates the fit using Eq. 10.20 with $c_1 = 11.6 \pm 2.1$, $c_2 = (8.7 \pm 2.1) \cdot 10^5$, $c_3 = 0.33 \pm 0.03$ and $c_4 = 6.46 \pm 0.68$.

Contrary to this, \tilde{b} can be described as expected as a function of the square root of the temperature for $T > 40$ K, using the decrease of the ArH^+ ions after closing the piezo valve (see Fig. 10.7). Here, no pressure dependence could be seen (see Fig. A.23). The decrease of the ArH^+ ions can be well described with the sum of two exponential decays with time constants \tilde{b}^{-1} and τ^{-1} . Here, τ^{-1} describes the slower decrease of the rest of the ArH^+ ions after \approx one fifth of the initial amount of ArH^+ has disappeared. As can be seen in Fig. 10.7, \tilde{b} becomes rapidly smaller for temperatures below 40 K. The large errors between ≈ 35 K and 40 K can be a result of an incorrect determined temperature. This is caused by electrical pick-up³ of the temperature diodes. To instabilities of the used heating power supply of the cold head the real temperature can fluctuate very easy by around 10 K. The rather steep decrease of \tilde{b} for temperatures below 40 K are a consequence the adsorption

³Due to the applied rf amplitude of the 22-pol rods.

effects (sticking or freezing out of H_2 molecules at the inner surface of the trap) that become more relevant for smaller temperatures. Nevertheless, \tilde{b} can be described for two temperature regimes with the following model:

$$\tilde{b}(T) = \begin{cases} c_1\sqrt{T} + c_2 & T > 39.7 \text{ K} \\ c_3T^4 & T < 39.7 \text{ K} \end{cases}$$

with $c_1 = 9.01 \pm 0.45$, $c_2 = 16.1 \pm 3.4$ and $c_3 = (2.86 \pm 0.18) \cdot 10^{-5}$. The errors are the statistical errors of the least squares fit. The reason for the observed difference of the dependence of \tilde{b} on pressure and temperature for the increase and decrease of the ArH^+ ions is not clear. A possible explanation for this is that the flow into the trap through the piezo valve is not instantaneously constant after the oscillating voltage is applied to the piezo element. Here a delay until the valve is fully opened as a function of the applied oscillating voltage can occur. Such a behavior could explain the observed difference. Since the model for the reaction gas flow (Eq. 10.11) into the trap does not any geometrical of the pumped volume, also other unknown factors due to the rather complex geometry of the inside of the trap could be responsible for the difference in the dependence of \tilde{b} . In order to get a more sophisticated model for the reaction gas flow into the trap and to avoid complex calculations due to geometrical factors, the first explanation of the time dependence of the opening of the piezo valve was used. Assuming that the flow into the trap should be constant after a while, the reaction gas flow \tilde{n} can be described using Eq. 10.8 and replacing the constant flow 'a' by $a(t) = a \cdot (1 - e^{-ct})$ via:

$$\tilde{n}(t, \tilde{b}, c) = n_0 \cdot \frac{\tilde{b} - \tilde{b}e^{-ct} + c \left(-1 + e^{-\tilde{b}t} \right)}{\tilde{b} - c} \quad (10.21)$$

where c^{-1} describes the time constant for a complete open piezo valve and n_0 the reached constant reaction gas number density. Substituting this equation in Eq. 10.19 for $[\text{H}_2]$ will lead to a description for the increase of the ArH^+ ions as a function of time. Using the values for $\tilde{b}(T)$ (Eq. 10), c can be fitted to the time depended increase of the ArH^+ ions. Figure 10.8 shows c as a function of the absolute pressure for two temperature regimes. As can be seen c is increasing with increasing absolute pressure p . Also here a rather large decrease of c was determined from the fit for temperatures below 28 K. This seems to be also a consequence of the freezing out of the hydrogen molecules at the inner walls. Nevertheless, since p is a good measure for the applied voltage to the piezo element, the increase of c with increasing pressure would support the above assumption for the opening behavior of the piezo valve. c can be described with the following model:

$$c(p) = \begin{cases} c_4p + c_5 & T > 28 \text{ K} \\ c_6\sqrt{p} & T < 28 \text{ K} \end{cases}$$

with $c_4 = (3.85 \pm 0.11) \cdot 10^7$, $c_5 = 1.63 \pm 0.95$ and $c_6 = (3.44 \pm 0.02) \cdot 10^3$. The errors are the statistical errors of the least squares fit. Using Eq. 10.21 in connection with

$\tilde{b}(T)$ (Eq. 10) and $c(p)$ (Eq. 10) the H_2 flow into the trap can be modeled (within some errors) as a function of the absolute measured pressure and the temperature of the trap

$$\tilde{n}(t, \tilde{b}, c) = \tilde{n}(t, \tilde{b}(T), c(p)). \quad (10.22)$$

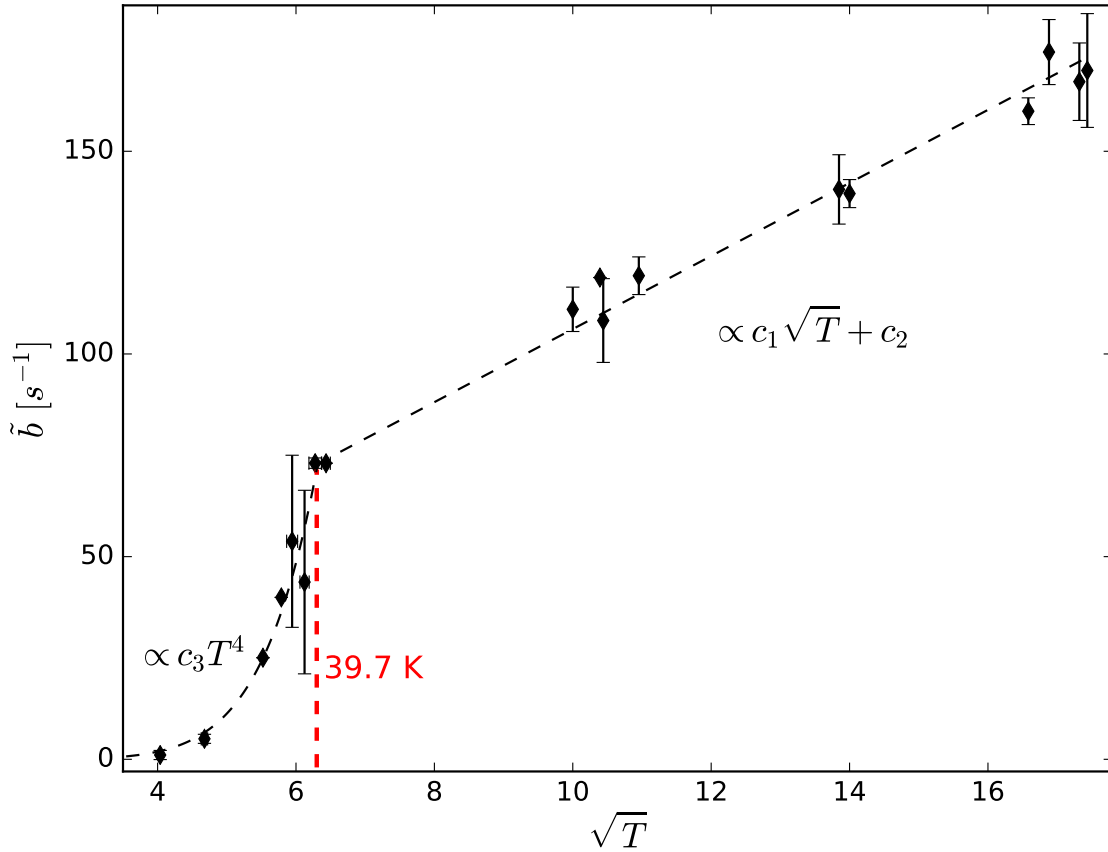


Figure 10.7: The plot shows \tilde{b} as a function of the square root of the temperature. \tilde{b} was averaged for equal temperatures. The dashed lines indicates the fit using the model Eq. 10 with $c_1 = 9.01 \pm 0.45$, $c_2 = 16.1 \pm 3.4$ and $c_3 = (2.86 \pm 0.18) \cdot 10^{-5}$.

It has been shown that most of the measurements could be described very well using the model for the reaction gas flow. Figure 10.9 shows three measurements of the increase of the ArH^+ ions as a function of time at 108 K, 39 K and 16 K. The black lines indicate the simulated $ArH^+(t)$ ions using the model Eq. 10.22 for the reaction gas flow. The abrupt decrease of the time constants \tilde{b} and c for temperatures below 35 K can be interpreted as a consequence of adsorption effects of the at the inner walls of the trap. This temperature regime is higher than expected^[76]. Corresponding to the vapor pressure curve of hydrogen one expects that H_2 freezes out below 20 K. Maybe there are some colder areas inside the trap housing than indicated by the temperature diode (mounted on the backside of the inner trap housing), where hydrogen can freeze out. Since the sticking of hydrogen molecules

at cold surfaces is a very complex mechanism, freezing effects at about 20 K can also not be excluded. A clear indication of cryosorbption effects at cold temperatures is seen in Fig. A.24. The picture shows a screen shot of the Labview data acquisition system to record the measurements which illustrates impressively the effect of the freezeout of H_2 at the inner walls of the trap. The plots in this picture show a measurement at 12 K for the increase of the ArH^+ ions (left panel, white lines) and corresponding measured pressure outside the trap (right panel). Nicely visible are the oscillations in the pressure (right) and the ArH^+ ions (left) with a frequency of 2 Hz. This is exactly the repetition rate of the helium expansion inside of the 10 Kelvin cold head. Cryosorbption effects are very sensible to changes in temperature, the oscillations in the pressure and the number of ArH^+ ions are a consequence of the oscillating cooling power of the cold head and clear ion of cryosorbption effects. Since cryosorbption effects were not the aim of this measurements they were not further investigated.

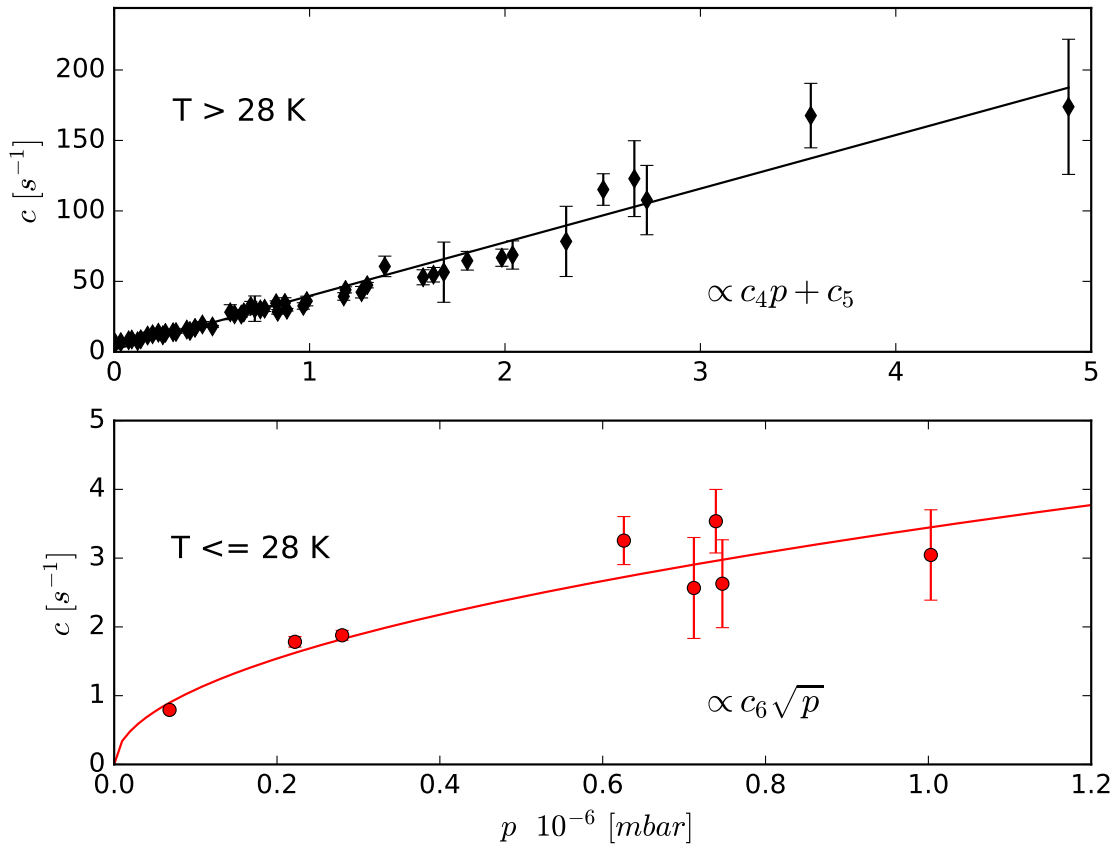


Figure 10.8: The plot shows c as a function of the absolute pressure for two temperature regimes as indicated. The solid lines indicates the fit using the model as indicated. with $c_4 = (3.85 \pm 0.11) \cdot 10^7$, $c_5 = 1.63 \pm 0.95$ and $c_6 = (3.44 \pm 0.02) \cdot 10^3$.

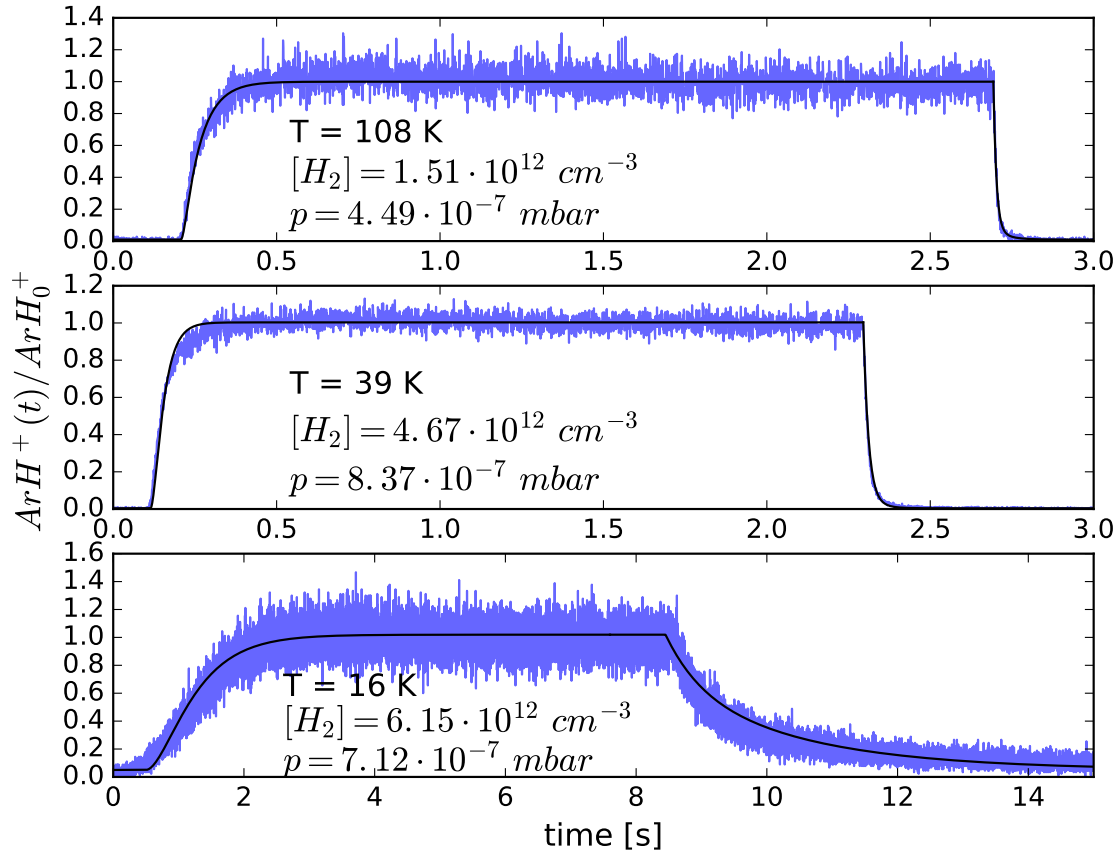


Figure 10.9: The plot shows three measurements of the increase of the ArH^+ ions as a function of time at temperature as indicated. The black lines indicates the simulated $\text{ArH}^+(t)$ ions using the model Eq. 10.22 for the reaction gas flow. The measurements were normalized to unity.

For reactions of ions with hydrogen, where the reaction is faster than the time until a constant flow of H_2 is reached, the rate coefficient must be calculated with the hydrogen number density using the time dependent reaction gas model. Since the reaction takes place in while the hydrogen number density is rising, small errors in this time dependence of the reaction gas can lead to significant errors for the rate coefficients. For slow reactions, where the reaction is slower or equal than the time until a constant flow of H_2 is reached, the rate coefficient can be calculated from the decay of the ions after a constant flow is reached. Here the rate coefficient is less susceptible to errors in the time dependent number density. A simulation of both scenarios is shown in Fig. 10.10 for rate coefficients of $k = 5.00 \cdot 10^{-12} \text{ cm}^3/\text{s}$ and $k = 8.00 \cdot 10^{-11} \text{ cm}^3/\text{s}$ and an assumed error of $\tilde{b}_{fit} = 0.85 \cdot \tilde{b}$ (Eq. 10) and $c_{fit} = 0.85 \cdot c$ (Eq. 10) at 35 K. As can be seen for the higher rate coefficient the reaction takes place while the number density reaches equilibrium and the relative error is $\approx 12\%$. For the smaller rate coefficient the relative error is $\approx 0.4\%$. To reduce the error for the faster reaction the number density can be reduced to fit the exponential decay after the number density reaches equilibrium. Since a reduction of the number density leads to an increase of the time until the number density of

the reaction gas reached a constant flow, the determined rate coefficients are more vulnerable to errors arising from errors in \tilde{b} and c for fast reactions.

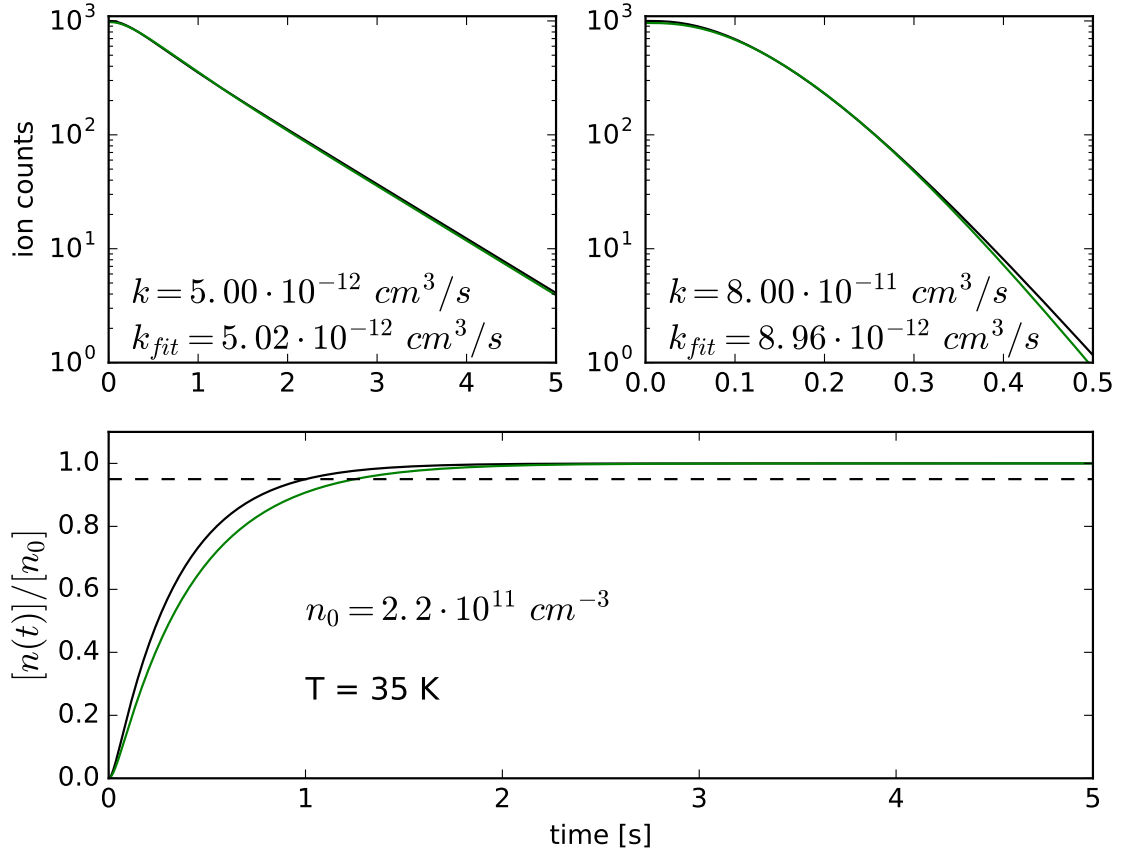


Figure 10.10: The plot compares a fit to a simulated exponential decay of ions for reaction rate coefficients, at a temperature and an equilibrium number density of the reaction gas as indicated in the plots. For the fits, a error in the constants \tilde{b} (Eq. 10) and c (Eq. 10) for calculation of the time depended number density of $\tilde{b}_{fit} = 0.85 \cdot \tilde{b}$ and $c_{fit} = 0.85 \cdot c$ was assumed. This error in the number density is shown as green line in the lower plot. The green lines in the upper plots indicates the fits using the wrong time dependent number density (green line lower plot). The fit was taken for values with $t > 120$ ms and an initial number of 1000 ions was assumed. The dashed black horizontal line in the lower plot indicates the 95 % limit of the reaction gas number density.

The model via Eq. 10.22 can be used to draw a timing map as function of temperature and number density. Fig. 10.11 (lower plot) shows such a timing map for $15 \text{ K} < T < 60 \text{ K}$ and $1.0 \cdot 10^{11} \text{ cm}^{-3} < [\text{H}_2] < 9.0 \cdot 10^{12} \text{ cm}^{-3}$. This map can be used to estimate the time for a given temperature and number density, i.e. how long one has to wait until the H_2 number density is constant.

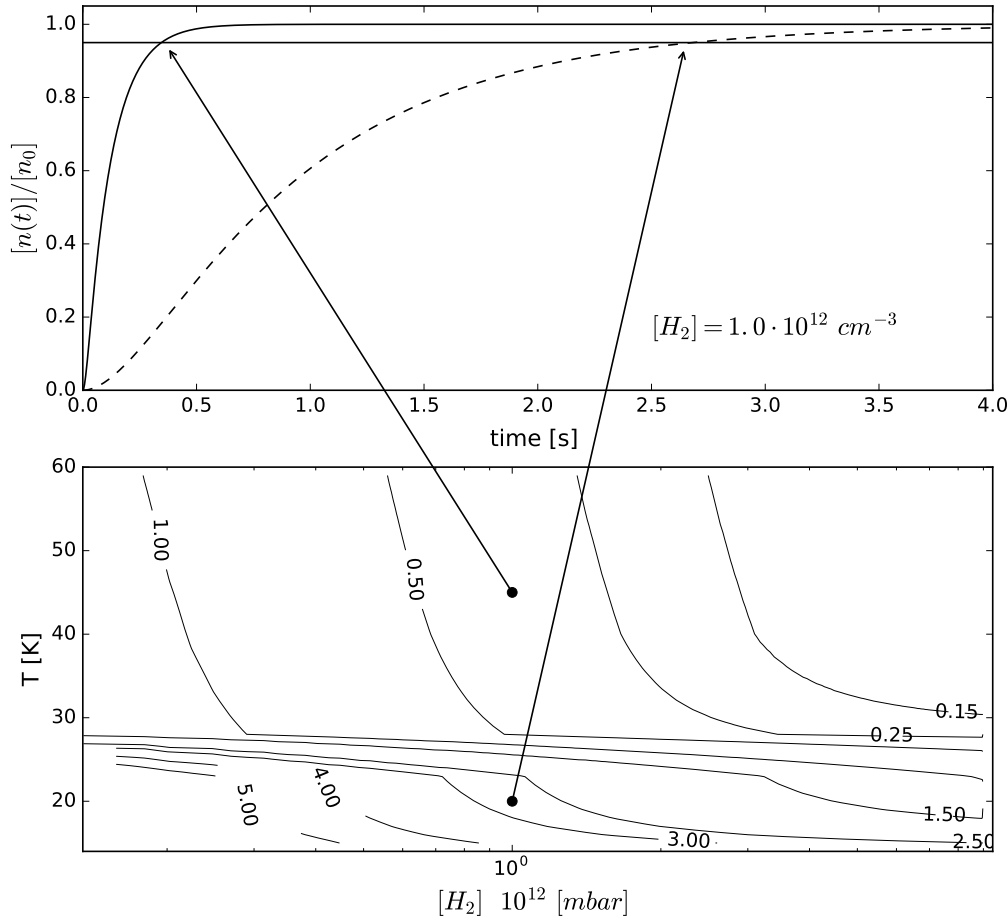


Figure 10.11: The lower plot shows a timing map for the piezo valve. The time t $H_2(t) > 0.95 \cdot H_2$ is reached is indicated as the numbers in the plot in seconds. The upper plot shows the simulated flow in to the trap using Eq. 10.22 and a H_2 number density as indicated for two temperatures $T = 20$ K and $T = 45$ K. These temperatures are indicated in the lower plot as points and the arrows pointing to the corresponding curve in the upper plot. The horizontal solid line in the upper plot indicates the 95 % limit.

Furthermore, this technique in principle allows the determination of the number density of the reaction gas. In the following the feasibility of this approach will be discussed. From the cross section (neglecting ternary effects), the number density can be calculated via:

$$n_{cross} = \frac{\log\left(\frac{Ar_0^+}{Ar_0^+ - ArH^+}\right)}{\langle l \rangle \sigma} \quad (10.23)$$

with Ar_0^+ the number of initial Argon ions, $\langle l \rangle$ the effective reaction path length and σ the cross section for the reaction. For σ the mean value of $\sigma_1 = (3.30 \pm 0.27) \cdot 10^{-15} \text{ cm}^2$ from Tab. 10.1 was used. The effective reaction path length was assumed to be $\langle l \rangle = 4.4 \pm 0.2 \text{ cm}$. Figure 10.12 shows the relative deviation $\frac{[n_{cal}] - [n_{cross}]}{[n_{cal}]}$ in % where n_{cal} is the number density calculated via Eq. 6.1. As can be seen in terms of the relative deviation, the number densities calculated with cross section n_{cross} are \approx

10% smaller as n_{cal} calculated via Eq. 6.1 for $T > 35$ K. Towards lower temperatures the deviation increases to positive values, which means that $n_{cal} > n_{cross}$. Since the effective reaction path length should not change and sigma increases with smaller temperatures of the hydrogen, one possibility to explain this behavior is that the initial number of Ar_0^+ ions is smaller at lower temperatures. As can be seen in Fig. 10.4 (upper plot), where the blue and black curves show the measurements for the Ar^+ ion with and without a hydrogen pulse, respectively, the number of Ar^+ converges slowly to its initial value without any hydrogen in the apparatus w.r.t. the time. Since the initial amount of the Ar_0^+ ions were calculated from the black curve, it seems to be possible that at lower temperatures the hydrogen stays longer in the apparatus and the calculated initial amount of the Ar_0^+ ions is too small. Remark: The used cross section in this calculation is smaller than the cross section calculated from Ervin and Armentrout [100] ($\sigma = (5.0 \pm 1) \cdot 10^{-15} \text{ cm}^2$) for this reactions. Using their value would lead to even smaller number densities.

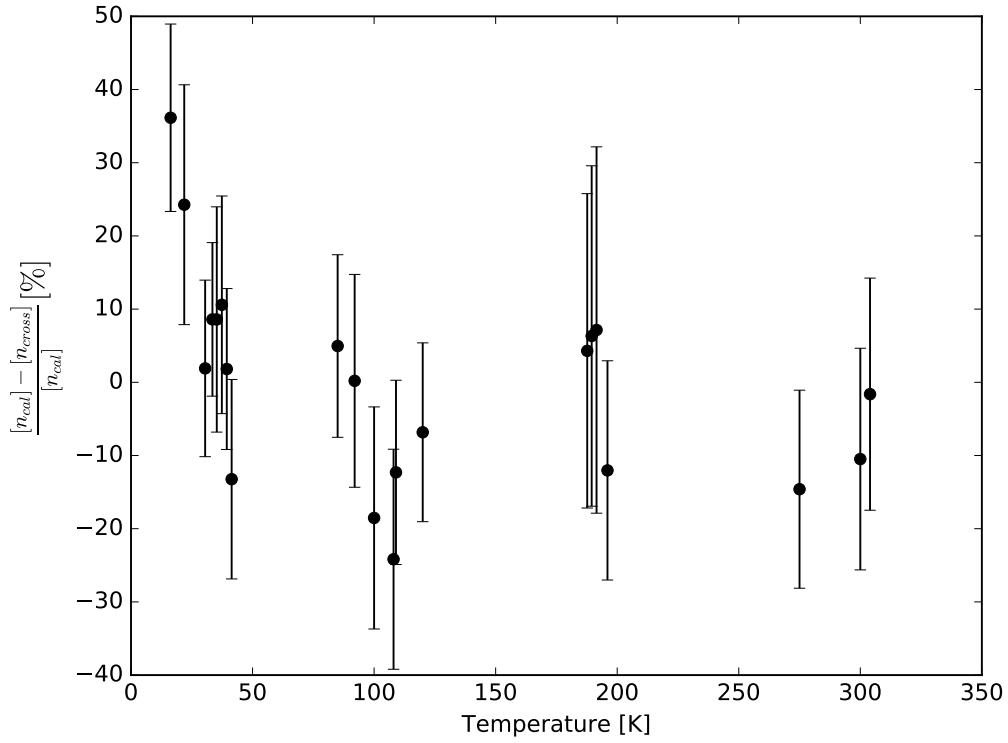


Figure 10.12: The plot shows the relative deviation of the number density n_{cal} determined via via Eq. 6.1 to the number density n_{cross} determined using reaction of Argon ion with hydrogen via Eq. 10.23 in %.

Due to i) the unknown energy of the Ar^+ ions, ii) the unknown exact cross section of the reaction, iii) large scattering effects and iv) the unknown reaction path length this method seems to be inappropriate and very inaccurate to determine the number density of the reaction gas.

Conclusion

The reaction of Ar^+ ions with H_2 was used to calibrate the reaction gas flow into the 22-pole trap via a piezoelectric valve in a temperature range of 15 K - 300 K. Here, a tickling mode was used to achieve a constant flow of H_2 . Due to the uncertainties in the exact translational energy of the Ar^+ ions, the effective reaction path length and large scattering effects, the calculated cross sections differ by a factor of ≈ 1.5 to the cross sections determined in other experiments. The observed reaction channels agree qualitatively very well with the expected ones. A model could be developed in order to describe the time dependent reaction gas flow of H_2 as a function of absolute pressure and trap temperature.

Below 35 K, cryosorption effects slow down the reaction gas flow, therefore the time for tickling the reaction gas into the trap should be increased in order to determine accurately the equilibrium number density of the H_2 . Due to very strong cryosorption effects below ≈ 15 K this method seems to be very inaccurate in order to determine the number density of the H_2 precisely. To evaluate the described reaction gas flow model in more detail, measurements of ion-hydrogen reactions with well known rate coefficients should be performed.

Chapter 11

Conclusion and Outlook

11.1 Experimental Part

Within this thesis, the reaction $\text{N}^+(\text{}^3\text{P}_{\text{ja}}) + \text{H}_2(\text{j}) \rightarrow \text{NH}^+ + \text{H}$ was investigated and analyzed in great detail. Since the role of the energy dependence on the nuclear spin configuration of the hydrogen molecule is largely understood, the aim was to investigate the influence of the energy of the fine structure of the N^+ ion in promoting this reaction.

Based on extensive measurements and a careful analysis of this reaction system, fine state specific rate and relaxation coefficients have been calculated.

It could be demonstrated that the adiabatic reaction model is suited to describe the effective rate coefficients as a function of the temperature across the whole data set. However, the fine state specific rate coefficients extracted within this model were not found to be appropriate in order to describe the experimentally observed exponential decay of the N^+ ions. Consequently, these fine state specific rate coefficients are only a first order approximation. In order to explain the mono exponential decay of the N^+ ions, reactivity and relaxation of the $\text{}^3\text{P}_2$ state of the N^+ ion were taken into account. By using a non-adiabatic model in connection with a global fit, fine state specific rate and relaxation coefficients have been calculated, which are able to describe the observed mono exponential decay. The large uncertainties of the rate coefficients of the $\text{}^3\text{P}_2$ state suggests, that they only have minor contributions to the reaction. In order to clarify the reactivity of the $\text{}^3\text{P}_2$ state more measurements above 100 K and well known ortho-para mixtures of the hydrogen are necessary.

Despite the observed trend of an increase of the rate coefficient while using a huge amount helium, the intensive analysis of the non-adiabatic model leads to the conclusion that relaxation processes under the influence of helium buffer gas are not able to increase the effective rate coefficients.

The increase of the rate coefficients in presence of helium is probable caused by ternary reaction processes which lead to the formation of a strongly bound NH_2^+ complex. In order to resolve the discrepancies between the measured and expected temperature dependence of the ternary rate coefficients, additional measurements

are necessary.

Furthermore, rate coefficients for the formation of $(\text{N-He}_n)^+$ ($n = 1, 2$) clusters were determined, in order to evaluate ternary reaction processes which can impede the determination of the rate coefficients of reaction $\text{N}^+ + \text{H}_2 \rightarrow \text{NH}^+ + \text{H}$ at low temperatures.

Based on the characterization of the piezoelectric valve, a model was developed to describe the reaction gas flow as a function of time in a quantitative way. This model could be used in future experiments in order to separate different reaction mechanisms from each other. For example the technique described could be useful to verify the influence of relaxation processes of the fine structure population of the N^+ ions on the reaction $\text{N}^+(\text{}^3\text{P}_{j_a}) + \text{H}_2(j) \rightarrow \text{NH}^+ + \text{H}$. Thus, relaxation processes using huge helium number densities ($\approx 10^{15} \text{ cm}^{-3}$) and a relaxation time of several seconds can be separated from the reaction processes with hydrogen.

In the course of the present experimental investigation, various parameters were identified which influence the reproducibility and the accuracy of the measured rate coefficients. In conclusion, the following parameters showed the highest impact w.r.t. the behavior of the number density of the neutral reaction gas, and thus on the derived rate coefficients:

- temperature fluctuations of the trap caused by an imperfect thermal contact of the heating elements which are mounted around the coldhead
- cryosorption effects at low temperatures
- the equilibrium of the pressure inside and outside the 22 pole trap is only reached after $\approx 2 \text{ h}$

For future experiments the heating system of the trap should be redesigned to allow for stable temperature measurements above 30 K. Here, heating cartridges¹ could be used, which can directly be mounted in the trap housing. Furthermore, a PID temperature controller would be very useful in order to control the heating of the trap and correct temperature changes automatically. To reduce unwanted reaction channels caused by contaminations of the ion source, it is necessary to clean them and replace the broken filament.

In addition, the problem of the rather bad purity of the produced para-hydrogen needs to be addressed, before additional measurements using p- H_2 can be performed.

11.2 Theoretical Part

The theoretical part of this thesis has covered different aspects of trapping charge particles. It was demonstrated that the boundary element method (BEM) is suited

¹<http://www.hs-heizelemente.de/productareas/pt-100/>

for highly accurate calculations of electrostatic potentials. In connection with the multipole analysis, this is a powerful tool in order to design new trap arrangements or to analyze the behavior of ions in oscillating electric fields. Based on various examples it was shown, how this tool can be used to study the influence of various design parameters on the trapping field in a systematic way or to evaluate perturbations of the field due to mechanical misalignments.

For a 22 pole trap it could be shown, that the kinetic energy distribution of an ion ensemble could be well described by a weighted sum of two Maxwell-Boltzmann distributions using the temperature of the buffer gas and a higher temperature which is governed by the coupling of the micro and macro motion of the ions. Also heating effects due to unwanted trap minima in a real 22 pole trap and how to avoid them were discussed. Based on the example of the split ring electrode trap (SRET) a formula was derived in order to calculate frequency shifts in the secular motion of the ion as a function of higher order multipole components of the field.

The last section of the theoretical part showed to what extent space charge effects must be taken into account in a 22 pole trap. It was demonstrated that space charge effects have the same consequence of pushing the ions towards the rf electrodes as the applied voltage at the exit and entrance lenses. Numerical simulations of varying number of stored ions in a realistic 22 pole trap considering space charge effects and elastic collisions did not show any increase of the axial energy of the ions. Thus, the discrepancy between the nominal trap temperature and the ion temperature, derived from the Doppler broadening in the experiments^[103], cannot be explained within these simulations. The simulations showed that the observed increase of the ion temperature is a consequence of the oscillating field in radial direction. Here, the ion temperature increases with increasing the number of stored ions and/or the applied axial trapping voltage.

Bibliography

- [1] E. E. Ferguson, “Ion-molecule reactions in the atmosphere,” in *Kinetics of Ion-Molecule Reactions*, edited by P. Ausloos (Springer US, Boston, MA, 1979) pp. 377–403.
- [2] D. L. Albritton, I. Dotan, W. Lindinger, M. McFarland, J. Tellinghuisen, and F. C. Fehsenfeld, *The Journal of Chemical Physics* **66**, 410 (1977), <https://doi.org/10.1063/1.433986> .
- [3] W. Paul, *Angewandte Chemie International Edition in English* **29**, 739–748 (1990).
- [4] H. Dehmelt, *Reviews of Modern Physics* **62**, 525–530 (1990).
- [5] D. Gerlich, in *Adv. Chem. Phys.: State-Selected and State-to-State Ion-Molecule Reaction Dynamics*, Vol. LXXXII, edited by C.-Y. Ng and M. Baer (Wiley, New York, 1992) pp. 1–176.
- [6] G. Werth, V. N. Gheorghe, and F. G. Major, *Springer Series on Atomic, Optical, and Plasma Physics* (2009), 10.1007/978-3-540-92261-2.
- [7] D. J. Griffiths, *Elektrodynamik : Eine Einführung* (Pearson Studium, München, 2011).
- [8] W. Paul and H. Steinwedel, *Zeitschrift für Naturforschung A* **8** (1953), 10.1515/zna-1953-0710.
- [9] J. H. Block, *Berichte der Bunsengesellschaft für physikalische Chemie* **81**, 777–777 (1977).
- [10] K. Fritzsche, (2013), 10.1007/978-3-642-37495-1.
- [11] W. H. Press, S. A. Teukolsky, W. T. Vetterling, and B. P. Flannery, “Numerical recipes in c: The art of scientific computing. second edition,” (1992).
- [12] Willers, *ZAMM - Zeitschrift für Angewandte Mathematik und Mechanik* **22**, 174–175 (1942).

- [13] C. Hägg and I. Szabo, International Journal of Mass Spectrometry and Ion Processes **73**, 277–294 (1986).
- [14] J. D. Jackson, *Classical Electrodynamics* (WileyRef, 1998).
- [15] A. Reuben, G. Smith, P. Moses, A. Vagov, M. Woods, D. Gordon, and R. Munn, International Journal of Mass Spectrometry and Ion Processes **154**, 43–59 (1996).
- [16] R. J. LeVeque, (2007), 10.1137/1.9780898717839.
- [17] A. C. Polycarpou, Synthesis Lectures on Computational Electromagnetics **1**, 1–126 (2006).
- [18] J. T. Katsikadelis, *Boundary elements : theory and applications*, 1st ed. (Elsevier, New York [u.a.], 2002) includes bibliographical references and index.
- [19] W. Ang, *A Beginner's Course in Boundary Element Methods* (Universal Publishers, 2007).
- [20] G. B. Folland, *Introduction to partial differential equations*, 2nd ed. (Princeton Univ. Press, Princeton, NJ, 1995).
- [21] C. Geuzaine and J.-F. Remacle, International Journal for Numerical Methods in Engineering **79**, 1309–1331 (2009).
- [22] W. Śmigaj, T. Betcke, S. Arridge, J. Phillips, and M. Schweiger, ACM Trans. Math. Softw. **41**, 6:1 (2015).
- [23] D. Cubric, B. Lencova, F. Read, and J. Zlamal, Nuclear Instruments and Methods in Physics Research Section A: Accelerators, Spectrometers, Detectors and Associated Equipment **427**, 357–362 (1999).
- [24] N. N. Lebedev, *Special functions and their applications*, 1st ed., edited by R. A. U. Silverman, Dover books on mathematics (Dover, New York, NY, 1972).
- [25] D. J. Douglas, T. A. Glebova, N. V. Konenkov, and M. Y. Sudakov, Technical Physics **44**, 1215–1219 (1999).
- [26] D. J. Douglas and N. V. Konenkov, Rapid Communications in Mass Spectrometry **16**, 1425–1431 (2002).
- [27] D. R. Denison, Journal of Vacuum Science and Technology **8**, 266 (1971).
- [28] G. Lee-Whiting and L. Yamazaki, Nuclear Instruments and Methods **94**, 319–332 (1971).

- [29] I. E. Dayton, F. C. Shoemaker, and R. F. Mozley, *Review of Scientific Instruments* **25**, 485 (1954).
- [30] S. Fanghänel, O. Asvany, and S. Schlemmer, *Journal of Molecular Spectroscopy* (2016), 10.1016/j.jms.2016.12.003.
- [31] D. Gerlich and S. Decker, *Applied Physics B* **114**, 257–266 (2013).
- [32] D. Gerlich and S. Decker, *Applied Physics B* **114**, 257–266 (2013).
- [33] S. Schlemmer, J. Illemaann, S. Wellert, and D. Gerlich, *Journal of Applied Physics* **90**, 5410 (2001).
- [34] S. Schlemmer, S. Wellert, F. Windisch, M. Grimm, S. Barth, and D. Gerlich, *Applied Physics A: Materials Science & Processing* **78**, 629–636 (2004).
- [35] M. Grimm, B. Langer, S. Schlemmer, T. Lischke, U. Becker, W. Widdra, D. Gerlich, R. Flesch, and E. Rühl, *Physical Review Letters* **96** (2006), 10.1103/physrevlett.96.066801.
- [36] T. K. Esser and K. R. Asmis, Private communication.
- [37] C. R. Howder, D. M. Bell, and S. L. Anderson, *Review of Scientific Instruments* **85**, 014104 (2014).
- [38] C. R. Howder, B. A. Long, D. M. Bell, and S. L. Anderson, *The Journal of Physical Chemistry C* **119**, 14561–14570 (2015).
- [39] D. Gerlich, *Physica Scripta* **1995**, 256 (1995).
- [40] D. Gerlich and S. Horning, *Chem. Rev.* **92**, 1509 (1992).
- [41] W. Paul, B. Lücke, S. Schlemmer, and D. Gerlich, *J. Mass Spectrom. Ion Processes* **150**, 373 (1995).
- [42] O. Asvany, I. Savić, S. Schlemmer, and D. Gerlich, *Chem. Phys.* **298**, 97 (2004).
- [43] O. Asvany, S. Schlemmer, and D. Gerlich, *Astrophys. J.* **617**, 658 (2004).
- [44] J. Mikosch, R. Otto, S. Trippel, C. Eichhorn, M. Weidemüller, and R. Wester, *The Journal of Physical Chemistry A* **112**, 10448 (2008).
- [45] L. Kluge, S. Gärtner, S. Brünken, O. Asvany, D. Gerlich, and S. Schlemmer, *Phil. Trans. Roy. Soc. A* **370**, 5041 (2012).
- [46] I. Zymak, M. Hejduk, D. Mulin, R. Plašil, J. Glosík, and D. Gerlich, *Astrophys. J.* **768**, 86 (2013).

- [47] S. Schlemmer, T. Kuhn, E. Lescop, and D. Gerlich, *Int. J. Mass Spectrom.* **185**, 589 (1999).
- [48] S. Schlemmer, E. Lescop, J. v. Richthofen, and D. Gerlich, *J. Chem. Phys.* **117**, 2068 (2002).
- [49] Y.-S. Wang, C.-H. Tsai, Y. T. Lee, H.-C. Chang, J. C. Jiang, O. Asvany, S. Schlemmer, and D. Gerlich, *J. Phys. Chem. A* **107**, 4217 (2003).
- [50] J. Mikosch, H. Kreckel, R. Wester, R. Plašil, J. Glosík, D. Gerlich, D. Schwalm, and A. Wolf, *J. Chem. Phys.* **121**, 11030 (2004).
- [51] O. Asvany, H. S. P. Müller, O. Ricken, M. C. Wiedner, T. Giesen, and S. Schlemmer, in *Contribution RB10, 63rd International Symposium on Molecular Spectroscopy, Columbus, OH, USA* (2008).
- [52] O. Asvany, E. Hugo, F. Müller, F. Kühnemann, S. Schiller, J. Tennyson, and S. Schlemmer, *J. Chem. Phys.* **127**, 154317 (2007).
- [53] O. Asvany, K. M. T. Yamada, S. Brünken, A. Potapov, and S. Schlemmer, *Science* **347**, 1346 (2015).
- [54] P. Jusko, O. Asvany, A.-C. Wallerstein, S. Brünken, and S. Schlemmer, *Phys. Rev. Lett.* **112**, 253005 (2014).
- [55] E. K. Campbell, M. Holz, D. Gerlich, and J. P. Maier, *Nature* **523**, 322–323 (2015).
- [56] S. Lee, D. Hauser, O. Lakhmanskaya, S. Spieler, E. S. Endres, K. Geistlinger, S. S. Kumar, and R. Wester, *Phys. Rev. A* **93**, 032513 (2016).
- [57] A. V. Zabuga, M. Z. Kamrath, O. V. Boyarkin, and T. R. Rizzo, *The Journal of Chemical Physics* **141**, 154309 (2014).
- [58] S. Trippel, J. Mikosch, R. Berhane, R. Otto, M. Weidemüller, and R. Wester, *Phys. Rev. Lett.* **97**, 193003 (2006).
- [59] O. Asvany and S. Schlemmer, *Int. J. Mass Spectrom.* **279**, 147 (2009).
- [60] R. Otto, A. von Zastrow, T. Best, and R. Wester, *Phys. Chem. Chem. Phys.* **15**, 612 (2013).
- [61] E. Haufler, *Niederenergetische Elektronen- und Protonen-Transfer Prozesse*, Ph.D. thesis, TU Chemnitz (1996), <https://www.tu-chemnitz.de/physik/ION/Publications/Doktorarbeiten.html>.
- [62] R. Otto, P. Hlavenka, S. Trippel, J. Mikosch, K. Singer, M. Weidemüller, and R. Wester, *Journal of Physics B: Atomic, Molecular and Optical Physics* **42**, 154007 (2009).

- [63] J. Jašík, J. Žabka, J. Roithová, and D. Gerlich, *International Journal of Mass Spectrometry* **354-355**, 204–210 (2013).
- [64] J. Walz, I. Siemers, M. Schubert, W. Neuhauser, R. Blatt, and E. Teloy, *Physical Review A* **50**, 4122–4132 (1994).
- [65] E. S. Weibel and G. L. Clark, *Journal of Nuclear Energy. Part C, Plasma Physics, Accelerators, Thermonuclear Research* **2**, 112–116 (1961).
- [66] L. S. Cutler, C. A. Flory, R. P. Giffard, and M. D. McGuire, *Applied Physics B Photophysics and Laser Chemistry* **39**, 251–259 (1986).
- [67] D. H. E. Dubin and T. M. O’Neil, *Reviews of Modern Physics* **71**, 87–172 (1999).
- [68] C. Champenois, *Journal of Physics B: Atomic, Molecular and Optical Physics* **42**, 154002 (2009).
- [69] Sven, *Pulshoehenverteilungen eines empfindlichen Ionendetektors*, Ph.D. thesis, Universität zu Köln (2012).
- [70] A. Sorgenfrei, *Ion-Molekül-Reaktionen kleiner Kohlenwasserstoffe in einem gekühlten Ionen-Speicher*, Ph.D. thesis, University of Freiburg, Germany (1994).
- [71] O. Asvany, F. Biellau, D. Moratschke, J. Krause, and S. Schlemmer, *Rev. Sci. Instr.* **81**, 076102 (2010).
- [72] S. Schlemmer and O. Asvany, in *J. Phys. Conf. Ser.*, Vol. 4 (2005) pp. 134–141.
- [73] S. Gärtner, *Charakterisierung einer Ionenwolke in einem kalten 22-Pol Ionen-speicher*, Master’s thesis, University of Cologne (2009).
- [74] K. G. Weil, *Nachrichten aus Chemie, Technik und Laboratorium* **44**, 1110–1110 (2010).
- [75] Sabrina, *Influence of Internal States on Ion-Molecule Reactions in a Temperature Variable 22-Pole Ion Trap*, Ph.D. thesis, University of Cologne (2014).
- [76] V. Baglin, in *CERN Accelerator School, vacuum in accelerators*, Platja d’Aro, Spain, 16-24 May 2006 (2006) pp. 351–367.
- [77] J. B. Marquette, C. Rebrion, and B. R. Rowe, *The Journal of Chemical Physics* **89**, 2041 (1988), <http://dx.doi.org/10.1063/1.455101>.
- [78] O. Asvany, S. Brünken, L. Kluge, and S. Schlemmer, *Appl. Phys. B* **114**, 203 (2014).

- [79] J. M. Brown, T. D. Varberg, K. M. Evenson, and A. L. Cooksy, **428**, L37 (1994).
- [80] C. P. Endres, S. Schlemmer, P. Schilke, J. Stutzki, and H. S. Müller, Journal of Molecular Spectroscopy **327**, 95 (2016), new Visions of Spectroscopic Databases, Volume II.
- [81] H. S. Müller, F. Schlöder, J. Stutzki, and G. Winnewisser, Journal of Molecular Structure **742**, 215 (2005), mOLECULAR SPECTROSCOPY AND STRUCTURE.
- [82] U. Wilhelmsson and G. Nyman, The Journal of Chemical Physics **96**, 1886 (1992), <http://dx.doi.org/10.1063/1.462089> .
- [83] C. L. Russell and D. E. Manolopoulos, The Journal of Chemical Physics **110**, 177 (1999), <https://doi.org/10.1063/1.478093> .
- [84] D. Gerlich, J. Chem. Soc. Faraday Trans. **89**, 2199 (1993).
- [85] T. Möller, I. Bernst, D. Panoglou, D. Muders, V. Ossenkopf, M. Röllig, and P. Schilke, “MAGIX: Modeling and Analysis Generic Interface for eXternal numerical codes,” Astrophysics Source Code Library (2013), ascl:1303.009 .
- [86] J. Gerke, *Production and Characterization of para-Hydrogen*, Master’s thesis, Universität zu Köln (2012).
- [87] E. Herbst and W. Klemperer, **185**, 505 (1973).
- [88] D. Smith, N. G. Adams, and W. Lindinger, The Journal of Chemical Physics **75**, 3365 (1981), <http://dx.doi.org/10.1063/1.442498> .
- [89] J. K. Kim, L. P. Theard, and W. T. H. Jr., The Journal of Chemical Physics **62**, 45 (1975), <http://aip.scitation.org/doi/pdf/10.1063/1.430236> .
- [90] F. C. Fehsenfeld, W. Lindinger, A. L. Schmeltekopf, D. L. Albritton, and E. E. Ferguson, The Journal of Chemical Physics **62**, 2001 (1975), <http://dx.doi.org/10.1063/1.430655> .
- [91] D. Smith and N. G. Adams, Monthly Notices of the Royal Astronomical Society **197**, 377 (1981).
- [92] J. A. Luine and G. H. Dunn, The Astrophysical Journal **299**, L67 (1985).
- [93] H. Böhringer, Chemical Physics Letters **122**, 185 (1985).
- [94] E. Herbst, D. J. DeFrees, D. Talbi, F. Pauzat, W. Koch, and A. D. McLean, The Journal of Chemical Physics **94**, 7842 (1991), <http://dx.doi.org/10.1063/1.460119> .

-
- [95] D. Smith and N. G. Adams, International Journal of Mass Spectrometry and Ion Processes **23**, 123 (1977).
- [96] O. Asvany, *Experiments with Ions and Clusters in a variable temperature 22-pole ion trap*, Ph.D. thesis, TU Chemnitz (2003).
- [97] W. Paul, B. Lücke, S. Schlemmer, and D. Gerlich, International Journal of Mass Spectrometry and Ion Processes **149**, 373 (1995), honour Biography David Smith.
- [98] D. Gerlich and G. Kaefer, The Astrophysical Journal **347**, 849 (1989).
- [99] C. Konietzko, “Bau und test eines piezoventils für einen gepulsten gaseinlass,” Bachelor Thesis.
- [100] K. M. Ervin and P. B. Armentrout, The Journal of Chemical Physics **83**, 166–189 (1985).
- [101] P. Tosi, O. Dmitrijev, Y. Soldo, D. Bassi, D. Cappelletti, F. Pirani, and V. Aquilanti, The Journal of Chemical Physics **99**, 985–1003 (1993).
- [102] D. Bedford and D. Smith, International Journal of Mass Spectrometry and Ion Processes **98**, 179–190 (1990).
- [103] P. Jusko, A. Stoffels, S. Thorwirth, S. Brünken, S. Schlemmer, and O. Asvany, J. Mol. Spectrosc. (2016), this volume.
- [104] N. R. Daly, Review of Scientific Instruments **31**, 264–267 (1960).
- [105] K. Janek, *Ionen-Molekül-Reaktionen in einem temperaturvariablen 22-Pol Ionen-speicher*, Master’s thesis, Universität zu Köln (2016).
- [106] M. T. Bowers, D. D. Elleman, and J. King, The Journal of Chemical Physics **50**, 1840–1845 (1969).
- [107] M. Tichý, A. Rakshit, D. Lister, N. Twiddy, N. Adams, and D. Smith, International Journal of Mass Spectrometry and Ion Physics **29**, 231–247 (1979).
- [108] M. Schwarzer, A. Hansel, W. Freysinger, N. Oberhofer, W. Lindinger, and E. E. Ferguson, The Journal of Chemical Physics **95**, 7344–7347 (1991).
- [109] R. H. Schultz and P. B. Armentrout, The Journal of Chemical Physics **96**, 1036–1045 (1992).
- [110] R. D. Levine, *Molecular Reaction Dynamics*: (Cambridge University Press, Cambridge, 2005).
- [111] T. N. Olney, N. Cann, G. Cooper, and C. Brion, Chemical Physics **223**, 59–98 (1997).

-
- [112] R. P. Clow and J. H. Futrell, International Journal of Mass Spectrometry and Ion Physics **8**, 119–142 (1972).
- [113] C. F. Giese and W. B. Maier, The Journal of Chemical Physics **39**, 739–748 (1963).
- [114] F. C. Fehsenfeld, A. L. Schmeltekopf, and E. E. Ferguson, The Journal of Chemical Physics **46**, 2802–2808 (1967).
- [115] J. F. von Richthofen, *Untersuchung der Bildung, des Isotopenaustausches und der Isomerisierung des Ionensystems HCO^+ / HOC^+* , Ph.D. thesis, Technische Universität Chemnitz (2002).
- [116] D. Gerlich, The Journal of Chemical Physics **90**, 3574 (1989), <http://dx.doi.org/10.1063/1.455816> .

Appendix A

Appendix

A.1 Approximation of Hyperbolic Shaped Electrodes

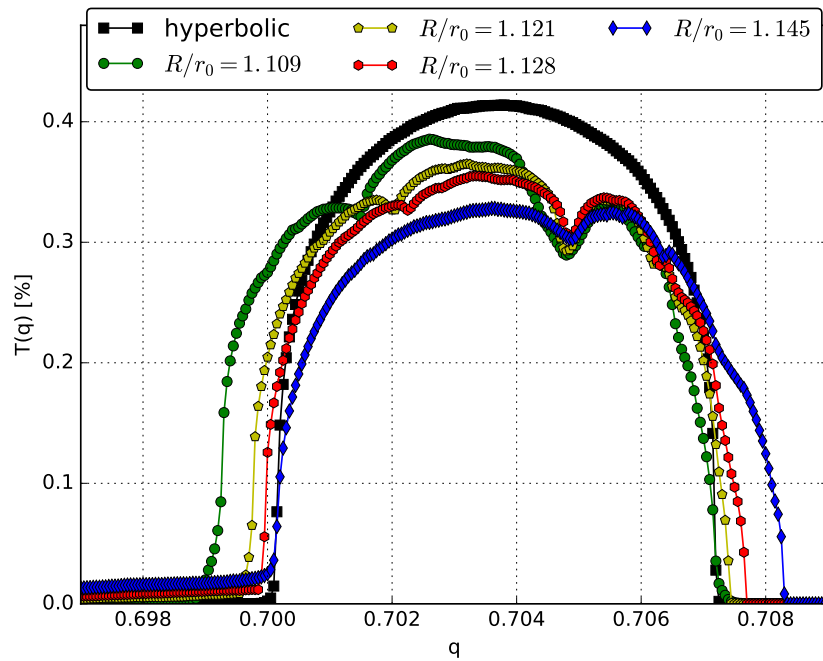
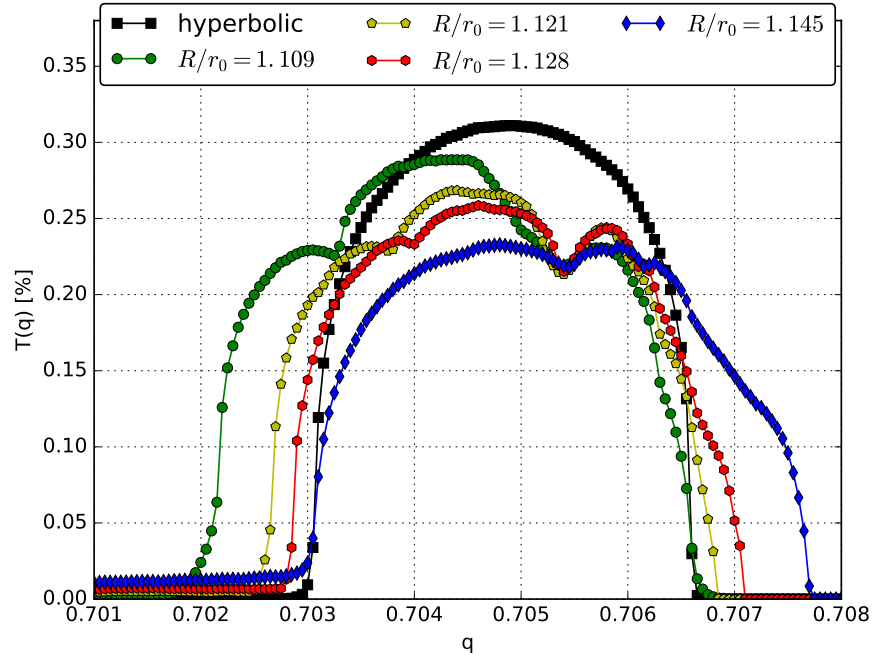
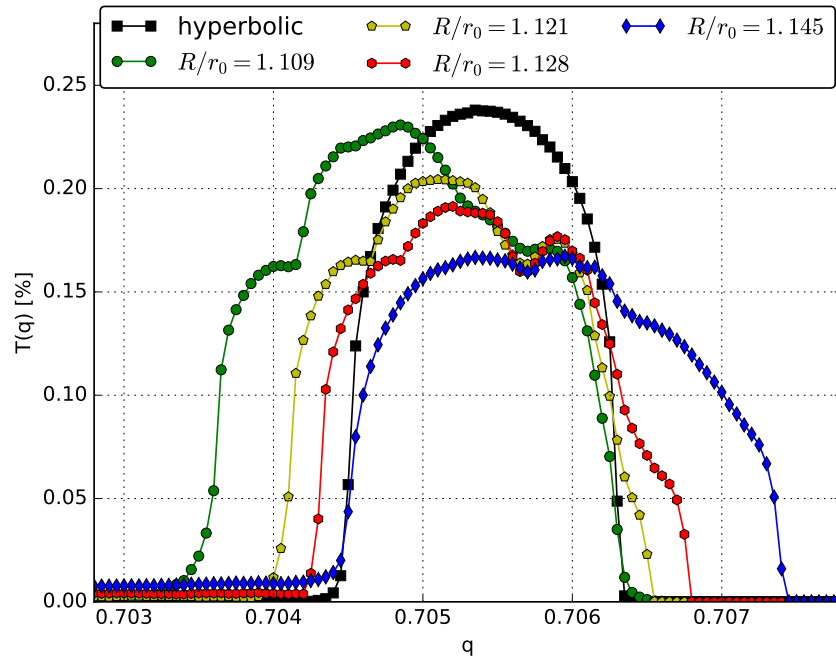


Figure A.1: The plot shows transmission curves $T(q)$ for $M = 100$

Figure A.2: The plot shows transmission curves $T(q)$ for $M = 200$ Figure A.3: The plot shows transmission curves $T(q)$ for $M = 400$

A.2 Space Charge Effects

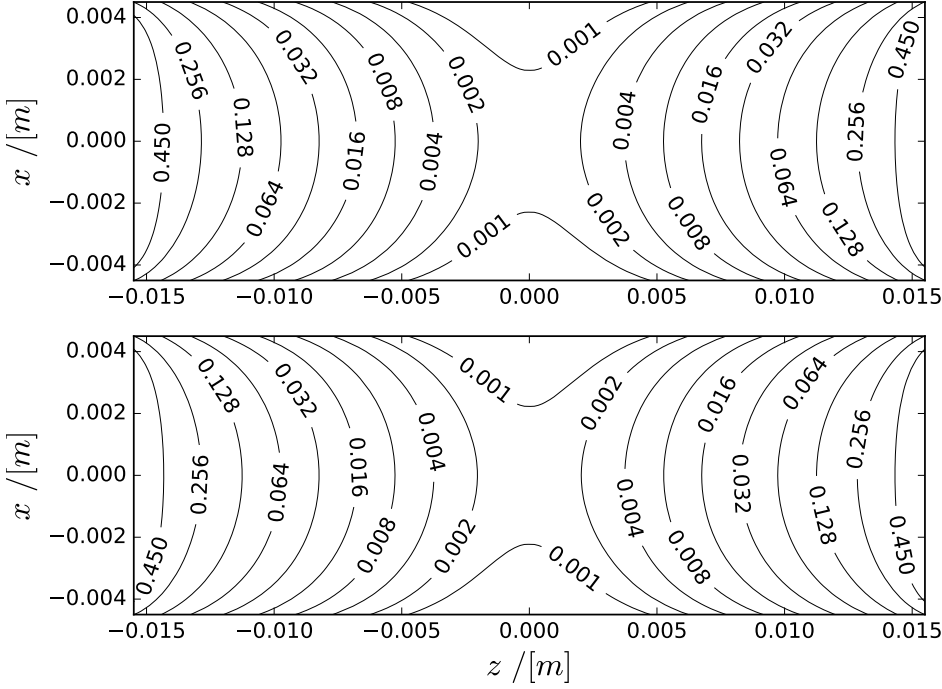


Figure A.4: The upper plot shows the full numerical solution for Φ_{st} . The lower plot shows the potential Φ_{st} fitted using Eq. 5.21. The applied voltage at entrance (SE) and exit (SA) electrodes are $V_{dc,SE} = V_{dc,SA} = 1$ V.

A.3 Tests to Improve the LIRtrap Setup

A.3.1 The Stability of Guiding and Trapping the Ions

For the quantitative analysis of a measurement one has to assume that the number of trapped ions is normal distributed at a certain storage time. This is caused by the fact that each measured point is recorded individually. The first problem was observed by having a closer look at the number of counted ions. Here, periodic instabilities were observed. Such problems were also reported by S. Gärtner. Measurements using a time of flight multichannel analyzer¹ have shown, that these periodic instabilities or fluctuations occur more significantly for higher mass resolution of the first QMF. The fluctuations appear with a frequency of around 50 Hz. It was revealed, that this periodic instabilities arose from the supplied heating voltage for the tubes of the rf-frequency generator of the first QMF. This tubes are responsible for the amplification of the rf-amplitude which guides the ions through the first

¹FAST ComTec MCA

QMF. It has been shown that the heating voltage for the tubes was supplied by a AC-voltage with a frequency of 50 Hz. After switching to a DC-voltage, the periodic instabilities in the number of counted ions could be reduced significantly. Next, the stability of trapping the ions was investigated. Figure A.5 shows a measurement of the reaction of N^+ with hydrogen at four different trapping times for 400 iteration. As can be seen the number of ions is nearly normal distributed. This figure also shows what happens if the number of iterations is chosen too small. The variance keeps almost the same for both cases, but the mean value can slightly shift. The variance is in the range of 1-1.6 of the square root of the number of counted ions. This also shows that statistical deviations can influence the results if the number of iterations for each measured point is chosen too small.

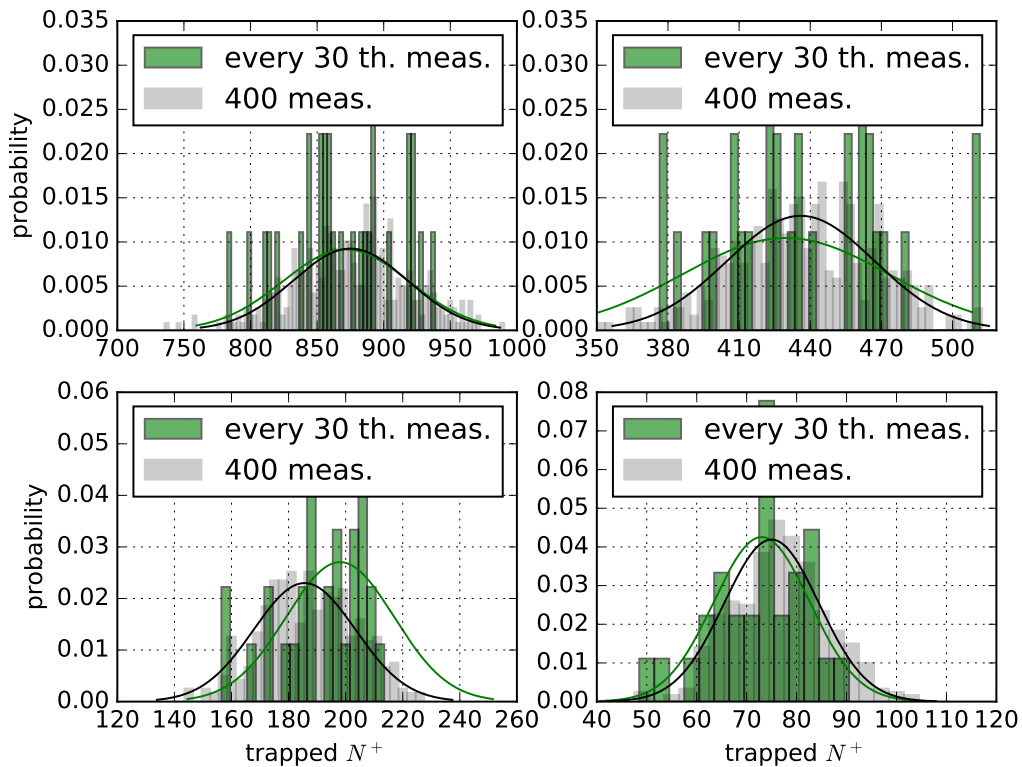


Figure A.5: The plots show a typical measurement of the reaction of N^+ with hydrogen at four different trapping times for 400 iterations. The black histogram shows the measurement for all 400 iterations. The black solid line indicates the fitted normal distribution. The green histogram shows the measurement for every 30 th. measurement and the green solid line indicates the corresponding fitted normal distribution. The mean and the variance for all 400 iteration are respectively 874.9 ± 43.2 , 436.0 ± 31.1 , 185.6 ± 17.8 and 75.0 ± 9.5 ion counts.

A.3.2 Saturation Effects of the Ion Detection System

A Daly detector^[104] in combination with a photomultiplier²(PMT) was used for the detection of the ions. Here, positively charged ions are accelerated by a high voltage (≈ 40 kV) against a aluminum surface and are converted by impact into electrons. These electrons are accelerated in the opposite direction onto a scintillator, where the produced photons are amplified by a PMT and converted in a voltage pulse. A discriminator³ is used to convert the PMT-signal above a certain threshold level into a NIM-pulse (see Fig. A.6) which can be counted by a counter⁴. A detailed description of such an ion detection system can be found in the Staatsexamensarbeit of Fanghänel [69]. This technique allows to count each single ion.

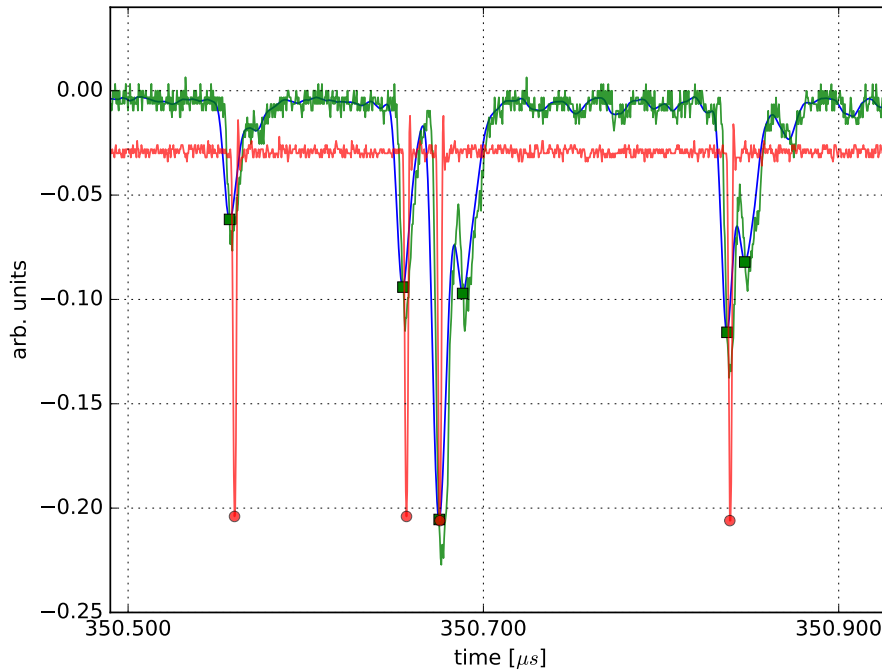


Figure A.6: The plot shows the PMT signal (green) and the answer signal of the discriminator (red). The blue line indicates the smoothed PMT-signal which was used to identify the signal numerically. The red circles and green squares indicate the counted discriminator and PMT signals. Clearly visible is, that not every single PMT-pulse can be identified by the discriminator as an ion. Such saturation effects appear, if too much ions arrive the detector within a small time interval.

A precise ion counting requires that each 'PMT-ion signal' is identified by the discriminator as an ion or in other words that one has a one-to-one correlation between the PMT-signal and the discriminator signal. To investigate this relation, the second output of the discriminator which provides the amplified original PMT-signal and the final output-signal of the discriminator were recorded by an oscilloscope⁵. From

²HAMAMATSU R647-01

³Philips Scientific 300 MHz Discriminator Model 6904

⁴Ortec 994 Dual Counter and Timer

⁵LECROY WAVERUNNER 64XI

this the individual signals were compared to each other (Fig. A.6). The measurements were performed using N^+ ions in the trapping modus (80 ms storage time) for different temperatures and trapping voltages⁶. To get the ions out of the trap, the exit lens voltage has to be lowered to accelerate the ions into the second QMF. In order to reduce saturation effects of the detector (very rapid sequentially arriving ion signals can not be separated by the PMT or the discriminator, see Fig. A.6) the entrance lens voltage was heightened and the exit lens voltage was lowered as a function of time to spread the ion cloud. This symmetrical lowering and heightening of the voltage as a function of the time will be called ramp-time (RT) in the following. As can be seen in Fig. 6.4 the more ions are trapped and the faster the ramp-time (RT) is, saturation effects of the detection system become more and more relevant. Therefore, the ramp-time should be chosen as small as possible. On the other hand, if the used time constant for ramping the voltages at the exit and entrance lenses is too slow, some ions will get lost due to the extraction process out of the trap. Figure A.7 shows the relation between PMT-signals and discriminator-signals as a function of the temperature and the trapping voltage. The variation of these parameters has no influence on the saturation effects. Figure 6.4 and A.7 show that with less than ≈ 1200 trapped ions saturation effects are negligibly small. To illustrate the influence of saturation effects on the time evolution of chemical reactions, the relation between detected ions (PMT-signals) and discriminator-signals was modeled and included in an ideal reaction system (see e.g. Eq. 6.2). Since one has an upper limit of the detection efficiency⁷ the relation between detected ions (PMT-signals) N_{PMT} and discriminator-signals N_{discr} can be modeled in first order as follows:

$$N_{discr}(N_{PMT}) = N_{max} \cdot (1 - e^{-N_{PMT} \cdot c}) \approx N_{max} \cdot c \cdot N_{PMT} + O(N_{PMT}^2) \quad (A.1)$$

where N_{max} is the maximum number of detectable ions at the discriminator in a certain time interval and $c \leq N_{max}^{-1}$ is a ramp-time specific constant. Figure A.8 illustrates the influence of the saturation for the reaction system (Eq. 6.2) for a ramp-time of $6 \text{ mV}/\mu\text{s}$ and 2000 ions at $t = 0$ in comparison to an ideal detection. It can be seen that in contrast to an ideal detection the total number of counts is not a constant. Since the detection efficiency decreases with the number of stored ions a small bump in the total number of ions occurs (see zoom right plot Fig. A.8). This is exactly what we have observed in previous measurements (Bachelor Thesis J.Klaus [105]).

⁶The trapping voltage denotes the relative voltage between the floating voltage of the trap itself and the voltages applied to the exit and entrance lenses.

⁷The number of counted ions in a certain time interval is limited by the dead time of the PMT and the width of the NIM-pulse of the discriminator.

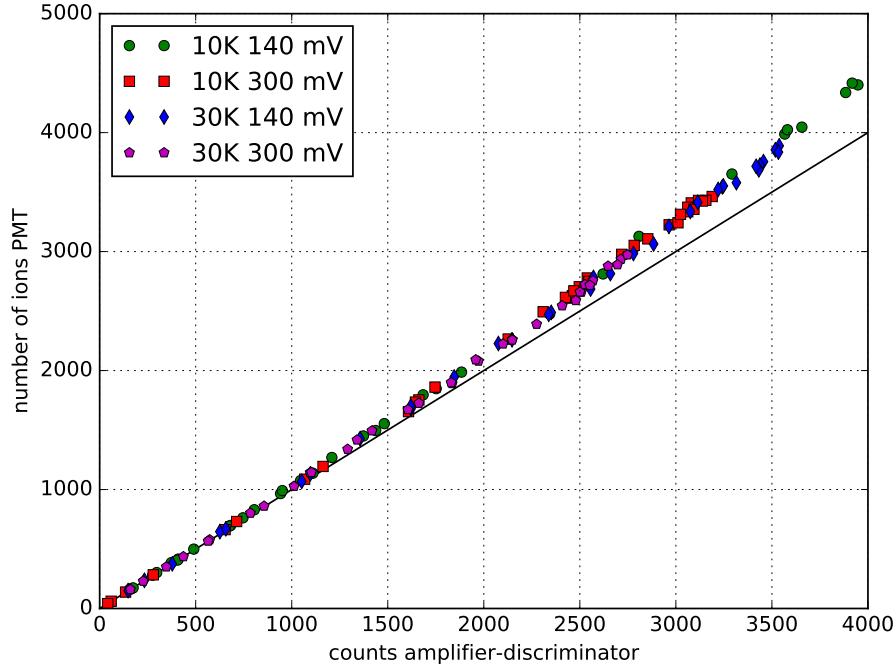


Figure A.7: The plot shows the relation between detected N^+ ions (PMT-signals) and discriminator-signals as a function of the temperature and the relative trapping voltage. The black solid line indicates a perfect one-to-one relation.

An important consequence of saturation effects is that the determined rates of the time evolution are always smaller than the real rate of the reaction. Take as an example: for a ramp-time of $6 \text{ mV}/\mu\text{s}$ and 1500 ions at $t = t_{\min}$, where t_{\min} is the shortest storage time of the ions which is usually about 15 ms, the determined rate is 2% smaller than the real one. A plot of the relative change in the rates in dependence of the ramp-time and the number of stored ions at t_{\min} is shown in Fig. A.9.

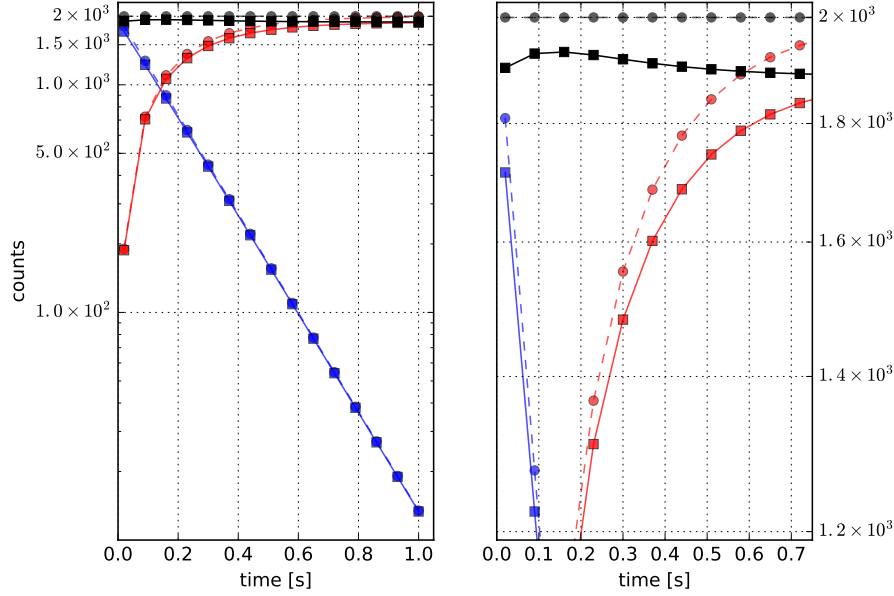


Figure A.8: The plots illustrate the influence of the saturation effects (solid lines and squares) for a general reaction system (see eq. 6.2) for a ramp-time of $6 \text{ mV}/\mu\text{s}$ and 2000 primary ions at $t = 0$ in comparison to an ideal detection (dashed lines and circles).

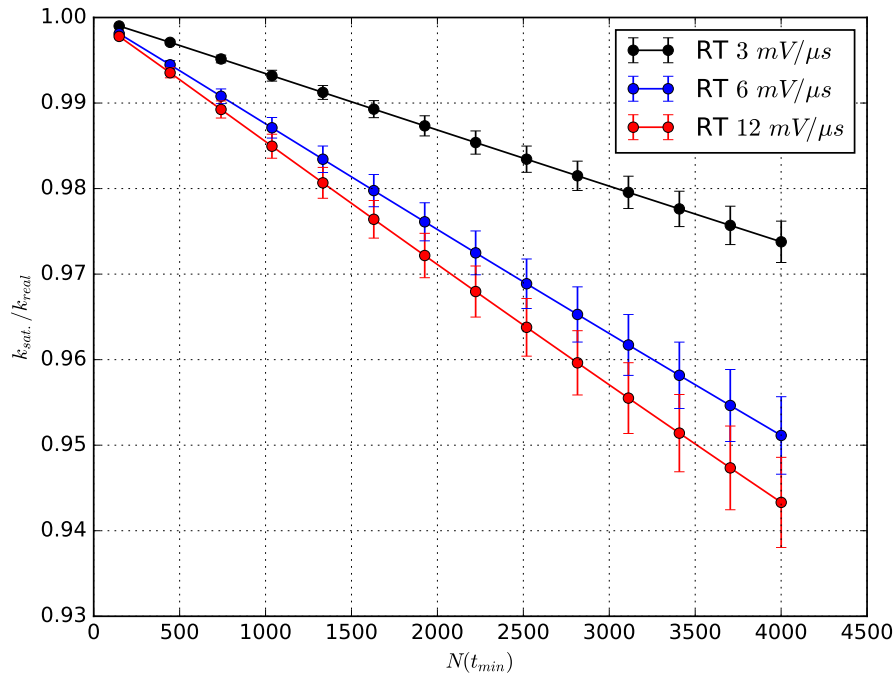
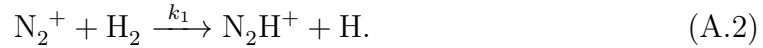


Figure A.9: The plot shows the relative change in the rates $k_{sat.}/k_{real}$ in dependence of the ramp-time and the number of stored ions at t_{min} .

A.3.3 Temperature Behavior of the Reaction Gas Calibration and the $N_2^+ + H_2$ Reaction

Since the number density of the neutral reaction gas is necessary to determine rate coefficients, also their calibration as a function of the temperature was tested (Eq. 6.1). Therefore, an exothermic reaction where the rate coefficient is expected to be independent from the temperature was used. For such a reaction the Arrhenius-curve is a constant.

Please note: From this only the temperature behavior of the calibration can be investigated. To verify also the correctness of the absolute number density⁸ the rate coefficient for the reaction has to be known very precisely from other experiments as a function of the temperature. To test the temperature behavior, the following Charge-Transfer-Reaction



was used.

This ion-molecule reaction was only studied up to now at room temperature by several authors [106–109]. They determined a rate coefficient in the range from $(1.4 - 2.0) \cdot 10^{-9} cm^3/s^{-1}$. From calculations of the reaction enthalpy one derives a value of $\Delta H_{reaction}^0 = -2.53$ eV and -2.55 eV for $T = 0$ K and $T = 298$ K under a standard state pressure $p = 0.1$ MPa. Table A.1 shows the used values for the calculation of reaction enthalpy of N_2^+ ions with H_2 to N_2H^+ and H . The values are taken from the KIDA data base⁹ [a] and from the NIST-JANAF Thermochemical Tables¹⁰ [b]. This calculation supports the assumption of an exothermic reaction and allows to use this reaction to verify the temperature behavior of the calibration for the number density.

temperature [K]	$\Delta H_{f,N_2^+}^0$	$\Delta H_{f,H_2}^0$	$\Delta H_{f,N_2H^+}^0$	$\Delta H_{f,H}^0$
0	1503.303 [b]	0 [b]	1042.75 [a]	216.035 [b]
298	1509.499 [b]	0 [b]	1045.33 [a]	217.999 [b]

Table A.1: Used values for the calculation of reaction enthalpy of N_2^+ ions with H_2 to N_2H^+ ions with H in kJ/mol.

The Langevin capture model^[110] was used in order to calculate a theoretic value for the rate coefficient of reaction A.2. The interaction between two colliding particles is described by the ion-induced dipole interaction which is proportional to $1/r^4$ (r is the distance of the two particles), the charge e and the isotropic polarizability α of the neutral collision partner. The Langevin collision rate coefficient k_L can be

⁸The calibration is not correct, the factor f_{cal} (Eq. 6.1) can have a shift which will lead to a 'global' offset of the number density!

⁹<http://kida.obs.u-bordeaux1.fr/>

¹⁰<http://kinetics.nist.gov/janaf/>

calculated as follows

$$k_L = \frac{e}{2\epsilon_0} \sqrt{\frac{\alpha}{\mu}}. \quad (\text{A.3})$$

where μ denotes the reduced mass of the colliding particles. For $\alpha = 0.787 \text{ \AA}^3$ ^[111] this leads to $k_L = 1.52 \cdot 10^{-9} \text{ m}^3/\text{s}^{-1}$. This theoretical value is in the same range as the experimental values at 300K.

Surprisingly, measurements using only the residual gas for the ionization in the ion source show a significant number of ions at mass 28 [amu], which will react to mass 29 [amu] in the presence of H_2 in the trap. As can be seen in Fig. A.10 (solid lines), measurements using additional N_2 in the ion source show further reaction channels to mass 2 and 3 [amu]. Schultz and Armentrout [109] reported that the reaction of $\text{N}_2^+ + \text{H}_2$ can lead to the products $\text{H}_2^+ + \text{N}_2$ with a branching ratio of 0.01. From this the reaction channel $\text{H}_2^+ + \text{H}_2$ to $\text{H}_3^+ + \text{H}$ with a rate coefficient of $k = 2.0 \cdot 10^{-9} \text{ cm}^3/\text{s}^{-1}$ ^[112,113] (at 300 K) is accessible. Due to the fact that the number of ions at mass 3 [amu] becomes constant after all ions at mass 2 [amu] disappeared, it seems obvious that the following reactions



have to be taken into account. Since in both measurements (with/without N_2 in the source) the same number of ions was trapped but different reaction channels could be observed, one can suggest that two different ions species at mass 28 [amu] are present in the ion source¹¹. One possible candidate, which reacts with H_2 is the CO^+ ion. Since the rate of this reaction $k = 2.0 \cdot 10^{-9} \text{ cm}^3/\text{s}^{-1}$ ^[114] is in the same order as the reaction of N_2^+ with H_2 it is difficult to confirm this assumption.

¹¹To ensure that roughly the same number of ions at mass 28 [aum] is stored using additional N_2 gas in the ion-source, only the potentials applied to the electrodes for guiding the ions into the 22-pole were adjusted.

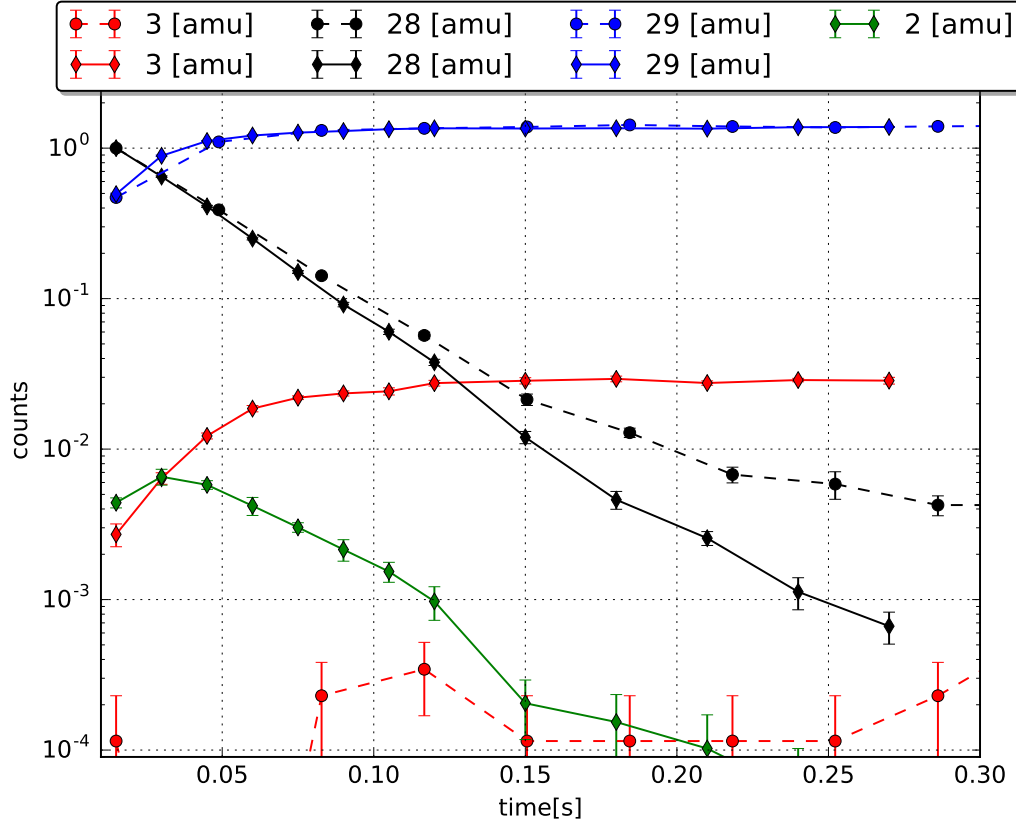


Figure A.10: Time evolution of the reaction of ions at mass 28 [amu] with H_2 at a temperature of 21 K and a H_2 pressure of $2.06 \cdot 10^{-7}$ [mBar]. The dashed lines show the reaction without N_2 inside the ion source. The solid lines show the same reaction with N_2 in the ion source. The difference in pressure measured at the ion gauge at the first quadrupole between both measurements is $5.8 \cdot 10^{-9}$ [mBar]

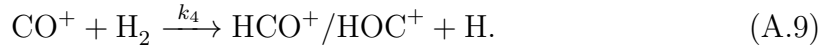
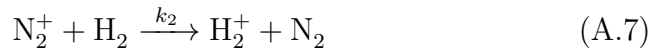
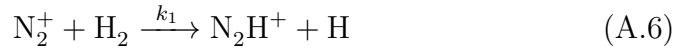
From the ratio of the number of H_3^+ ions at maximum storage time for both cases (see Fig. A.10) one can estimate roughly a ratio of $\text{N}_2^+ / (\text{CO}^+ + \text{N}_2^+) \approx 0.01$. In order to clarify the root of this possible contamination of the ion source with CO, different test were performed.

1. A leak detector¹² was connected to the machine to exclude the contamination due to a small leak in the apparatus.
2. A residual gas mass scan with and without N_2 in the source was measured for different ionization energies.

The leak test has shown, that there was no measurable leak in the apparatus. Assuming a natural abundance of isotopes of CO^+ and N_2^+ at mass 28 [amu] and mass 30 [amu], a ratio of $\text{N}_2^+ / (\text{CO}^+ + \text{N}_2^+) \approx 0.04$ N_2^+ in the source could be estimated as a consequence of the second test. From the ratio of mass 14 [amu] N^+ to mass 28 [amu] (CO^+ and N_2^+) a ratio of $\text{N}_2^+ / (\text{CO}^+ + \text{N}_2^+) \approx 0.03$ could be derived. Since we

¹²Pfeiffer Adixen ASM 380 Helium Leak Detector

do not see any ions at mass 32 [amu] (O_2^+), the oxygen forming CO^+ could come from the water molecules inside the ion-source, which is one of the most dominant species in the residual-gas mass spectrum. Furthermore, deposits from old experiments with methane e.g. CH_5^+ or one broken filament in the ion-source can lead to reactions to CO^+ in the ion-source. It is also entirely possible that the amount of carbon is caused by the stainless steel parts of the ion-source, because of its high temperature. A complete reaction scheme including all mentioned reaction channels looks as follows:



$\text{HCO}^+/\text{HOC}^+$ indicates that both isomers can be formed within this reaction. Since both isomers have the same mass, it is not possible to distinguish between them. The difference in the proton affinity of HCO^+ and HOC^+ in connection with the reaction of $\text{HOC}^+ + \text{CH}_4 \longrightarrow \text{CH}_5^+ + \text{CO}$ can be used to distinguish between both isomers^[115]. Using $f \cdot \text{M}^+$ as the number of N_2^+ ions and $(1 - f) \cdot \text{M}^+$ as the number of CO^+ ions where $f = \text{N}_2^+ / (\text{CO}^+ + \text{N}_2^+)$ denotes the fraction of N_2^+ ions, the corresponding model for the time evolution of this reaction system can be written as:

$$\begin{aligned} \frac{d\text{N}_2^+}{dt} &= -k_1[\text{H}_2]f\text{M}^+ - k_2[\text{H}_2]f\text{M}^+ \\ \frac{d\text{N}_2\text{H}^+}{dt} &= k_1[\text{H}_2]f\text{M}^+ \\ \frac{d\text{H}_2^+}{dt} &= k_2[\text{H}_2]f\text{M}^+ - k_3[\text{H}_2]\text{H}_2^+ \\ \frac{d\text{H}_3^+}{dt} &= k_3[\text{H}_2]\text{H}_2^+ \\ \frac{d\text{CO}^+}{dt} &= -k_4[\text{H}_2](1 - f)\text{M}^+ \\ \frac{d\text{HCO}^+/\text{HOC}^+}{dt} &= k_4[\text{H}_2](1 - f)\text{M}^+ \end{aligned} \quad (\text{A.10})$$

This system of coupled first order differential equations can be solved analytically¹³. Using the solution of this system, all nine measurements were fitted with a least-square-method at once. The fit of four of these measurements by a single set of rate-coefficients with different amounts of N_2 in the source at 21 K are shown in Fig. A.11. Table A.2 summarizes the calculated rate coefficients, the N_2 pressures and fraction of f of N_2^+ ions. The value for k_1 is in accordance with values from

¹³Calculated with mathematica.

other experiments^[106–109] and with the calculated Langevin rate coefficient. The branching of the first reaction in the products N_2H^+ and H_2^+ is by a factor of two greater as reported by Schultz and Armentrout [109]. The value for k_3 is slightly higher than the reported value by Clow and Giese[112, 113]. Furthermore, the value of f for no N_2 in the source, estimated using the isotopes, is in the same range as the value calculated by the global fit of the data set.

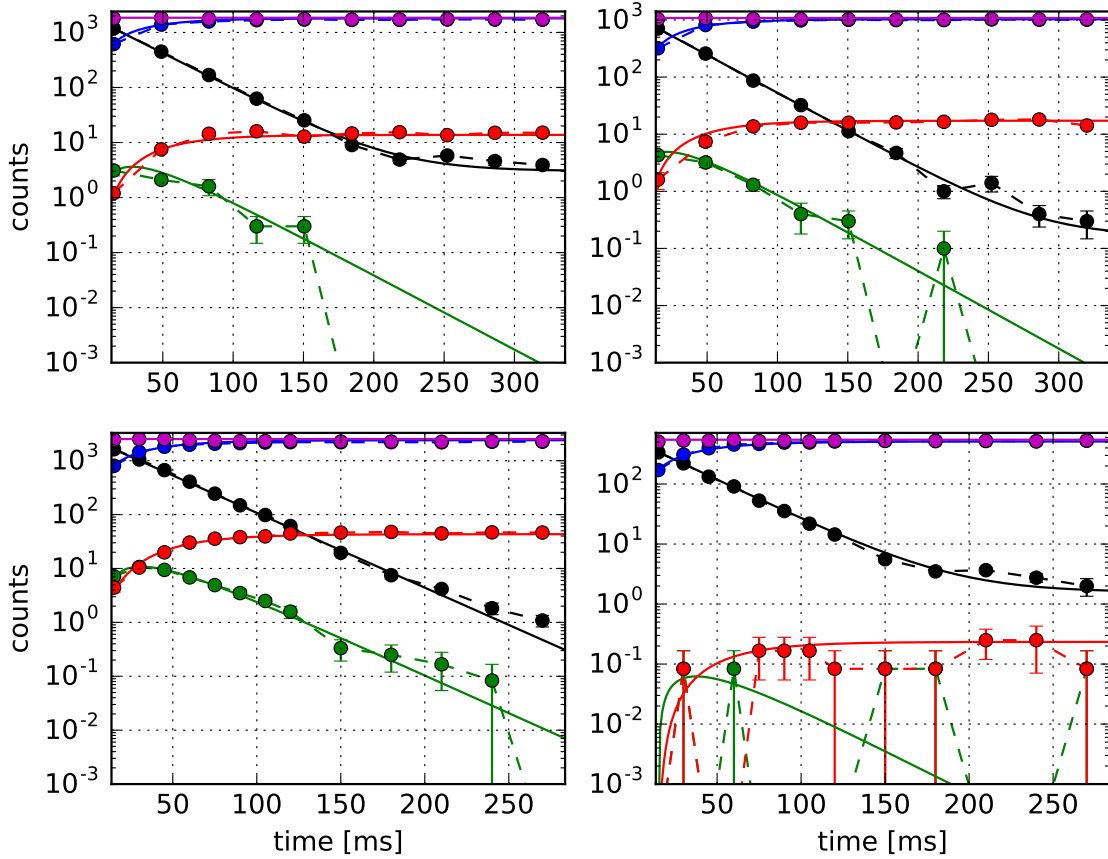


Figure A.11: The plots show the time evolutions of reaction A.9 for four different N_2 -pressures in the ion-source at 21 K and a constant number density of H_2 of $(2.09 \pm 0.05) \cdot 10^{10} \text{ cm}^{-3}$. The black dots indicate the decrease of the N_2^+ and the CO^+ ions. The green and red dots indicate the number of H_2^+ and the H_3^+ ions, respectively. The blue dots are the number of the N_2H^+ and the $\text{HCO}^+/\text{HOC}^+$ ions. The solid lines indicate the fit. The pressure measured at the first QMF from the upper left to the lower right are $4.6 \cdot 10^{-9} \text{ mBar}$, $6.2 \cdot 10^{-9} \text{ mBar}$, $1.0 \cdot 10^{-8} \text{ mBar}$ and $1.9 \cdot 10^{-8} \text{ mBar}$. (The last pressure corresponds to the background pressure measured at the first QMF after 2 days of pumping the whole apparatus.) The rate coefficients calculated for this measurements are given in table A.2.

pressure [mBar]	$1.9 \cdot 10^{-9}$	$4.6 \cdot 10^{-9}$	$6.2 \cdot 10^{-9}$	$1.0 \cdot 10^{-8}$
f	0.03	0.42	0.61	0.91
k_i [cm^3/s^{-1}]	k_1	k_2	k_3	k_4
	$1.50 \cdot 10^{-9}$	$3.72 \cdot 10^{-11}$	$2.60 \cdot 10^{-9}$	$1.42 \cdot 10^{-9}$

Table A.2: The calculated rate coefficients, N_2 pressures and the ratio of $f = N_2^+/(CO^+ + N_2^+)$ for the measurements shown in Fig. A.11 at 21 K.

The calculated rate coefficients for reaction A.2 varies more or less around the theoretic calculated Langevin-rate of $k_L = 1.52 \cdot 10^{-9}$ [cm^3/s^{-1}]. Apart from the small deviation one can assume that the temperature behavior of the calibration for the number density is correct in a temperature range from 10-100 Kelvin.

A.3.4 The Number Density of the Reaction Gas at Low Temperatures

Since the number density is calculated from the difference between the pressure measured with and without reaction gas (section 6.1.1), one has to assume that this difference is not changing during the whole measurement. Due to problems with respect to the reproducibility of the measured rate coefficients this assumption was investigated. Therefore, the apparatus was cooled down to a specific temperature and the background pressure was measured. Afterwards, H_2 was injected in the 22-pole-trap until the pressure, measured at the ion-gauges, reached a constant. During this time (1.5 h) the temperature and pressure was recorded. Figure 6.6 shows a measurement at 10 K. It can nicely be seen that the stability of the pressure can not be assumed. Small variations in the temperature leads to large fluctuations in the pressure. The reason for this is the effect of cryosorption^[76], that means that H_2 (and also other gases) will freeze out at the inner walls of the housing of the 22-pole-trap. Since cryosorption effects are strongly temperature depended, a small change in temperature results in a change of the pressure due to adsorption and desorption of H_2 . Figure 6.6 shows that this effect of changing temperature appears randomly and can not be predicted. Furthermore, this fluctuations in the pressure are significant enough to influence the measured reaction rates. Since no heating is applied to the coldhead in order to increase the temperature, problems in the thermal contact of the heating wires around the coldhead can be excluded in this case. Therefore the temperature variations must be a consequence of an imperfect cooling of the coldhead. To overcome this problem, one has to measure the pressure during the whole measurement in order to correct this effect afterwards. Unfortunately, this is not possible due to the fact, that for trapping and thermalizing the ions an initial helium buffer-gas pulse is used which distorts the pressure measurement. Another possibility is to record the temperature during the whole measurement and delete measured points at times where temperature fluctuations are detected. Figure A.12 shows such a measurement for the reaction with N_2^+ with hydrogen (Eq. A.2) at 10

K for 200 iteration at four different measured trapping times on the depletion curve of the N_2^+ ion. As can be seen, a change in the temperature leads to a change in the reaction rate (middle plot Fig.A.12). In terms of the measured rates this also demonstrates, that the pressure fluctuations, which can only be measured outside of the trap, are obviously present inside of the trap. In order to get the most reliable results one has to accumulate a large number of measurements and decide based on the fluctuations in the temperature and the rates if they can be used. Obviously, this technique is associated with a huge time effort. Since cryosorption effects are temperature dependent, the described problem is reduces towards higher temperatures $\gtrsim 20$ K H_2 .

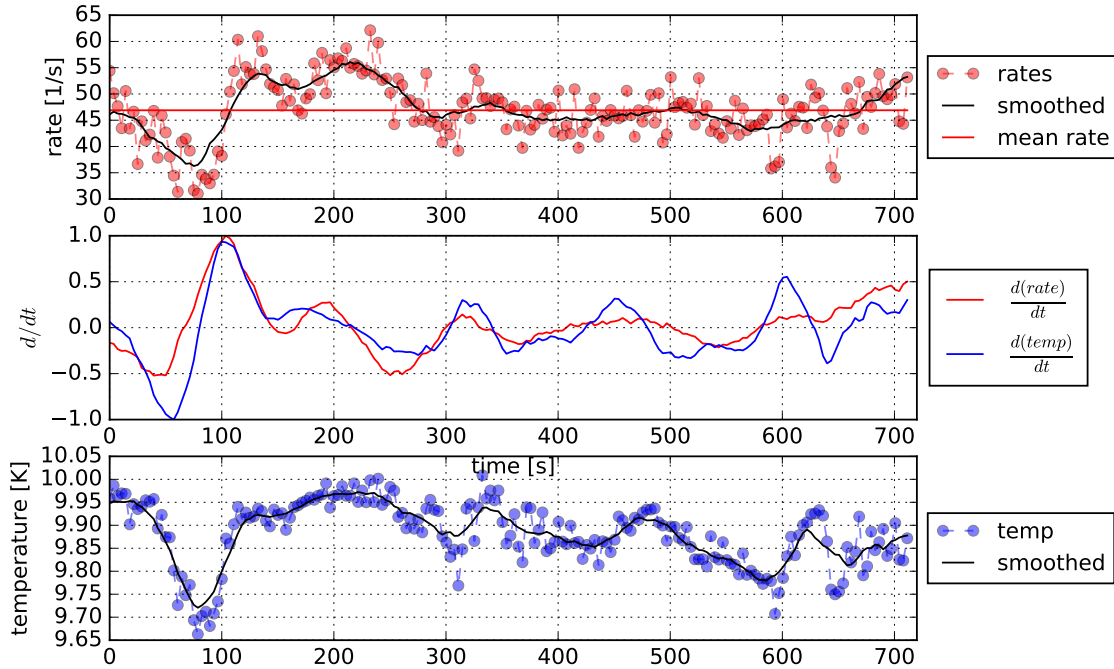


Figure A.12: The plots show a measurement of the reaction $N_2^+ + H_2 \rightarrow N_2H^+ + H$ (see eq. A.2) for 200 iterations at four different measured trapping times at around 10 Kelvin. 4 measurements are grouped together in order to fit an exponential decay to the depletion curve of the primary ion N_2^+ . In the upper plot each blue dot shows the calculated rates where 4 measurements for each 4 different measured trapping times (16 single measurements) are grouped together in order to fit an exponential decay to the depletion curve of the primary ion N_2^+ . The lower plot shows the corresponding temperature grouped in the same way. The solid lines in the upper and lower plot indicate the smoothed data. The middle plot shows change of the rates or temperature w.r.t. the time, calculated from the smoothed data.

Another important factor for the determination of the number density is the stability of the valves for injecting gas into the apparatus. It is necessary to ensure that the used leakage valves¹⁴ are stable for several hours, because the time requirements for a typical experiment are usually in the range of 3-10 hour. Since the gas flow

¹⁴pfeiffer-vacuum UDV 040

rate through the leakage valves can be very low in our experiment (especially for fast reactions), the stability of this flow is very sensitive to small changes in the room temperature. In order to minimize the effect of drifting pressures during the measurements due to low gas flows through the leakage valves one could use a higher flow rate and split the flow into a low one guided into the trap and a larger one that will be guided into a turbo pump.

A.3.5 Measuring Rate Coefficients during the Cool Down Phase of the Apparatus

In order to speed up the measurement of rate coefficients over several temperature ranges, the following measuring technique was tested based on the reaction of $\text{CO}^+ + \text{H}_2 \rightarrow \text{HCO}^+ + \text{H}$ (last Eq.A.9): Because of the large rate coefficient and the temperature independence, this reaction is very sensitive to small fluctuations of reaction gas pressure and therefore is used to improve this technique. The following steps describe the used measuring process.

1. Performing the steps of a typical measurement (section 6.1.1).
2. Starting the coldhead to cool down from 300 to 10 Kelvin.
3. Applying a heating current to slow down the rate of cooling the trap.
4. Measuring 4 points at the exponential decay of the depletion curve of the CO^+ ions during the whole cooling down phase.

Figure 6.7 shows a measurement in temperature range from 10-100 Kelvin (the different colors mark different measurements). The rates were calculated by grouping all measurements within a temperature range $T \pm \Delta T$ together (maximum 6 measurements) to fit an exponential decay of the depletion curve of the CO^+ ions. Taking into account the number density of the reactions gas as a function of temperature, the fitted rates were multiplied by \sqrt{T} additional. As can be seen, in the range from 100 to ≈ 25 Kelvin the rates slightly increase. Below 25 Kelvin the rates decreases strongly initially and increase again later. The lower the temperature, this effect is the more pronounced. A reason for the small increase of the rates above 25 K could be an increase of the pressure of the reaction gas due to drifting effects of the leakage valves. The initially observed strong decrease below 25 K is caused by adsorption of the H_2 . Here, the H_2 is freezing out at the inner walls of the trap housing which results in the observed decrease of the rate. After a certain time, all inner surfaces are saturated with H_2 and the number densities rise again in terms of the increase of the rates. Thus, this method can lead to huge errors of the measured rate coefficients.

Therefore, the usage of this technique in order to determine rate coefficients efficiently and accurately as function of the temperature is not very appropriate. Figure A.13 reveals a further problem which occurs using the above mentioned technique. This plot shows a measurement of the cooling down phase of the apparatus to

10 K followed by a heating up to ≈ 25 Kelvin with N_2 gas in the storage ion source. As can be seen the background pressure decreases with decreasing the temperature of the trap. This effect can cause too low calculated reaction gas densities which will result in an additional error for the determined rate coefficients.

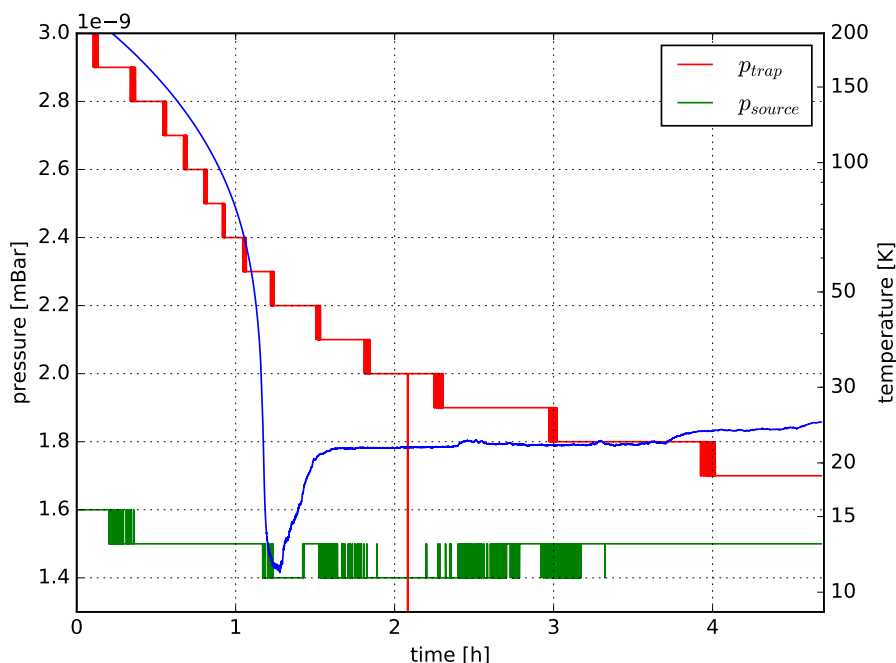


Figure A.13: The plot shows a measurement of the cooling down of the apparatus to 10 Kelvin followed by a heating up to ≈ 25 Kelvin with N_2 gas in the storage ion source. The red and green line indicate the pressure measured at both ionization gauges at the first QMF and the chamber of the 22-pole trap. The blue line shows the temperature.

A.3.6 Steady State of the Apparatus

To calculate the number density of the neutral reactant from the pressure measured at the ionization-gauge in the trapping chamber, one has to assume that the gas flow in and out of the 22-pole trap is in an equilibrium. To investigate this assumption the reaction $N^+ + n-H_2 \xrightarrow{k_{f,1}} NH^+ + H$ was used. For this the apparatus was cooled down to 10 K and the leakage valve for the H_2 gas was opened. The decrease of the N^+ ion was recorded at two fixed trapping times and the rate of the reaction was calculated. Additionally the pressure in the trap chamber was recorded. This measurement was performed within 4 hours. Figure 6.8 illustrates impressively that the above mentioned assumption is a function of time. It can be seen that outside the trap an almost stable pressure is measured¹⁵. The determined rates suggest that this is not true inside the trap. In terms of the rates, a steady state of the

¹⁵The steep decrease of the calculated rates for $t \leq 0.25$ h is a consequence of the abrupt pressure increase after opening the gas valve.

gas flow is reached after ≈ 2 hours with respect to the time since opening the valve for the neutral reactant. The apparent reached stable H_2 pressure after $t \approx 0.5$ h is increasing until the end of the measurement of about $\approx 3\%$ while the calculated rate is increased by $\approx 65\%$. As a result of this behavior, the rate coefficients are systematically smaller if the experiment is performed in a time interval of 0.5-1.5 hours after opening the neutral gas valve. As a consequence of this, fluctuation by more than 50% in the estimated rates at different days can appear. This behavior is due to cryosorption effects of the neutral reactant and probably a function of the trap temperature which should be investigated in more detail. Since this problem was not taken into consideration at the beginning of this thesis, the smaller rate coefficients and their large fluctuation below ≈ 25 Kelvin (see Fig. 6.3 black dots) could be explained. For temperatures above 25 Kelvin this effects should be significantly smaller and should not influence the measured rates (Fig. 6.3 black dots).

A.3.7 Improving the Measurement Procedure

In this section, an improved measurement strategy will be given with respect to the reaction 8.3.

The depletion of the primary ion N^+ was recorded at four different trapping times (4-point measurement) for a certain temperature and H_2 pressure. This allows to increase the number of performed measurements within a sufficient period of time. In dependence of the temperature, up to 100 measurements could be accumulated which help to reduce the statistical errors. For the calculation of the rates $\tilde{k}_{f,1}$ (see Eq.6.6), 10 measurements were grouped together and an exponential decay was fitted to that curves in order to identify possible changes in the experimental condition. Using this strategy, measured points where changes in the experimental condition occur e.g. a temporarily rising of the reaction gas pressure as a consequence of adsorption effects, can be identified and excluded. Additionally, all measurements can be grouped together and can be compared to the smaller grouped measurements. Figure A.14 shows a measurement performed with the strategy mentioned above. For reasons of clearness only two of ten grouped measurements are plotted (red and blue dots). Also the average of all 100 measurements are plotted (black dots). Figure A.15 (upper plot) shows the calculated rate $\tilde{k}_{f,1}$ (blue) for all ten grouped measurements as a function of time to perform the whole measurement. Furthermore, the average of the calculated rate $\tilde{k}_{f,1}$ of all 100 measurements (black) is plotted. The lower plot Fig. A.15 shows the nominal trap temperature as a function of time for the whole measurement.

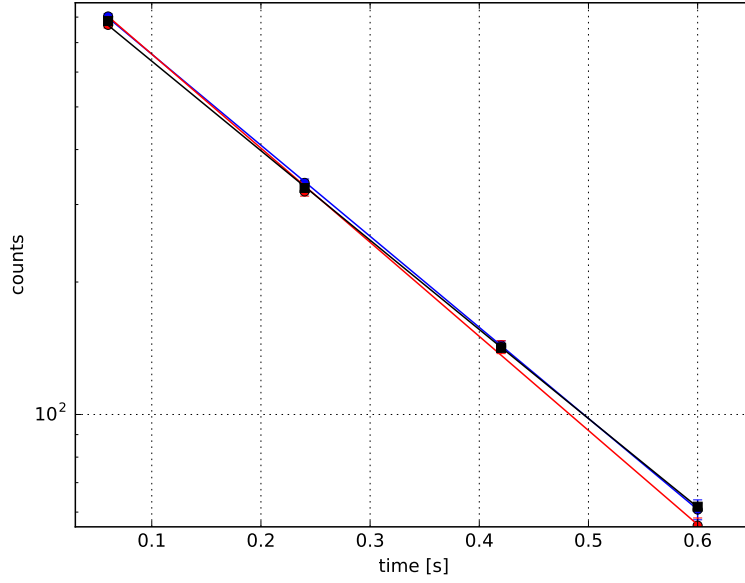


Figure A.14: The plot shows a 4-point measurement of the decrease of the N^+ ions at 24 K and a H_2 number density $[n_{H_2}] = 1.02 \cdot 10^{11} \text{ cm}^{-3}$. The red and blue dots indicate two (singly averaged about 10 measurements) of ten measurements. The black dots indicate the average of all 100 measurements. The lines correspond to the fitted mono exponential decays of the N^+ ions.

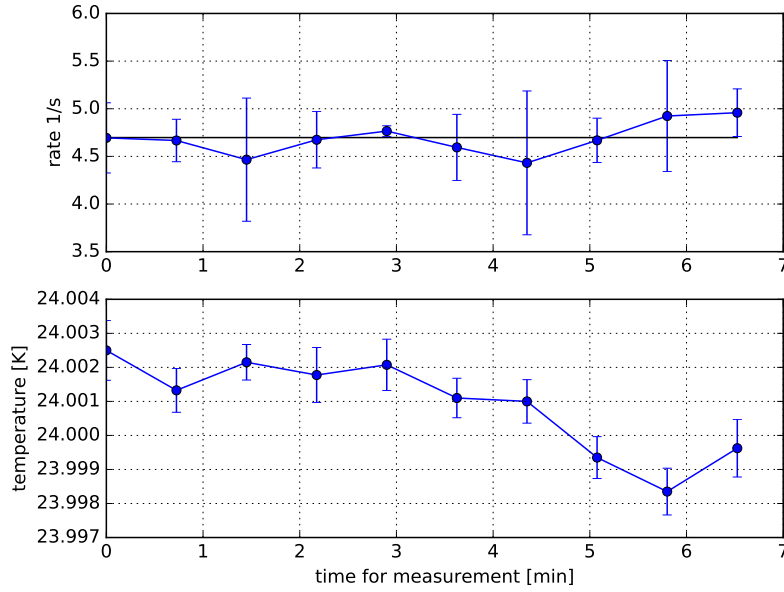


Figure A.15: The upper plot shows the calculated rates $\tilde{k}_{f,1}$ for ten grouped measurements (blue) and the rate calculated from the average of all 100 measurements (black line) as a function of the measurement time at ≈ 24 Kelvin. The lower plot show the corresponding nominal trap temperature as a function of the time.

In order to increase the accuracy of the determined rate coefficients the measurements should be performed for different H_2 pressures at a fixed trap temperature. Here, the advantage is that the rate coefficients $k_{f,1}$ can be calculated from the relative change of the reaction rate $\tilde{k}_{f,1}$ as a function of the number density (Eq. A.11). In contrast to the determination of the rate coefficient using only a single measurement at a certain H_2 pressure, this method is less susceptible to small experimental drifts.

$$\tilde{k}_f = k_{f,1} \cdot [H_2] \quad (\text{A.11})$$

Figure A.16 shows this linear dependence for a 10 K, 13.3 K and for 24 K measurement. The large uncertainties in the H_2 number density at 10 K and for 13.3 K are a consequence of the cooling cycle of the cold head (repetition rate of 1 Hz) and the cryosorption effect of the neutral reaction gas at temperatures below ≈ 25 Kelvin. As can be seen in this figure an additional offset has to be taken into account to fit a linear behavior. Therefore a constant b was added to Eq. A.11.

$$\tilde{k}_f = k_{f,1} \cdot [H_2] + b \quad (\text{A.12})$$

This offset could be partially explained with the delay of the equilibrium between the number density inside and the pressure outside of the trap, mentioned in section 6.3.1. If the measurements are performed too early, the derived rates are too small which could explain a negative rate at zero H_2 number density. Such an offset was also observed for the measurements of the reaction of N_2^+ with H_2 (section 6.3.1). This offset could also be a consequence of the evaluated number density of the hydrogen pressure measured outside of the trap. As mentioned in section 6.1.1 the number density of the neutral reactant is calculated from the difference of the background pressure p_{back} and the measured pressure of the reaction gas. Figure A.13 shows a measurement of the cooling down of the apparatus to 10 Kelvin followed by a heating up to ≈ 25 Kelvin with N_2 gas in the storage ion source. This plot nicely illustrates that an equilibrium background pressure is not completely achieved after 4.5 hours after starting the cooling phase of the trap. This effect can cause a too low calculated reaction gas density depending on the reaction gas pressure and as a function of time. A too large value of the calibration factor f_{cal} (Eq. 6.1) for the hydrogen calibration which would lead to a too large number density could not compensate this effect and can therefore be excluded most likely. Since the temperature behavior of the calibration of the number density should also be correct (section 6.3.1), it is not clear yet which effect causes this offset. Probably there is a complex interplay between the pressure measured by the ion gauge outside the trap, cryosorption effects below 25 Kelvin, the calculation of the background pressure p_{back} and the time of the measurement w.r.t. time of opening the valve for the neutral reaction gas. To clarify this problem and to investigate into the influence of this effect on the accuracy of the calculated rate coefficients in more detail, more measurements should be performed. Since all measurements for determining the rate coefficient as a function of the temperature show a linear dependence between

the number density and the reaction rate $\tilde{k}_{f,1}$ one can conclude that the calculated rate coefficients (see Fig.6.3) are correct.

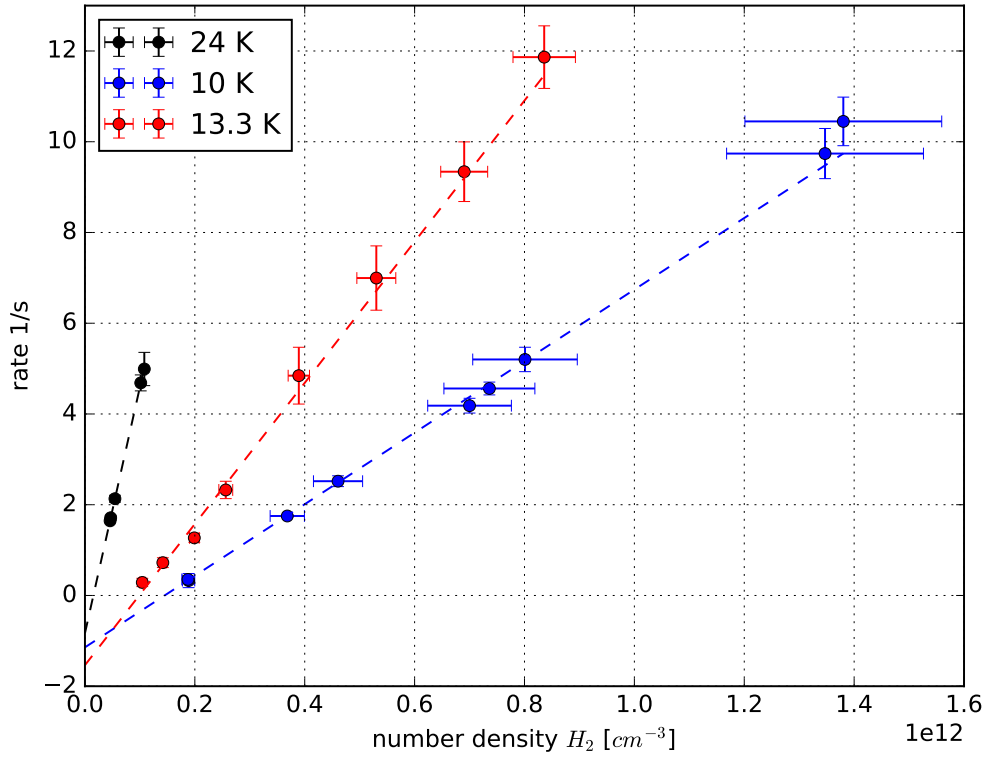


Figure A.16: The plot shows the linear dependence of $\tilde{k}_{f,1}$ as a function of the H_2 number density for a 10 K, 13.3 K and for 24 K measurement. The dashed lines indicate the fitted linear dependence of the rate coefficient $k_{f,1}$ (eq. A.12)

A.4 The $N^+(^3P_{ja}) + H_2(j)$ Reaction

A.4.1 A Simple Approach for the Analysis of Reaction $N^+ + H_2(j)$

A first approach to evaluate the temperature dependence of the rate coefficients for reaction



is to use a simple Arrhenius function

$$k(T) = k_A \cdot \exp(-T_A/T) \quad (A.14)$$

where $T_A = E_A/k$ is the activation temperature, E_A is the activation energy and k is the Boltzmann constant. The fit to the measurements using the normal- H_2 sample (black circles) show a rather bad agreement with the data. From this an activation temperature of $T_a = 41.66$ K could be calculated. Using a simple Arrhenius function in order to describe the measurements of the para- H_2 sample is not reasonable. Nevertheless, the much steeper decline of the rate coefficient above ≈ 40 K measured with the para- H_2 sample (green circles Fig. A.17) is a clear indicator that the rotational energy of the Hydrogen ($j=0,1$) plays a significant role in promoting reaction 7.1.

As can be seen Fig. A.17 the fitted curves using Eq. 7.3 show a good agreement with the measured data. The following effective rate coefficients (in $10^{-10} \text{ cm}^3/\text{s}$) could be determined from the fit:

$$k_{eff}(T, f = 0.75) = 1.03 \exp(-26.44/T) + 4.01 \exp(-69.91/T) \quad (A.15)$$

and

$$k_{eff}(T, f = para) = .02 \exp(-27.74/T) + 6.43 \exp(-187.65/T). \quad (A.16)$$

As can be seen, the activation temperature in the first term of Eq. A.15 and A.16 are comparable in contrast to latter ones. Since the reaction with ortho- H_2 is less temperature depended, these first term in can be interpreted as the temperature dependence of the rate coefficient with ortho- H_2 . From this one can calculate that the used para- H_2 sample contains some $o - H_2$ of $f = 0.015 \pm 0.005$. Due to large the deviations of activation temperature in the last term of Eq. A.15 and A.16, a similar interpretation for temperature dependence of the rate coefficient with para- H_2 within this approach is not possible.

Table A.3 summarizes the results from this and from previous works using the above mentioned approaches.

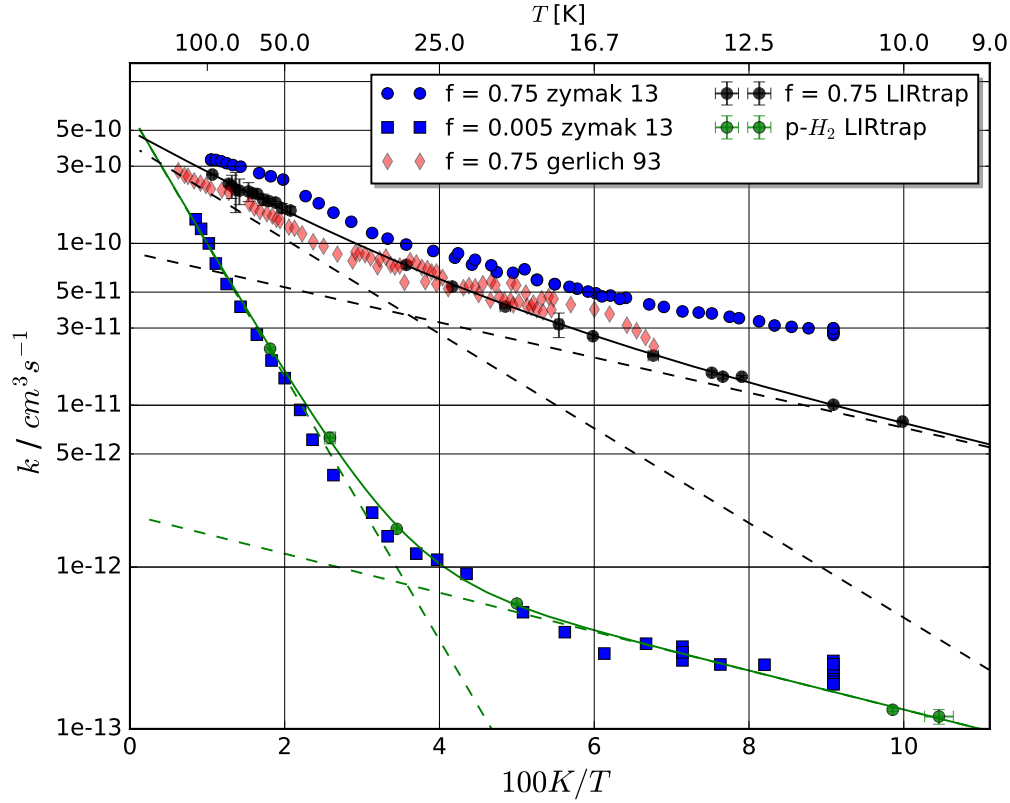


Figure A.17: Arrhenius plot of experimental rate coefficients for reaction 8.3 with $n\text{-H}_2$ and $p\text{-H}_2$ from the actual measurements and previous experiments (see legend). The black and green dashed lines indicates the individual contributions of two Arrhenius functions. The black and green solid corresponds to sum of both Arrhenius functions. The errors are calculated from the statistical deviation of the least squares fit.

k_A [$10^{-10}\text{cm}^3/\text{s}^{-1}$]	T_A [K]	Notes	Reference
4.16	41.9	$n\text{-H}_2$	Marquette ^[77]
8.35	168.5	$p\text{-H}_2$	
4.06	42.5	$n\text{-H}_2$ from (27-45 K)	Gerlich ^[116]
15.3	177.5	$p\text{-H}_2$	
1.1	26	$n\text{-H}_2$ from (10-40 K)	Gerlich ^[84]
14.0	230	$p\text{-H}_2$	
3.76 ± 0.14	41.66 ± 0.84	$n\text{-H}_2$ mono exponential fit	this work
4.01 ± 0.19	69.91 ± 7.37	$n\text{-H}_2$ $T > 40$ K	
1.03 ± 0.35	26.44 ± 3.25	$T < 40$ K	
6.43 ± 1.25	187.65 ± 9.05	$p\text{-H}_2$ $T > 40$ K	
0.021 ± 0.004	27.74 ± 1.93	$T < 40$ K	

Table A.3: Parameters of a least square fit of a simple Arrhenius-type function for reaction 8.3 with $n\text{-H}_2$ and $p\text{-H}_2$.

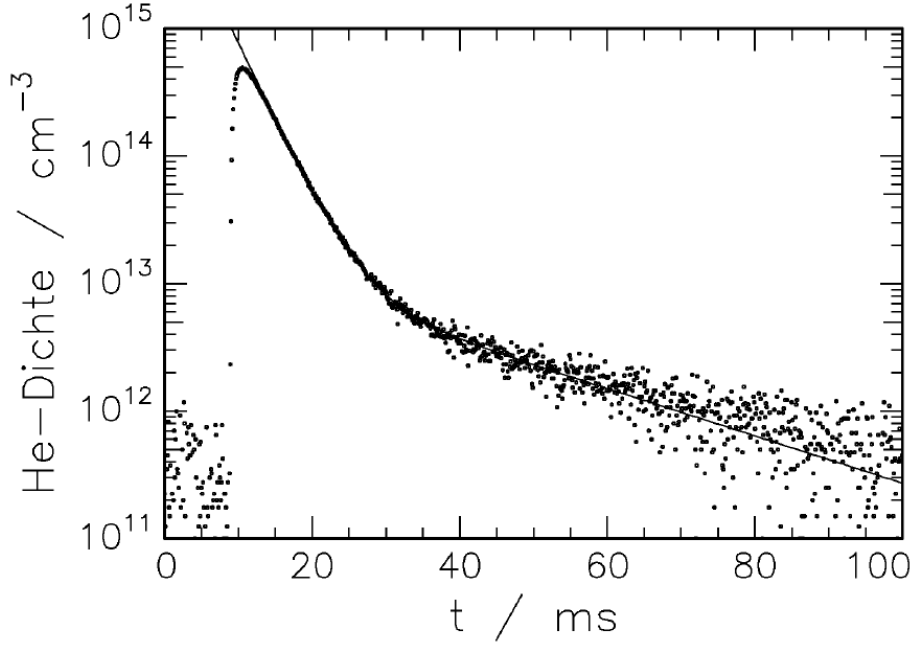


Figure A.18: Time dependent Helium density in the 22-pol trap for a $\approx 100\mu s$ pulse via the piezo electric valve. The pulse can be described via exponential decay by two time constants of 3.5 ms and 23 ms. The plot was taken from A. Sorgefrei [70]

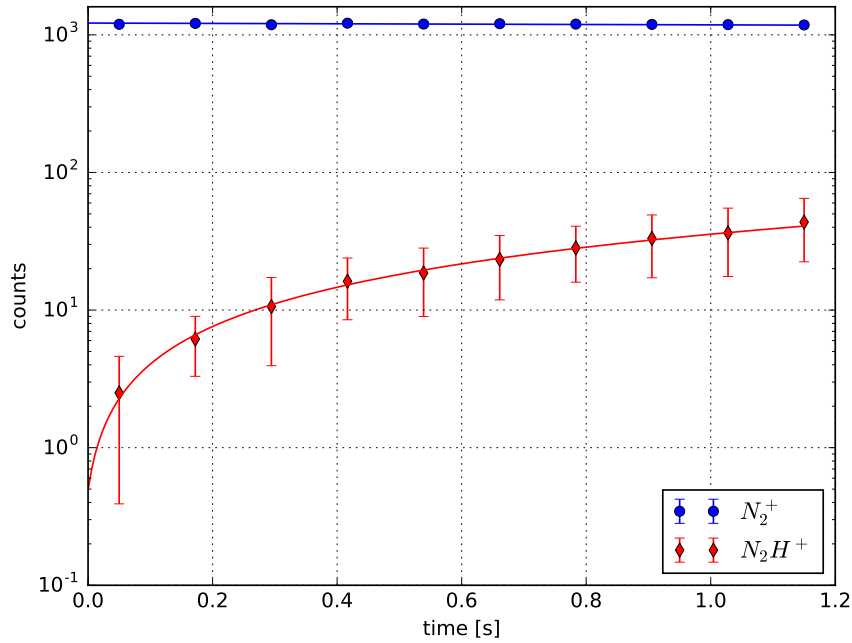


Figure A.19: The plot shows a measurement of N_2^+ with Helium $[He] = 1.77 \cdot 10^{14} \text{ cm}^{-3}$ at 16 K.

A.5 The Ternary Reaction of

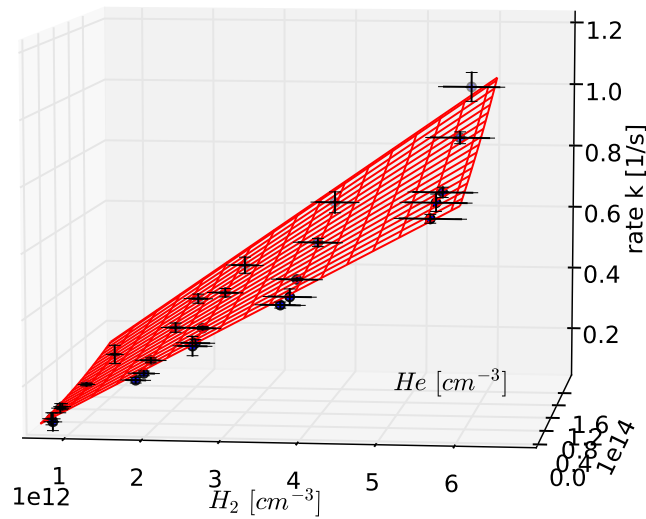
$$\text{N}^+ + \text{H}_2 + \text{He} \rightarrow \text{NH}_2^+ + \text{He}$$


Figure A.20: The plot shows the measured rates k as a function of the Hydrogen and Helium number density at 10.15 K. The red surface shows the fit via the ternary model.

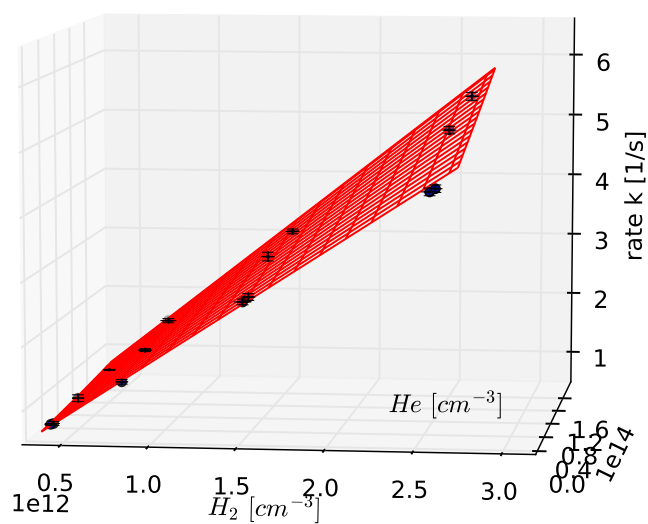


Figure A.21: The plot shows the measured rates k as a function of the Hydrogen and Helium number density at 29 K. The red surface shows the fit via ternary model.

A.6 Characterization of a Piezoelectric Valve

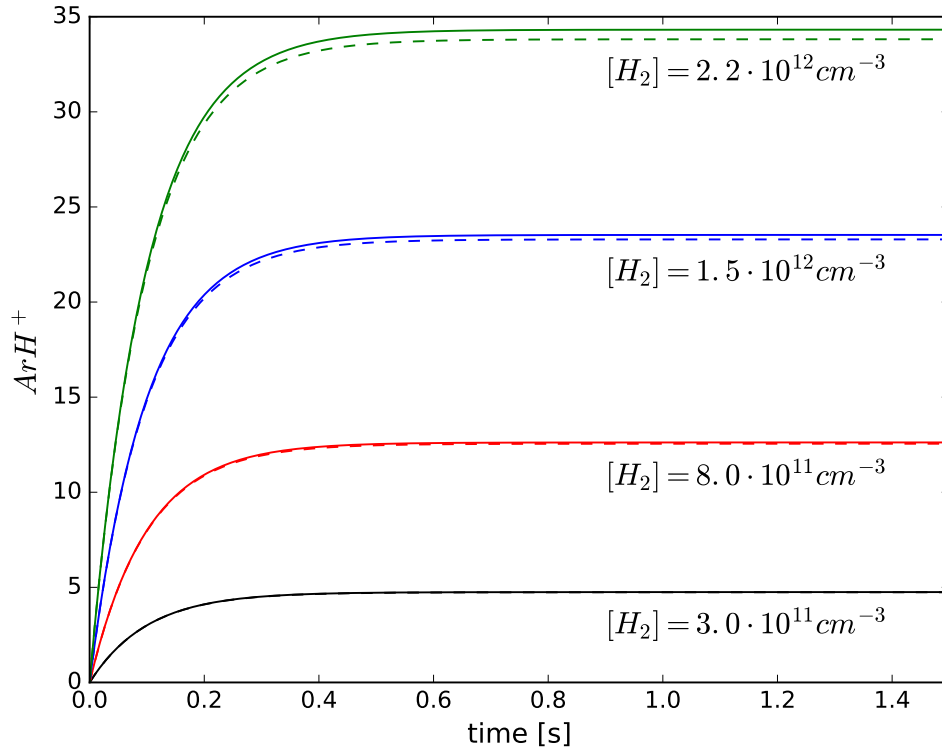


Figure A.22: The plot compares the increase of the ArH^+ ions assuming a $\tilde{b} = 10 \text{ s}^{-1}$ (see Eq. 10.12) and substituting the Eq. 10.11 for the reaction gas flow $[Rg(t)]$ in the simple reaction model Eq. 10.6 (solid lines) and into the more sophisticated reaction model 10.19 (dashed lines) for different Hydrogen number density as indicated. The values for the cross section are taken from Tab. 10.1. An effective reaction path length of 4.4 cm is assumed.

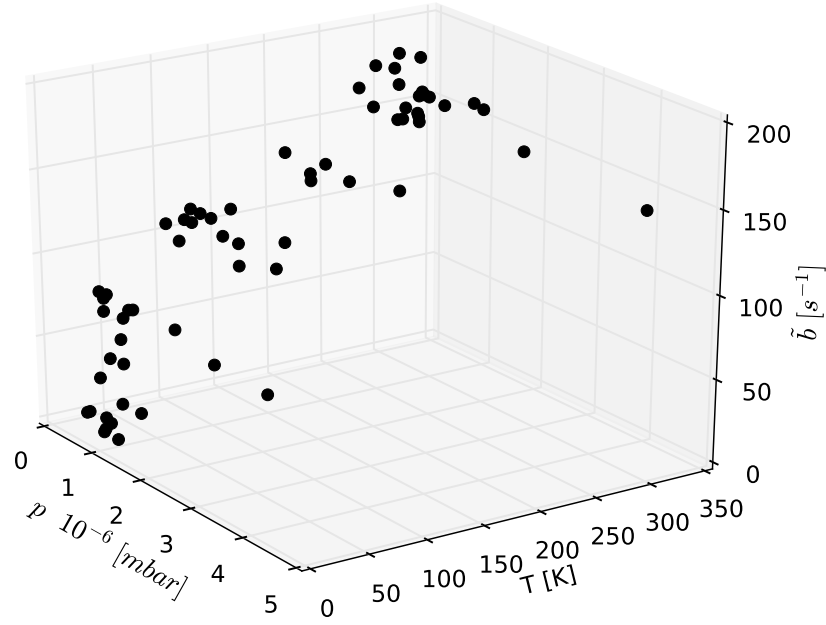


Figure A.23: The plot shows \tilde{b} as a function of the temperature and pressure determined from decaying of the ArH^+ ions.

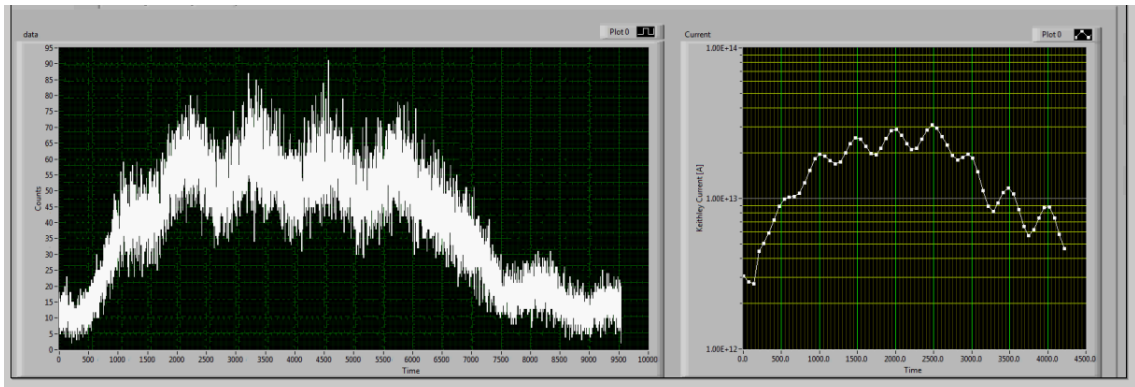


Figure A.24: The plot shows a screen shot of the labview program to record the measurements. The left window shows a time of flight measurement at 12 K trap temperature with Ar^+ and a H_2 tickling pulse with a width of 5.5 s. The white lines in the left window shows the increase of the ArH^+ ions and the right panel shows the pressure measured outside of the trap a function of the time. Nicely visible are the oscillations in the pressure (right) and the ArH^+ ions (left) with a frequency of 2 Hz. This is exactly the frequency of the 10 Kelvin cold head which means that the oscillations are a consequence the oscillating cold head power and cryosorption effects where Hydrogen molecules are freezing out the inner wall of the 22-pole trap.

Danksagung

Danke, liebe **Esther**, für die Unterstützung, die Aufmunterung, deine Geduld und für alles andere während der Erstellung dieser Doktorarbeit.

Ganz besonders danken möchte ich Prof. Dr. Stephan Schlemmer für die Betreuung dieser Arbeit, für sein kontinuierliches Interesse und die intensiven und anregenden Diskussionen, welche immer wieder zu neuen Impulsen und Ideen führten.

Bedanken möchte ich mich weiterhin bei Prof. Dr. Gereon Niedner-Schatteburg für die Übernahme des Zweitgutachtens und bei Prof. Dr. Joachim Krug für den Vorsitz im Prüfungskomitee.

Weiterhin möchte ich mich bedanken bei Oskar Asvany für seine lockere Art, den Wortwitz, für die Beantwortung aller meiner Fragen und das Korrekturlesen dieser Arbeit.

Ein weiteres Dankeschön an das Problemlösebüro Hanno, Christoph und Stefan, für die tollen, oft sehr lustigen Diskussionen, nicht nur über Physik. Tausend Dank an Nadine Wehres, Thomas Salomon, Sven Thorwirth, Sandra Brünken, Sabrina Gärtner und Super-Marius 'es ist noch Eis im Kühlschrank' Hermanns für das Korrekturlesen einzelner Kapitel dieser Arbeit. Bedanken möchte ich mich auch bei Dr. Frank Schlöder für die großartige und immer schnelle Hilfe bei Computer-Problemen aller Art.

Danke auch an die der Entspannung dienlichen und lustigen Mittagspausen nach der Mittagspause im Problemlösebüro mit Oli, Hanno, Marius und all den anderen. Darüber hinaus geht mein Dank an die gesamte MolSpek Gruppe für die großartige Arbeitsatmosphäre und an alle weiteren Personen, die ich an dieser Stelle vergessen habe und die mich während dieser Zeit unterstützt haben.

Ein großes Dankeschön auch an alle meine Freunde außerhalb der Physik, besonders an meine Band 'Cobretti' für das Verständnis, dass ich in der Schreibphase dieser Doktorarbeit nicht immer die Zeit hatte, mich vollständig einzubringen.

Vielen Dank auch an meine Familie für Entlastungen jeglicher Art, sei es bei der Kinderbetreuung, einem guten Essen oder gebügelten Unterhosen :-).

Zu guter Letzt: **Danke Franka** für die Ablenkung und Entspannung während unseres fortwährenden "Schulkind und Kindergartenkind " Spiels daheim :-).

Erklärung

Ich versichere, dass ich die von mir vorgelegte Dissertation selbständig angefertigt, die benutzten Quellen und Hilfsmittel vollständig angegeben und die Stellen der Arbeit – einschließlich Tabellen, Karten und Abbildungen –, die anderen Werken im Wortlaut oder dem Sinn nach entnommen sind, in jedem Einzelfall als Entlehnung kenntlich gemacht habe; dass diese Dissertation noch keiner anderen Fakultät oder Universität zur Prüfung vorgelegen hat; dass sie – abgesehen von unten angegebenen Teilpublikationen – noch nicht veröffentlicht worden ist, sowie, dass ich eine solche Veröffentlichung vor Abschluss des Promotionsverfahrens nicht vornehmen werde. Die Bestimmungen der Promotionsordnung sind mir bekannt. Die von mir vorgelegte Dissertation ist von Prof. Stephan Schlemmer betreut worden.

Ort, Datum

Unterschrift

Teilpublikationen

- S. Fanghänel, O. Asvany, and S. Schlemmer, Optimization of RF Multipole Ion Trap Geometries, Journal of Molecular Spectroscopy (2016), 10.1016/j.jms.2016.12.003.

Curriculum Vitae

Persönliche Daten:

Name: Sven Fanghänel
Nationalität: deutsch
Geburtstag: 20.10.1978, Gera
Familienstand: ledig, liiert, ein Kind

Ausbildung:

2013 - 2017: Dr. rer. nat. in experimenteller Physik, Universität zu Köln
(erwartet) "Low Temperature Collisions and Reactions in a 22-Pole Ion Trap"
2006 - 2013: Staatsexamen für das Lehramt an Gymnasien und Gesamtschulen
in Mathematik und Physik, Universität zu Köln
Staatexamensarbeit: "Pulshöhenverteilungen eines empfindlichen
Ionendetektors"
2002 - 2005: Abitur (zweiter Bildungsweg), Köln-Kolleg, Weiterbildungskolleg Köln
1995 - 1998: IHK Facharbeiterausbildung 'Zerspanungsmechaniker - Frästechnik'
SMK Präzisionsmechanik Gera GmbH

Berufserfahrung:

seit 2012: Tutor und wissenschaftlicher Mitarbeiter
I. Physikalisches Institut, Universität zu Köln
2008 - 2012: Tutor und Studentische Hilfskraft
I. und II. Physikalisches Institut, Universität zu Köln
20011 - 2012: Vertretungslehrer für Physik und Mathematik
am Gymnasium Schaurtestraße Köln Deutz
für die Jahrgangstufen 9 - 12
2010: Vertretungslehrer für Physik am Ernst-Mach-Gymnasium Hürth
für die Jahrgangstufen 7 - 10
2005 - 2011: Nachhilfelehrer für Mathematik und Physik beim Studienkreis Köln
2003 - 2006: Angestellter Detlef Meyer's Fahrradladen Köln
2000 - 2002: Angestellter Busy-P Fachgeschäft für BMX-Räder Köln

2000 : Angestellter Funbox - Actionsports Coburg
1999 - 2000: Zivildienst - Mobiler sozialer Hilfsdienst
 beim Arbeiter Samariter Bund Coburg
1998 - 1999: Angestellter als Zerspanungsmechaniker - Frästechnik
 bei SMK Präzisionsmechanik Gera GmbH

Konferenzen:

2016: ISMS 2016 - 71st International Symposium on Molecular Spectroscopy
 Champaign-Urbana, IL, USA
2015: Spectroscopy and applications of cold molecular ions
 Bad Honnef, Deutschland
2013: 2. COST-IOTA Workshop on Cold Molecular Ions
 Arosa, Schweiz

Weitere Tätigkeiten:

1996 - 2004: professioneller BMX Freestyle Fahrer